Title
Structural regulation of activity in nitric oxide synthase

Author
Knudsen, Giselle Marcelline

Publication Date
2003

Peer reviewed|Thesis/dissertation

STRUCTURAL REGULATION OF ACTIVITY IN NITRIC OXIDE SYNTHASE

by

Giselle Marcelline Knudsen

DISSERTATION

Submitted in partial satisfaction of the requirements for the degree of

DOCTOR OF PHILOSOPHY

in

Chemistry and Chemical Biology

in the

GRADUATE DIVISION

of the

UNIVERSITY OF CALIFORNIA, SAN FRANCISCO

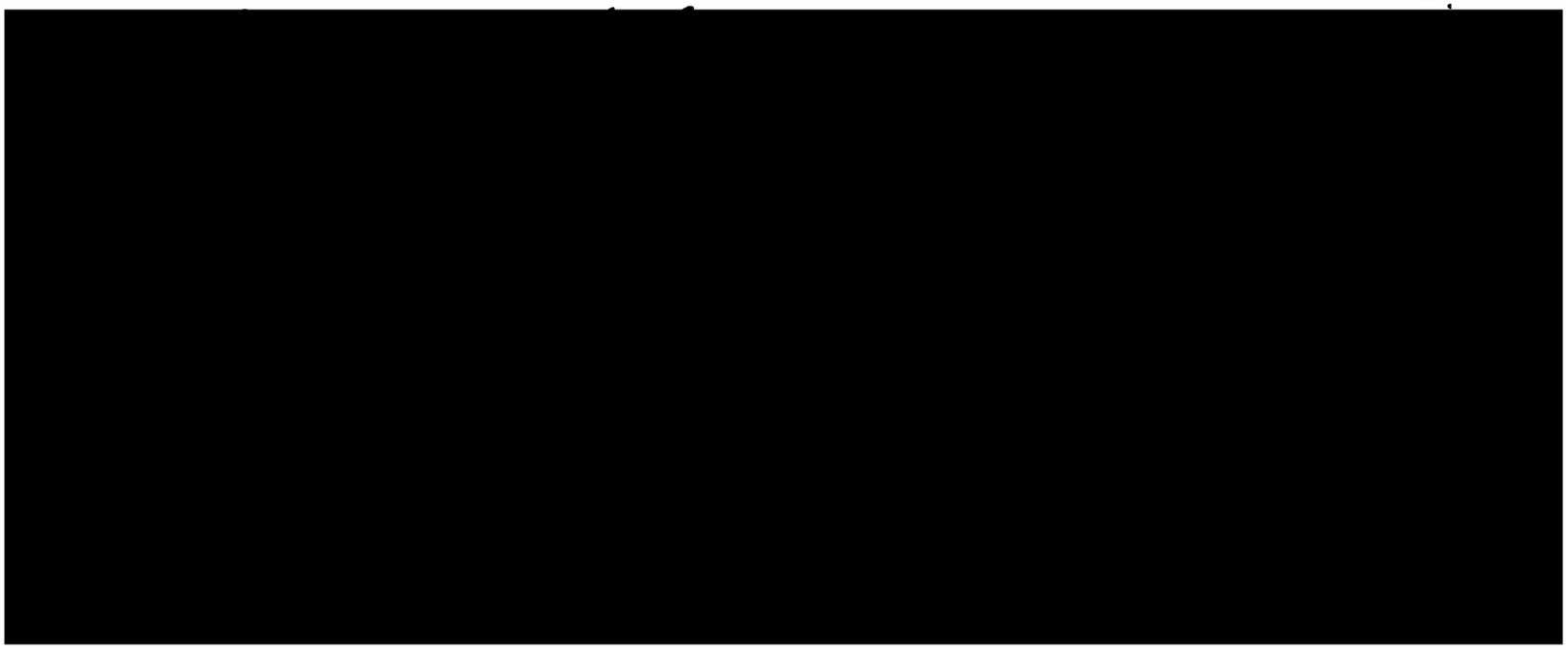

Dedication

To my family.

ACKNOWLEDGEMENTS

I am first of all indebted to my advisor Dr. Paul R. Ortiz de Montellano for understanding my ambitions and misgivings, and for supporting my successes throughout my graduate career. To Drs. R. Kip Guy, M. Almira Correia, and to Paul, I thank you for many hours of good discussions; you are the scientists that I wish to be. I have enjoyed six years of camaraderie with all the POM lab members, and we have shared many good-natured disputes/discussions, cultural exchanges, and fine wine tastings together. It has been a privilege to work with you all.

Drs. Ignacio Rodríguez-Crespo and Clinton R. Nishida deserve formal recognition, as they were the postdoctoral researchers who mentored me in the POM lab. Work with Nacho taught me genetic manipulation, expression and spectroscopic characterization of NOS and resulted in a first coauthored publication in the *J. Biol. Chem.* originally published in July 1999, and which forms the basis of Chapter 2 of this work. With the help of Dr. Sean Mooney then a student in the lab of Dr. Teri Klein, I was later able to perform a bioinformatics and molecular modeling analysis for Clinton that nicely complemented his work with splice chimeras of regulatory elements in the NOS reductase domain. That also led to a publication with Clinton and Sean in the *J. Biol. Chem.*, originally published in August 2003, and which forms the content of Chapter 3.

I also thank the Pharmaceutical Chemistry Program for giving me the opportunity to work in the UCSF intellectual environment. I am infinitely proud of the Chemistry and Chemical Biology Group that has grown out of the Medicinal Chemistry pathway that I

joined in 1997. The quality of the C.C.B. group is entirely defined by its talented students, professors and administrative staff. The new Mission Bay campus will rejuvenate a venerable program that is continuing to reshape its interests. I look forward to watching its development in the coming years.

My family brought me to this point. My grandmother Marcelline was a peasant woman with elementary education who later earned la Medialle de la Legion d'Honneur, the highest civilian honor in France. She displayed fierce loyalty during the French resistance of WWII, when she raised six children, harbored hidden fugitives, and fed many poor travelers on her farm in the Loire valley. Marcelline passed away in the fall of 2001, but her ambition, integrity, and good humor remain strong values in my family. My parents, Gisèle and Dave, gave my brother and I every opportunity in our small rural community in northern Michigan. I hope that I can achieve as much as my family has in their lives.

I met my husband Sean at UCSF. Graduate school would have been an unbalanced, exhausting experience without him, and I credit him with my every happiness during this time.

Finally, I thank you my friends and colleagues for reading my work.

THESIS ABSTRACT

Nitric Oxide Synthase (NOS) represents a family of isoforms that differ in regulation but are found ubiquitously in mammalian tissues. These isoforms serve important roles in production of NO· for neurotransmission, immune response and regulation of vascular tension. Dysregulation of NO· production by specific NOS isoforms has been linked to many diseases including arthritis, stroke, and hypertension. Therefore there is therapeutic interest in developing isoform-specific inhibitors or activators of NOS. The work in this thesis addresses enzymatic regulatory aspects that are unique to the NOS family: i) the requirement for tetrahydrobiopterin (H_4B) for catalysis of a P450-like oxidation, ii) the Ca^{2+}-dependence of Calmodulin (CaM) binding that differs between inducible and constitutively expressed isoforms, and iii) the regulation of dimerization that is highly tuned to ligand and CaM binding.

Comparison between NOS and homologous enzymes has resulted in extremely useful hypotheses for NOS regulation. By analogy with amino acid hydroxylases, the only other enzymes known to utilize tetrahydrobiopterin, H_4B was proposed to activate oxygen with the assistance of a non-heme iron for catalysis. We used site-directed mutagenesis of the proposed metal-binding histidines within the oxygenase domain, followed by UV-Vis spectroscopic characterization, to determine that NOS activation does not require non-heme redox active metals. There is evidence that instead pterin serves as a transient electron donor. Next, we addressed unique elements found only within the reductase domain of constitutive NOS isoforms proposed to mediate CaM regulation of electron transfer. Using comparative modeling techniques, we built

reductase domain models that revealed potential direct interactions between these unique elements and the CaM-binding region. These models were consistent with results from spectroscopic activity analyses of chimeric enzymes that swapped these elements between NOS isoforms. Finally, dimerization affinity differences between the NOS isoforms were analyzed, using analytical ultracentrifugation techniques to determine binding affinity between full-length or subdomain NOS constructs in the presence of various substrates and ligands. We determined that ligand-binding significantly affected dimer affinity, and the surprising result that activating conditions often destabilize dimers of the complete active complex, formed with pterin, substrate, and CaM fully bound.

Signed by Dr. Paul R. Ortiz de Montellano,

Thesis committee chair.

TABLE OF CONTENTS

LIST OF TABLES

LIST OF FIGURES

CHAPTER 1.

Figure 4-5. Sedimentation equilibrium fits of CaM-bound eNOS, in the presence of *L*-Arg and H_4B to a monomer-dimer model.

ABBREVIATIONS

AAH	aromatic amino acid hydroxylase
AI	NOS autoinhibitory element; residues 595-642 eNOS, 835-880 nNOS
AMBER	Assisted Model Building with Energy Refinement (P. Kollman laboratory)
BLAST	Basic Local Alignment Search Tool
BLAT	Blast-like Alignment Tool
$P450_{BM-3}$	CYP102 from *Bacillus megaterium*
CaM	Ca^{2+}-dependent calmodulin
Comparer	comparison program to align 3-D structures (T.L. Blundell laboratory)
CPR	NADPH cytochrome P450 reductase, P450 reductase
cyt *c*	cytochrome c^{3+}, oxidized form
DTT	dithiothreitol
eCD2A	eNOS connecting domain loop residues 834-843
EGTA	ethylene glycol bis(β-aminoethyl ether N,N,N',N'-tetraacetic acid
eNOS	NOS-III, endothelial NOS
$eNOS_{oxy}$	eNOS oxygenase domain construct with the CaM-recognition element
$eNOS_{red}$	eNOS reductase domain construct including the CaM-recognition element
eNOS(ΔAI)	eNOS with the AI element deleted
eNOS(iCD2A)	eNOS with the iCD2A loop swapped in place of the eCD2A
FAD	flavin adenine dinucleotide
FMN	flavin mononucleotide
FNR	ferredoxin reductase, 1.18.1.2
FPLC	fast performance liquid chromatography
H_4B	(6*R*)-5,6,7,8-tetrahydro-*L*-erythrobiopterin, tetrahydrobiopterin
heme	iron protoporphyrin IX
HEPES	N-2-hydroxyethyl-piperazine-N'-ethanesulphonic acid
HO-Arg	N^G-hydroxy-*L*-arginine
iCD2A	iNOS connecting domain loop residues 809-813
I/E	iNOS oxygenase and CaM domains, eNOS reductase domain
iNOS	NOS-II, inducible or macrophage NOS
$iNOS_{1-495}$	iNOS oxygenase domain construct lacking the CaM-recognition element
$iNOS_{1-531}$	iNOS oxygenase domain construct including the CaM-recognition element
IPTG	isopropyl β-D-thiogalactopyranoside
$JPred^2$	enhanced secondary structure prediction server (G. Barton group, EMBL)
***L*-Arg**	*L*-arginine
LB	Luria Broth; Miller's L Broth
***L*-Cit**	*L*-citrulline
MIDAS	program for Molecular Interactive Display And Simulation, (CGL, UCSF)
Modeller	Program for Comparative Protein Structure Modelling by Satisfaction of Spatial Restraints (A. Sali laboratory)
MSR	methionine synthase reductase, EC 1.16.1.8
NADPH	nicotinamide adenine dinucleotide phosphate (reduced form)
NOS	nitric oxide synthase
nNOS	NOS-I, neuronal NOS
NTA	nitrilotriacetic acid

P450	cytochrome P450
PAH	phenylalanine 4-monooxygenase, EC 1.14.16.1
PCR	polymerase chain reaction
Pfam	protein domain database curated by the Sanger Institute
PROCHECK	program to check the stereochemical quality of protein structures (J. Thornton laboratory, EMBL-EBI)
PROSA II	program for recognition of errors in 3-D structures of proteins (CAME)
PSI-BLAST	Position-Specific Iterative BLAST
SDS-PAGE	sodium dodecyl sulfate-polyacrylamide gel electrophoresis
SiR	sulfite reductase, EC 1.8.1.2
SiR-FP	sulfite reductase flavoprotein domain, the β-subunit
TH	tyrosine 3-monooxygenase, EC 1.14.16.2
WHAT IF	Protein Structure Analysis Program (Center for Molecular Bioinformatics)

SIGNIFICANCE

Nitric oxide synthase (NOS)[1] is responsible for production of nitric oxide (NO·), a highly reactive radical diatomic gas that has many important physiological roles. NOS comprises a family of isoforms found throughout the body, and which are defined by their dependence upon Ca^{2+}-dependent calmodulin (CaM). The inducible isoform (iNOS) binds CaM irreversibly in a Ca^{2+}-independent manner, and its expression is stimulated by cytokines and endotoxin, consistent with its critical role in the immune response (1,2). The constitutively expressed isoforms, endothelial and neuronal NOS (eNOS and nNOS) bind to CaM reversibly, and in a Ca^{2+}-dependent manner. Endothelial NOS serves an important role in smooth muscle contraction and vasodilation (3). Neuronal NOS serves a key function in neurotransmission, cell signaling (4), and apoptosis (5). Several disease states are associated with unbalanced NO· production, including inflammatory disorders, such as arthritis (6), asthma (7), stroke and shock (8,9), as well as NO· homeostasis-related diseases including atherosclerosis (10), systemic hypertension (11), kidney disease (12) and diabetes (13,14). Tissues affected by these diseases often express multiple NOS isoforms that have contrasting effects, thus it is critical that NOS-targeted therapeutics are able to selectively modify one isoform over another (14).

For example, in stroke it is proposed that NO· production serves a dual role: ischemia triggers NO· release to increase blood flow to hypoxic tissues, whereas the excess NO· present after reperfusion is connected to cellular damage (15,16). In a mouse model of cerebral ischemia, neuronal NOS has pathogenic effects partially mediated by

[1] Abbreviations are listed within the preliminary pages of this thesis, page xii.

S-nitrosylation resulting in activation of a matrix-metalloproteinase, MMP9 (17), which itself is associated with tissue damage in stroke and other neurodegenerative disorders. In other interesting experiments with NOS knockouts, a cerebral artery occlusion was created in either neuronal (18) or endothelial (19) NOS knockout mice. If the nNOS knockout mice were then treated with the general NOS inhibitor nitro-*L*-arginine, the infarct size was increased, thus inhibition of eNOS was deleterious. In the eNOS knockout mice, the infarction size was decreased by administration with the NOS inhibitor, supporting the hypothesis that it is nNOS that is partially responsible for the tissue destruction that is associated with stroke. Recent experiments using partially selective inhibitors for eNOS or nNOS in a chemical knockout study confirm the concept that a successful treatment for ischemia and stroke will need to target neuronal NOS and not affect endothelial NOS (20), thus demonstrating the requirement for isoform selective inhibitors of NOS.

OVERVIEW

Nitric oxide synthase is an exquisitely controlled enzyme due to the noxious character of its products, NO· and oxygen radicals. Understanding the differential regulation of the various NOS isoforms in various tissues and under differing physiological conditions has been the goal of structure-function analyses in the NOS field since the initial cloning and heterologous expression of the NOS genes from various species (21-25). The research presented here employs functional genomics analyses of sequence and structure to better define the functional differences between NOS isoforms

and homologous enzymes. An alignment of the three major splice-forms of the NOS isoforms is given in Appendix A for reference.

Similarity between NOS and the cytochrome P450 (P450) system was readily apparent from the cofactor requirements and oxidation reactions catalyzed by both enzymes. NOS catalyzes two P450-like oxidation steps in the conversion of *L*-arginine (*L*-Arg) to *L*-citrulline (*L*-Cit) and nitric oxide, consuming oxygen and NADPH. Identical to P450, NOS contains a thiolate-ligated heme that receives electrons from an NADPH - FAD - FMN electron transfer chain in the NOS reductase domain that is homologous to cytochrome P450 reductase (CPR). Unique to the NOS system however, is the requirement of an additional cofactor, tetrahydrobiopterin (H_4B) for catalysis.

Amino acid hydroxylases (AAH) are the only other class of enzymes known to require H_4B as a catalytic cofactor. Therefore, one interesting mechanism proposed for the function of H_4B in NOS (26) involved oxygen binding at the C4a-position of the pterin for an aromatic amino acid hydroxylase-like mechanism (27,28). This would require an additional metal-binding site to activate the pterin-dioxygen intermediate as found in the AAH. Indeed a potential "DHH" (29) motif comprised of D419, H420, and H421 (eNOS numbering) could be found near the predicted pterin binding site and is conserved in all three NOS isoforms. Although the stoichiometry of metals found bound to NOS is dependent upon the protein preparation method, stoichiometric binding of ferrous iron was reported to increase NOS activity in the iNOS and nNOS isoforms (26).

To test for the possibility of metal binding by NOS, we used mutagenesis to explore the roles of the five NOS-conserved histidine residues in the oxygenase domain

of endothelial NOS: H420, H421, H461, H146 and H214. Alanine mutants of these histidines perturbed the enzyme significantly from wild-type enzyme in all five mutants; however, more attractive structural explanations than metal loss could be found for these perturbations. Our activity assays testing for metal dependence and determination of metal-binding furthermore found no evidence that these residues formed a non-heme redox-active metal-binding site (30) (Chapter 2). A potential explanation for the binding of transition metals to wild-type enzyme was provided by the identification of a Zn^{2+} binding site between the oxygenase domains of the NOS dimeric complex (31,32). Furthermore, divalent cations were found to affect electron transfer within the reductase domain, partially explaining the inhibitory function of ions such as Zn^{2+} and Cu^{2+} (33,34).

In addition to the numerous cofactors described above, the three NOS isoforms require CaM for activity. Ca^{2+}-dependent CaM is a key regulator of NOS activity, affecting both intramolecular electron transfers between flavins within the reductase domain, and intermolecular electron transfers between the FMN of the reductase domain and the heme of the oxygenase domain. CaM is proposed to function as an activation switch by binding to a conserved recognition motif found between the oxygenase and reductase domains, and is proposed to alter the quaternary conformation of the active NOS complex upon binding. Sequence and structural bioinformatics analyses of the genetic and protein sequences of the NOS isoforms have enabled the identification of a number of unique functional elements that differ between NOS and homologous proteins, and also that differ between the inducible and constitutive isoforms. These loops, subdomains, and large domains have been extensively characterized through functional

element complementation studies in this lab and by others (35-39). Until very recently, structural information on NOS was limited to crystal structures of the oxygenase domain (40-42). Since structures of proteins with homology to the reductase domain were available, we built a model for the reductase domain of all three NOS isoforms (Chapter 3). Well into the modeling project, a partial structure of the nNOS reductase domain became available (43); therefore, it was also included as a template in our modeling analyses.

Using our reductase domain models, we were able to present a functional model for CaM recognition in relation to the various known regulatory elements, aided by the solution of the crystal structure of CaM, bound to its eNOS recognition element (44). Of particular interest are the regulatory elements that are unique to the constitutive isoforms, since these should contribute to the reversibility of CaM-binding. The most studied element, beyond the CaM recognition motif itself, is the autoinhibitory element at residues 595-642 (eNOS numbering) that is found in the constitutive isoforms. Chimeras that swap the autoinhibitory element between isoforms demonstrated its ability to inhibit electron transfer in the absence of CaM (36,38,39,45). Interestingly, an additional short loop inserted at 834-843 (eNOS numbering) is also found to be larger in the constitutive isoforms than in the inducible form. We designed and characterized chimeras that swap this short loop in wild-type protein and ΔAI chimeras, and we were able to demonstrate that this loop has its own modulatory effect on the Ca^{2+}-dependence of CaM stimulated activity (37) (Chapter 3). Both of these elements could participate in direct interactions with the CaM-binding region of the NOS reductase domain models, thus the modeling process yielded a very useful functional model for CaM-mediated regulation of activity.

Initial research in the NOS inhibition field resulted in potent substrate analogs that bind in or near the active site, yet few of these inhibitors were sufficiently isoform-selective (18). However, during recent years a new class of isoform-selective inhibitors has emerged which also bind in the active site, but function to prevent productive dimerization and activation of NOS (46). Dimerization as a form of regulation is also unique to the NOS family with respect to the P450/CPR system. In fact, NOS is an obligate dimer, where electron transfer occurs *in trans* from the reductase domain of one subunit to the oxygenase domain of the other subunit within the dimer (47,48).

To directly address the regulation of dimerization in NOS, a thorough analysis of NOS hydrodynamic properties was required to define the proper assembly model and then query for effects of ligand binding to the three different isoforms (Chapter 4). Using our sensitive and relatively non-perturbing technique of analytical ultracentrifugation, the sedimentation analysis of the three NOS isoforms has allowed us to better define the substrate dependence for the formation of the active NOS dimeric complex. A practical description of the analytical ultracentrifugation technique and data analysis is given in Appendix B. Our model for control of dimerization has predictive potential for the design of ligands that target the dimerization interface.

Once the reductase domain was modeled, the question of protein-protein interactions between the reductase and oxygenase domains as well as between the NOS and CaM was addressed (Chapter 5). These models incorporate known biochemical information to predict key subdomain interactions and their effects on electron transfer control. Active work is underway to solve the structure of the NOS "holo" complex (T.

Poulos, *personal communication*), including all required cofactors and binding partners. The only module missing from the nNOS structure is the FMN-binding subdomain, and it will be extremely interesting to compare our predictions for the holo-complex structure with that which is soon to be solved.

A complete understanding of NOS regulation will certainly require characterization of the protein-protein level interactions of NOS with other cellular regulatory proteins. These interactions can be queried using biological screening techniques such as yeast two-hybrid analyses, and the use of genetic knockout organisms. Already, much is known about NOS motifs that are recognized by various proteins, and numerous sites have been mapped onto the structure of our NOS holo-complex model. Phosphorylation is an important mode of NOS activity regulation. eNOS is phosphorylated by Akt, PKC (49-51), AMPK (52), and cyclic-nucleotide-dependent protein kinases (53); nNOS is phosphorylated by the CaM-kinases (54). Heat shock protein 90 has been shown to specifically recognize eNOS (55,56), and nNOS (57) through defined interactions that stimulate activity. Caveolin recognizes eNOS at a consensus binding motif in the oxygenase domain (55,58), and caveolin 3 also recognizes nNOS (59). Dystrophin recognizes the PDZ domain within the N-terminal portion of nNOS (60,61), serving to localize NOS to the sarcolemma membrane of skeletal muscle. Indeed, blockage or stimulation of any one signaling point within these complex pathways of interactions could serve as a reasonable method to address isoform-specific regulation of NOS.

As the structure-function aspects of NOS continue to be solved through combinations of functional units *in vitro*, and through protein-protein regulatory networks studied *in vivo*, we will soon find that multiple dimensions exist in the regulation of NOS. My family and I await impatiently the development of nNOS-specific inhibitors to target the local overactive population of nNOS protein within the brain that is involved with neurodegeneration in Parkinson's or Alzheimer's diseases, and iNOS-specific drugs that inhibit the autoimmune-related tissue degradation related to rheumatoid arthritis.

THE STRUCTURAL AND FUNCTIONAL REGULATION OF NITRIC OXIDE SYNTHASE

Chapter 1.

I. NITRIC OXIDE SYNTHASE ISOFORMS

Isoforms and Tissue Distribution

There are three known isoforms of NOS, named for the tissues from which they were first isolated: neuronal (nNOS, Type I), macrophage or inducible (iNOS, Type II), and endothelial (eNOS, Type III) which share 50-60% sequence identity between them. The tissue distribution and sub-cellular localization of these isoforms is complex, in that more than one isoform is often found in the same cell type, and it is through differential regulation that their functions are distinct. Table 1-1 lists the tissue distribution of the three isoforms (62). The neuronal and endothelial isoforms are constitutively expressed and regulated primarily by intracellular Ca^{2+} concentration through CaM binding (63,64). The inducible isoform binds CaM nearly irreversibly, is regulated at the transcriptional level, and is induced by cytokines and endotoxin (3,65).

Table 1-1. Tissue and Cellular distribution of NOS isoforms (3).

nNOS	iNOS	eNOS
Neurons of the CNS	Any inflamed or	Arterial/venous
Spinal cord,	Cytokine induced cells	Endothelial tissue
Sympathetic Ganglia	Macrophages, Lymphocytes	Neuronal tissue
Peripheral nitrinergic nerves	Spleen	Kidney epithelium
Kidney Macula Densa cells	Neutrophils	Colon
Skeletal Muscle	Colon	Syncitiotrophoblasts of
Pancreatic Islet Cells	Endothelial Tissue	human placenta
Adrenal Glands	Adrenal Glands	
Epithelial tissue (uterus, lungs and stomach)		

Splice variations of the NOS isoforms

The constitutive isoforms, nNOS and eNOS, are encoded by one gene each, located on human chromosomes 12q24.2 and 7q35-q36 respectively (66,67). Multiple

splice forms have been identified for nNOS, named nNOSα or nNOS-1, nNOSβ, nNOSγ, nNOSμ, and nNOS-2 (68,69), Table 1-2. Isoform 1 of nNOS, nNOSα, is the form that has been most characterized *in vitro* and is found throughout the nervous system; the other splice forms are described as variants of this form. Alternate splice forms nNOSβ and nNOSγ are only found in specific regions in the brain, and are truncated by 230 and 331 amino acids at the N-terminus respectively. Both nNOSβ and nNOSγ are missing a PDZ domain (a protein-protein interaction domain) that mediates interactions with the dystrophin complex (69). nNOSμ contains a 39 amino-acid insert adjacent to the site recognized by Ca^{2+}-dependent CaM, and has been detected only in mature skeletal muscle and the heart tissues (70,71). Like the parent protein nNOSα, nNOS-2 is widely expressed (68); it lacks 104 amino acids in the distal pocket above the heme active site of the protein. In contrast to the variety of nNOS and iNOS protein transcripts, the only reported variations in the eNOS gene seem to be single nucleotide polymorphisms, and only one is coding, E298D (12).

Splice variants of the iNOS isoform have also been detected: NS2A-1 and NS2A-2, NS2B, NS2C, and NS2D (72,73). A BLAT search of the human genome using the sequence of the major isoform NS2A reveals that there are at least four NS2A-like genes in close proximity on human chromosome 17, within 17p11.2 and 17q11.2, consistent with results from Southern blot hybridization analyses (74,75). One gene is identical to the query sequence of NS2A, but the other three genes share less sequence similarity, at best with the C-terminal portion of the protein and they have not been annotated as NOS genes. NS2A is the form most characterized using protein chemistry techniques, and it

was identified both in macrophages and hepatocytes (21,72,76). A splice variant of NS2A, called isoform 2 or NS2A-2, was identified in macrophages, differing by two deletions totaling 39 amino acids in the first half of the protein. Isoforms NS2B and NS2C were identified only as fragments from leukocytes (74), with sequences that vary in exons 23 and 24, but the gene that encodes them is not confirmed (75). Finally, NS2D was found in human heart and skeletal muscle, in relation to chronic heart failure, and it has a unique sequence distinct from NS2A (77). Table 1-2 lists the various iNOS and nNOS splice forms and their distinguishing features. Appendix A also contains a full alignment of the three major NOS splice forms. Further characterization of the unique iNOS isoforms B, C, and D and nNOS isoforms β and γ could nicely complement the structure-function analyses performed over the last decade of NOS research, and which will be partially described in later sections of this chapter.

Table 1-2. Transcript variants of NOS.

isoform	contains residues:
nNOSα or nNOS-1	1-1434
nNOSβ,	231-1434, where 231-236 = MRGLGS
nNOSγ	332-1434
nNOSμ	@ 839 K=KYPEPLRFFPRKGPSASHVDSEAHSLVAARDSQHR
nNOS-2	del 504-608
NS2A or NS2A-1	1-1153
NS2A-2	del 264-288, del 298-311
NS2B	fragments, exon 23/24
NS2C	fragments, exon 23/24
NS2D	1-1147, 80% identical to NS2A
NOS3	1-1203

II. NOS Cofactors and Mechanism

Cofactor Binding sites and Subdomain Locations

NOS is a self-sufficient monooxygenase with a modular combination of an N-terminal oxygenase domain connected to a C-terminal reductase domain by a short CaM recognition sequence (78) (Figure 1-1). The oxygenase domain contains an iron-protoporphyrin IX (heme) prosthetic group, the substrate *L*-arginine (*L*-Arg) and cofactor (6*R*)-5,6,7,8-tetrahydro-*L*-erythrobiopterin (H_4B) binding sites. The reductase domain is structurally homologous to cytochrome P450 reductase (CPR) and binds flavin adenine dinucleotide (FAD), flavin mononucleotide (FMN), and reduced nicotinamide adenine dinucleotide phosphate (NADPH) (78,79). CaM binding acts as a switch that allows electrons to transfer from NADPH in the reductase domain to the heme for catalysis. Additionally, NOS is dimeric and electron transfer occurs in a trans mode, where the flavin domain of one subunit provides electrons for the oxygenase domain of the other subunit across the dimer, thus NOS is an obligate dimer (48,80).

Figure 1-1. Representation of the NOS sequence showing the location of cofactor binding sites within the oxygenase and reductase domains.

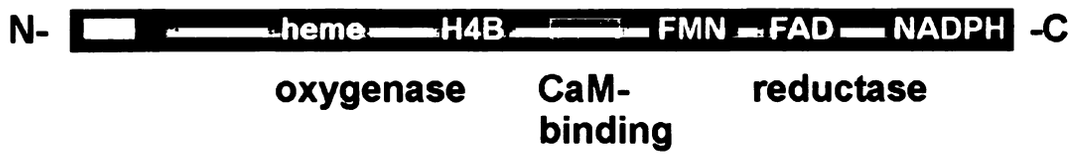

NOS catalyzes the two-step oxidation of *L*-Arg first to N^{γ}-hydroxy-*L*-arginine (HO-Arg) then to *L*-citrulline (*L*-Cit), producing the gaseous signaling molecule nitric oxide (NO·) and $NADP^{+}$ (81-83), (Figure 1-2). To balance the overall redox equation, two molecules of oxygen are consumed and 1.5 equivalents of NADPH plus a single electron from the substrate are required. The two reactions are P450-like, catalyzed by a thiolate-ligated heme in a hydrophobic active site, yet the overall fold of the oxygenase domain is non-homologous to that of the cytochromes P450 (84). Crystal structures for the oxygenase domains of all three NOS isoforms have been solved, revealing a unique "winged β-sheet" structure, with the heme bound at the base of a deep channel in the palm (41,42,85) (Figure 1-3, panel A). P450s have an *alpha-beta* fold, with an *alpha* subdomain that binds heme at its core and a *beta* subdomain that is distinct (Figure 1-3, panel B) (86,87).

Figure 1-2. The overall reaction catalyzed by NOS is shown. *L*-arginine is oxidized first to N-hydroxy-*L*-arginine, then to nitric oxide and *L*-citrulline, consuming a total of 1.5 NADPH equivalents.

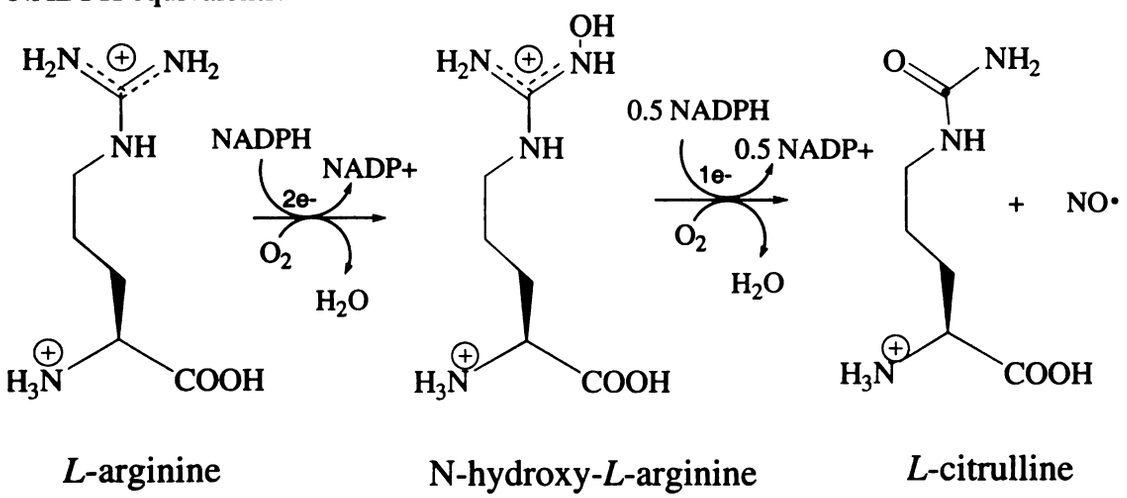

Figure 1-3. The oxygenase domain dimer of NOS (4NSE) (panel A) and the structure of Cytochrome $P450_{CAM}$ (1DZ4) (panel B) are displayed as ribbon diagrams (41,87). Secondary structure is colored red for the *alpha*-helices and cyan for the *beta*-sheets, and the heme is shown in stick representation, drawn with SwissPDB viewer (88).

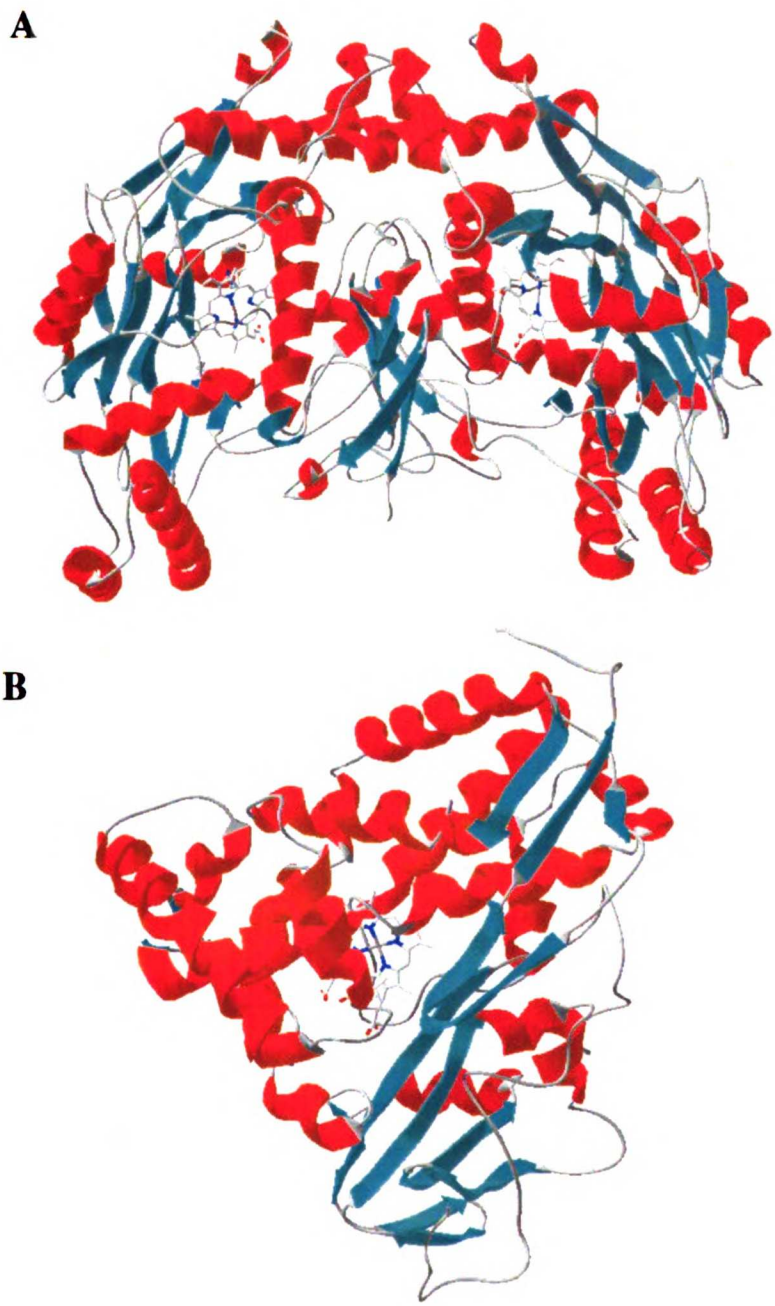

The unique requirement for Tetrahydrobiopterin

NOS differs from cytochrome P450 in its absolute requirement for tetrahydrobiopterin (H_4B) for catalysis. H_4B binds NOS cooperatively with the substrate *L*-Arg (89,90), causes the spin shift in the heme iron from low to high spin (91), stabilizes the ferrous form of the iron for catalysis (92), and promotes and stabilizes dimers (93,94). These structural and allosteric effects can be attributed to its binding at the dimeric interface, one pterin per monomer, and its direct interactions with the heme (95-97) (Figure 1-4). Additionally, H_4B redox activity is strictly required for catalysis, since structural analogs of H_4B, such as dihydrobiopterin and 4-aminotetrahydrobiopterin, can still produce the same structural and allosteric effects but do not catalyze NO· production (90,92,98,99), Figure 1-5. These analogues of H_4B have been found by X-ray crystallography to provide many of the same contacts within the pterin binding site (100).

Figure 1-4. The orientation of H_4B is shown relative to the heme and N-hydroxy-*L*-arginine as observed in the crystal structure of the eNOS oxygenase domain dimer (4NSE).

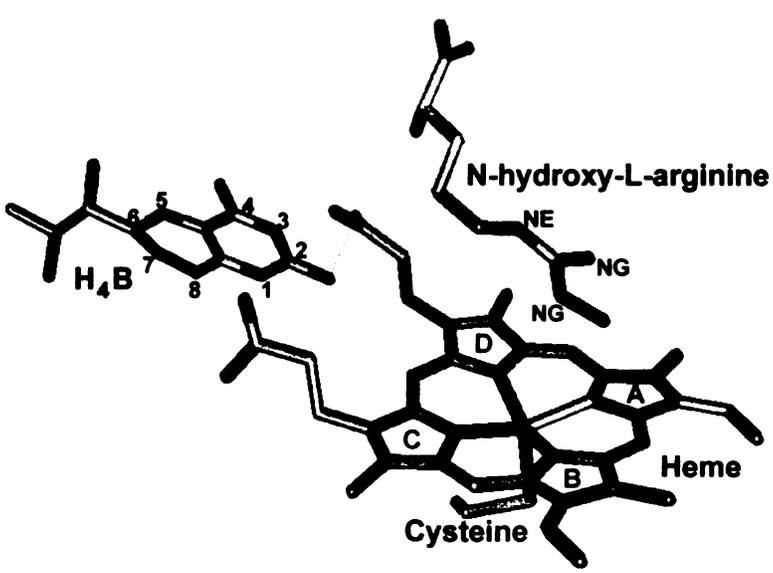

Figure 1-5. The catalytic cycling of tetrahydrobiopterin (H_4B) during catalysis by NOS and aromatic amino acid hydroxylase (AAH). NOS catalysis proceeds through the $H_4B^{+\cdot}$ radical (95-97,101), but no dihydrobiopterin (H_2B) has been detected. The AAH mechanism proceeds through 4a-peroxo- then 4a-hydroxyl-H_4B intermediates to produce the product H_2B (102). Also shown are two inhibitors, 4-amino- and 5-methyl-H_4B.

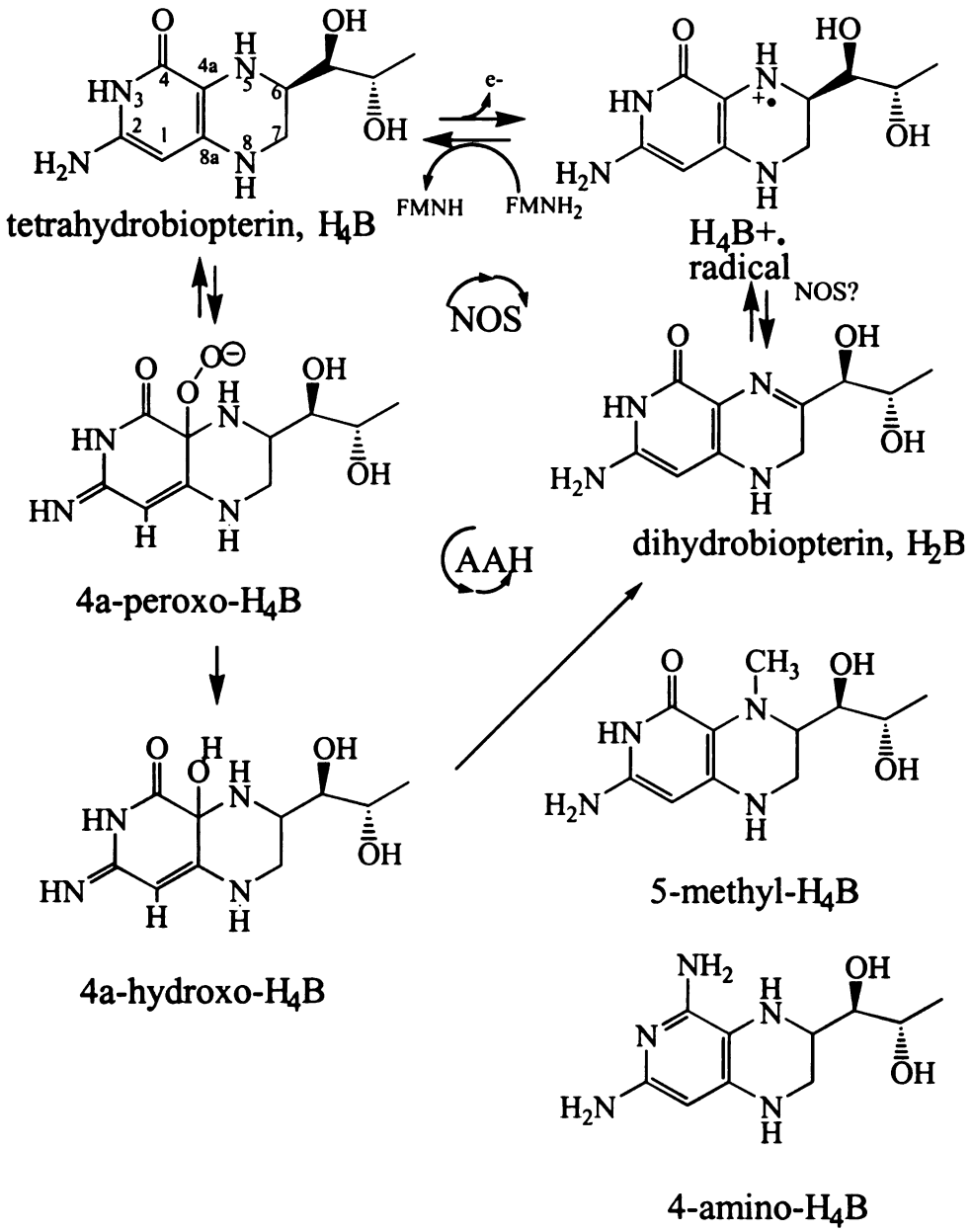

Early predictions for the pterin function in NOS postulated a role in reductive O_2 activation (26), since a specific requirement for tetrahydro-biopterins (92) and binding of transition metals was observed (26). By analogy with the aromatic amino acid hydroxylases, a 4a-peroxo- intermediate species of tetrahydrobiopterin was proposed, possibly formed in conjunction with heme iron reduction (28,103). Work by Rodríguez-Crespo *et al.* eliminated the possibility that a non-heme redox metal was bound by NOS, Chapter 2 (30), as is required in the amino acid hydroxylases, but this did not exclude the possibility that pterin activates oxygen for binding to the heme. 5-Methyl-tetrahydrobiopterin is catalytically active, but unable to react with oxygen; therefore the 4a-peroxopterin intermediate hypothesis could be eliminated (104). Some "diaphorase" activity was reported for NOS, where high concentrations of H_2B could be reduced to H_4B allowing for pterin redox cycling during catalysis (105), suggesting that some pterin-reducing activity of NOS was possible.

Low-temperature spectroscopy and stopped-flow experiments demonstrated the formation of a radical pterin intermediate under anaerobic conditions. H_4B has been shown to provide a single electron to the oxyferrous intermediate, forming $H_4B\bullet^+$ and the active hydroxylating species, the oxyferryl, during the first reaction producing HO-Arg (95-97,101), Figure 1-6. The flavins slowly reduce the formed $H_4B\bullet^+$; thus, it is the electrons transferred from the reductase domain that limit the overall catalytic rate (95,96), Figure 1-5. Crystal structures of H_4B and pterin analogs bound to the oxygenase domain of eNOS reveal the ability of the binding pocket to stabilize a pterin cationic intermediate, consistent with this mechanistic model (42).

Mechanism of the two step arginine to citrulline + NO· conversion

The proposed mechanism for oxygen activation and conversion of *L*-arginine into N-hydroxy-*L*-arginine is shown in Figure 1-6. First, electron transfer to the resting ferric iron from reduced FMN ($FMNH_2$) allows oxygen to bind, yielding a ferrousdioxygen intermediate (101). A second electron is transferred from H_4B to give a ferricperoxo adduct, which undergoes O-O bond cleavage upon protonation, yielding the oxyferryl with loss of water. Reaction of the oxyferryl species with *L*-Arg produces HO-Arg and regenerates the starting ferric resting state (101). The oxidation of *L*-Arg is hypothesized to proceed via a cytochrome P450-type hydroxylation mechanism (106,107).

Figure 1-6. Oxygen activation by NOS during the first step of catalysis (101).

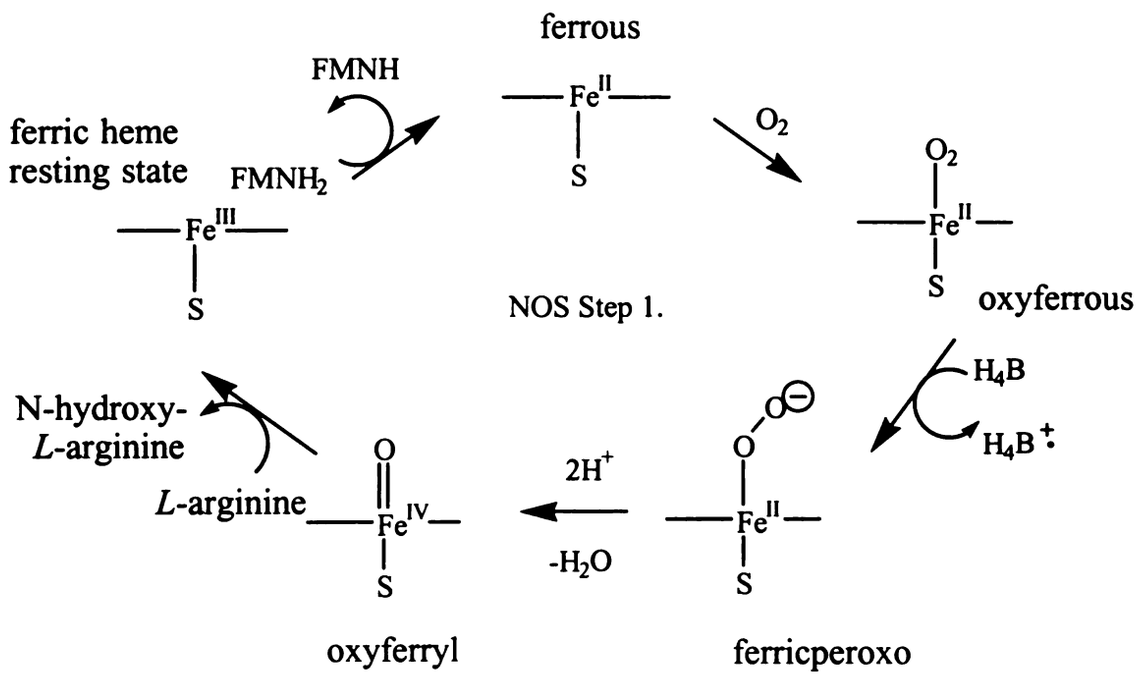

In the second oxidation step, the ferric resting state is again reduced by the flavin $FMNH_2$, with the ferrous form binding oxygen, giving the oxyferrous intermediate (Figure 1-7). The key difference between the reaction with *L*-Arg and HO-Arg is that only 0.5 equivalents of NADPH are consumed in the second step. The mechanism is modeled with the ferric superoxo adduct abstracting a hydrogen atom directly from either the hydroxyl group or the H-N^{ω} of HO-Arg to give the ferric hydroperoxy species (85,108). The central carbon atom of the guanidino group then undergoes nucleophilic attack by the iron hydroperoxy species, generating a transient tetrahedral intermediate that collapses to eliminate NO· and give *L*-Cit. Crystal structures of HO-Arg and derivatives bound to iNOS or nNOS oxygenase domains support a tetrahedral intermediate model resulting from this nucleophilic mechanism (85,100).

Figure 1-7. The second step of NOS catalysis, NO· production.

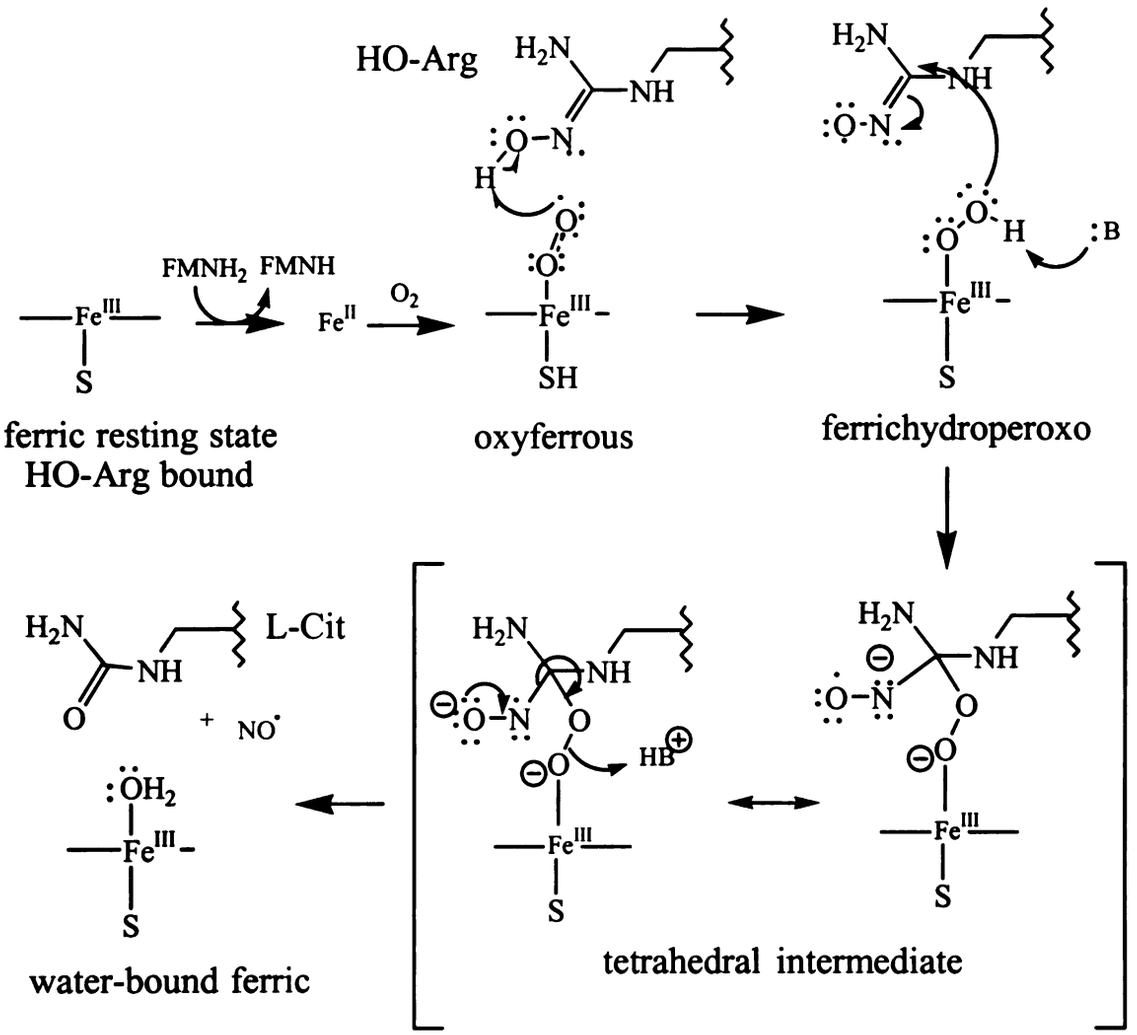

III. Dimerization is Modulated by Ligand Binding within the Oxygenase Domain

Isoform differences in Dimer Assembly

Dimerization is mediated primarily by interactions between oxygenase domains, as detected in yeast-two-hybrid assays and size-exclusion chromatography performed on isolated oxygenase and reductase domains (109). CaM stabilizes dimers, thus when iNOS is CaM-bound, independent of Ca^{2+} concentration, it is driven toward the dimeric form and activity is limited by substrate/cofactor availability. CaM stabilization of eNOS and nNOS involves protection from proteolytic cleavage, but dimers can form in the absence of CaM, especially in the case of eNOS. Because CaM-binding to the constitutive NOS is reversible and dependent on Ca^{2+} concentration, the equilibrium model for dimerization differs from that for the inducible isoform, Figure 1-8.

Although the constitutive isoforms, eNOS and nNOS, dimerize independently of ligands, dimers are stabilized by H_4B, *L*-Arg and heme. Full activation requires Ca^{2+} levels that allow CaM to bind (64,94). This process is shown in Figure 1-8 (right) where K_{d1} would apply to constitutive NOS dimerization. The inducible isoform binds CaM irreversibly and independently of the Ca^{2+} concentration (65), Figure 1-8 (left), thus K_{d2} and K_{d3} apply, depending on the true stimulation of dimerization by CaM.

Figure 1-8. Equilibrium model for dimerization control by ligands and CaM in the inducible and constitutive isoforms (3). Oxygenase domains (h) are colored brown, reductase domains (r) green, and CaM as the small purple spheres.

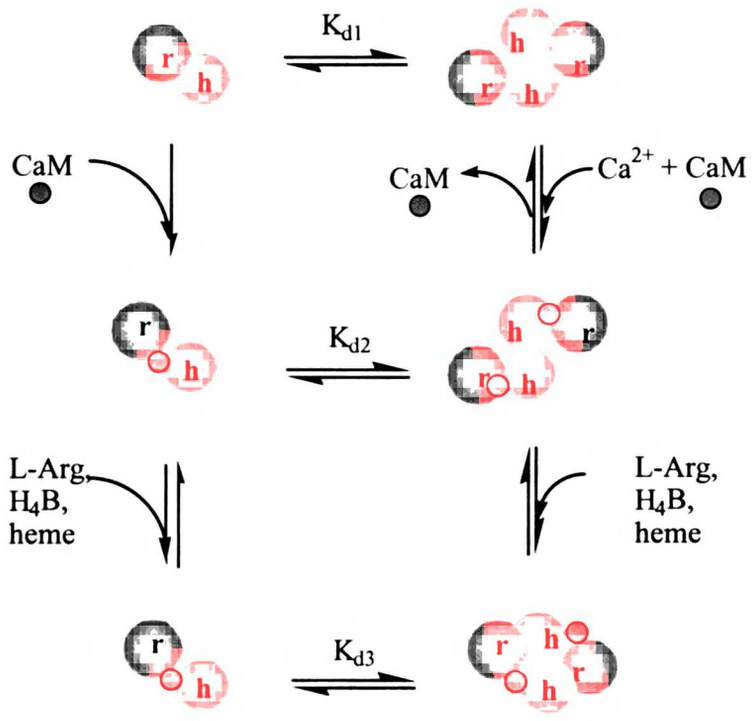

This model is supported by gel filtration chromatographic and low-temperature SDS-PAGE characterization of dimer content in full-length and truncated constructs of NOS (93,109,110). Binding of *L*-Arg, H_4B and heme are reported to induce dimerization and activation of iNOS either from prokaryotic expression systems or from denatured preparations in 5M urea (98,111,112). From gel shift assay observations, it was proposed that weak dimers form in the absence of substrate and cofactors, and that ligand binding stabilizes these dimers (113). The structural end-points of this equilibrium have been solved in crystal structures of the pterin-free monomeric form (of iNOS) compared with

the dimeric form bound to various combinations of ligands (eNOS and iNOS). The pterin-free monomeric form of iNOS is partially unfolded in the pterin-binding pocket and the dimeric interaction surface (32,40,41,114), Figure 1-9. Comparison of the H_4B-bound and -free dimers of eNOS show that the H_4B-binding site is preformed in the H_4B-free dimer (32,42), and the structures differ by only 0.22 Å rms. Thus either pterin-binding could induce dimer formation, or sampling of the dimeric conformation under normal equilibrium conditions eventually would present the correct pterin-binding conformation, and both modes would effectively drive dimerization.

The stabilization effects of pterin, heme and substrates on dimerization depend on the protein expression and purification methods employed. iNOS expressed in eukaryotic systems (*e.g.* macrophages) is 50-75% monomeric, and in the total absence of H_4B and *L*-Arg it loses its heme prosthetic group (94,112). eNOS and nNOS expressed in insect ovary cells are respectively 98% and 40% dimeric in the absence of H_4B and *L*-Arg. Interestingly, H_4B binds cooperatively with *L*-Arg to promote dimerization of nNOS resulting in stabilization of nNOS against SDS denaturation as assayed in low temperature SDS-PAGE experiments (93). eNOS dimers incubated with H_4B are partially stabilized against SDS (115); however, iNOS dimers bound to *L*-Arg and H_4B are still SDS-labile (109,115). A relevant issue is whether endogenous pterin and CaM are bound to these proteins when purified from mammalian sources, as the pterin affinity for initial binding has a K_d <1 nM (90), and CaM binds irreversibly to iNOS.

Figure 1-9. H_4B binding at the oxygenase domain dimeric interface. The iNOS oxygenase domain dimer shown in Panel A (1NSI) is fully bound to Zn (gray sphere), heme (red sticks), *L*-Arg (green sticks) and H_4B (yellow spheres), and is colored by secondary structure as before (32). The structure in dark blue represents the portion of the oxygenase domain that was crystallized (1NOS) free of *L*-Arg and H_4B in Panel B (40). Panel C shows one subunit of the dimer above, and defines three structural elements that form the dimeric interface: the H_4B binding helical lariat, Helices 11-13 that are unstructured in the monomer, and the N-terminal β–hairpin that binds Zn.

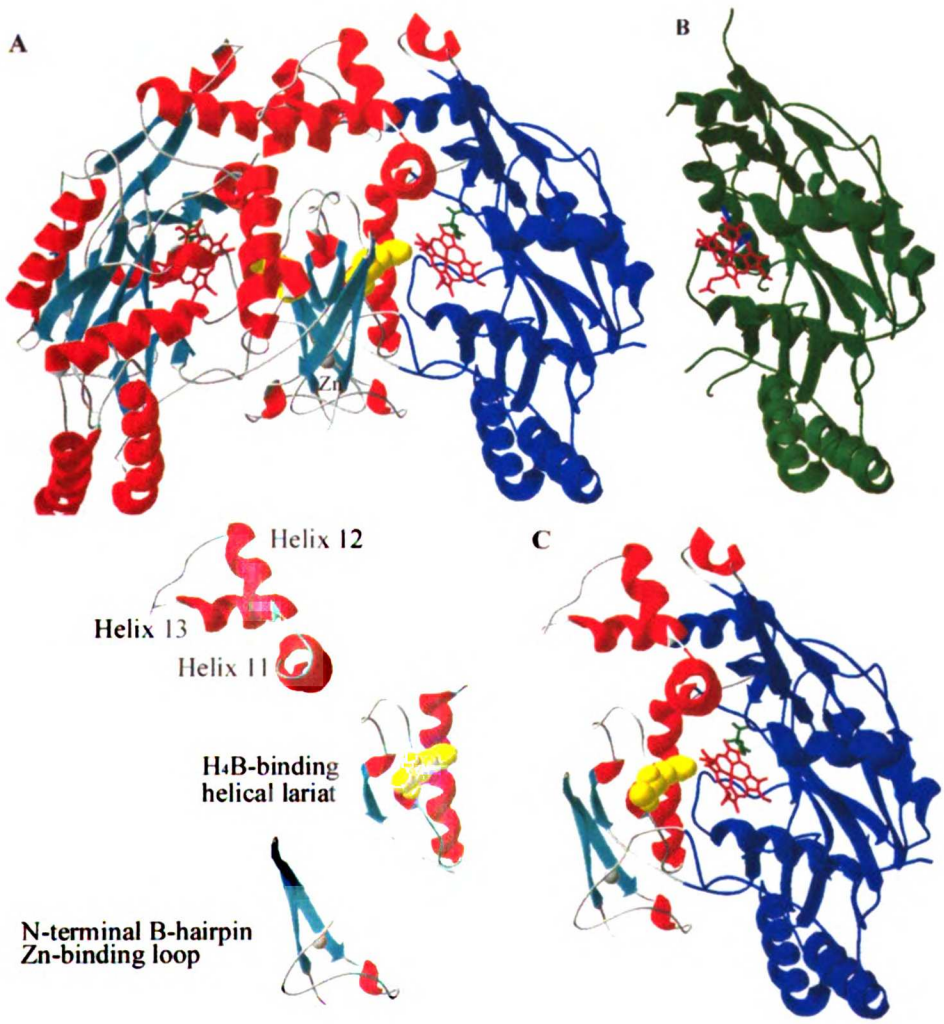

Innovations in the technologies used to measure dimerization affinity have allowed quantitative measurement of the dimer affinity of the three NOS isoforms by purifying ligand-free protein from a bacterial expression source, then supplementing with the desired ligands. The technique of analytical ultracentrifugation, coupled with protein chromatography, has resulted in determination of the true ligand dependences of dimer formation, as described in Chapter 4. It is through careful analysis of dimerization control by ligand binding that inhibition of dimerization can be examined with isoform-specific NOS inhibitors.

IV. NOS Inhibition

Substrate and Cofactor Analog Inhibitors

The first group of NOS inhibitors pursued were substrate and cofactor analogs, some of which are shown in Figures 1-5, 1-10, and 1-11 (92,94,116). Inhibitors also have been identified for CaM binding or reductase activity, including EDTA or EGTA (Ca^{2+} chelators) and diphenyleneiodonium derivatives that compete with flavin binding, (117); however, these inhibitors have broad inhibitory effects against CaM and flavin-containing reductases respectively, and are therefore not suitable as therapeutic agents. Therefore, the most promising rationally-designed isoform-selective inhibitors bind in or near the oxygenase domain active site, with one of the three following characteristics: i) binding competitively with *L*-Arg, ii) binding competitively with H_4B, as do the pterin analogs previously discussed (Figure 1-5) or iii) directly coordinating to the heme.

The substrate analogs compete with *L*-Arg binding and include guanidino amino acids such as N^{γ}-methyl-*L*-arginine (118,119), amidino amino acids such as N^{γ}-(1-imino)-*L*-ornithine (120), and amino acid isothioureas such as *L*-thiocitrulline (121,122), reviewed in (123). Unfortunately, these inhibitors have generally low isoform selectivity due to the high degree of similarity between isoform active sites (32,124). Newer derivatives of the acetamidines, such as N-(5(S)-amino-6,7-dihydroxyheptyl)-ethanimidamide, bind iNOS preferentially over eNOS with a 700-fold difference in K_d (125) by taking advantage of the slightest differences between ligand binding pockets. In fact, only a single H-bond contact difference is seen between the iNOS and eNOS active site contacts with *L*-Arg (32). The differential binding of this amidine inhibitor was modeled into the iNOS active site with an added H-bond contact of approximately 2.7 Å in length and corresponding to a bond strength of 3.9 kcal/mol (32), a value consistent with the 700-fold difference in K_d ($\Delta G = -1.4 \log K$ in kcal/mol). This demonstrates the concept that other peripheral interactions besides those specifically contacting *L*-Arg are required for the improvement of isoform selectivity (124). By this same argument, dipeptides containing N^{γ}-nitroarginine have been designed that are selective for nNOS over both iNOS and eNOS (126). For example, the dipeptide N-nitro-*L*-arginine-*L*-2,4-diaminobutyric acid (Figure 1-10) has a K_i for nNOS of 0.13 μM, and is selective for nNOS over iNOS by ~200-fold, and over eNOS by ~1500-fold (126). Also included among the list of *L*-Arg analogs is noformycin, a natural product isolated from *Nocardia formica* with a Ki of 1.3 μM for iNOS (127). Noformycin could have an interesting role for evasion of the host immune response through inhibition of iNOS.

Figure 1-10. *L*-Arg analog inhibitors of NOS.

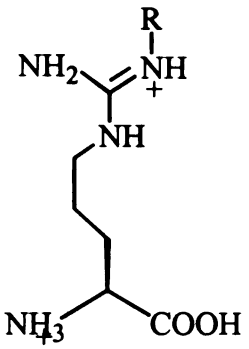

R=CH_3 N^{γ}-methyl-*L*-arginine
R=NH_2 N^{γ}-amino-*L*-arginine
R=NO_2 N^{γ}-nitro-*L*-arginine

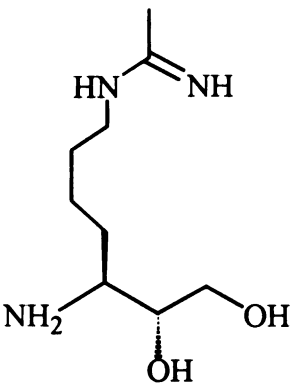

N-(5-(S)-amino-6,7-dihydroxyheptyl) ethanimidamide

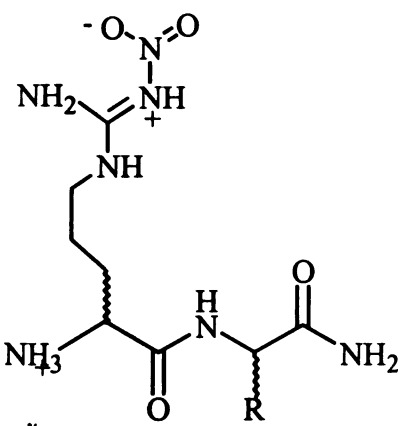

N^{γ}-nitro-*L*-arginine-dipeptide amides

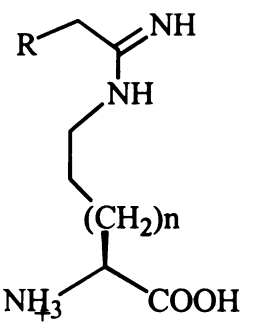

R=H n=1, N^5-[1-imino]-*L*-ornithine
R=CH=CH_2, n=1, N^5-[1-vinylimino]-*L*-ornithine
R=H n=2, N^5-[1-imino]-*L*-lysine

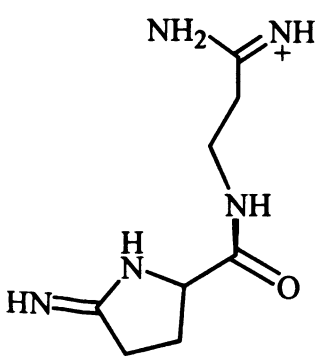

noformycin

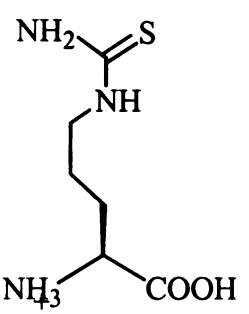

L-thiocitrulline

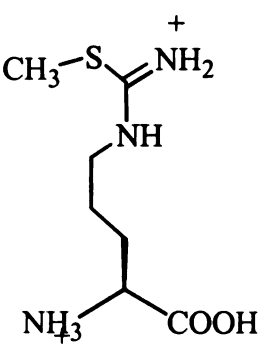

S-methyisothiourea

The imidazole and pyrimidine inhibitors break into dimerization

The imidazoles, which coordinate to the heme iron, have also been studied for selective inhibition of iNOS (Figure 1-11). Small coordinating ligands such as 1-phenyl imidazole, 7-nitroindazole and imidazole itself stabilize the dimeric form of iNOS (113). These compounds are mediocre non-selective inhibitors of all three isoforms, and are easily displaced in the presence of *L*-Arg and H_4B (113). However, substituted imidazoles such as the *L*-homohistidine analog, S-2-amino-5-azolylpentanoic acid (Figure 1-11), show better inhibition (2 μM K_i nNOS) and partial selectivity (128).

Figure 1-11. Imidazole inhibitors of NOS.

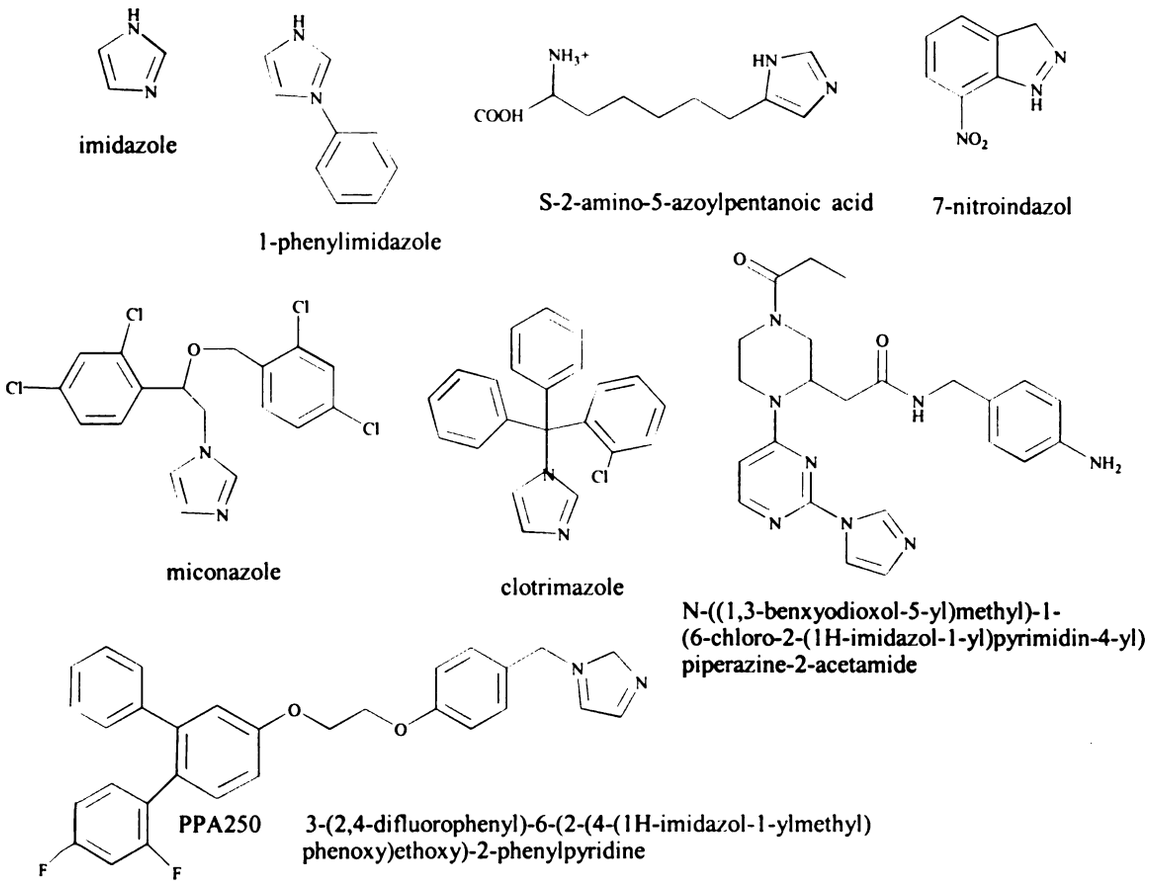

Even more exciting are the large, substituted imidazoles such as the pyridine-imidazoles and antifungal imidazoles, which inhibit iNOS by disrupting dimerization (46,113,129). Dimerization inhibition is a newer concept in the NOS field, but has been explored in several obligate dimer systems through sequestration of monomers, including HIV protease, HIV reverse transcriptase, and HSV ribonucleotide reductase (130-132). In these situations, either inactive mutants or short peptides that mimic interface structures bind to the wild-type subunit and inhibit activity through dissociative inhibition (133). Inactive chimeras containing an nNOS oxygenase domain connected to a P450 reductase function as dominant negative mutants when coexpressed with full-length nNOS by sequestering nNOS monomers (134).

Imidazoles all bind to the partially formed active site in the monomeric iNOS subunit and, depending on their steric bulk, can either stimulate or inhibit proper dimerization of iNOS. The antifungal imidazoles, clotrimazole and miconazole, bind iNOS monomers or *L*-Arg and H_4B-free dimers with low μM affinity, stabilizing the monomeric form (113). The substituted pyrimidine imidazoles bind iNOS monomers with tighter binding affinity, K_d = 1.8 nM, and have been shown to inhibit iNOS activity selectively over eNOS by >1000-fold in a cell-based assay (46,129). Crystal structures of the substituted pyridine imidazoles bound to iNOS monomers show that the inhibitors coordinate to the heme and fold into the *L*-Arg-binding site, but the dimeric interface is unformed in these structures (Figure 1-12). These inhibitors demonstrate that even mild disruption of the dimeric interface can shift the monomer-dimer equilibrium to the inactive monomeric form. A similar inhibitor, PPA250, also a large derivatized imidazole

compound has recently been reported to inhibit iNOS dimerization in animal models for chronic arthritis with an IC_{50} of 82 nM (135).

Figure 1-12. The structure of iNOS is shown bound to the bulky imidazole, PPA, (N-[(1,3-benzodioxol-5-yl)methyl]-1-[2-(1h-imidazol-1-yl)pyrimidin-4-yl]-4-methoxy-carbonyl)- piperazine-2-acetamide (46). Panel A shows the chemical structure of PPA (left) and the ribbon fold of the monomeric iNOS oxygenase domain (right). The active site is overlaid between two nearly identical structures, that with two imidazoles bound (blue) iNOS (1NOS) (40) and PPA bound (gold) iNOS (1DD7). In panel B, this active site structure is shown in stereo view, with imidazole in blue, PPA in cpk, and the heme group in red.

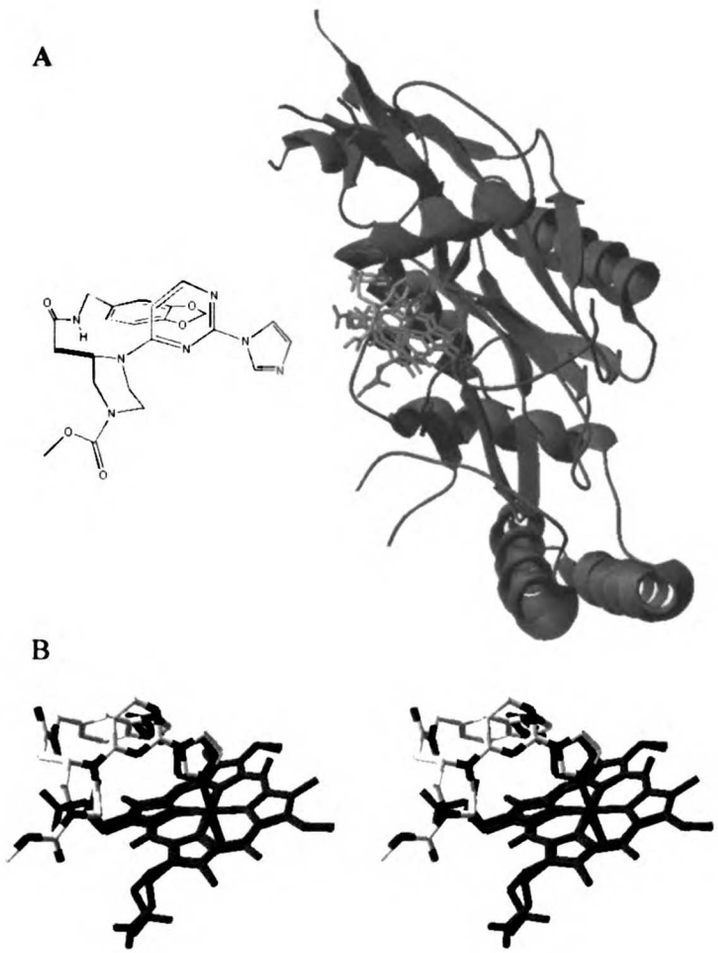

V. CALMODULIN REGULATION

The function of Calmodulin

CaM plays a critical role in regulating NOS activity through two distinct effects. At the level of quaternary structure, it has been demonstrated to stabilize (but is not absolutely required for) formation of the eNOS oxygenase domain dimer (91,136). CaM binding also is thought to result in a conformational change within the reductase domain that is detectable by changes in phenyldiazene probe reactivity and tryptophan/flavin fluorescence (23,137). The functional result is that CaM stimulates electron transfer both between the flavins in the reductase domain (138,139) and between the reductase and oxygenase domains (64,138-141).

The Calmodulin Recognition Element

CaM recognition of NOS differs greatly between the inducible and constitutive isoforms; CaM binds iNOS irreversibly, but reversibly in a Ca^{2+}-dependent manner to nNOS and eNOS. In all three NOS isoforms, calcium-bound CaM binds to a canonical CaM-recognition motif 20-26 residues long, consisting of an amphipathic helix with positively charged residues interspersed with hydrophobic residues at key positions (142). A crystal structure has been solved for CaM bound to the recognition helix from eNOS (44). An alignment of the CaM-recognition motif sequences in this linker region is shown in Figure 1-12 (44,143,144). The CaM-recognition motif from the constitutive isoforms fits into a Type A category of hydrophobic "1-5-8-14" binding motif (with hydrophobic residues in the 1,5,8, and 14 positions of the recognition element), similar to that recognized in smooth muscle myosin light chain kinase and calcineurin (142).

Peptides derived from the eNOS and nNOS sequences have low nM dissociation constants for Ca^{2+}-dependent CaM binding that are sufficient to account for the tight binding affinity observed for the full-length proteins (143-145).

Figure 1-13. Alignment within the CaM recognition region of NOS indicating CaM-recognition motifs. The 1-5-8-14 motif (cyan) in constitutive NOS is confirmed, but the IQ-like motif (yellow) is only hypothetical. Stars (*) indicate the key residues for these motifs in the upper alignment, but in the lower alignment periods (.), colons (:) and stars (*) indicate increasing sequence conservation as assigned by ClustalW, v. 1.82.

```
IQ-motif              **    *    *  *
neuromodulin      ATKIQA-SFRGHITRKKLKGE
NOS2A        497  KTHVWQ-DEKRRPKRREIPLKVLVKAVLFACMLMRKTMASR
NOS1α        717  NTHVWKGTNGTPTKRRAIGFKKLAEAVKFSAKLMGQAMAKR
NOS3         481  KGSAAKGTGITRKKT----FKEVANAVKISASLMGTVMAKR
mastoparan                        INLKALAALAKKIL
calcinueurinA                     IRNKIRAIGKMARV
1-5-8-14 motif                    *   *   *     *

CLUSTAL W (1.82) multiple sequence alignment

NS2A    KTHVWQDEKR-RPKRREI---------PLKVLVKAV---LFACMLMRKTMASRVR
PhK     SVRIYYQYRRVKPVTREIVIRDPYALRPLRRLIDAYAFRIYGHWVKKGQQQNRAA
        ..:::: : :* :*  ***         **: *:.*    ::.  : :    .*.
```

Recognition of the iNOS sequence by CaM remains unresolved however. The iNOS (NS2A) sequence aligns with eNOS and nNOS, and could arguably contain a 1-5-8-14 Type A binding motif as well, between residues 515-528, Figure 1-12. However, this motif is associated with reversible CaM-binding and does not explain the Ca^{2+}-independence observed for iNOS. Ca^{2+}-independent binding motifs for CaM include an IQ motif (IQX_3RGX_3R), but iNOS does not have a perfect IQ motif (142,146). The closest portion of the iNOS sequence that could match an IQ motif is contained in residues 501-513. This potential IQ-like motif is aligned with the sequence of an

irreversible CaM-binding sequence from human neuromodulin in Figure 1-12 to demonstrate sequence similarity but imperfect identity conservation between them. In general, the two lobes of CaM are able to recognize various motifs by adjusting their position along the target amphipathic helix, and the hinge region connecting the CaM lobes is flexible, thus it is not unreasonable that the position of the CaM-recognition motif in iNOS is partially shifted relative to other characterized IQ motifs (147). Some insight can be found through comparison with another unconventional CaM recognition motif found within the γ-subunit of skeletal muscle phosphorylase kinase (PhK) (148). The PhK CaM-recognition region has been shown to contain two non-contiguous binding motifs, peptides from each motif display nanomolar binding affinity for CaM, and it is the sum of their binding affinities that is proposed to account for tight binding of CaM to PhK. By analogy, iNOS may be recognized by CaM at both sites, Figure 1-12.

CaM has been shown to recognize a peptide derived from residues 509-535 of iNOS in a Ca^{2+}-free condition, and in an unexpected conformation. Circular dichroism spectroscopy reveals that the iNOS peptide (509-535) binds to apo-CaM in a Type II β-turn conformation, and its conformation becomes helical when Ca^{2+} binds to CaM (149). CaM conformation changes are known to be significant between the apo and holo forms (150), shown in Figure 1-13. Depending on the length of the peptide derived from the iNOS recognition element sequence, the observed binding affinity for CaM has been measured to be irreversibly tight, with a sub-nanomolar K_d as determined by surface plasmon resonance for a peptide with residues 503-528 (144), whereas CaM binding is reversible and weaker for the shorter peptide composed of residues 507-528, observed in a gel-shift assay (145). A possible explanation for these varied iNOS peptide-binding

observations is that the entire CaM-recognition region contributes partially to the observed tight binding affinity as well as to the Ca^{2+}-independence of CaM binding. The findings from model peptide binding studies are complementary to those of chimera studies where the CaM-binding sequence is swapped between the different NOS isoforms to be described in the next section.

Figure 1-14. Apo and Holo conformations of Ca^{2+}-dependent CaM. Shown are the extended apo conformation (1CFC) in panel A (95), the partially Ca^{2+} bound CaM recognition in an adenylyl cyclase (1K93) in panel B (104), and the holo conformation wrapped around its target recognition helix in eNOS (1NIW) in panel C (105). CaM secondary structure is composed of 4 helices in each lobe (red), connected by a hinge (arrow). Ca^{2+}-free loops in the apo form have β-sheet character (cyan), but tighten upon Ca^{2+} binding and target helix (blue) recognition.

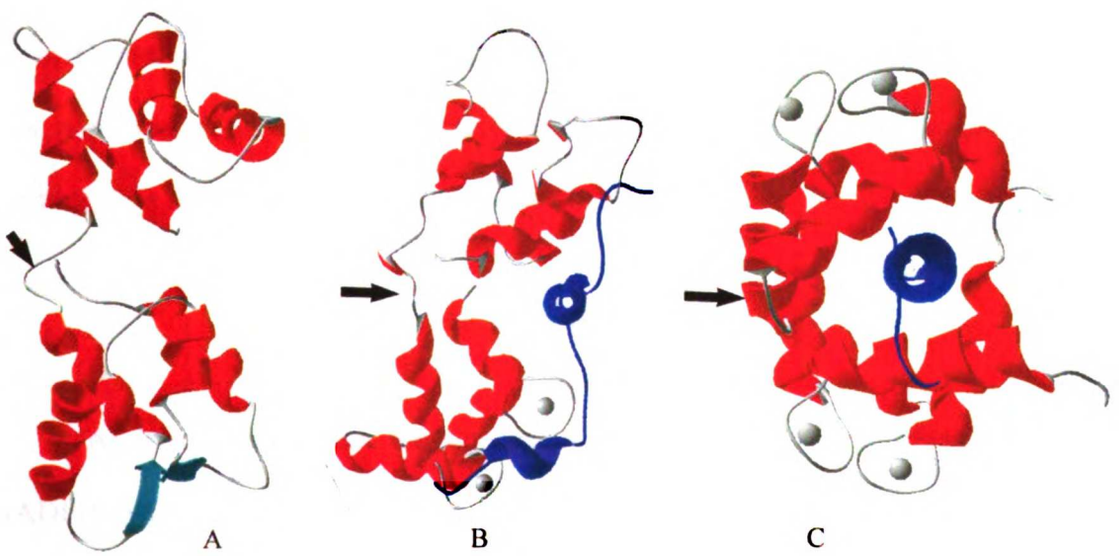

Interactions Beyond the CaM-recognition helix affect Ca^{2+}-dependence

Further interactions in iNOS beyond the canonical CaM recognition helix contribute to the Ca^{2+}-independence of CaM activation of iNOS. Replacement of the CaM-binding sequence in eNOS (145) or nNOS (35,151) with that of iNOS, as well as the reciprocal chimeras all yielded proteins whose Ca^{2+}-dependence of CaM activation was intermediate between the inducible and constitutive extremes. The Ca^{2+}-dependence of activity was also reduced in nNOS chimeras that contain either the iNOS oxygenase or reductase domain along with the iNOS CaM recognition helix (146). However, the closest approach to Ca^{2+}-independence was achieved by combining the iNOS reductase and CaM-recognition helix with an nNOS oxygenase domain (146). Through successive N- or C-terminal deletions, the region required for full Ca^{2+}-independent CaM binding was narrowed down to iNOS residues 490-732, which include the canonical CaM-binding helix and a portion of the reductase domain (151).

VI. Control of Electron Transfer

As introduced earlier, the similarities between the NOS reductase domain and NADPH-cytochrome P450 reductase include significant sequence identity, the NADPH-FAD-FMN electron transfer route, and the ability of the flavin groups to reduce external electron acceptors such as cytochrome c^{3+} (cyt *c*) and ferricyanide. The differences between NOS and CPR are equally useful for analyzing functions unique to NOS, including CaM-regulation and dimerization aspects, especially when differences are also sought between the constitutive and inducible NOS isoforms.

Structural Homology with Cytochrome P450 Reductase

Sequence and structural analyses of the NOS reductase domain allow useful structural comparisons both between NOS isoforms and with homologous reductases. The reductase domain of NOS shares 27-29% sequence identity and is structurally and functionally homologous to CPR, Figure 1-14. Furthermore, the more distantly related bacterial members of the CPR family have identified parallels between similar systems that employ NADPH-FAD-FMN electron transfer routes. For example, the flavin domain of cytochrome P450 BM-3 ($P450_{BM-3}$) shares 28% identity with the NOS reductase domain, and the α-subunit of sulfite reductase (SiR) shares 27% sequence identity with the NOS reductase domain. The NOS, CPR, $P450_{BM-3}$ and SiR reductases themselves consist of smaller functional domains (79,152,153), the FMN and FAD/NADPH domains, that are structurally homologous to flavodoxin and ferredoxin reductase, respectively (152,154). These two distinct domains are connected by an α-helical "connecting domain" that is uniquely found in the CPR family (155).

The crystal structure of CPR, the only structure available that contains all three subdomains, shows that the α-helical connecting domain orients the FMN and FAD/NADPH domains relative to each other (155). This connecting domain is poorly conserved between CPR, SiR, $P450_{BM-3}$ and the NOS isoforms and therefore fulfills a unique structural role. It is structurally intertwined with the FAD/NADPH domains by a β-sheet segment that is inserted between two regions of the connecting domain sequence, but the β-sheet segment is an integral part of the FAD/NADPH domain as seen in the

ferredoxin reductase structures (154-158). The hinge-like flexible coil differs in sequence and length in CPR, SiR, $P450_{BM-3}$ and the NOS isoforms (37,155,158), Figure 1-14.

Figure 1-15. The fold of CPR is shown from its crystal structure (1AMO) (155), along with homologous flavoproteins flavodoxin (1AG9) (159) and ferredoxin reductase (1QUE) (160). A cartoon diagram of the sequence alignment between the NOS reductase domain and the CPR family of proteins is shown below, indicating sequence similarity to the structure above by color. Deleted sequences are denoted as dotted lines and the position of the large inserted AI sequence found in constitutive NOS is indicated as a solid black line.

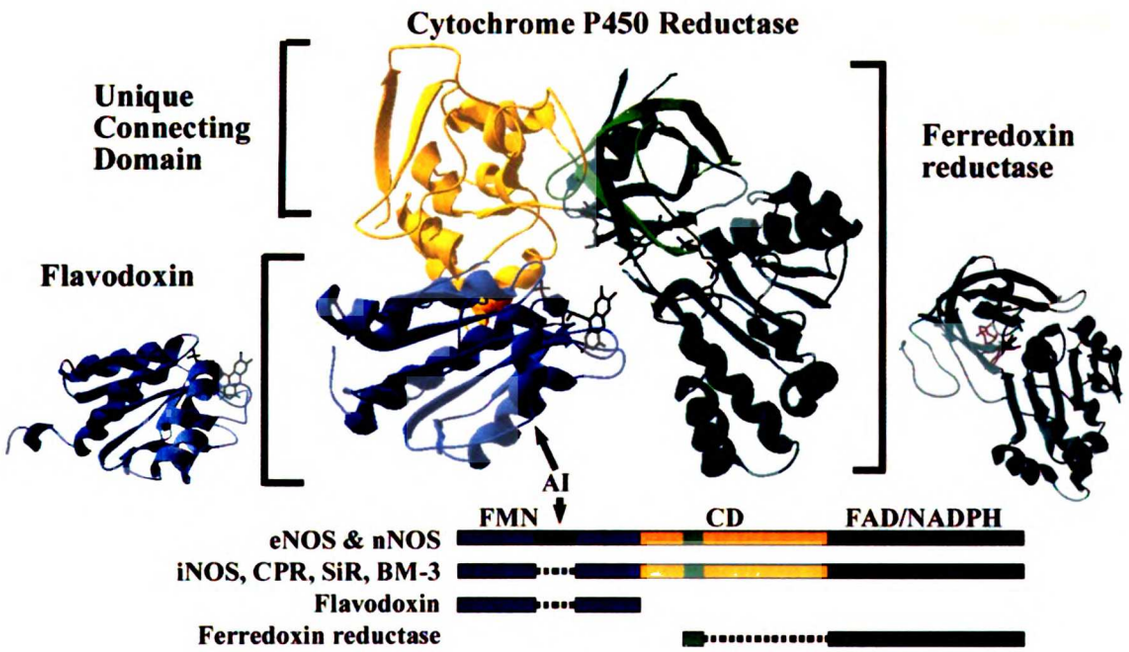

Following the logic of searching for NOS-unique elements in comparison with homologous reductase sequences and structures, extensive protein-engineering experiments have sought to characterize chimeras that combine different domains and elements between NOS isoforms and also in a limited way with subdomains from related proteins. These chimeras include the initial CaM-recognition element swapped forms

previously introduced (161), chimeras that swap the reductase domain for that of other isoforms or CPR family members (35,45,134,162,163), chimeras that examined a 43-45 amino acid insert within the FMN domain of constitutive NOS isoforms (36,45), and truncation mutations of the C-terminal tail extension found in all three NOS isoforms (164,165).

Overall Activity is Limited by the Reductase Domain

Catalysis of NO· production is much higher in iNOS and nNOS than eNOS; the specific activity V_{max} for human hepatic iNOS is 800 nmol min^{-1} mg^{-1} (166), for rat nNOS is 355 nmol min^{-1} mg^{-1} (22), and for bovine eNOS is 90-120 nmol min^{-1} mg^{-1} (115). Work by Nishida *et al.* has demonstrated that the overall NO· activity correlates with the reductase domains through the use of chimeric NOS proteins that swap the reductase domains between all three isoforms (35). Thus, eNOS oxygenase domains can be induced to produce 2- to 4-fold higher levels of NO· when combined with iNOS or nNOS reductase domains (to form the "E/I" or "E/N" chimeras respectively) (35,45). The inverse chimeras with eNOS reductase domains, I/E and N/E, display eNOS-like NO· production levels (35). Thus, it is the reductase domain that limits overall activity.

Through these chimeras, it was further demonstrated that the Ca^{2+}/CaM regulation of activity also correlates generally with the reductase domain, as discussed in section V of this chapter. The other important result from these oxygenase/reductase chimeras is the demonstration that the oxygenase and reductase domains from alternate isoforms are able to function together, thus the interactions of the oxygenase domains with alternate reductase domains must be partially conserved (35,45). Chimeras that swapped the CPR

or $P450_{BM-3}$ reductase domain into nNOS were also created, but these reductases transfer electrons much more slowly than the NOS reductase domains and were shown to function as effective dominant negative mutants in a cell-based assay (134). However, recent *in vitro* analysis of nNOS/CPR chimeras have demonstrated high activity levels (162). This has opened the search for NOS-unique and isoform-unique elements within the reductase domain that determine the Ca^{2+}- and CaM-dependence of electron transfer in an isoform-specific way.

The Autoinhibitory Element Modifies Ca^{2+}/CaM Dependence

A model of the NOS FMN domain constructed by Salerno *et al.* was used to predict the residues that might interact with CaM (167). They were among the first to identify a 43-45 amino acid insert in the sequence of eNOS and nNOS that is missing from iNOS and CPR. Peptides based on the eNOS (but not nNOS) insert sequence were demonstrated to inhibit NO· activity by altering CaM binding (167). This insert was therefore postulated to be an autoinhibitory (AI) domain. This inference was confirmed for eNOS (38,45), and later nNOS (36,39,168), by the construction of AI deletion and insertion mutants.

In further studies by Nishida *et al.*, the deletion of the AI from constitutive NOS (eNOS(ΔAI) or nNOS(ΔAI)) retained full catalytic activity when CaM was bound, but the concentration of Ca^{2+} required for stimulation of activity was reduced 7- or 15-fold respectively (36,45). In the quest to identify the elements that confer Ca^{2+}-dependence upon eNOS, a further chimera was created by deleting the AI element from I/E, thereby

producing a chimera that possessed the iNOS oxygenase and CaM-recognition domains, and an eNOS reductase domain stripped of its autoinhibitory element (I/E(ΔAI)). This chimera closely approached the behavior of Ca^{2+}-independent iNOS, displaying 50% activity at sub-nanomolar levels of free Ca^{2+}. However, completely Ca^{2+}-independent chimeric constructs remain undetermined.

Chapter 3 describes NOS chimeras that directly address the question of whether additional interactions within the iNOS reductase domain account for irreversible, Ca^{2+}-independent CaM-binding, or additional eNOS and nNOS sequences interfere with CaM-dependent activation (37). Through the use of sequence alignment and structural modeling, a new loop (CD2A) was identified within the connecting domain of the NOS reductase domain whose sequence is highly conserved by isoform and which is proposed to directly interact with the CaM-binding region (37). The eNOS CD2A loop (eCD2A) has the sequence ^{834}KGSPGGPPPG^{843}, and is truncated to ^{809}ESGSY^{813} (iCD2A) in iNOS. Replacing the eCD2A with the iCD2A sequence, producing the eNOS(iCD2A) chimera, reduced the Ca^{2+} requirement for CaM-bound activity to the same level as that of the eNOS(ΔAI) mutant. Like the larger AI element, the eCD2A plays an autoinhibitory role in the control of NO· activity, but its autoinhibitory function is masked by the dominant AI element and is only detectable in the double mutant eNOS(iCD2A)(ΔAI) (37). Through this piece-wise approach of combining chimeras between iNOS and eNOS reductase domain elements, it is becoming increasingly clear that the complete Ca^{2+}-independence of iNOS is likely to be mediated by many interactions between CaM and the reductase domain through elements that are non-contiguous in sequence but structurally contained within the FMN and connecting domains.

Shielding by the C-terminus

Another structurally unique region of the NOS reductase domains relative to other reductases is the C-terminal "tail" region. The C-termini of the NOS reductase domains are 20-40 amino acids longer than that of cytochrome P450 reductase, and sequence alignments show poor conservation of residue identity between the inducible and constitutive isoforms in this region. Truncation mutants with the C-terminal tail deleted were constructed for all three isoforms (164,165). The main effect of these C-terminal deletions was to increase the internal electron transfer rate; however, CaM-dependent stimulation of activity differed between the inducible and constitutive isoforms.

CaM is required for full NO· production activity in all three isoforms. The reductase activity measured by electron transfer to exogenous electron acceptors such as cyt *c* is also repressed in the CaM-free state, such that wild-type eNOS and nNOS normally exhibit a 4 to 10-fold lower cyt *c* reducing activity and their NO· -synthesizing activity is virtually undetectable when compared to CaM-bound activity. Removal of the C-terminal element from eNOS or nNOS relieves the self-inhibition of internal electron transfer rates, resulting in a slightly higher (less than 2-fold) cyt *c* activity when compared with wild-type enzyme. The role of the C-terminal element in iNOS is proposed to be of greater importance for internal electron transfer, because deletion of the C-tail results in a greater than 10-fold increase in reductase activity over that of both wild-type iNOS or cytochrome P450 reductase. The C-terminal tail thus attenuates electron flow through the reductase in the inducible form but does so in the constitutive forms to a much lower extent. The C-terminus of the constitutive isoforms does not affect

the intermolecular flavin to heme electron transfer however, because NO· production by the C-tail deletion mutants of eNOS and nNOS remains completely shut off in the absence of CaM. NO· production is slightly increased in the iNOS C-tail deletion mutant, but this is likely due to the excessive increase in reductase activity. Therefore, the C-terminal extension participates in the control of internal electron transfer within the reductase domain by CaM, but it does not affect intermolecular reductase-to-heme electron transfer.

VII. NOS PHOSPHORYLATION

Phosphorylation of the AI domain has been directly observed in vitro as part of the multi-phosphorylation of eNOS by cGMP-dependent protein kinase II (cGK II) and the catalytic subunit of cAMP-dependent protein kinase (cAK) (53). *In vitro,* phosphorylation was found at Ser633 (within the AI), Ser1177 (near the C-terminus), and Thr495 (within the CaM-recognition element). This phosphorylated eNOS exhibited a fractional (10%) CaM-independent activity, and a 4-fold enhancement of this activity upon binding of CaM. Therefore, phosphorylation of eNOS may serve as an alternate, Ca^{2+}-independent pathway for activation. However, since multiple phosphorylations occurred at once in these assays, it was not possible to differentiate between the role of AI phosphorylation and the possible effects of phosphorylation at other sites. It is to be noted that protein kinase AKT has been shown to activate eNOS via phosphorylation at bovine eNOS Ser1179 (49-51).

Phosphorylation of the AI in nNOS also has been shown to inhibit activity. Both *in vitro* (54) and in NG108-15 neuronal cells expressing nNOS and co-transfected with

CaM kinase IIα, the nNOS AI domain was phosphorylated at Ser847 and the phosphorylated protein exhibited a 30% loss of activity (169). The point mutation S847D, which mimics the electrostatic alteration caused by phosphorylation, was also able to decrease the activity by ~50% (169). These results point to a clear inhibitory effect of AI phosphorylation. Furthermore, the inhibitory effect of AI phosphorylation has been shown to be independent of CaM-binding through the use of an nNOS mutant deficient in CaM-binding. This regulation of nNOS by CaM kinase may function as an alternate mechanism for NOS regulation under conditions where CaM activates these kinases, but not nNOS itself. Alternatively, phosphorylation could be limited to the CaM-NOS complex, so that release of CaM under resting Ca^{2+} conditions would leave an nNOS that is partially inhibited against subsequent activation.

VIII. Summary of NOS Catalytic Regulation

NOS is regulated in multiple dimensions, i) on the order of transcription, ii) on the chemical level of enzymatic activity, and iii) on the mechanical level of protein-protein interactions. The research presented in this thesis contributes to improved understanding of the latter two points. On the level of enzymatic activity, the function of H_4B was explored through the use of site-directed mutation in the eNOS oxygenase domain (30), and the regulation of activity by the reductase domain was analyzed through structural modeling coupled with chimera mutagenesis that swapped regulatory elements between isoforms (37). On the mechanical level, dimerization regulation was carefully dissected using hydrodynamic analyses to characterize the structural properties of the full-length NOS as well as the oxygenase and reductase domain constructs of eNOS. These

dimerization analyses found significant effects of ligands and CaM upon dimer stability, and we report for the first time quantitative measurements of dimer affinity in a standardized format that compares all three isoforms. Taken together, these studies begin to describe a complete picture for the structural regulation of activity in Nitric Oxide Synthase.

MUTATION OF THE FIVE CONSERVED HISTIDINES IN THE ENDOTHELIAL NITRIC OXIDE SYNTHASE HEMOPROTEIN DOMAIN: NO EVIDENCE FOR NON-HEME METAL REQUIREMENT FOR CATALYSIS[2].

Chapter 2.

This work was originally published on July 30, 1999 in the *Journal of Biological Chemistry*, volume **274**, issue 31, pp. 21617-21624. The work is included here with permission from the coauthors Drs. Ignacio Rodríguez-Crespo[‡], Clinton R. Nishida[§], and Paul R. Ortiz de Montellano[§] who directed the research, from the [‡]Departamento de Bioquímica y Biología Molecular, Facultad de Ciencias Químicas, Universidad Complutense, 28040 Madrid, Spain and the [§]Department of Pharmaceutical Chemistry, University of California, San Francisco, California 94143-2280.

[2] This work was supported by National Institutes of Health Grant GM25515.

I. ABSTRACT

Five conserved histidine residues are found in the human endothelial nitric-oxide synthase (NOS) oxygenase domain: H420, H421, and H461 are close to the heme, whereas H146 and H214 are some distance away. To investigate whether the histidines form a non-heme iron-binding site, we have expressed the H146A, H214A, H420A, H421A, and H461A mutants. The H420A mutant could not be isolated, and the H146A and H421A mutants were inactive. The H214A mutant resembled the wild-type enzyme in all respects. The H461A mutant had a low-spin heme, but high concentrations of *L*-Arg and tetrahydrobiopterin led to partial recovery of activity. Laser atomic emission showed that the only significant metal in NOS other than calcium and iron is zinc. The activities of the NOS isoforms were not increased by incubation with Fe^{2+}, but were inhibited by high Fe^{2+} or Zn^{2+} concentrations. The histidine mutations altered the ability of the protein to dimerize and to bind heme. However, the protein metal content, the inability of exogenous Fe^{2+} to increase catalytic activity, and the absence of evidence that the conserved histidines form a metal site provide no support for a catalytic role for a non-heme redox-active metal.

II. INTRODUCTION

Since the identification of H_4B binding to the NOS purified from neuronal tissues, its utilization by NOS for catalysis of an otherwise P450-like oxidation mechanism has been the subject of intense discussion. H_4B has several unique functions in NOS, including both structural/allosteric functions as well as redox function. As described in Chapter 1, H_4B promotes and stabilizes nNOS and iNOS dimers (93,94), binds NOS

cooperatively with the substrate *L*-Arg (89,90), causes the spin shift in the heme iron from low to high spin (91), and stabilizes the ferrous form of the iron for catalysis (92). Structurally, pterin has an important function in dimerization; two molecules of H_4B bind at the dimeric interface between oxygenase domains, and provide H-bond interactions with the propionyl groups of the heme (32). Monomeric structures of iNOS oxygenase domains solved in the absence of pterin are missing structure at the dimerization interface, and some helices are unfolded (40), Figure 1-9. Comparison of dimeric structures of eNOS solved in the presence or absence of pterin reveals that the H_4B binding site is fully formed in the pterin-free structures (42). Thus, it can be inferred that pterin connects dimerization with active site function (95-97). H_4B redox function is also required for activity, since redox-inactive structural analogs cannot support catalysis (90,92,98,99), in spite of being able to bind properly within the pterin binding site (100). Therefore, H_4B functions as an allosteric modulator of activity, a structural component of dimerization, and a redox active cofactor in NOS.

The other enzymes known to utilize H_4B as a cofactor are the aromatic amino acid hydroxylases, in which H_4B reacts with O_2 to form a peroxo-bridged complex between reduced iron and H_4B, shown in Figure 2-1 (102). The peroxy intermediate forms first, then reacts with a 2-histidine-1-carboxylate coordinated iron atom to form the Fe(IV)=O oxidative species that catalyzes amino acid hydroxylation (102). In the crystal structure of human phenylalanine hydroxylase (PH), the iron is coordinated by H285, H290, and E330, with H290 as the axial ligand and three water molecules that complete the square pyramidal geometry, Figure 2-2. This "2-his-1-carboxylate" facial triad motif is present throughout the aromatic amino acid hydroxylase enzyme family (29).

Figure 2-1. Proposed mechanism for the hydroxylation of phenylalanine by phenylalanine hydroxylase (PH) to form tyrosine (170,171). Shown are the oxygen activation steps of tetrahydrobiopterin, forming the 4a-peroxy, and 4a-hydroxy intermediates, and the ferrous and oxy-ferryl species of the non-oxygenase iron.

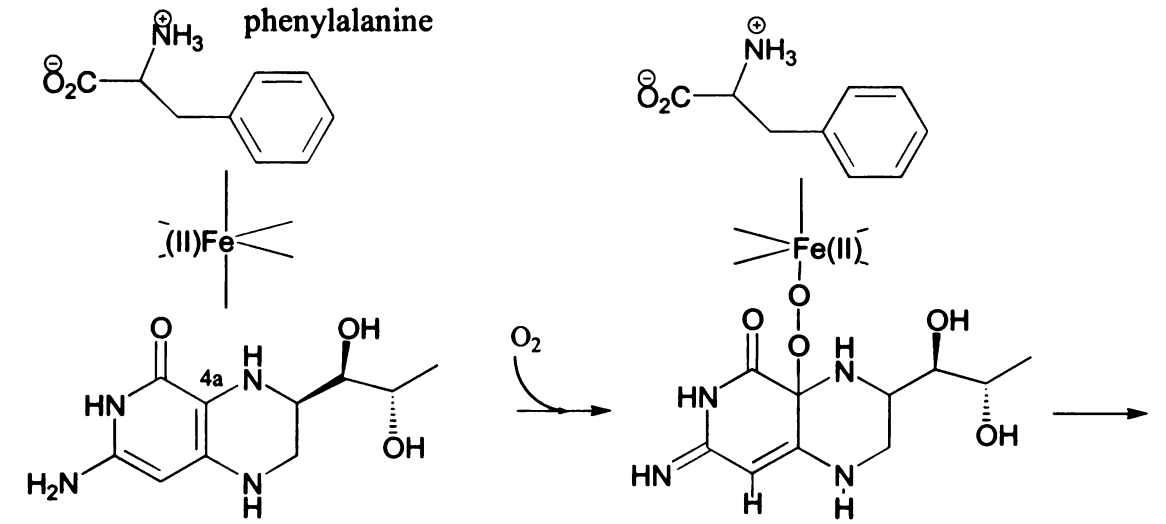

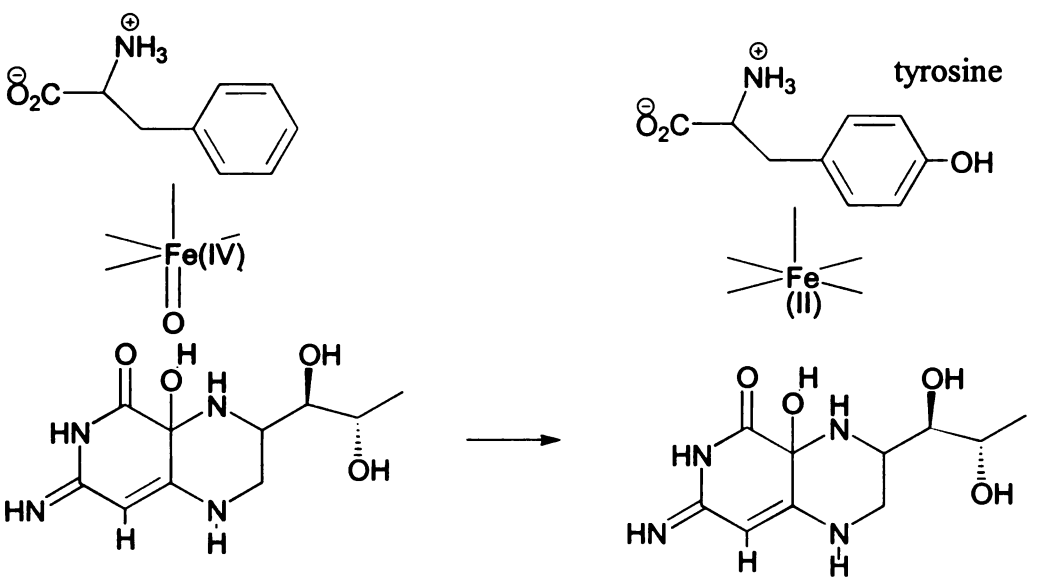

Figure 2-2. The structure of human phenylalanine hydroxylase, bound to H_4B (sticks) and iron (golden sphere). The iron is coordinated by H290 (sticks) and water (red sphere) at axial positions, and by H285, E330, and two more water molecules at equatorial positions (172). Image made using UCSF Chimera[3], v. 1 (173).

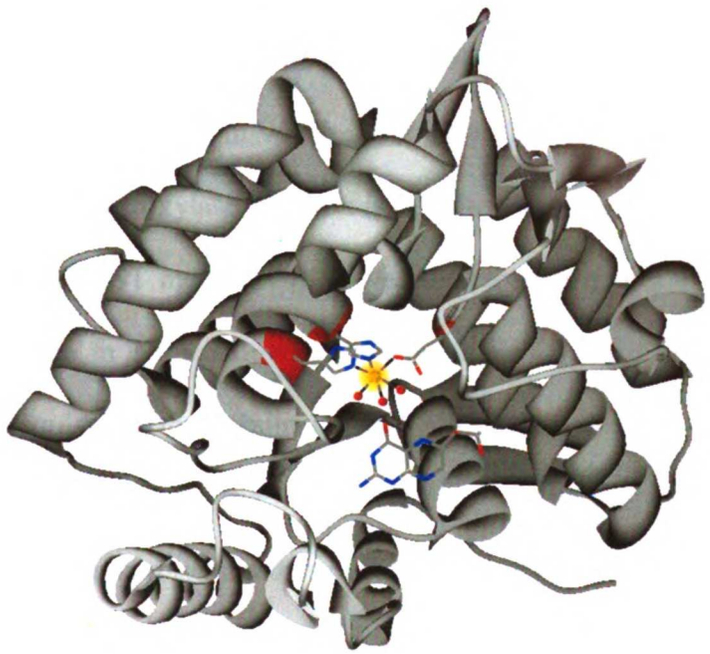

Evidence supporting a similar 4a-hydroperoxy-H_4B intermediate mechanism in NOS includes metal binding studies that report significant binding of transition metals to the NOS isoforms, the observation of partial "diaphorase" activity in nNOS which recycles H_2B to H_4B that would support pterin redox cycling (105), and the identification of a potential 2-his-1-carboxylate motif that is conserved within the NOS oxygenase domains (eNOS residues ^{419}DHH^{421}). Initial reports for iNOS and nNOS indicated that these proteins purified from *E. coli* expression sources are found with nearly stoichiometric amounts of zinc and copper bound, and after desalting, these proteins could be reconstituted with ferrous chloride to give approximately two equivalents of

[3] Molecular graphics images were produced using the UCSF Chimera package from the Computer Graphics Laboratory, University of California, San Francisco (supported by NIH P41 RR-01081).

bound iron per subunit of NOS (26). Furthermore, this iron reconstitution was reported to increase the NO· -synthesizing activity of both nNOS and iNOS (26).

The presence of the conserved ^{419}DHH(S/A)AT^{424} motif (eNOS numbering) near the H_4B binding site is reminiscent of a similar HHDAST motif in another amino acid hydroxylase, lysyl hydroxylase, in which 2-oxoglutarate and non-heme iron are required for catalysis. In lysyl hydroxylase, the iron is coordinated by the aspartate and the second histidine of the HHDAST motif (174). It was therefore proposed that the aspartate and the second histidine in NOS similarly coordinate Fe^{2+} (26). Furthermore, the nNOS H652A mutant (equivalent to the human eNOS H421A mutant) was found to be inactive, a result that seemed to support the iron-binding hypothesis for the DHH motif (26). By analogy with lysyl hydroxylase, another of the proposed metal ligands in nNOS would be H692, which corresponds to H461 in human eNOS.

The three-dimensional structure of the bovine eNOS oxygenase domain indicates that the NOS enzymes have a metal-binding site at the dimeric interface consisting of a Zn^{2+} coordinated to four cysteine residues, two from each monomer (42,124). Crystallization of the iNOS oxygenase domain in slightly oxidizing conditions can result in loss of the zinc and the formation of a disulfide bridge involving Cys-109 of the two subunits (41,124). However, no evidence was found in the crystal structures for an additional histidine-dependent metal-binding site (26). Moreover, incubation of eNOS with 10 mM $FeSO_4$ failed to identify new metal-binding sites in crystallization experiments (42).

We report here the site-directed mutagenesis of the five conserved histidines in the human eNOS oxygenase domain, determination of the metal content of NOS expressed in *Escherichia coli* and purified by affinity chromatography, and analysis of the effect of exogenous Fe^{2+} and Zn^{2+} on the activity of human eNOS and nNOS.

III. Experimental Procedures

Materials and General Methods -- NOS was coexpressed with human CaM and purified as reported (91,115). Expression of the eNOS oxygenase domain, consisting of residues 1-521 plus a six-His tag, in pCWori will be reported separately in Chapter 4. *L*-Arg was obtained from Aldrich; 2',5'-ADP-Sepharose and 2'-AMP were from Sigma, and H_4B was from Alexis Biochemicals (San Diego, CA). The Superdex HR200 gel filtration column was from Amersham Pharmacia Biotech; *Vent* polymerase and restriction enzymes were from New England Biolabs Inc. (Beverly, MA); and the pGEM-T vector and isopropyl-β-D-thiogalactopyranoside were from Promega (Madison, WI). DNA purification kits and Ni^{2+}-NTA-agarose were purchased from QIAGEN Inc. (Chatsworth, CA). Bacto-yeast extract, Bacto-Tryptone, and *E. coli* DH5α cells were from Life Technologies, Inc., and BL21 DE3-competent cells were from Novagen (Madison, WI).

Construction of the His-to-Ala Mutants -- The five His-to-Ala mutants were constructed by overlap polymerase chain reaction, with two complementary mutagenic primers that introduced a new restriction site (silent mutations) to facilitate screening of the clones. The reverse mutagenic primer was used together with one primer that annealed at the polyhistidine N-terminal tag of pCWori (115) in order to perform the first partial reaction. The forward mutagenic primer was used together with a primer that

annealed after the unique *Kpn*I site for the second partial reaction. Once the two partial reactions were completed, the two fragments were copurified and gel-extracted with the purpose of using them as templates for the long polymerase chain reaction in which only the primers that annealed at both ends were used. The sequences of the forward primers that were used in the mutagenesis are given below (the reverse primers used are the exact complementary strand), with the residues in boldface indicating the new restriction site and the underlined residues the mutated site: H146A, 5'-AGCGGCTCCC AGG**CCGCGG**A ACAGCGGCTT CAA-3', which introduces a new *Sac*II site; H214A, 5'-GAAATGTTCA CCTA**CATATG** CAACGCCATC AAGTATGCCA CC-3', which introduces a new *Nde*I site; H420A, 5'-GTCACCATC**G TCGAC**GCCCA CGCCGCCACG-3', which introduces a new *Sal*I site; H421A, 5'-ACCATCGTGG ACCAC**G*CCG*C G**GCCACGGCC-3', which introduces a new *Sac*II site; and H461A, 5'-CCCATCTCGG G**AAGCTT**AAC TCCTGTTTTC GCTCAGGAGG AGATGGTC-3', which introduces a new *Hind*III site.

The polymerase chain reaction products were double-digested with *Nde*I plus *Kpn*I and ligated into the corresponding site of human eNOS-poly-His-pCWori (91) from which the wild-type sequence had been removed. The positive colonies were screened for the new restriction sites introduced with the mutation. The positives were sequenced at the University of California, San Francisco, sequencing facility to confirm the presence of the mutation.

Expression and Purification of the Mutant Proteins -- The mutant DNA was used to transform BL21 DE3-competent cells containing a human CaM coexpression system

(91). A fresh colony was picked and used to inoculate 2 ml of LB medium that was grown overnight at 37 °C in the presence of 0.1 mg/ml ampicillin plus 0.034 mg/ml chloramphenicol. This culture was used to initiate a larger culture of 1.5 liters of 2×YT (16 g of bacto-tryptone, 10 g of bacto-yeast, 5 g of NaCl in 1 liter of deionized water, pH 7.0) that was grown in 2-liter flasks at 200 rpm at 37 °C. When the cell growth had reached an OD_{600} of 0.8, the cultures were induced with 1 mM isopropyl-β-D-thiogalactopyranoside and allowed to grow at 23 °C for 16 hours (91,115). The cells were then harvested by centrifugation in a GS3 rotor and frozen as a film in a plastic bag at -70 °C until purification of the protein was undertaken. Six liters of medium were used in a typical preparation. All subcloning and cloning was performed in *E. coli* DH5α cells, whereas protein expression was always performed in the protease-deficient *E. coli* BL21 DE3 strain.

The cell paste was resuspended in buffer A (50 mM HEPES, pH 7.5, 100 mM NaCl, 10% glycerol, plus protease inhibitors: 0.1 mM phenylmethylsulfonyl fluoride, 1 mM leupeptin, 1 mM pepstatin, and 1 mM antipain) with 0.5 mg/ml lysozyme. When needed, 1 mM *L*-Arg plus 10 μM H_4B were also added to the lysis buffer and kept throughout the entire purification process. The cells were then disrupted by pulse sonication, followed by ultracentrifugation to remove the cell debris (91,115). Then the supernatant was loaded on a Ni^{2+}-NTA-agarose column, pre-equilibrated in buffer A, then washed with 5 column volumes of a high-salt buffer A with 500 rather than 100 mM NaCl plus 100 μM $CaCl_2$, and the proteins were then eluted from the column with 150 mM imidazole in buffer A.

The protein eluted from the Ni^{2+}-NTA-agarose column was diluted 2-fold with distilled water to lower the ionic strength and was loaded onto the 2',5'-ADP-agarose column pre-equilibrated with buffer B (50 mM HEPES, pH 7.5, 10% glycerol, plus protease inhibitors) in the presence, when desired, of 1 mM *L*-Arg plus 10 μM H_4B. The column was washed with 3 volumes of buffer B containing 100 μM $CaCl_2$, and the protein was eluted with 10 mM 2'-AMP in buffer C (50 mM HEPES, pH 7.5, 1 M NaCl, protease inhibitors, and 10% glycerol). The purified proteins were stored at -70 °C, and freeze-thawing was avoided.

The only exception to the above procedure was the purification of EDTA-treated iNOS. In this case, the procedure was as described previously (175), except that imidazole was never used, and the protein was eluted from the Ni^{2+}-NTA column by stripping the Ni^{2+} with 50 mM EDTA in 50 mM Tris, pH 7.5, 500 mM NaCl, 10% glycerol, and protease inhibitors (as above). The protein was then bound to ADP-agarose and washed with 4 column volumes of 50 mM EDTA in buffer D (50 mM HEPES, pH 7.5, 300 mM NaCl, and 10% glycerol) to remove protein-bound Ni^{2+}. Another wash was performed with 8 column volumes of buffer D. Purification was then continued as before in the absence of EDTA. Since the H421A and H146A mutants displayed a high tendency to lose the heme prosthetic group, spectral analyses were also performed for these proteins immediately after the protein was eluted from the Ni^{2+}-NTA-agarose column.

Restoration of the Heme Environment in the H461A Mutant -- To study the time-dependent binding of H_4B to the protein, the base-line spectrum of the protein was recorded in the presence of 10 mM *L*-Arg. Addition of 100 μM H_4B induced a

progressive increase in the high-spin component and a progressive decrease in the low-spin component of the spectrum. The first difference spectrum was recorded 1 min after H_4B addition, and successive spectra were recorded every 5 min at 25 °C. The spectra were plotted, and the A_{390nm} - A_{430nm} values were calculated. The spin change (A_{390nm} - A_{430nm}) was plotted *versus* time, and the plot was fitted to the following equation, where A is the maximum absorbance value and k is a kinetic refolding constant:

$$(1) \qquad A_{390nm} - A_{430nm} = A * (1 - e^{-kt})$$

FPLC Assays -- Aliquots of the mutant proteins (200 µl, ~0.5 mg/ml) were analyzed at 25 °C on an LCC 500-Plus FPLC system equipped with two P-500 pumps, a Superdex HR200 column, and a monitor set at 280 nm. The flow rate was 0.5 ml/min, and the buffer consisted of 50 mM HEPES, pH 7.0, and 100 mM NaCl. When desired to promote dimer formation, the buffer included 1 mM *L*-Arg and 0.5 µM H_4B. The column void volume was determined with dextran blue, and the total volume with potassium ferricyanide. The column was calibrated with the following proteins (Sigma): thyroglobulin (669 kDa), apoferritin (443 kDa), β-amylase (200 kDa), alcohol dehydrogenase (150 kDa), bovine serum albumin (66 kDa), carbonic anhydrase (29 kDa), and horse myoglobin (17 kDa). The calibration curve was obtained by plotting the $(v_e - v_0)/(v_t - v_0)$ ratio against the log of the molecular mass, where v_e is the elution volume of the protein, v_0 is the void volume of the column, and v_t is the total bed volume of the column. The elution positions of the dimer (~10.5 ml) and monomer (~11.5 ml) were used as a reference (91).

Anaerobic Formation of CO Complexes -- Absorption spectra were obtained by placing the proteins (2-5 μM) in a septum-sealed cuvette under vacuum and adding NADPH (100-300 μM). No CaM was added since the proteins were coexpressed with human CaM (91). The Ca^{2+} concentration was kept constant at 100 μM. After recording the spectrum, CO was purged into the cuvette for 3 min, and the cuvette was resealed to preserve the CO atmosphere. Spectra were recorded immediately on a Varian Cary 1E spectrophotometer connected to a Lauda circulating water bath set at 30 °C.

NO· Assay and Incubation with Divalent Cations -- The activities of the eNOS mutant proteins were determined at 37 °C by measuring the conversion of oxyhemoglobin to methemoglobin (91,115). The initial rates of NO· production were determined from $\Delta A_{401\text{-}411nm}$ ($\Delta\varepsilon_{400\text{-}411nm}$ = 60 mM^{-1} cm^{-1}) on a Cary 1E spectrophotometer. The final assay sample volume was 0.5 ml. The protein concentration was calculated using ε_{400nm} = 100 mM^{-1} cm^{-1} for the ferric enzyme under conditions that maximized the high-spin state (*i.e.* high concentrations of *L*-Arg and H_4B). When the NO· -releasing activities of the NOS enzymes were assayed in the presence of divalent cations, freshly prepared stock solutions of 4 mM ferrous sulfate or zinc sulfate in 100 mM Tris buffer, pH 7.0, were utilized. These solutions were used to prepare 0.4 mM stock solutions of both salts, again in 100 mM Tris buffer, pH 7.0. Addition of 5 μl of these fresh solutions to a final assay volume of 0.5 ml (see above) resulted in a 100-fold dilution (final concentrations of 40 and 4 μM). The Fe^{2+} or Zn^{2+} solutions were added to the assay mixture, and the rates were immediately measured.

Metal Determination -- The metal content in NOS samples was determined by inductively coupled plasma (ICP) atomic emission spectroscopy by Ernest Appelhans of Garratt-Callahan Co. (Millbrae, California).

Cytochrome c Reduction Assay -- The rate of reduction of cytochrome *c* was measured at 37 °C using ε_{550nm} = 21 mM^{-1} cm^{-1}. Reaction mixtures containing 50 mM HEPES, pH 7.5, 100 μg/ml bovine serum albumin, 100 μM $CaCl_2$, 500 μM NADPH, 50 μM cytochrome *c*, 50 units of catalase, and 2-5 μg of eNOS were initiated by adding cytochrome *c* and NADPH. Both H_4B and dithiothreitol were avoided when cytochrome *c* reduction was assayed to minimize the buffer-mediated reduction.

IV. RESULTS

The five histidines mutated are shown within the oxygenase domain dimer structure of eNOS in Figure 2-3, and each section will refer back to this figure.

Characterization of the H146A Mutant -- H146 is located far from the active site in the α2 helix of eNOS (Figure 2-3) (42). Expression of the H146A mutant and elution from Ni^{2+}-NTA-agarose yielded a protein with a Soret absorption maximum at 408 nm despite the presence of the 150 mM imidazole used to elute the protein from the column (Figure 2-4, *trace 1*). Addition of up to 30 mM *L*-Arg plus 30 μM H_4B did not induce a low- to high-spin shift in the Soret maximum. The absence of a distinct 427 nm absorption peak in the H146A mutant in the presence of imidazole indicates that either the heme distal site is occupied by another ligand or the proximal thiolate ligand has been lost. The absence of a Soret band shift in the presence of high concentrations of *L*-Arg

and H_4B confirms that major alterations have occurred in the heme environment. When the H146A mutant was reduced with NADPH under a CO atmosphere, the reduced CO difference spectrum exhibited only a cytochrome P420 peak (Figure 2-4, *inset*).

Figure 2-3. Three-dimensional structure of the bovine eNOS oxygenase domain dimer, showing the positions of the mutated histidine residues. The histidines are H146, H214, H420, H421, and H461 in human eNOS (in green). The heme (blue sticks), hydroxyarginine (cyan sticks), and Zn^{2+} ion (red sphere) are also shown relative to the two subunits (grey and blue ribbons) of the dimer.

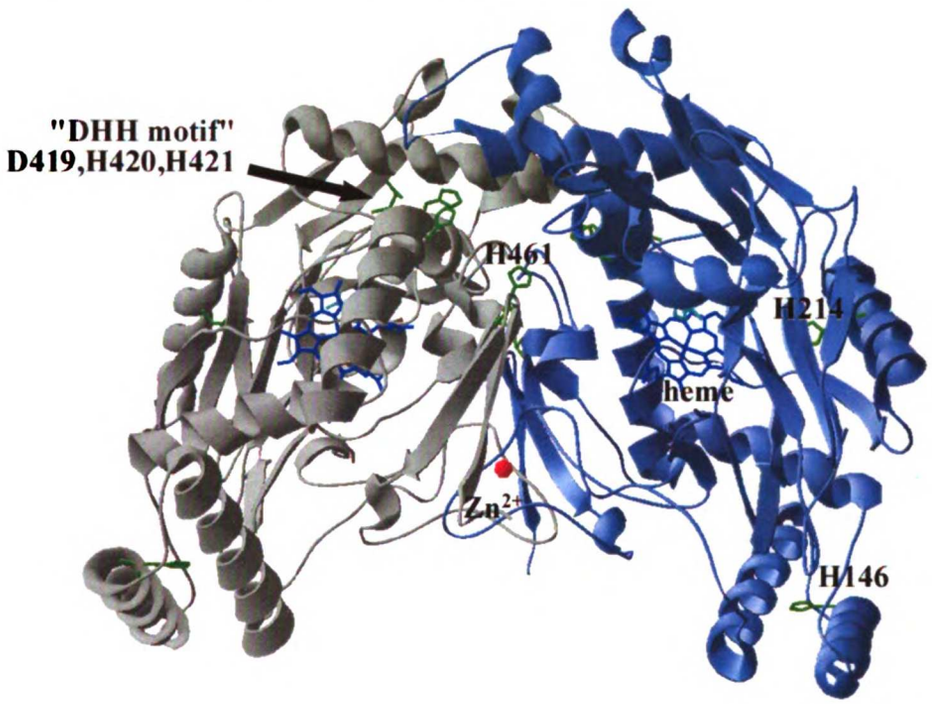

The H146A mutant eluted from Ni^{2+}-NTA-agarose was further purified by chromatography on a 2',5'-ADP-agarose column. The absorption spectrum of the resulting protein (Figure 2-4, *trace 2*) shows that the heme was lost during the column washes, leaving only the residual electronic absorbance of the flavin domain. The H146A mutation, despite its distance from the heme group, perturbed the active site sufficiently that the heme was incorrectly coordinated and dissociated from the protein during normal chromatographic procedures.

Figure 2-4. Spectral characterization of the H146A mutant. Trace 1, electronic absorption spectrum of the H146A mutant purified from the Ni^{2+}-NTA-agarose column and incubated with 30 mM *L*-Arg plus 30 μM H_4B for 15 min; trace 2, electronic absorption spectrum of the full-length H146A mutant eluted from the 2',5'-ADP-agarose column. The inset shows the NADPH-dependent formation of a reduced CO complex of the H146A mutant eluted from the first affinity column (trace 1). A spectrum was taken every 3 min. Identical results were obtained with three different preparations of this mutant.

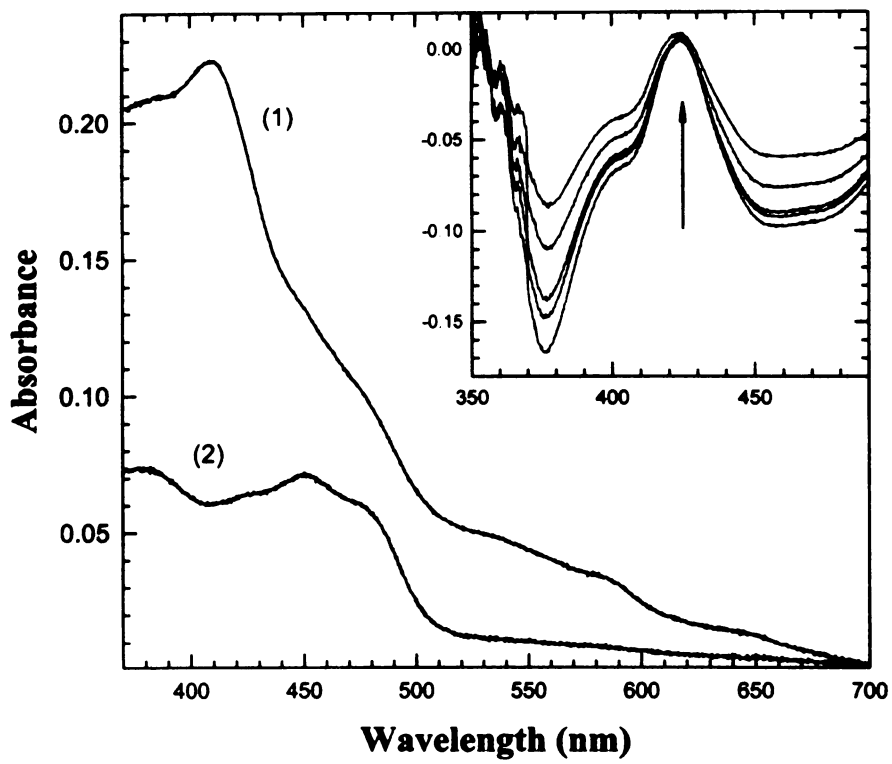

Characterization of the H214A Mutant -- H214 is located at the C-terminal end of the α4 helix at some distance from the heme group (Figure 2-3) (42). The recombinant protein was obtained in high purity by the procedure employed previously to purify wild-type human and bovine eNOS. Spectroscopically, this mutant is indistinguishable from wild-type eNOS (Figure 2-5). The Soret maximum at 395 nm (Figure 2-5, *trace 1*) obtained in the presence of *L*-Arg and H_4B indicates that the heme is in the high-spin state in the presence of these factors. Addition of 30 mM imidazole to this protein induced a high- to low-spin shift, as indicated by the final Soret maximum at 427 nm with an α/β-band at 550 nm (Figure 2-5, *trace 2*). When this mutant was analyzed by gel filtration on a Superdex HR200 column, the protein dimer was found to predominate. An asymmetric peak was seen at ~10.5 ml, with a broad shoulder at longer elution volumes that masked the position of the monomer at ~11.5 ml (Figure 2-5). This elution profile is identical to that for the wild-type protein analyzed under similar conditions (91,115).

The NO· -synthesizing activity of the H214A mutant (230 nmol min^{-1} mg^{-1}) is slightly higher than that of wild-type human eNOS (200 nmol min^{-1} mg^{-1}). The cytochrome *c*-reducing activity of the H214A mutant in the presence of CaM (2500 nmol min^{-1} mg^{-1}) is similar to that of the wild-type enzyme (3000 nmol min^{-1} mg^{-1}).

Figure 2-5. Characterization of the H214A mutant. The left panel depicts the spectroscopic behavior of the H214A mutant. Trace 1 shows the high-spin electronic absorption spectrum of H214A eNOS after elution from the 2',5'-ADP-agarose column in the presence of 2 mM *L*-Arg and 10 μM H_4B. Trace 2 shows the low-spin electronic absorption spectrum of the H214A mutant in the presence of 30 mM imidazole. An amplification of the α/β-bands is also shown (inset). The right panel shows the FPLC profile of the H214A mutant on a Superdex HR200 gel filtration column monitored at 280 nm. The letters D and M indicate the positions of the dimer (~10.5 ml) and monomer (~11.5 ml), respectively.

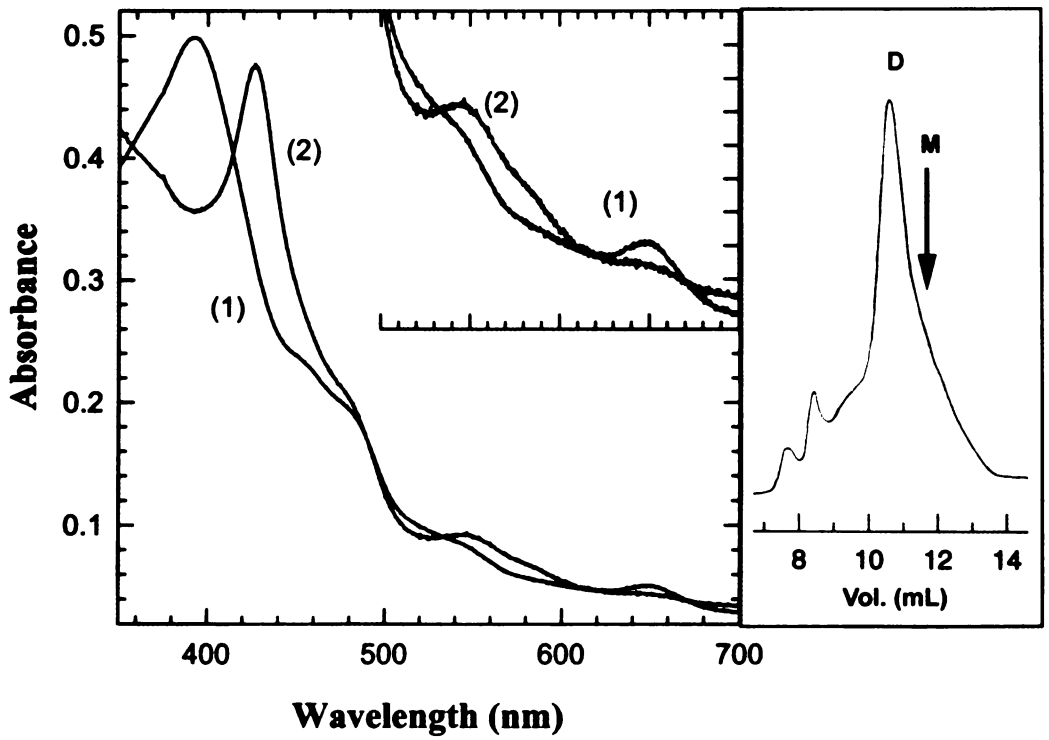

Characterization of the H420A and H421A Mutants -- H420 and H421 are located at the beginning of the α9 helix (Figure 2-3) (42) in a region close to the heme site proposed to undergo a large rearrangement upon dimerization (41). The imidazole side chains of H420 and H421 are hydrogen-bonded to Asp-397 in the neighboring subunit and thus participate in interactions that stabilize the dimer structure.

We were unable to obtain the full-length H420A mutant, apparently because it is proteolyzed in the *E. coli* expression system. Heme insertion in the isolated protein was imperfect, as the protein eluted from the Ni^{2+}-NTA-agarose column did not exhibit the usual low-spin spectrum due to the imidazole complex. Its absorption maximum was at 406 nm and did not shift to a high-spin spectrum in the presence of large concentrations of *L*-Arg and H_4B (data not shown).

The full-length H421A mutant could be expressed and purified, although its heme group was mostly in the low-spin state (Figure 2-6, *left panel*). Addition of NADPH under a CO atmosphere to the protein eluted from the Ni^{2+}-NTA column resulted in reduction of the flavins and the progressive formation of an $Fe^{2+}\cdot$ CO complex with a maximum at 450 nm (Figure 2-6, *left panel* and *inset*). Although formation of the cytochrome P450 complex did not go to completion, the extent to which it was formed correlated with the fraction of full-length dimers in the sample as judged by FPLC. Since electron transfer in the NOS dimer appears to be a *trans*-process (*i.e.* from the flavins of one monomer to the heme of the other) (48), only full-length dimers can form the reduced CO complex with NADPH as the reductant. These results contrast with those for the nNOS H652A mutant, equivalent to the H421A mutant studied here (26), for which the 450 nm $Fe^{2+}\cdot$ CO complex could be obtained only when the iron was reduced with dithionite. This difference is not surprising given the higher stability of the eNOS than nNOS dimers and, consequently, the likelihood that the nNOS H652A mutant is primarily in the monomeric state.

Figure 2-6. Characterization of the H421A mutant. The left panel depicts the spectroscopic behavior of the H421A mutant. Trace 1 shows the electronic absorption spectrum of H214A eNOS after elution from the Ni^{2+}-NTA-agarose column in the presence of 30 mM *L*-Arg and 30 μM H_4B. Excess imidazole was then added, and a CO complex was formed as described under "Experimental Procedures." The arrow indicates the formation of the 450 nm $Fe^{2+}\cdot$ CO complex. The inset shows the difference spectrum due to $Fe^{2+}\cdot$ CO complex formation as a function of time, with a spectrum being taken every 3 min. The right panel shows the FPLC profile of the H421A mutant on a Superdex HR200 gel filtration column monitored at 280 nm. The three elution profiles correspond to three different preparations of the H421A mutant. Similar variability was obtained with four other preparations. D, dimer; M, monomer.

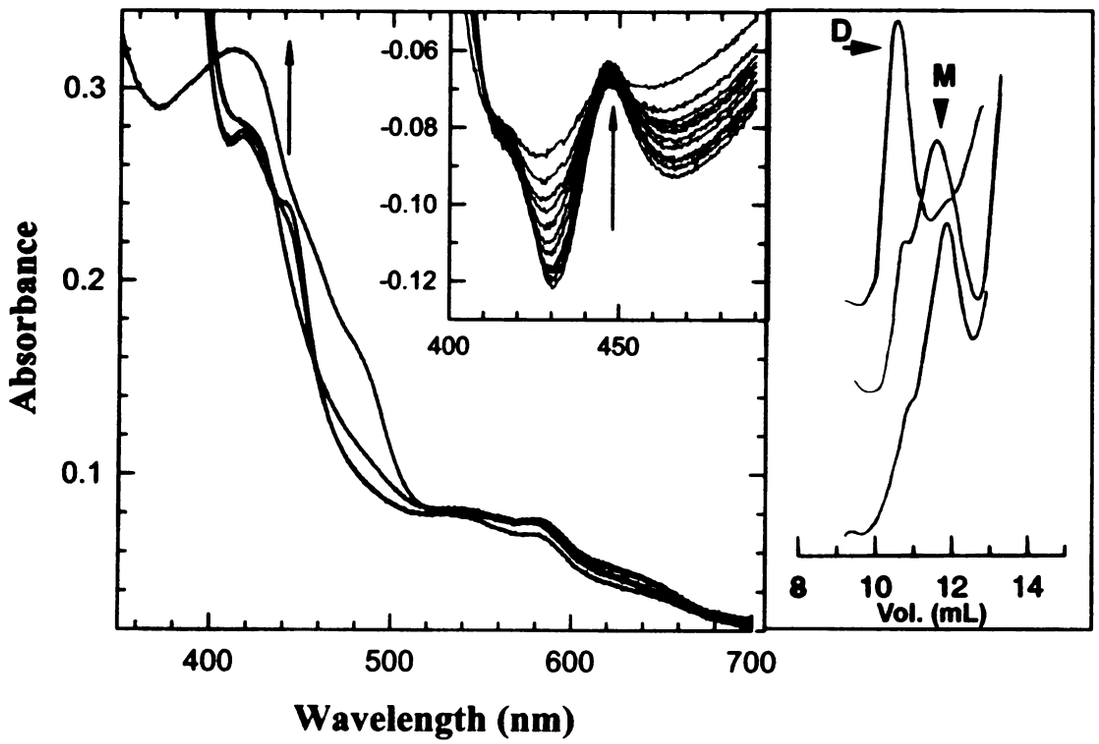

The dimer/monomer ratio for the H421A mutant varied from one preparation to another, depending on the amount of heme removed during the column washes. Figure 2-6 (*right panel*) shows FPLC traces of three different preparations of the H421A mutant after elution from Ni^{2+}-NTA-agarose. Peaks due to contaminating fragments that eluted after 13 ml have been omitted for clarity. H421A dimers and monomers were consistently observed, but in a widely varying ratio.

When the H421A mutant was further purified on an ADP-agarose column, the heme Soret maximum of the protein was at 415 nm, and even large concentrations of *L*-Arg and H_4B did not induce a low- to high-spin shift (data not shown). The purified H421A mutant had no NO· -synthesizing activity, but had wild-type cytochrome *c*-reducing activity (2700 nmol min^{-1} mg^{-1}).

Characterization of the H461A Mutant -- H461 in human eNOS (H463 in bovine eNOS) is located at the end of the α11b helix. Although it does not interact directly with H_4B, it contributes to the electrostatic interactions that stabilize the pterin moiety (Figure 2-3). One of the H461 imidazole nitrogens forms a hydrogen bond with a water molecule that, in turn, hydrogen bonds to a hydroxyl of the pterin dihydroxypropyl moiety from a different monomer (42). In iNOS (41), the backbone carbonyl group of F460 is also directly hydrogen-bonded to the dihydroxypropyl group. Replacement of H461 by an alanine gives a protein that is defective in the binding of H_4B (and consequently of *L*-Arg). This permits the low- to high-spin shift associated with the binding of H_4B to be monitored (91,115,176).

The H461A mutant purified in the absence of H_4B and *L*-Arg was almost completely in the low-spin state (Figure 2-7, *trace 1*). This contrasts with the wild-type protein, which, even in the absence of the cofactor and substrate, is predominantly in the high-spin state (91,115,176). Incubation of the H461A mutant with 1 mM *L*-Arg in the absence of H_4B engendered a moderate low- to high-spin shift (Figure 2-7, *trace 2*), but even prolonged incubation with up to 10 mM *L*-Arg did not produce a complete shift to the high-spin state. Binding of H_4B thus appears to be required for a complete shift in the

spin state. The spin state shift in the mutant appears to involve a slow refolding process keyed to the residues that bind H_4B and *L*-Arg because only after incubation of the mutant with 10 mM *L*-Arg plus 100 μM H_4B for 30 min at 30 °C did we obtain a high-spin absorption spectrum identical to that of the wild-type protein (Figure 2-7, *trace 3*). However, even under these optimal conditions, the H461A mutant was less active than the wild-type enzyme (see below).

Figure 2-7. Characterization of the H461A mutant. The left panel shows the electronic absorption spectrum of H461A eNOS after elution from the 2',5'-ADP-agarose column in the complete absence of *L*-Arg and H_4B (trace 1). Trace 2 was obtained after incubation of the same sample with 1 mM *L*-Arg in the absence of H_4B for 15 min. Subsequently, this mutant was incubated with 10 mM *L*-Arg plus 300 μM H_4B for 30 min at 25 °C (trace 3). The right panel shows the FPLC profile of the H461A mutant on a Superdex HR200 gel filtration column monitored at 280 nm. The two traces show the maximum (~70:30) and minimum (~40:60) dimer (D)/monomer (M) ratios observed for the H461A mutant in a total of six different preparations. In both cases, 10 mM *L*-Arg and 100 μM H_4B were present.

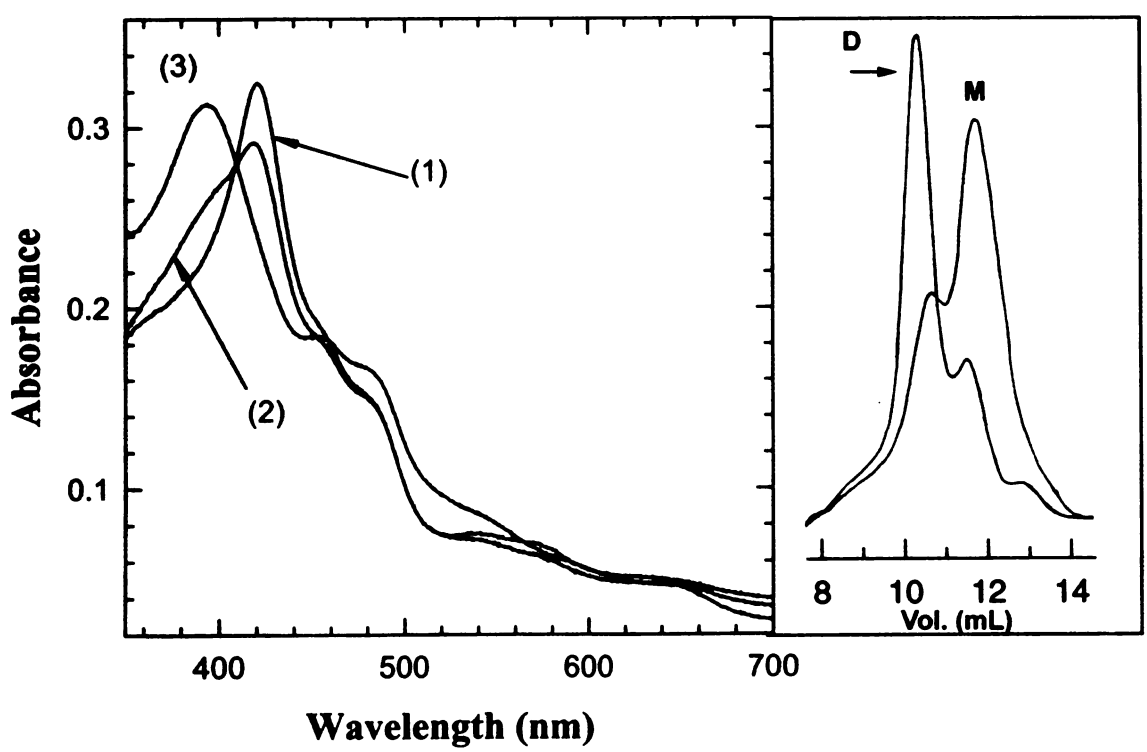

H_4B- and *L*-Arg-dependent alterations in the monomer-dimer equilibrium were also evident when the H461A mutant was examined by FPLC. The relative ratio of dimers to monomers was preparation-dependent, ranging from a maximum of 70:30 to a minimum of 40:60 (Figure 2-7, *right panel*). Incubation of this mutant with 10 mM *L*-Arg plus 100 μM H_4B elevated the dimer population at the expense of the monomer population regardless of the initial dimer/monomer ratio (data not shown). However, in no instance did we observe the 90:10 dimer/monomer ratio typical of the wild-type protein under identical conditions (91).

NO· synthesis was not detected when the H461A mutant was assayed immediately after the protein was purified and 1 mM *L*-Arg and 1 μM H_4B were added. However, after incubation of the H461A mutant with 10 mM *L*-Arg plus 100 μM H_4B for 30 min at 30 °C, a value of ~50 nmol min^{-1} mg^{-1} was reproducibly obtained using the hemoglobin method. This corresponds to ~25% of the wild-type eNOS activity.

To characterize the refolding of the H461A mutant in the presence of high concentrations of *L*-Arg and H_4B, we recorded the low- to high-spin Soret band changes over a 30-min interval. The spectra were recorded at 25 °C in the presence of 10 mM *L*-Arg after addition of 100 μM H_4B (Figure 2-8, panel A). Plotting the A_{390nm} - A_{430nm} absorbance difference *versus* time yielded a kinetic constant for the binding of H_4B (Figure 2-8, panel B). The average value of the constant from four independent measurements is $k = 0.2 \pm 0.1$ min^{-1}. This slow binding of the pterin to the H461A mutant is to be compared with the binding of H_4B to the wild-type protein, for which both the low- to high-spin Soret transition and the NO· -releasing activity of the H_4B-deficient

enzyme are recovered immediately upon addition of H_4B (115). All of these results argue that the binding of H_4B is associated with a slow restructuring of the protein that restores the integrity of the heme site and the protein-protein interactions required for dimer formation and catalysis. The integrity of the reductase domain of the H461A mutant was confirmed by the cytochrome *c*-reducing activity in the presence of CaM (3500 nmol min^{-1} mg^{-1}), which compares favorably with the activity of the wild-type protein (3000 nmol min^{-1} mg^{-1}).

Figure 2-8. Refolding of the heme environment of the eNOS H461A mutant upon incubation with H_4B. The purified H461A mutant was incubated with 10 mM *L*-Arg before 100 μM H_4B (final concentration) was added, and the spectroscopic changes were monitored as described under "Experimental Procedures." The first difference spectrum was recorded 1 min after addition of H_4B, and spectra were subsequently recorded every 5 min at 25 °C (A). A plot of A_{390nm} - A_{430nm} versus incubation time is given in B. The curve was fitted to a single exponential equation (solid line) as described under "Experimental Procedures." The curve shown is representative of six different experiments.

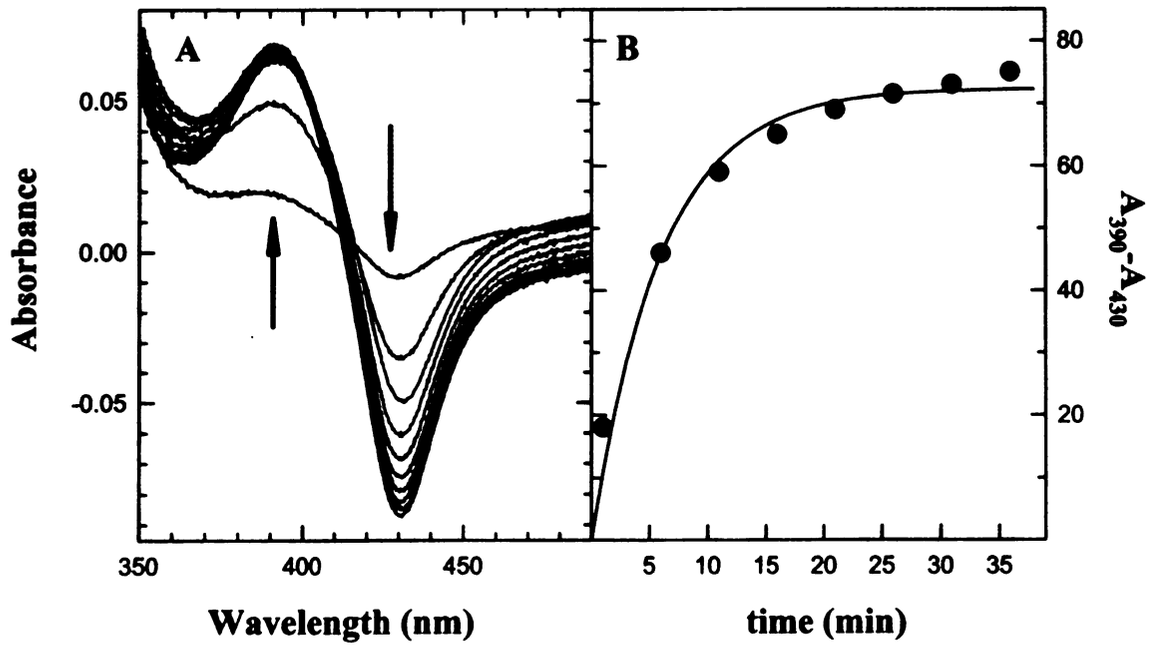

Metal Content of the NOS Isoforms-- The metal content of the NOS isoforms was determined by inductively coupled plasma atomic emission spectroscopy. As the iron content of the protein was difficult to quantitate precisely, the results are expressed relative to the iron content (Figure 2-9). The metals that were analyzed for were calcium, cobalt, copper, iron, magnesium, molybdenum, nickel, and zinc. The calcium level in all the samples was 3-6-fold higher than the iron level (data not shown).

Figure 2-9. Metal content of NOS isoforms determined by inductively coupled plasma atomic emission spectroscopy. The iNOS, eNOS oxygenase domain, and nNOS samples were purified by normal procedures. The iNOS (EDTA-treated) sample was obtained by the usual procedures, except that the protein was exposed to 50 mM EDTA when eluted from the Ni^{2+}-NTA-agarose column and while bound to the ADP-agarose column (for details, see "Experimental Procedures"). Only the results for copper, iron, and zinc are shown. None of the other metals tested (cobalt, magnesium, molybdenum, and nickel) was found in amounts much above the detection limit except in the EDTA-untreated iNOS sample, which contained appreciable amounts of magnesium, molybdenum, and nickel. These metals were not present after the EDTA washes.

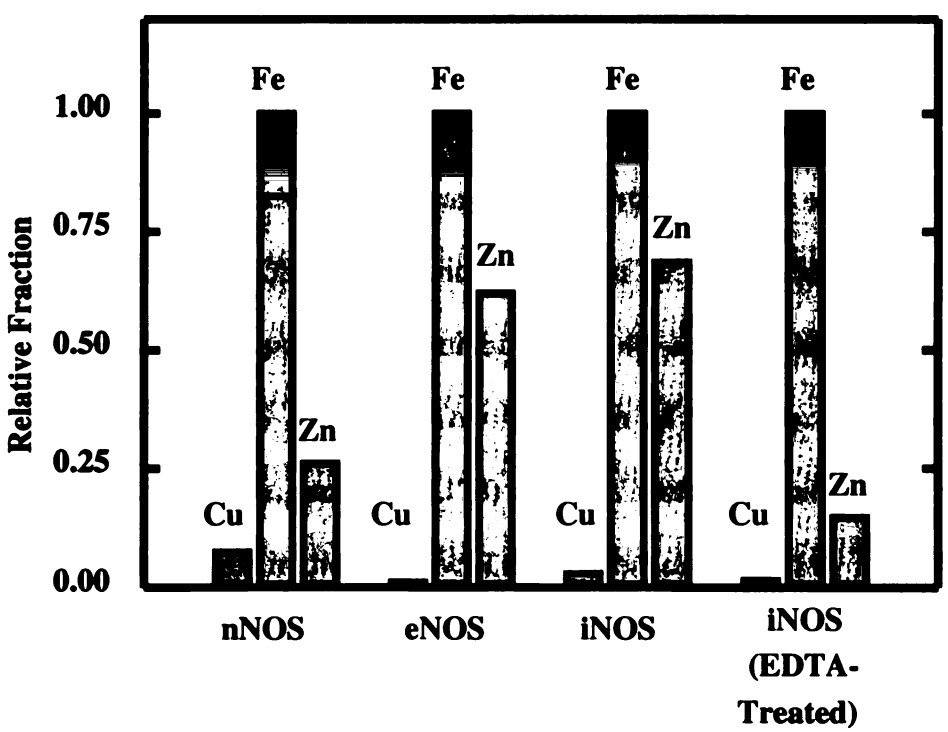

The eNOS oxygenase domain contained, in addition to calcium and iron, significant amounts of only zinc. Full-length nNOS contained, in addition to calcium and iron, a substoichiometric amount of zinc (relative to iron) and traces of copper and nickel. iNOS purified by the normal procedure contained a variety of metals, but when purified with EDTA-treated buffer washes, contained only calcium, iron, and small amounts of zinc and magnesium. No other metal apart from iron and calcium appeared to be present in significant amounts. In particular, copper was not found as a significant constituent, in contrast to an earlier report that copper is a major constituent of nNOS when it is isolated (26).

Incubation of eNOS and nNOS with Divalent Cations-- Fe^{2+} reportedly increases NOS activity (26). Zn^{2+}, which is present in the eNOS structure (42,124), has been shown at high concentrations to inhibit the enzyme (177,178). We compared the effect of these two divalent cations on NOS activity (Figure 2-10). In our hands, 4 μM Fe^{2+} had no effect on eNOS activity and only slightly enhanced the nNOS and inhibited the iNOS activities. Addition of 40 μM Fe^{2+} decreased the activities of eNOS and iNOS and caused little change in that of nNOS. Larger concentrations of Fe^{2+} (>80 μM) decreased all three NOS activities. Zn^{2+} is a potent NOS inhibitor, and 40 μM Zn^{2+} almost suppressed the eNOS, nNOS, and iNOS activities. This inhibition of NOS by Zn^{2+} was observed previously by other investigators (177,178) and was tentatively attributed to defective reduction of the heme iron in the presence of the divalent cation (178).

Figure 2-10. Effect of divalent cations on NOS activity. Fe^{2+} or Zn^{2+} at concentrations of 40 and 4 μM were included in the NOS assay mixture, and NO· formation was determined at 37 °C with the hemoglobin assay. The data are plotted using the eNOS, nNOS, or iNOS activity in the absence of any added metal as the reference 100% value. The activities of recombinant human eNOS (gray bars), rat nNOS (cross-hatched bars), and mouse iNOS (black bars) were examined. Similar results were obtained in three independent measurements.

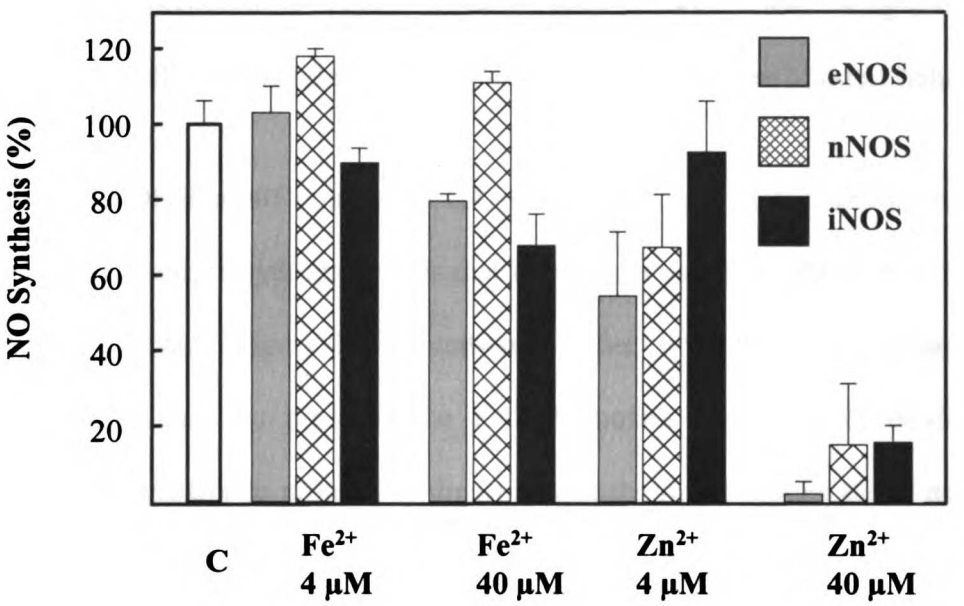

V. DISCUSSION

The roles of the five histidines conserved among all the known mammalian NOS sequences have been examined by site-directed mutagenesis. These studies have a direct bearing on the report that the activity of NOS is increased by divalent cations that coordinate to one or more of these histidine residues (26). This proposed histidine-dependent metal-binding site is distinct from the zinc site at the dimer interface (42,124) in which the metal is coordinated to four cysteine residues.

Three of the five conserved histidines (H146, H420, and H421) are part of secondary structural elements that are required for the enzyme either to fold properly or to assemble into the catalytically active eNOS dimer. H146 is distant from the active site (Figure 2-3), but its replacement with an alanine produces an inactive protein with an improperly incorporated heme group (Figure 2-4). These long-distance effects presumably reflect a critical role of H146 in the folding of the α2 and α1 helices.

The DHH motif containing H420 and H421 lies at the dimer interface and is involved in multiple hydrogen bonds that implicate it as a critical region in the monomer-monomer interface (Figure 2-3). Mutation of either of the histidine residues in the DHH motif destabilizes the protein. The H420A mutant is apparently misfolded and is sufficiently sensitive to proteolytic digestion that the intact protein could not be isolated. The purified H421A mutant has a low-spin heme Soret maximum and is both unstable and inactive. However, the dimeric form of the protein retains the heme prosthetic group and forms an Fe^{2+}· CO complex when reduced with NADPH (Figure 2-6). The CO complex is formed only by the lower (*versus* wild-type) fraction of the protein in the dimeric state, as electron transfer to the iron reportedly occurs from the reductase domain of one monomer to the oxygenase domain of the other (48). This behavior contrasts with that observed when H652, the equivalent residue in nNOS, was mutated (26). The inability of NADPH to reduce the H652 mutant of nNOS led to the proposal that loss of a divalent metal coordinated to the histidine interrupted the electron transfer pathway. The present results with the eNOS H421A mutant make this explanation untenable, at least as a general one. Our data indicate that the inactivity of the eNOS H421A mutant, and presumably its nNOS H652A counterpart, is due to the formation of a defective heme

environment and dimer interface, as evidenced by an increase in the proportion of the protein in the monomeric state. Although the H420/H421 pair from each of the eNOS monomers faces the corresponding H420/H421 pair of the other monomer, the arrangement of these four imidazole side chains does not seem to be appropriate for metal coordination since no metal was bound in this region when the eNOS oxygenase domain was incubated with 10 mM $FeSO_4$ (42). H214 does not fulfill an apparent major catalytic or structural role because the H214A mutant displays a wild-type phenotype (Figure 2-5).

Mutation of H461, which binds to H_4B, alters the monomer-monomer interaction, the heme chromophore (Figure 2-7), and the NO· -releasing activity of eNOS. Indeed, one of the electrostatic interactions necessary for proper binding of H_4B involves a hydrogen bond through a water molecule to one of the imidazole nitrogens of H461. This stabilizing interaction implicates the histidine residue of one subunit in binding the pterin molecule of the other subunit (42). In contrast to wild-type eNOS, which binds H_4B almost instantaneously (115), the H461A mutant binds H_4B slowly even in the presence of 10 mM *L*-Arg. This suggests that H_4B binding requires gradual refolding of the biopterin site and dimer interface (Figure 2-7). This reorganization of the biopterin-binding site, which is accompanied by a low- to high-spin shift of the iron, occurs over a period of ~30 min at 25 °C (Figure 2-8). When reconstituted with H_4B, the H461A mutant has ~25% of the catalytic activity of the wild-type enzyme. The lower activity of fully reconstituted H461A eNOS, despite its full conversion to the high-spin state, stems, at least in part, from a subtle disruption of the monomer-monomer interface. Direct evidence for this is provided by FPLC analysis, which shows that the dimer/monomer ratio for the H461A mutant is lower than that for the wild-type protein (Figure 2-7, *right panel*). A comparable

alteration in the binding of H_4B has been reported for the nNOS C331A mutant, which requires prolonged incubation with *L*-Arg and H_4B to bind the biopterin and to reconstitute the catalytic activity (179). Sequence comparisons suggest that C331 is one of the cysteines in nNOS that coordinate to the Zn^{2+} cation. The structural alteration due to defective binding of Zn^{2+} is presumably overcome by the slow binding of *L*-Arg and H_4B (179).

Metal analysis of the eNOS, nNOS, and iNOS samples indicates that the only significant metal associated with the proteins, apart from calcium and iron, is zinc. Zinc is present in the eNOS oxygenase domain at a ratio of ~0.6 eq. relative to the total iron; in nNOS at a ratio of ~0.3 eq.; and in iNOS at ratios of ~0.7 and 0.2 equivalents in the enzyme isolated with normal and EDTA-treated buffers, respectively (Figure 2-9). The zinc content roughly correlates with the stability of the homodimer to dissociation because the eNOS homodimer is the most stable and the iNOS homodimer the least stable among the isoforms. It is likely that the monomeric enzyme does not retain the zinc because the zinc-binding site, as shown by crystal structures of eNOS and iNOS (42,124), is at the dimer interface and is composed of two thiolate groups from each of the monomers in the dimer. Thus, a completely dimeric enzyme would be expected to have 0.5 equivalents of zinc relative to heme iron, close to the value found for the eNOS oxygenase domain and iNOS purified without exposure to EDTA. Monomerization of the protein should decrease the proportion of bound Zn^{2+}, as found for nNOS and EDTA-treated iNOS. The metal content studies provide no support for the presence of a catalytic metal other than the heme iron, although it has not been possible to quantitate the iron content sufficiently well to determine whether any non-heme iron is present.

The metal independence of the activities of eNOS and nNOS found here differs from the report that the activities of nNOS and iNOS increase upon incubation with Fe^{2+} (26). In our hands, the maximum increase in NO· production by nNOS upon incubation with iron, as judged by the hemoglobin assay, is only 18% (Figure 2-9). No increase in the eNOS and iNOS activities was observed upon incubation with 4 μM iron, and a reproducible decrease in the these activities was observed with 40 μM Fe^{2+}. The reason for the discrepancy in our findings and those of Perry and Marletta (26) is unclear. One difference in the two experiments is that Perry and Marletta measured activity by measuring the conversion of [^{14}C]arginine to [^{14}C]citrulline, whereas we determined the production of NO· by the hemoglobin assay. The oxidation of guanidoximes such as *N*-hydroxyarginine is catalyzed by a variety of oxidizing systems, including cytochrome P450 (180), horseradish peroxidase/H_2O_2 (181), hemoglobin (II), H_2O_2 alone (182), and superoxide (183). This oxidation primarily produces nitrites or nitrates rather than NO. It is possible that exogenous iron accelerates the NOS reaction by oxidizing *N*-hydroxyarginine via a non-physiological mechanism that yields Cit, but does not produce NO. A second difference in the two sets of experiments is that the previous work intentionally used metal-depleted buffer in these activity assays, a treatment that might result in loss of the Zn^{2+} bound to the Zn^{2+}-binding site at the dimer interface. The different stabilities of the three isoforms toward monomer formation suggest that this might have the most severe consequences for iNOS, for which the dimer is the least stable, and the least consequences for eNOS, for which it is the most stable (59). A recovery of activity could reflect a divalent metal-induced increase in dimer formation due to reformation of catalytically active dimer. This explanation, however, is

inconsistent with the stoichiometry reported by Perry and Marletta, who found that both nNOS and iNOS could be reconstituted with one non-heme iron per monomer. Even if one of these iron atoms occupies the Zn^{2+}-binding site at the monomer-monomer interface, a second site would have to be found for the additional iron atom.

In summary, one of the conserved histidines distant from the active site (H214) is not critical for protein folding or catalytic activity, whereas the other (H146) fulfills an important role in assembly of the protein and its active site. The three conserved histidines near the heme and biopterin are all critical for intersubunit interactions and catalytic activity: mutations of H420 and H421 irreparably alter the active site, but mutations of H461 can be partially overcome by high concentrations of *L*-Arg and H_4B. Malfunction of the protein due to the histidine mutations appears to reflect alterations in the protein structure and its ability to bind heme and to form dimers rather than loss of a metal coordination site. The metal content of the proteins and their lack of activation by exogenous Fe^{2+}, in conjunction with the findings on the conserved histidines, provide no support for the proposed involvement of a metal other than the heme iron (and the structural Zn^{2+}) in the catalytic process (26).

NOS REDUCTASE DOMAIN MODELS SUGGEST A NEW CONTROL ELEMENT IN eNOS THAT ATTENUATES CaM-DEPENDENT ACTIVITY[4].

CHAPTER 3

This work was originally published on August 22, 2003 in the *Journal of Biological Chemistry*, volume **278,** issue 34, pp. 31814-24. The work is included here with permission from the coauthors Clinton R. Nishida, Sean D. Mooney, and Paul R. Ortiz de Montellano from the Department of Pharmaceutical Chemistry, University of California, San Francisco, California 94143-2280.

[4] This work was supported by National Institutes of Health Grant GM25515. G. Knudsen was partially supported by a fellowship from the Medicinal Chemistry Division of the American Chemical Society sponsored by Pfizer Global Inc. Sean Mooney was funded by NIH Grant AR47720-01 (T. Klein, PI).

I. ABSTRACT

Inducible (iNOS) and constitutive (eNOS, nNOS) nitric oxide synthases differ in their regulation by Ca^{2+}-dependent calmodulin (CaM). iNOS binds CaM irreversibly but eNOS and nNOS, which bind CaM reversibly, have inserts in their reductase domains that regulate electron transfer. These include the 43-45 amino acid autoinhibitory element (AI) that attenuates electron transfer in the absence of CaM, and the C-terminal 20-40 amino acid tail that attenuates electron transfer in a CaM-independent manner. We constructed models of the reductase domains of the three NOS isoforms to predict the structural basis for CaM-dependent regulation. We have identified and characterized a loop (CD2A) within the NOS connecting domain that is highly conserved by isoform and that is within direct interaction distance of the CaM-binding region as is the AI element. The eNOS CD2A loop (eCD2A) has the sequence ^{834}KGSPGGPPPG^{843}, and is truncated to ^{809}ESGSY^{813} (iCD2A) in iNOS. The eCD2A contributes to the Ca^{2+}-dependence of CaM-bound activity to a level similar to the AI element. The eCD2A plays an autoinhibitory role in the control of NO, and CaM-dependent and -independent reductase activity, but this autoinhibitory function is masked by the dominant AI element. Finally, the iCD2A is involved in determining the salt-dependence of NO· activity at the level of post-flavin reduction. Electrostatic interactions between the CD2A loop and the CaM-binding region, and CaM itself, provide a structural means for the CD2A to mediate CaM regulation of *intra*-subunit electron transfer within the active NOS complex.

II. INTRODUCTION

Nitric oxide synthase (NOS) is a modular homodimeric protein that contains in each subunit an N-terminal oxygenase domain that catalyzes cytochrome P450-like oxidations and a C-terminal two-flavin domain homologous to that of cytochrome P450 reductase (CPR) (3,106). The NOS oxygenase and reductase domains are linked by a calmodulin (CaM) binding helix. The NOS oxygenase domain is completely different from a cytochrome P450 (P450), however, in that it has no sequence identity with that family of enzymes and has an α,β-fold structure distinct from the highly α-helical structure of the P450 enzymes (41,42,124,184) (Figure 1-2). Furthermore, the two-stage mechanism for the oxidation of *L*-arginine (*L*-Arg) to *L*-citrulline (*L*-Cit) and nitric oxide (NO·) by NOS is more complex than that of a P450 enzyme, as it requires tetrahydrobiopterin (H_4B) as a transient electron donor (95). In contrast, the NOS reductase domain exhibits considerable sequence identity with CPR, and the electrons, as in P450/CPR, flow from NADPH to the FAD, then to the FMN, and finally, upon substrate binding, to the heme (106,155).

In the P450 system, the principal control on inter-protein electron transfer is the requirement for association of the P450 with CPR. The NOS complex also requires interactions between independently transcribed proteins because it is a homodimer in which the reductase domain of one subunit provides electrons to the oxygenase domain of the other (48,80). However, inter-domain electron transfer in NOS also requires the

binding of CaM, and the Ca^{2+} dependence of CaM-binding differs between the constitutive and inducible isoforms (64,65).

The three NOS isoforms are classified according to their dependence on Ca^{2+} for CaM binding (3). The inducible isoform (iNOS or NOS II) is regulated primarily at the transcriptional level. It irreversibly binds CaM in a Ca^{2+} independent manner and exhibits the highest catalytic activity of the three isoforms (65). The constitutively expressed isoforms, eNOS (or NOS III) and nNOS (or NOS I), bind CaM reversibly in a Ca^{2+} dependent manner (64,65,80). These differences in activity and regulation reflect the functions of the proteins: a tempered activity is consistent with the roles of the constitutive forms in functions such as blood pressure regulation and neuronal signaling, and a strong burst of activity with that of the inducible form in the immune response to pathogens. Interest in controlling the activities of the individual NOS isoforms currently centers on their roles in inflammatory responses such as arthritis and septic shock as well as in homeostatic diseases such as hypertension (185).

We have sought to define the structural and chemical elements that control electron transfer in the different NOS isoforms by comparing the NOS family with homologous proteins. The redox behavior of the iNOS reductase domain is similar to that of CPR, and iNOS is capable of high electron transfer rates to exogenous acceptors in the absence of CaM. The flavin domain of iNOS is most similar to that of CPR in sequence, whereas those of eNOS and nNOS exhibit slightly lower identity to CPR due to the site-specific insertion of additional residues (106).

The elements within the eNOS and nNOS reductase domains that distinguish them from the iNOS reductase domain and CPR may help to govern the high and low activities of the CaM-bound and CaM-free enzymes, respectively, since CaM-binding strictly regulates electron transfer between the reductase and oxygenase domains as well as between flavins within the reductase (139). These differences in electron transfer activity with and without CaM can be observed when the nNOS oxygenase and reductase domains are independently expressed (137,186). Furthermore, the elements that control the CaM dependence and relatively low rate of electron transfer to the oxygenase domain in eNOS appear to be localized entirely within the reductase domain since NOS chimeras with the eNOS oxygenase domain fused to the iNOS or nNOS reductase domain exhibit high activities (35). Conversely, chimeras in which the eNOS reductase domain is fused to the iNOS or nNOS oxygenase domain have low, eNOS-like activities (35). This CaM regulation of electron transfer rates is postulated to be mainly conformational in nature, because CaM binding has been shown to have no effect on the midpoint potentials of the flavins (187) and no effect on spin-relaxation rates of the flavin radical (188) in nNOS. CaM binding accelerates electron flow within the reductase domain, but electron transfer through the flavins and from them to alternate exogenous acceptors still occurs at low rates even in the absence of CaM (189).

Alignment of the NOS primary sequences identifies differences that could be responsible for the differences in the constitutive and inducible isoforms. The largest sequence difference between the reductase domains of the three NOS isoforms is a 43-45 amino acid insert (at residue 595 of eNOS and 835 of nNOS) that is absent in iNOS. Excision of this autoinhibitory (AI) element from eNOS or nNOS enhances the CaM-

dependent NO-synthesizing activity to a level approaching that of iNOS (36,45). However, complete Ca^{2+}-independence analogous to that of iNOS is not obtained upon deletion of the AI element, suggesting that other reductase domain elements may also interact with CaM.

An approximately 20-40 amino acid extension at the C-terminus is a second feature that distinguishes the NOS enzymes from CPR (190). Trimming this extension causes CaM-independent hyperactivity of inter-flavin electron transfer in all three NOS isoforms, but NO· production is only slightly increased in iNOS and is decreased in eNOS and nNOS (164,165). However, in contrast to removal of the AI insert, truncation of the terminal extensions does not alter the Ca^{2+}-dependence of CaM binding. In eNOS, phosphorylation of the C-terminus provides an alternative route for activation of electron transfer that is independent of the Ca^{2+}-dependent regulatory mechanism (190). Altering the C-terminus may loosen a tightly tuned electron transfer system, so that either deletion of the unique tails or phosphorylation increases flavin reduction and consequently NO· activity in a CaM-independent manner. Further supporting this argument, mutation in nNOS of the C-terminal aromatic residue that is highly conserved within the ferredoxin reductase (FNR) family increases electron transfer rates in the absence of CaM (191).

We have added structural models to the sequence-based analysis of CaM-related regulatory elements. Partial reductase structures of nNOS have been solved (43) or predicted (167), but our models of the full reductase domain allow placement of the various regulatory elements relative to the flavin subdomains. Furthermore, comparison between isoforms identifies a unique loop (CD2A) within the connecting domain that is

highly conserved by isoform, but non-conserved between them and CPR (Figure 3-1).

Figure 3-1. Sequence alignment of the CD2 region of NOS and CPR from several mammalian species[5]. The figure was created using the Pileup program in the GCG suite of software (192). Black and gray highlighting indicates highly conserved residues across the sequences in the alignment.

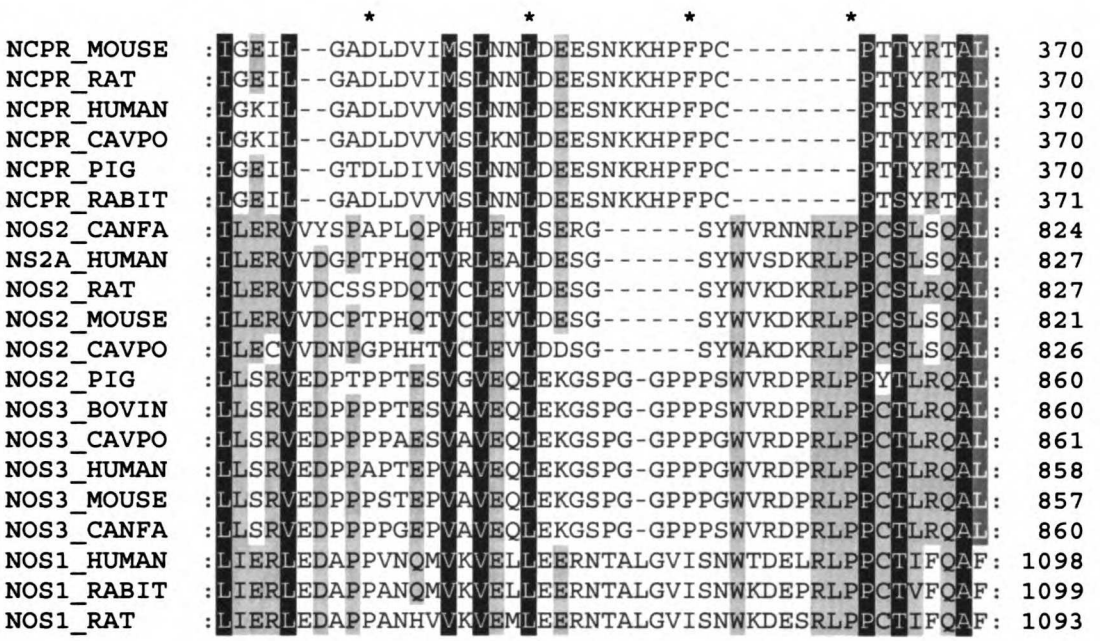

In eNOS, the NOS isoform with the slowest electron transfer and overall activity rates, the CD2A loop is five amino acids longer than in iNOS. In our models, this CD2A loop is extended towards the base of the CaM-binding helix (145), and is able to provide several electrostatic interactions with either the FMN subdomain or CaM itself. The structure of CaM bound to a peptide corresponding to eNOS residues 492-510 was recently solved and includes residues at the N-terminus of the eNOS model (44). Given the distance and orientation constraints for the position of the peptide bound by CaM,

[5] GenBank Accession Numbers 548338, 127966, 2851393, 548337, 1346670, 127965, 8473511, 1352513, 1709334, 266649, 8473504, 8473477, 266647, 8473528, 266648, 8473673, 5814292, 1709333, 8473494, 266646.

both the CD2A and the AI elements are modeled to be within contact distance of the CaM-binding region (Figure 3-2).

Figure 3-2. The homology model of the eNOS reductase domain is shown as a ribbon diagram, with the FMN, FAD and NADPH cofactors shown in black stick representations. Below is a schematic alignment of the NOS reductase domain against CPR, flavodoxin and ferredoxin reductase (FNR). The FMN subdomain is shown to be of the flavodoxin fold, and it contains the last turn of the CaM-binding helix at the N-terminus. The position of the constitutive NOS AI insertion point is indicated on the structure by arrows and within the sequence as a black insert. The connecting domain is split into two portions, the CD1 and CD2, by a short section of the FAD/NADPH domain. The FAD/NADPH subdomain corresponds to the fold of FNR.

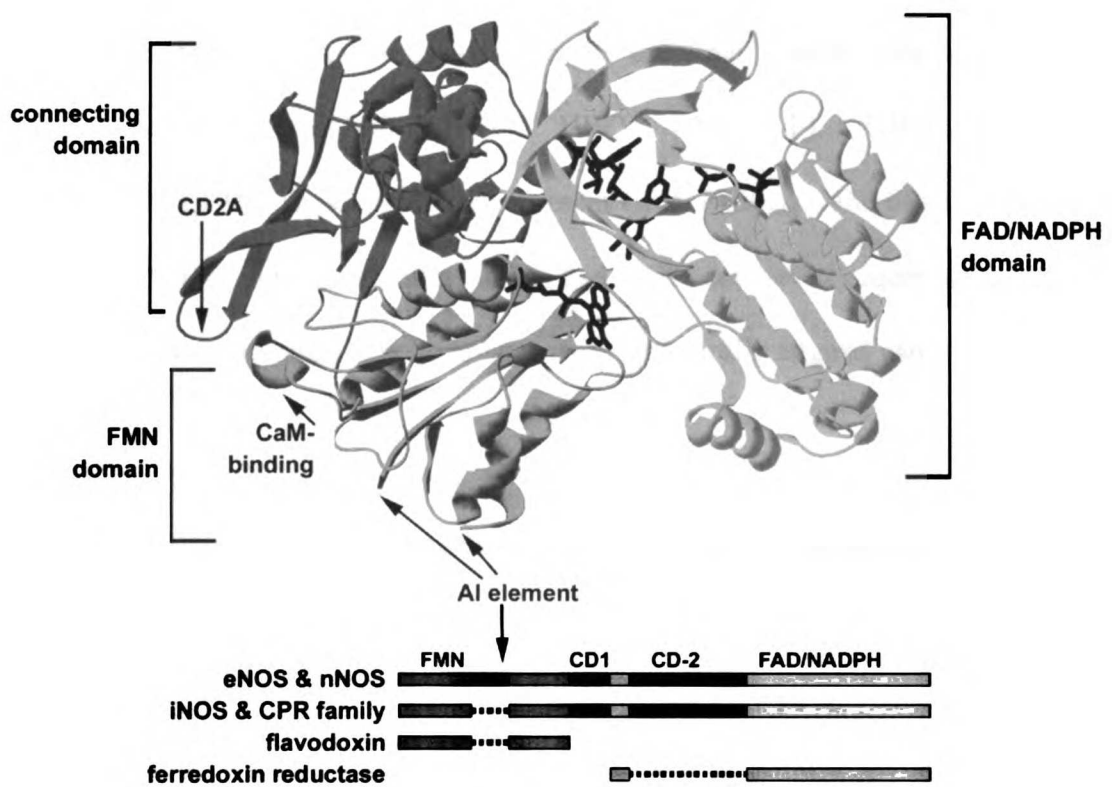

To test the hypothesis that the CD2A loop provides a control mechanism that links CaM binding to intra-reductase electron flow, we have investigated mutants of both the wild-type and chimeric enzymes in which the AI and CD2A sequences were either deleted or exchanged. We report here that the CD2A loop, in concert with the AI

element, cooperatively governs electron transfer within the reductase domains of the constitutive NOS isoforms.

III. Experimental Procedures

A. Modeling

Alignments – Related proteins were identified using PSI-BLAST (193), and sequence conservation was evaluated. Multiple rounds of modeling were performed, using various sets of templates ranging from CPR alone to a maximum of five templates (described in Appendix A). Reported here are the final models generated using the following templates: 1AMO, 1B1C, 1BVY (chain F), 1DDG, and 1F20 (43,155,157,158,194). These structures represent CPR, $P450_{BM-3}$, the β-subunit of sulfite reductase (SiR-FP), and nNOS, all of which had >20% conserved sequence identity with the NOS reductase domains. The templates were structurally aligned using COMPARER (195).

To align each NOS reductase to the templates, pair-wise alignments between NOS and 1AMO were initially created using PSI-BLAST. These PSI-BLAST alignments were then compared with results from other alignment algorithms, including ClustalW and Pfam, as well as with secondary structure prediction algorithms on the JPred^2 server (196-198) and manually resolved. The exon/intron splice sites in the human NOS genes were also identified, Appendix A, Table A-1 (66,72,199). In the C-terminal portion of the NOS reductase for which the rat nNOS structure was solved in 1F20, the human NOS sequences were aligned to 1F20 using ClustalW. The final NOS-to-templates alignment

was combined with the templates alignment from COMPARER and used as input for Modeller (200).

Model validation – After processing in Modeller, the AMBER simulation package version 6.0 was used to minimize the proteins (201). To do this, the LEAP program of AMBER was used to prepare the structures. The structures were minimized by performing 4000 steps of steepest-descent minimization to resolve moderate and large energy conflicts. After minimization, the models were evaluated and compared to the template structures as well as un-minimized models using WHAT IF v. 4.99, PROCHECK v. 3.5.4, and PROSA version 2.0 (202-204). The WHAT IF Quality Check module evaluates for overall packing quality, and good scores were considered to be greater than –1.35 (205). The overall "G-score" from a PROCHECK stereochemistry analysis was considered good when greater than –0.5 (202). PROSA z-scores were normalized for sequence length into a "goodness" probability, pG, as described by Sanchez and Sali (206). Scores >0.51 in pG would represent a structure that is reliable, so in our case of ~600 amino acid reductase domains this results from a combined PROSA z-score <-5.2.

PROSA combined energy scores were also calculated across a fifty amino acid window for each of the models, and plotted against sequence similarity. Sequence similarity was calculated across a ten amino acid window between NOS and the multiple sequences in the modeling alignment using PlotSimilarity from the Wisconsin Package Version 9.0, Genetics Computer Group (GCG) software package (192). Finally, the side chain conformations within the cofactor binding sites were compared between each modeled NOS structure and CPR. MidasPlus software from the Computer Graphics

Laboratory, UCSF[6], was used to align the two structures, and the coordinates from the CPR cofactors were transposed directly onto the NOS models[7] without further minimization (207).

B. Chimera Preparation

Materials – HEPES (N-2-hydroxyethyl-piperazine-N'-ethanesulphonic acid) and agarose were from Fisher. DNA manipulations were done using enzymes, buffers, and reagents from New England Biolabs and purification kits from QIAGEN, which also supplied the Ni-NTA resin. Oligonucleotide primers were synthesized, and the DNA sequenced, by the Biomolecular Resource Center (University of California, San Francisco). Agar was from GibcoBRL, H_4B from Alexis (San Diego, CA), IPTG from Promega, and LB, yeast extract, and tryptone from DifCo (Detroit, MI). All other materials were purchased from Sigma.

General PCR cycling – A Progene thermocycler from Techne (Cambridge, UK) was employed. Mutagenesis was accomplished by standard overlap extension PCR techniques, utilizing as the template previously constructed NOS chimeras that possess engineered endonuclease *Nhe*I splice sites at amino acids 760-761, 538-539, and 527-528 in nNOS, iNOS, and eNOS, respectively (45). End primers utilized the *Nhe*I splice site, the post-termination *Xba*I cloning site, or preexisting unique sites within the gene (iNOS *Bsr*GI and eNOS *Kpn*I). All PCR reactions utilized 0.5 μM primers, Vent® polymerase,

---

[6] We acknowledge the NIH Research Resource for Biomolecular Graphics at UCSF for use of their facilities.

[7] Coordinates of the nNOS, eNOS, and iNOS reductase domain models are available upon request from Dr. Paul Ortiz de Montellano.

which possesses 3' to 5' proofreading activity, and Vent® polymerase buffer. DMSO was added when necessary as specified.

Construction of Parental N/I(eCD2A) – The first step toward creating CD2A-swapped mutants was construction of N/I(eCD2A), which was the parent for the /iNOS(eCD2A) reductase module.

A "megaprimer" method was used to fuse sequences from iNOS and eNOS (208). First, flanking primers (forward, 5'-CAAACTGTGT GCCTGGAGGT TCTGGAGAAA GGATCCCCAG GCGGCCCTC) and (reverse, 5'-GGCTGAGTGA GCAGGGGGGC AGCCGTGGGT CCCGCACCCA GCTGGGAGGA GGGCCGCCTG GGGATC) produced megaprimer $Iecd_{mega}$, which possessed external sequences corresponding to iNOS (up to L800 and after K811), an internal sequence corresponding to the eNOS CD2A domain (E835 to P850), and a silent *Bam*HI site to facilitate screening. This megaprimer was used with Primer "pre-BsrGI" (5'-CACAGTCCTC TTTGCTAGCG AGACAGGGAA GTCT) to produce PCR product A, and with Primer (5'-GCGCGCCGAA GCTTTCAGAG CCTCGTGGCT TTG) to give B. Final PCR product AB was synthesized using 10 ng each of A, B, and the two end primers (A plus B, 3% DMSO, one cycle of 5 min at 94 °C and 5 min at 72 °C; the end primers were then added, followed by 25 cycles of 1 min at 94 °C, 1 min at 55 °C and 1 min at 72 °C, then one 15 min 72 °C extension). AB was subcloned into the N/I via *Bsr*GI and *Xba*I sites to produce the N/I(eCD2A) chimera.

Construction of I/I(eCD2A) – I/I(eCD2A) was subcloned from N/I(eCD2A) into I/E via *Nhe*I and *Xba*I sites.

Construction of E/E(iCD2A) and E/E(ΔAI)(iCD2A) – The procedure was identical to that used for the construction of N/I(eCD2A), except primers EimF (5'-GTCTGTGGCT GTGGAGCAGC TGGATGAGAG CGGATCCTAC TGGGTCAAAG AC) and EimR (5'-CGCACGGTGC ACGGGGGCAG CCTCTTGTCT TTGACCCAGT AGGATC) were used to synthesize the megaprimer, and 5' primer (5'-CCAGACCCCT GGAAAACTAG TGCGACCAAG GGCGC) and 3' primer (5'-GCCCTTTCGT CTTCAAGCAG ATCTGAAAAA AAAGCC) were used as end primers. Two-minute steps at 94 °C were used in place of 1 min 94 °C steps. Subcloning into E/E or E/E(ΔAI) was accomplished using *Kpn*I and *Xba*I to produce E/E(iCD2A) and E/E(ΔAI)(iCD2A), whose eNOS reductase CD2A sequence (E835 to P850) has been replaced by that of iNOS CD2A (D801 to K811).

Activity Assays – The rates of NO· synthesis, determined using the oxyhemoglobin assay, and cyt *c* reduction were both determined at 37 °C according to previously published methods (35,45). In specific cases, 100 mM KCl was added to determine the effect of salt on activity (45). To determine the Ca^{2+} dependence of activity, free Ca^{2+} was calculated at a constant ionic strength of 100 mM KCl using the K_d (Ca^{2+}-EGTA) = 27.9 nM at pH 7.50, 37 °C (45).

IV. RESULTS

Alignments and Template Selection for Modeling

Modeling of the reductase domains for each NOS isoform was accomplished through several iterations of sequence alignment followed by structural modeling with Modeller (200). Initially PSI-BLAST was used to query the peptide databank hosted by the National Center for Biotechnology Information for non-redundant proteins with sequence homology to the NOS reductase domains (209). After three iterations of PSI-BLAST, the diverse list of homologous proteins included, as expected, the NOS isoforms, the CPR family, flavodoxins and ferredoxin reductases (FNR). More distant flavoproteins were also found, but sequence homology was limited to flavin binding motifs.

Besides NOS, the CPR family specifically includes the reductase domain of $P450_{BM-3}$, the reductase domain of sulfite reductase, and methionine synthase reductase (MSR) (78,157,158,210). The N-terminal FMN-binding domain of the reductase is structurally homologous to flavodoxins (211,212) and the C-terminal FAD/NADPH-binding domain is homologous to ferredoxin reductase (FNR) (154,160). Unique to the CPR family is the disjointed connecting domain of ~150 amino acids that is interrupted by the first fifty amino acids of the FAD/NADPH domain (154,155,160) (Figure 3-2). The secondary structure predicted using the JPred[2] server for the NOS reductase domain matches that of the CPR family of reductases nearly exactly, confirming this structural relationship (Figure 3-3).

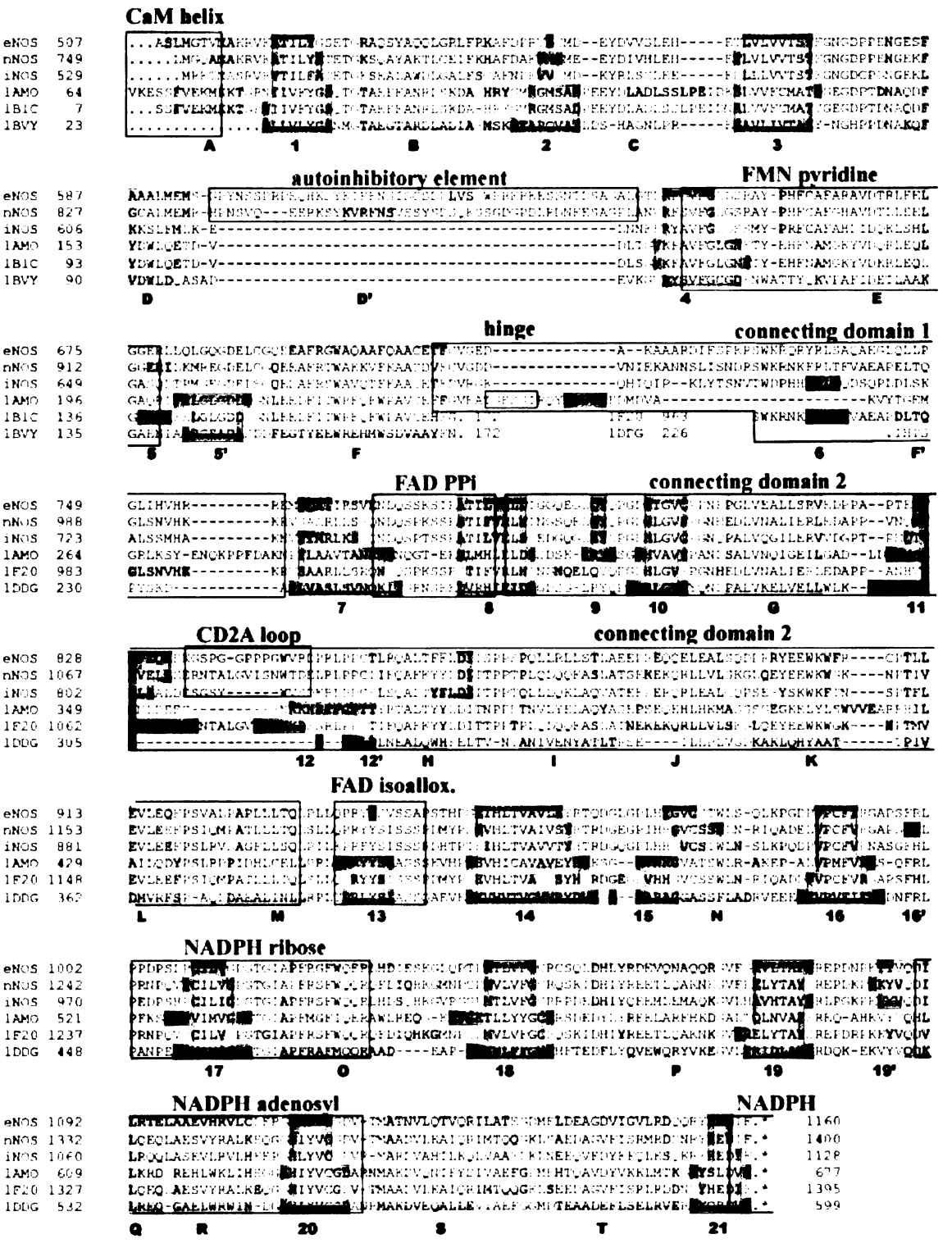
CaM helix
autoinhibitory element
FMN pyridine
hinge
connecting domain 1
FAD PPi
connecting domain 2
CD2A loop
connecting domain 2
FAD isoallox.
NADPH ribose
NADPH adenosyl
NADPH
eNOS
nNOS
iNOS
1AMO
1B1C
1BVY
1F20
1DDG
Helix
Sheet

Figure 3-3, previous page. Sequence alignment between the reductase domain of the human NOS isoforms and the template structures used for generating the reductase structural models. The secondary structures highlighted within the NOS reductase sequences are those predicted using JPred[2], and those highlighted in the template sequences are taken directly from their crystal structures (43,155,157,158,160,194,197,211). Helices are highlighted in light gray and sheets are in dark gray. The cofactor binding motifs and the CD1 and CD2 regions are approximately defined according to the CPR structure (155). Helix and Sheet indexing is also labeled according to the CPR convention (155). These structures are available at the PDB databank, codes: 1AMO, 1B1C, 1BVY, 1F20, 1DDG.

To model the NOS reductase domain, template structures from the CPR family were chosen that align with NOS above the ~20% threshold required for accurate alignments (213). These templates are: 1AMO, the structure of CPR that includes all the reductase subdomains (155); 1B1C, the FMN domain of CPR (194); 1BVY, the FMN domain of $P450_{BM-3}$ (157); 1DDG, the CD2 plus FNR domain of SiR-FP (158); and finally 1F20, the CD plus FNR domain of rat nNOS (43). Sequence identity conservation between the subdomains of these templates and iNOS is shown in Table 3-1. Our models include residues 529-1128 of human iNOS, 507-595 and 642-1160 of human eNOS, and 749-835 and 880-1400 of human nNOS.

Table 3-1. Conserved sequence identity (%) with human iNOS. Conserved sequence identity is calculated as the percentage of identical residues within each subdomain based on the multiple sequence alignment in Figure 3-3. Using human iNOS numbering, the FMN subdomain corresponds to residues 529-685 of iNOS, CD1 is 686-727, CD2 is 756-898 and the FNR subdomain residues are 728-755 plus 899-1129. Numbers in **bold** are calculated for subdomains whose PDB coordinates were used as templates for modeling of the NOS reductase domains. *Italicized* values were calculated for the other subdomains of the multi-domain proteins that do not have solved structures. [b]Sequence identity between nNOS and iNOS within the FMN domain was calculated with the 47 amino acids of the AI deleted.

Template	***Protein name***	***residues***	***FMN***	***CD1***	***CD2***	***FNR***	***Overall***
1AMO	rat CPR	**64-678**	**27.1**	**5.6**	**31.9**	**36.2**	**30.3**
1B1C	human CPR	**7-172**	**27.1**	-	-	-	-
1BVY	*B. megaterium* $P450_{BM-3}$	**21-172**	**21.6**	*9*	*23*	*38*	**28**
1DDG	*E. coli* SiR-FP	**226-599**	*27*	*4*	**18.7**	**34.3**	**27**
1F20	rat nNOS	**963-1397**	*51.9*	**20**	**44.3**	**54.6**	**47.3**

In generating the NOS-to-template alignments, 1AMO was used as the internal register for the N-terminal FMN domain plus part of the CD1, and 1F20 for the C-terminal CD1-FNR subdomains. The individual NOS-to-template alignments from ClustalW, PSI-BLAST, Pfam and JPred[2] agreed to within two residue positions throughout the regions of high conserved sequence identity, within the FMN, CD2 and FNR subdomains. The only region of low sequence conservation is within the first portion of the connecting domain (CD1, eNOS residues 709-753 Figure 3-3). 1AMO is nearly complete in this region, missing only six "hinge" residues (1AMO residues 237-242 Figure 3-3). However, sequence conservation with iNOS is 6%, well below the "twilight" zone of sequence alignment accuracy (213). 1F20 has much better sequence

conservation in the CD1, 20% or 35% with iNOS or eNOS respectively, but the structure begins past the hinge region (at residue 729 of eNOS). Therefore, the short hinge region was unaligned from the templates, and left in the models only for approximation of the backbone position (eNOS residues 719-728, Figure 3-3). The 45-47 residue AI element was excluded from the models of eNOS and nNOS, due to the absence of a homologous element within the templates.

Structure Accuracy

The resulting models from Modeller were evaluated for structural quality relative to the template structures using PROSA, WHAT IF and PROCHECK. Plots of PROSA combined energy scores versus residue number allow recognition of misfolded sequences within a structure and are regularly used to evaluate homology models (214). We found strong correlation between low (good) PROSA combined energy scores and high conservation of sequence between the models and their structural templates (Figure 3-4). The gap in the nNOS and eNOS traces at residues ~835 and ~595 respectively (Figure 3-4, panels A & B), correlates to the position of the AI element, which has zero sequence conservation with the templates. The models have similar PROSA energy scores to the 1F20 structure in the C-terminal domain (Figure 3-4, panel A).

Figure 3-4. Plots of structural quality versus sequence position and conservation for nNOS (panel A), eNOS (panel B) and iNOS (panel C). Mapped at the top of each panel are two representations of the subdomain and secondary element structures of each NOS sequence, residues numbered as in Figure 3-3. The subdomain coloration is as defined in Figure 3-2. Alpha helices are drawn as cylinders, and beta sheets are drawn as black arrows. Plotted against the sequence is percent sequence conservation, in solid white representation, calculated by the Plotsimilarity (192). The PROSA combined energy score is plotted as solid black circles, for the models and solid white squares for the partial nNOS structure, 1F20 in panel A (203). The AI element was deleted from the eNOS and nNOS structure models due to lack of scaffold structures, thus the gap in the PROSA combined energy trace corresponds to a region of zero sequence conservation in the Plotsimilarity trace.

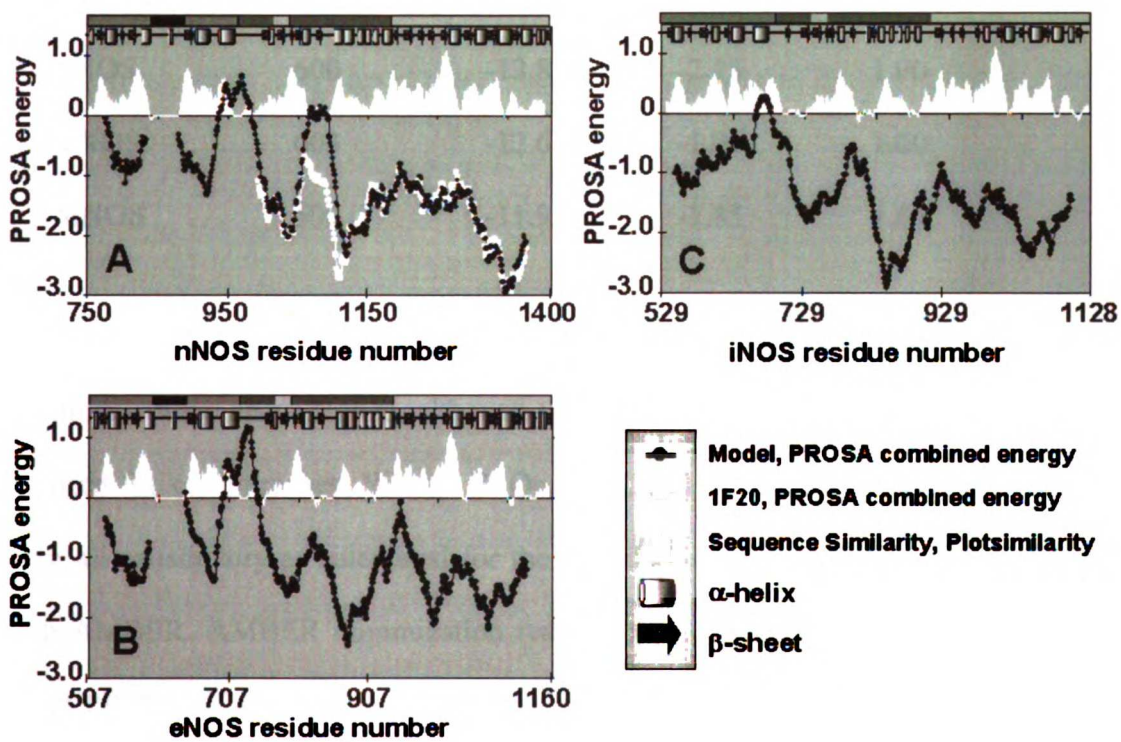

The PROSA energy scores were greater than zero only in the CD1, as expected from poor sequence conservation among templates. In light of these poor scores, the CD1 was treated as only a backbone strand for reference in modeling, and specific CD1 residue interactions are uncertain. The PROSA z-score was also used as a general quality assessment for compatibility of the NOS sequences with the reductase fold (Table 3-2).

When normalized for sequence length into a probability of goodness pG, all the models were given highly reliable scores.

Table 3-2. PROSA Combined z-scores for the three NOS reductase models and templates. The Prosa z-scores were analyzed according to Sanchez and Sali (206) in order to normalize for protein length. Q-Score = (Zp-comb)/ln(length). The probability for "goodness" (pG) is based on distributions of Q-scores for good and bad structures. pG = p(Q-score good)/[p(Q-score good) + p(Q-score bad)] If pG > 0.5, the models are said to be approximately correct, and pG = 1.00 are reliable (http://guitar.rockefeller.edu/pg/).

Protein	length	Zp-comb	Q-Score	pG
1AMO	601	-14.6	-2.28	1.00
1F20	435	-13.6	-2.23	1.00
iNOS	600	-13.8	-2.15	1.00
eNOS	603	-12.6	-1.96	1.00
nNOS	606	-11.9	-1.85	1.00

The more refined qualities such as stereochemistry and packing of residues within the models were also checked, although these scores represent a level of refinement not required for our purposes. WHAT IF Quality Check scores and PROCHECK G-scores were all satisfactory as calculated for the models before and after energy minimization with AMBER. AMBER minimization reduced minor steric clashes, but did not greatly effect PROCHECK and WHAT IF scores, when compared with scores for un-minimized models, (see Appendix A for further details). In no case were the scores outside of an acceptable range. These scores were comparable to the PROCHECK and WHAT IF scores of the templates (Table 3-3).

Table 3-3. PROCHECK G-scores and WHAT IF Quality Check scores for the models and the templates. PROCHECK G-scores and WHAT IF Quality Check scores were calculated for all the templates in addition to the NOS reductase domain models. The overall "G-score" from a PROCHECK stereochemistry analysis was considered good when greater than –0.5 (47). The WHAT IF Quality Check module evaluates for overall packing quality, and good scores were considered to be greater than –1.35 (205). [a]The AI was deleted from the eNOS and nNOS models due to lack of template structure in this region.

Templates	PROCHECK	WHAT IF
1AMO:A	0.19	-0.82
1B1C	0.32	-0.37
1BVY:F	-0.07	-0.68
1DDG	-0.17	-0.73
1F20	0.34	-0.78
iNOS	-0.25	-1.04
eNOS	-0.25	-1.10
nNOS	-0.27	-0.96

For functional reference it was also useful to place the cofactors within these minimized reductase structures. Comparison of the cofactor binding sites between NOS and CPR as well as the templates showed excellent conservation of binding pocket residues, as identified in the CPR structure (155). Thus, the coordinates of the FMN, FAD and NADPH cofactors could be transposed into the NOS reductase domain models by visual superimposition of the NOS and CPR structures in MIDAS.

Modeled Interactions

Of greatest interest in the present context are the potential CaM binding interactions with NOS, with reference to the proposed NOS regulatory elements. Two of the stabilizing salt-bridges in the structure of CPR are between acidic residues at the base of the CD2A loop and basic residues in the N-terminal helix region (155). Similar acidic and basic residues in the CD2A loop and the N-terminal helix are conserved in NOS, although at the resolution of the models specific salt-bridge interactions cannot be specified with high confidence. The structure of CaM bound to a peptide corresponding to residues 492-511 of eNOS enables distance and orientation restrictions to be applied (44). In this structure, the last direct CaM interactions are with residue M510 of the eNOS peptide, and the last turn of this peptide is modeled in the reductase models. If the position of CaM along this canonical recognition helix remains fixed, the approximately 40x20 Å elliptical shape of the CaM structure can be used as a limitation estimate for nearby interactions. The CD2A is within 5-7 Å of the CaM recognition helix at its base. The AI element is inserted between two points that are within 20 Å of residue M510 in eNOS, thus it is also within contact distance of CaM, consistent with the ability of AI-derived peptides to inhibit CaM-binding (167). One of several possible binding modes for CaM binding to eNOS is drawn in Figure 3-5, showing relative orientation.

Figure 3-5. A proposed binding mode for CaM recognition of eNOS. The reductase domain model of eNOS is shown as a semi-transparent solvent accessible surface in blue, with its FMN, FAD, and NADPH cofactors shown as black sticks. The structure of CaM (in yellow) is shown bound to the eNOS peptide (1NIW) (dark ribbon). From residue M510 at the N-terminus of the eNOS model, the shortest Cα-to-Cα distances are 7.5 Å to the CD2A and 15-20 Å to the AI element insertion point.

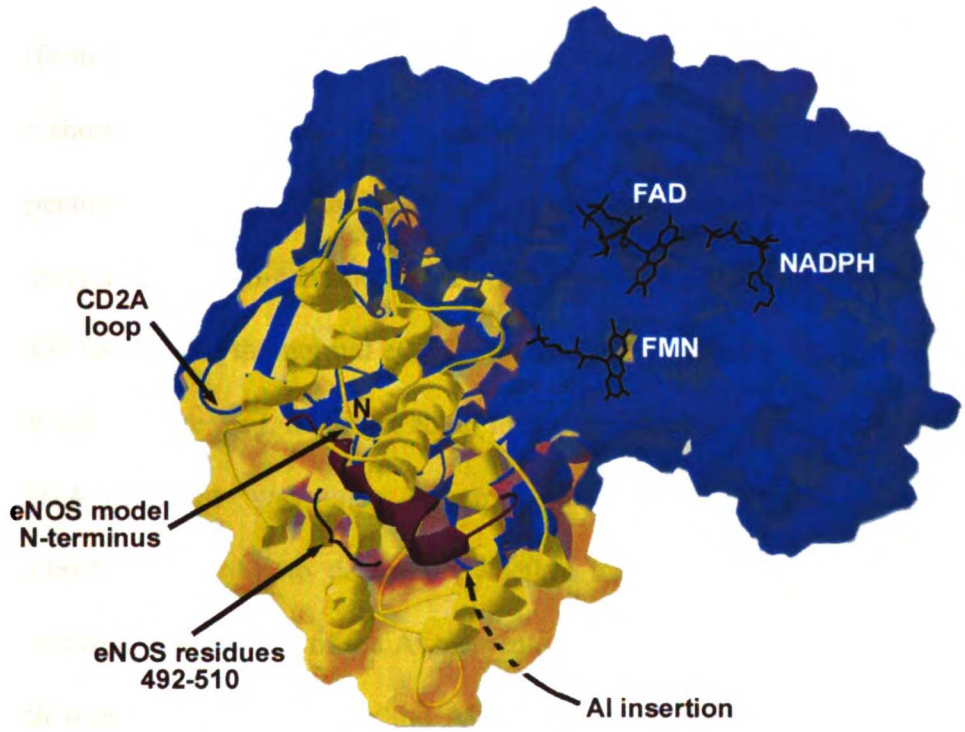

Calcium Dependence

The *in vivo* modulation of NOS activity by the free Ca^{2+} concentration, a primary mechanism for regulating eNOS and nNOS activity, can be simulated *in vitro* by the use of Ca^{2+}/EGTA buffers (Figure 3-6). CD2A-swapped proteins are labeled according to the isoform that provided the CD2A element, either *e*CD2A for eNOS CD2A or *i*CD2A for the shorter iNOS CD2A. The wild-type isoforms represent the two extremes of Ca^{2+} dependence; eNOS has an $EC_{50}(Ca^{2+})$ of approximately 100 nM, whereas iNOS retains activity even at sub-nanomolar Ca^{2+} levels (45). Insertion of the iCD2A element into eNOS in place of the normal eCD2A loop led to a dramatic decrease of the Ca^{2+} EC_{50} to ~30 nM (Figure 3-6), an effect equal to that obtained by deleting the AI insert (45). The iCD2A element was also swapped into the eNOS(ΔAI) construct, yielding eNOS(ΔAI)(iCD2A), to determine whether the effect of the CD2A replacement was sensitive to the absence of the AI element. An $EC_{50}(Ca^{2+})$ of 20-30 nM was measured for both mutants. Thus, whether the AI domain was deleted, the native eCD2A loop was replaced, or both changes were made at once, the observed effect was a decrease of the EC_{50} to about 30 nM. Conversely, insertion of the eCD2A into iNOS did not alter the Ca^{2+} dependence significantly from wild type, thus it is a function of the CD2A within the context of an eNOS reductase domain that contributes to Ca^{2+}/CaM dependence of NO· activity. The eNOS derived chimeras with an iCD2A loop also exhibited decreased activity at Ca^{2+} levels greater than 100 nM. At these levels, the amount of added Ca^{2+}-EGTA required to achieve the desired Ca^{2+} concentration exceeds 10 mM. It is notable that only the iCD2A containing chimeras were sensitive to these high Ca^{2+}-EGTA

conditions, whereas the eNOS(ΔAI) and iNOS(eCD2A) chimeras were unaffected (Figure 3-6). This observation was consistent with a more general salt inhibition observed in wild-type iNOS (34). Whereas wild-type iNOS was not inhibited in the conditions of the Ca^{2+}-dependence assay, the salt sensitivity threshold has been decreased by the iCD2A swaps. Further observations on the high salt inhibition of NOS activity in assays done at a fixed 1 mM Ca^{2+} concentration in the presence or absence of 100 mM KCl are discussed later.

Figure 3-6. Ca^{2+}-dependence of NO· activity. NO· activity was measured for the CD2A chimeras using the oxyhemoglobin assay.

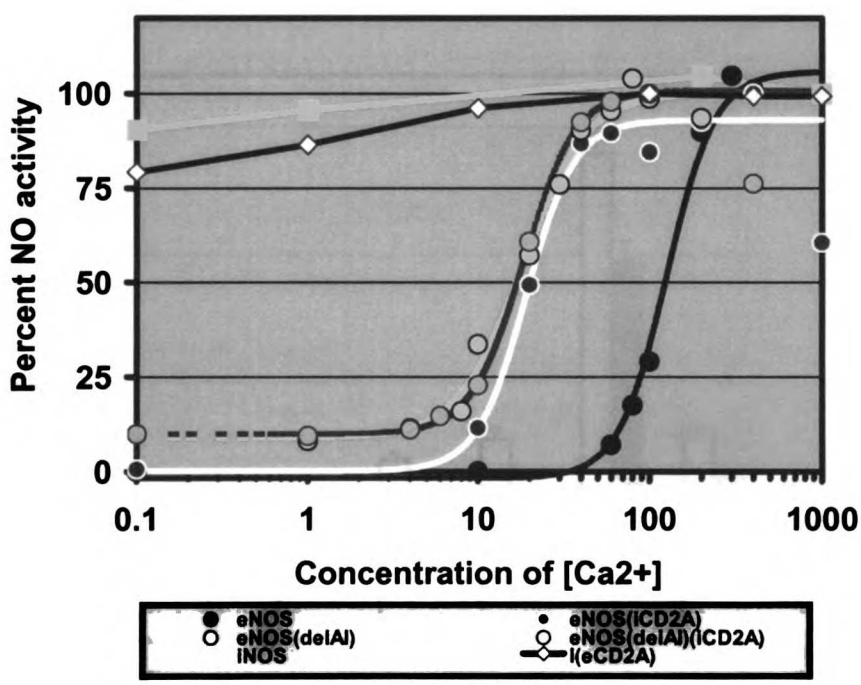

Overall Activity

The rate of NO· production is limited by the activity of the reductase module in NOS oxygenase-reductase chimeras (35,36,45). Deletion of the AI element from eNOS enhances activity more than two-fold, while swapping the eNOS AI into iNOS decreases NO· activity (36). A similar pattern was observed for the CD2A chimeras, but this effect was modified by the KCl concentration of the assay (open versus solid bars, Figure 3-7); therefore, both the autoinhibitory effect and high salt effect are to be analyzed here.

Figure 3-7. Salt dependence of NO· activity. NO· synthesis was measured for the CD2A chimeras measured in the presence (solid bars) or absence (open bars) of 100 mM KCl. Values reported for the E/I and I/E chimeras were taken from reference (45).

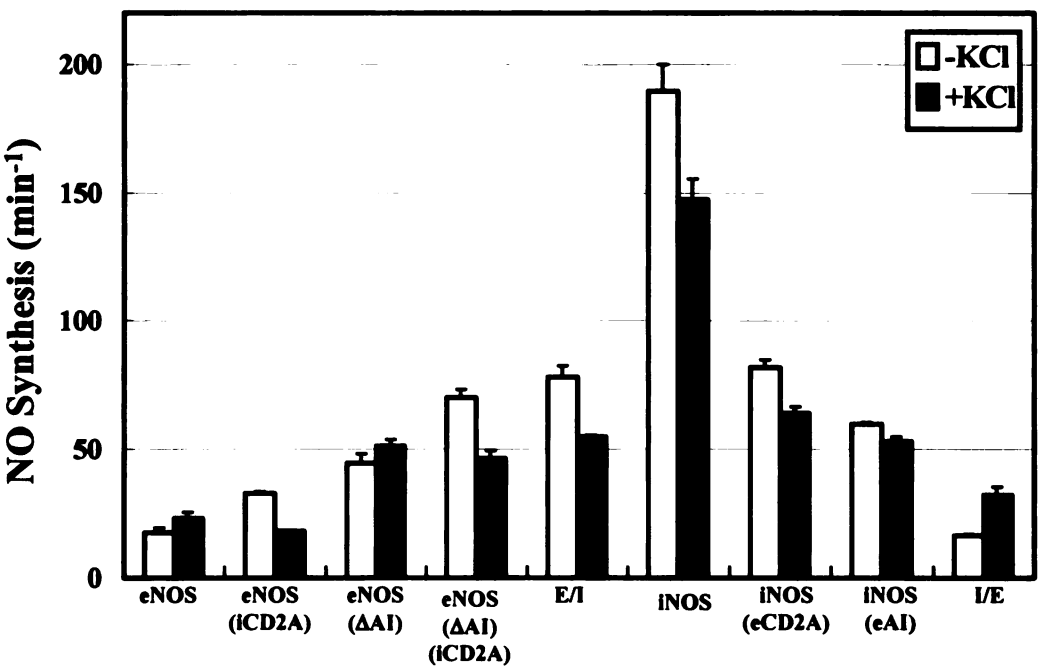

Under low salt conditions, the eNOS(iCD2A) mutant was twice as active as eNOS itself, and this effect was enhanced when combined with the AI deletion in the double chimera eNOS(ΔAI)(iCD2A). This double chimera was nearly as active as the E/I

chimera, which represents the endpoint form that would result from progressive replacements of sequences within the eNOS reductase with those from iNOS (open bars, Figure 3-7). Thus replacement of the eNOS CD2A releases some autoinhibitory function that it had in the context of an eNOS reductase domain.

When the concentration of KCl was increased to 100 mM in the NO· assay, replacement of the eNOS CD2A with iCD2A had, if anything, a mild inhibitory effect, consistent with general iNOS-like inhibition by high salt (compare eNOS(iCD2A) to eNOS, and eNOS(ΔAI)(iCD2A) to eNOS(ΔAI), solid bars, Figure 3-7). The percent activation by addition of KCl is calculated in Table 3-4 to demonstrate the unique alteration of activity by the iCD2A. From the calculated values, it is apparent that eNOS activity is normally stimulated by high salt (31%), and the AI deletion does not greatly alter this stimulation (13%). However, the iCD2A conferred high salt sensitivity to the eNOS reductase domain, causing a loss of 45% activity. The combined effect of AI and iCD2A replacement was also inhibitory (34% decrease), attaining a value equivalent to the inhibition observed with the E/I chimera (30% decrease) Table 3-4.

Table 3-4. The percent activation by KCl measured for NO· production and cyt *c* activity in the NOS chimeras. The percent activation is calculated as the difference between activity values measured +KCl and -KCl, divided by the initial -KCl value. "%NO· activation" is percent activation calculated for NO· production from the oxyhemoglobin assay, and "%Reductase" is the percent activation calculated for reductase activity measured as cyt *c* reduction, either with or without CaM.

NOS chimera	% NO· activation	% Reductase -CaM	% Reductase +CaM
eNOS	+31%	+158%	+132%
eNOS(iCD2A)	**-45%**	+95%	+45%
eNOS(ΔAI)	+13%	+87%	+118%
eNOS(ΔAI)(iCD2A)	**-34%**	+180%	+223%
E/I	**-30%**	**-55%**	**-66%**
iNOS	**-22%**	**-79%**	**-78%**
iNOS(eCD2A)	**-22%**	**-69%**	**-62%**
iNOS(eAI)	**-22%**	**-57%**	**-57%**
I/E	+99%	+118%	+102%

The eNOS CD2A element decreased NO· activity when introduced into iNOS, but did not alter the sensitivity of iNOS to high salt. Similarly, the iNOS(eAI) chimera was also unaltered in its high salt sensitivity when compared to wild type iNOS. The activity of the iNOS(eCD2A) mutant, similar to the iNOS(eAI) mutant, was about half as active as wild type iNOS (Figure 3-7), and this activity was reduced by 22% in the presence of added KCl (Table 3-4). Interestingly, when placed in the context of the iNOS reductase, which has NO· AI element, the eNOS CD2A element could lower the overall activity of iNOS to a level similar to that of "activated" eNOS with its AI domain deleted or CD2A replaced. Comparison with the "endpoint" chimera I/E indicates that still other determinants are required to lower the activity of the iNOS chimeras to the activity level of eNOS, and to switch over to salt-stimulation of activity (Table 3-4).

Reductase Activity

The ability of the mutants to reduce cytochrome *c* (cyt *c*) was used to measure the intrinsic activity of the reductase domain in the absence (Figure 3-8) or presence (Figure 3-9) of added salt. CaM-stimulation of reductase activity could be tested in all proteins containing an eNOS-oxygenase domain module (compare empty with filled bars, Figures 3-8 and 3-9). Those chimeras containing an iNOS oxygenase domain (and CaM-recognition helix) were coexpressed with CaM for stability, and sufficient Ca^{2+} was present for CaM to remain bound (35). Thus the activities observed for these chimeras reflected CaM binding even when CaM was not added to the assay (gray bars in Figures 3-8 and 3-9). In all cases, the cyt *c* reduction rates for the NOS chimeras exceeded the heme reduction rate calculated from the observed overall activity, a clear indication that electrons are transferred more readily from the NOS reductase domains to cyt *c* than to the adjacent oxygenase domain in the NOS dimer.

In the absence of KCl, the effect of swapping the iCD2A into eNOS was minimal on the reductase domain activity (Figure 3-8) under conditions where NO· production had been enhanced by the iCD2A (Figure 3-7). This was the case for CaM-independent and CaM-dependent cyt *c* activity (open and solid bars, Figure 3-8).

Figure 3-8. CaM-dependence of Cytochrome *c* reduction activity of the CD2A mutants in the absence of KCl. The electron transfer activity of the reductase domain in the CD2A chimeras was measured in the absence of KCl. Black bars represent the CaM-bound activity, and CaM-free activity is represented as white bars. Gray bars indicate the activity of protein that was coexpressed with CaM but had no additional CaM added to the assay.

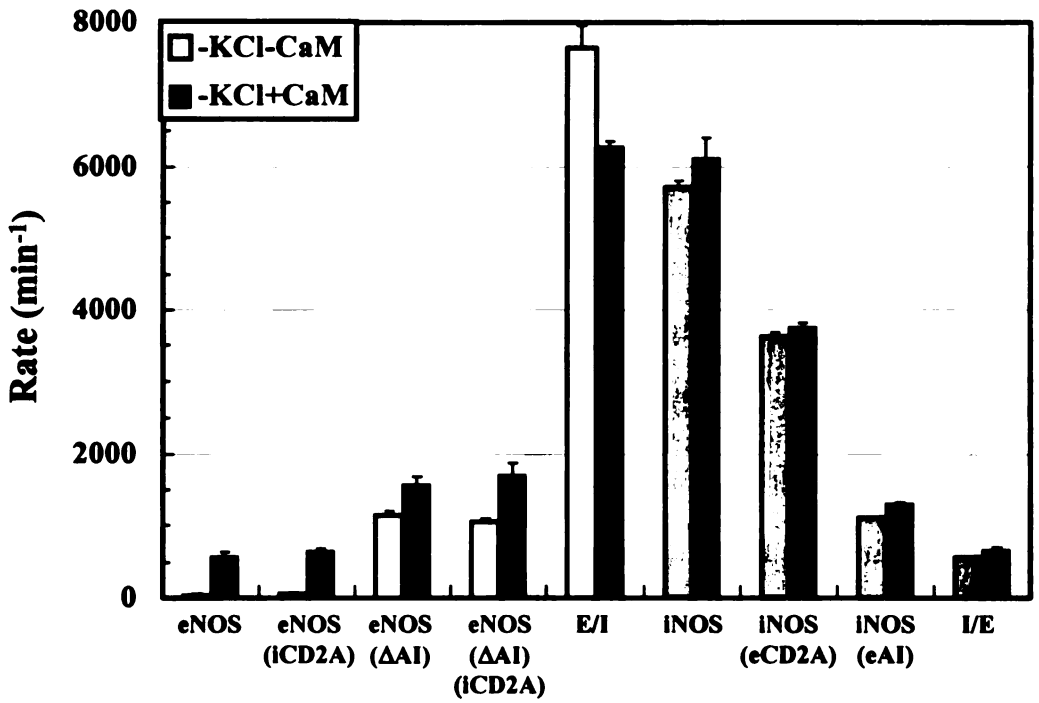

In the presence of KCl, the iCD2A could, however, increase electron transfer when combined with the AI deletion, and this was observed for both CaM-free and CaM-dependent reductase activity (Figure 3-9). The eNOS(ΔAI)(iCD2A) chimera reached reductase activity levels on par with the E/I chimera under high salt conditions and in the absence of CaM. CaM-*de*pendent activity of the double chimera even exceeded the activity of the E/I chimera, suggesting that the AI and iCD2A replacements were sufficient to attain a parent-like, regulated, high reductase activity (Figure 3-9). Alone the iCD2A was ineffective, yet it enhanced the AI deletion effect. A further general

observation was that high salt increased the activity of all the eNOS reductase-containing chimeras (Table 3-4), thus the high salt inhibition of NO· activity previously observed in the iCD2A chimeras must result from altered reaction rates post-flavin reduction.

Figure 3-9. CaM-dependence of Cytochrome *c* reducing activity of the iCD2A mutants in the presence of KCl. The electron transfer activity of the reductase domain in the CD2A chimeras was measured in the presence of added 100 mM KCl. Bar colors are as in Figure 3-8.

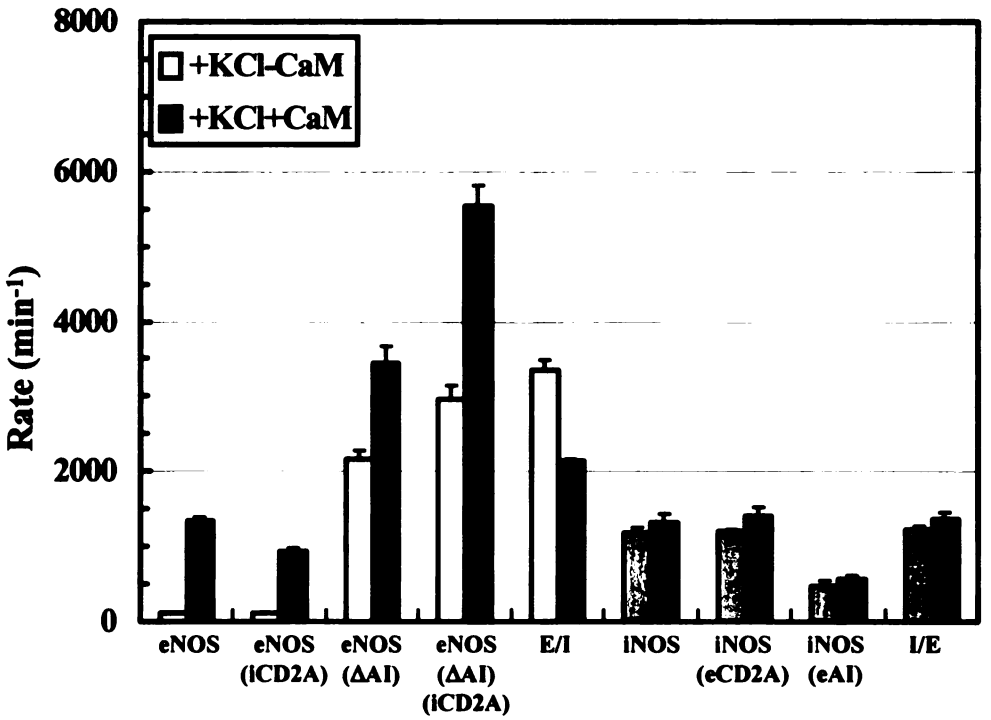

We showed previously that insertion of the eNOS AI domain into iNOS, giving iNOS(eAI), lowered both the reductase and overall activities, although to varying degrees depending on the salt concentration (36). The iNOS(eCD2A) mutant had a low salt activity of two-thirds that of wild-type iNOS, a less dramatic decrease than observed in the iNOS(eAI) chimera, that was one-fifth as active as wild-type iNOS, (Figure 3-8). When assayed with added KCl, the reductase activity of iNOS(eCD2A) was equivalent to

that of wild-type iNOS, which itself was reduced by 80% from the maximal activity observed in the absence of salt (Figure 3-9). Thus the eCD2A had little effect on the activity of iNOS when assayed under low salt conditions, and no effect at all under high salt conditions. Furthermore, in both high and low salt assay conditions CaM-stimulation was minimal, and unaltered from wild-type iNOS.

In general, KCl inhibition of the iNOS(eCD2A) and iNOS(eAI) chimeras was more severe in the cyt *c* assay, whereas NO· production was inhibited only slightly by added KCl. (Table 3-4). In no case did the iNOS-derived chimeras deviate from the salt-dependence of wild-type iNOS (Table 3-4). This indicates that salt inhibition of iNOS occurs on a more general level within the reductase, and that it was independent of the AI or eCD2A alterations. This is an important difference from the iCD2A replacement effects in eNOS, where the iCD2A exerts its effects at the reductase-to-heme electron transfer step or later.

V. Discussion

An enticing structural hypothesis for the function of the NOS connecting domain emerges from models of its potential interactions with both CaM and the FMN subdomain. The CD subdomain itself is highly variable in sequence and size among the CPR family members, and it is currently hypothesized to flexibly orient the FMN and FAD/NADPH subdomains (43,155,158,215,216). In CPR, a change in conformation within the FMN domain is directly linked to cofactor binding and internal electron transfer (217). Interactions between the CD and FMN subdomains in CPR are primarily hydrophilic, including two salt-bridges connecting the base of the CD2A and the N-

terminal helix (43). These salt-bridges likely stabilize subdomain interface interactions (158), and similarly placed acidic and basic residues are conserved in our models. The structure of the short N-terminal helix of our reductase models is based on the non-CaM binding helix found in CPR, and is meant only to represent the anchor point where the true structure of the canonical CaM-recognition helix in NOS begins. The structure of CaM bound to its recognition helix in eNOS includes residues at the N-terminus of the reductase models, thus from distance constraints alone, it can be inferred that CaM is within contact distance of both the CD2A and the AI element, establishing a structural link between CaM-binding and the regulation of inter-subunit electron transfer.

The CaM recognition helix of the NOS family has been extensively studied both on the peptide binding level as well as within several NOS chimeras. Ca^{2+}-bound CaM binds to NOS via its canonical amphipathic helix, with a hydrophobic (1-5-8-14) binding motif (142), Figure 1-13. The 20-26 amino acid recognition helix includes residues 492-511 of eNOS, 509-534 of iNOS, and 730-752 of nNOS, by human sequence numbering (44,143,144). The low nanomolar dissociation constant for CaM binding to peptides derived from these eNOS and nNOS sequences is sufficient to account for tight, Ca^{2+}-dependent CaM binding to the full-length protein (143-145). In a surface plasmon-resonance study of the equivalent iNOS peptide, irreversible binding with K_d <0.1 nM was observed (144), in contrast with an alternate gel-shift assay for CaM binding to a slightly longer iNOS-derived peptide (507-538) that observed weaker, Ca^{2+}-dependent binding (145). Circular dichroism spectroscopic observations show that the CaM recognition element from iNOS (residues 509-535) actually binds to apo-CaM in a Type II β-turn conformation, and its conformation becomes helical when CaM is Ca^{2+}-bound

(149), therefore iNOS has at least two modes in which to bind CaM. NOS chimeras that swap CaM-recognition helices between isoforms have the same Ca^{2+}-dependence of CaM binding, intermediate between cNOSs and iNOS and only slightly reduced overall activity when compared to the parent isoform (145,146,151). Thus, only part of the Ca^{2+}-dependence of CaM binding is due to the canonical CaM binding helix itself.

Further interactions in iNOS beyond the canonical CaM recognition helix were shown to contribute to its irreversible, Ca^{2+}-independent affinity for CaM. The Ca^{2+}-dependence of NOS activity could also be reduced in various nNOS chimeras that contain either the iNOS oxygenase or reductase domain along with the iNOS CaM recognition helix, but only the iNOS reductase- containing chimera demonstrated full Ca^{2+}-independence (146). iNOS truncation mutants with successive N- or C-terminal deletions demonstrated a similar requirement of iNOS residues between 490-732 for Ca^{2+}-independent CaM binding (151). This evidence has implications for the work presented here, because residues 490-732 include the CaM recognition helix, the FMN, and the CD-1 subdomains, all of which are within direct contact distance of either the AI element or the CD2A loop (Figure 3-2). Both the CD2A loop and AI inserts are found only in the constitutive NOSs, and their sequences are highly conserved by isoform, fulfilling the predictive requirements for isoform specific regulatory elements. We hypothesize that the CD2A element provides a structural connection between CaM-binding and regulation of NOS activity, analogous to the function of the AI element.

The iCD2A loop alters the Ca^{2+}-dependence of CaM-activated NO· activity of eNOS in a manner similar to deletion of AI element. Attempts to lower the Ca^{2+}-

dependence of eNOS to the Ca^{2+}-independence of iNOS were unable to break the $EC_{50}(Ca^{2+})$ limit of 30 nM, achieved with eNOS(iCD2A) and eNOS(iCD2A)(ΔAI) chimeras (Figure 3-6). This is consistent with other observations that Ca^{2+}-dependence of NO· activity, and therefore CaM-binding, is determined by multiple interactions in the CaM binding region (145,146,151). Progressive replacement of the eNOS reductase domain segments with sequences from iNOS would eventually lead to the E/I chimera, which indeed exhibited virtual Ca^{2+}-independence (45). The eCD2A did not alter the Ca^{2+}-independence of iNOS (Figure 3-6), consistent with the already tight binding of CaM to the CaM-recognition helix (144). The K_d of CaM for Ca^{2+}-binding to the last Ca^{2+} site has been measured as ~1.2 nM (218), but recognition by CaM of its target sequences is likely a sum of cooperative interactions. The ability of the eNOS(iCD2A) chimeras to bind CaM at 30 nM would indicate recognition of a partially apo-CaM conformation. The CD2A therefore has a role in direct or indirect interactions that are required for CaM-binding.

The eCD2A serves as an autoinhibitory element as well, since replacement with the iCD2A resulted in increased overall NO· production in both the eNOS(iCD2A) and eNOS(iCD2A)(ΔAI) chimeras. However, at the reductase activity level the iCD2A replacement appeared to be masked in the presence of the AI element when assayed under low salt conditions. This masking was released in the high-salt assay, revealing an additive effect of the iCD2A and AI deletion on both CaM-dependent and independent reductase activity. Thus, the AI is dominant, but the eCD2A also provides autoinhibitory function in eNOS.

Placing the eCD2A into iNOS had a mixed effect, in that it was visible in the low salt condition favoring iNOS activity, but not in the high salt condition. High salt reduced the activity of iNOS, iNOS(eCD2A) and iNOS(eAI). Insertion of the eCD2A into iNOS reduced both NO· and cyt *c* activity; however, this does not indicate it is functioning on an autoinhibitory level. It is more likely that the lost iCD2A interactions would be needed for full iNOS activity. All the conditions assayed here point to non-specific inhibition in the iNOS(eCD2A) chimera: CaM-binding is virtually Ca^{2+}-independent, the CaM-binding does not affect the inherent reductase activity, and the low-salt preference for iNOS activity is unaltered. Thus, for the eNOS CD2A to function in its autoinhibitory capacity, it needs to be in the context of an eNOS reductase, a conclusion similar to that made for the iNOS(eAI) chimera.

The subtle salt effects of the iCD2A insertion into eNOS are worth further consideration. From Table 3-4 it is clear that the iCD2A does not alter the inherent preference of eNOS reductase activity for higher salt, and that high salt inhibition in the iCD2A chimeras arises after the inter-flavin electron transfer steps. A logical interpretation of this salt-inhibition of the reductase-to-heme electron transfer step includes the participation of electrostatic interactions. If the eNOS(iCD2A) chimera has electrostatic interactions that are disrupted by high salt concentrations, this implies that the electrostatic interactions provided by the iCD2A still are able to form within the context of an eNOS protein, and that these interactions have become the limiting factor. Other limiting factors that can be stimulated by high salt must exist in wild-type eNOS, at the reductase level. It is extremely interesting to consider conserved electrostatic interactions within the eNOS and iNOS reductase domains contributed by the flaking

amino acids near the CD2A. Given their poised locations near the FMN-CD subdomain interface and connections to the CaM-recognition helix, it is highly likely that these same interactions connect CaM-binding to regulation of electron transfer.

We have shown that: i) The eCD2A element contributes to the Ca^{2+}-dependence of CaM-bound NO· activity, and this contribution is equal to that observed for the AI element. However, the CD2A does not alone determine the Ca^{2+}-dependence of CaM binding, since complete Ca^{2+}-independence is not observed in the eCD2A deletion, nor is Ca^{2+}-dependence conferred when the eCD2A is introduced into iNOS. ii) The eCD2A also plays an autoinhibitory role in the control of NO· production and electron transfer activity. The AI element serves as the main autoinhibitory switch that masks the effect of the eCD2A deletion in the eNOS(iCD2A) mutant, but the two elements are revealed to be additive when both substitutions are made, eNOS(iCD2A)(ΔAI). iii) The CD2A is involved in determining the salt-dependence of NO· activity but not reductase activity, possibly through electrostatic interactions connecting the CaM-binding helix with the CD-FMN interface. In conclusion, our models for the interplay between CD2A loop interactions with the CaM-binding helix and with CaM itself provide a meaningful structural basis for the isoform-specific functional effects of the CD2A on CaM-dependent regulation of NOS activity.

DIMERIZATION AFFINITY OF NITRIC OXIDE SYNTHASE: DEPENDENCE UPON LIGAND BINDING AND CALMODULIN[8]

CHAPTER 4

Work included in this chapter will be submitted for publication in early 2004.

[8] This work was supported by NIH grant GM25515. We acknowledge the NIH Research Resource for Biomolecular Graphics at UCSF for use of their facilities.

I. ABSTRACT

Nitric oxide synthase (NOS) is an obligate homodimer in which electrons transfer in a *trans* mode between opposing subunits in the dimer, and full activation requires Ca^{2+}-dependent calmodulin (CaM) binding to each subunit. The primary dimeric interaction site between subunits is between oxygenase domains; therefore, we analyzed the binding effects of oxygenase domain effectors upon dimerization. Through sedimentation equilibrium and velocity analytical ultracentrifugation techniques, we report here that the three NOS isoforms exhibit dimerization affinities that are dependent upon CaM, substrate *L*-Arg, and cofactor tetrahydrobiopterin (H_4B). The weakest dimer is nNOS, with a K_d of 12-70 μM, independent of the CaM or ligand binding state. CaM binding alters the ranking of eNOS and iNOS as the tightest dimers. CaM-free eNOS with *L*-Arg and H_4B bound is tighter than iNOS (eNOS: K_d = 0.09 μM, iNOS: K_d = 1.5 μM). CaM binding to eNOS is destabilizing, however, resulting in a 4-9 μM K_d and iNOS is significantly stabilized by CaM, with a 61-185 nM K_d. To analyze the CaM effects on eNOS dimerization, eNOS oxygenase and reductase domains were compared with iNOS oxygenase domains in the presence or absence of CaM. Hydrodynamic analysis of the eNOS subdomains indicated for the first time *in vitro* that both can dimerize, with a K_d for the reductase of 23 μM and for the oxygenase of 90 nM. The equivalent CaM-bound iNOS oxygenase domain construct had a K_d of 11 μM, thus CaM-bound eNOS oxygenase domains are tighter than iNOS. In the absence of CaM, iNOS oxygenase domains had a tighter K_d ranging from 0.14-4.6 μM, than did eNOS oxygenase domains with a K_d of 1.2-1.7 μM, thus reversing the trend for dimer tightness observed in full-length eNOS and iNOS in the absence or presence of CaM. Furthermore,

CaM is stabilizing to eNOS subdomains but not to full-length protein. A Gibbs free energy analysis calculated the CaM stabilization effect to be -1.6 kcal/mol for eNOS oxygenase domain dimers, -0.4 kcal/mol for reductase domains, and +1.2 kcal/mol for full-length eNOS. From these analyses it was also possible to calculate the entropic cost of dimerization to be on the order of 7.5-8.7 kcal/mol. We report here that CaM, *L*-Arg and H_4B have distinct stabilization effects on the three NOS isoforms that can be exploited for dissociative inhibitor design.

II. INTRODUCTION

Nitric oxide synthase (NOS)[1] is a modular homodimeric protein that contains in each subunit an N-terminal oxygenase domain that binds a heme prosthetic group as well as the cofactor tetrahydrobiopterin (H_4B), and a C-terminal reductase domain homologous to cytochrome P450 reductase (CPR) that binds NADPH, FAD and FMN (78,106). Calmodulin (CaM) binds to a recognition element in the linker region between the NOS oxygenase and reductase domains (44,64,65), and functions as a switch that stimulates electron transfer for catalysis. NOS catalyzes the two-step oxidation of *L*-arginine (*L*-Arg) first to the intermediate N^G-hydroxy-*L*-arginine (HO-Arg), then to *L*-citrulline (*L*-Cit) and nitric oxide (NO·) (106).

NOS is an obligate dimer, and electrons transfer in a *trans* mode from the reductase domain of one subunit to the heme of the other subunit in the dimer (47,48). As will be discussed herein, substrates and cofactor binding affect dimerization. A class of isoform-selective NOS inhibitors derived from imidazole or pyrimidine moieties has emerged that takes advantage of the dimerization requirement for activity by binding to

the heme pocket and altering the dimeric interface between the oxygenase domains, thus effectively preventing productive dimerization and activation (46,113,129). These dissociative inhibitors have been analyzed qualitatively for their effects on dimerization. However, the thermodynamic and kinetic components of this transformation must be analyzed individually to correctly state how ligand binding stabilizes either the monomeric or dimeric form, and how it affects the energy barrier of the conformational change that accompanies dimerization. The first step to defining the effects of inhibitor binding on the free energy transformations that accompany dimerization is to first define the natural cofactor and substrate driven dimerization effects. This work characterizes the energetic endpoints of the equilibrium between monomeric and dimeric states under various ligand-bound conditions.

The three NOS isoforms are categorized by the Ca^{2+} dependence of CaM binding (3,5). The inducible isoform (iNOS or NOS II) is regulated primarily at the transcriptional level and binds CaM irreversibly, in a Ca^{2+} independent manner (65). The neuronal (nNOS or NOS I) and endothelial (eNOS or NOS III) isoforms are constitutively expressed and bind CaM in a Ca^{2+}-dependent, reversible manner (64,65,219). CaM binding is thought to result in a conformational change that is detectable by changes in phenyldiazene probe reactivity and tryptophan/flavin fluorescence (23,137). The functional result is that CaM stimulates electron transfer both between the flavins in the reductase domain (138,139) and between the reductase and oxygenase domains (64,138-141). At the level of quaternary structure, CaM has been demonstrated to stabilize and improve yields of iNOS and eNOS during expression in *E.*

coli (91,166), and it stabilizes but is not absolutely required for formation of the eNOS oxygenase domain dimer (91,136).

The cofactor H_4B has been shown to promote dimerization and stabilize the resulting dimers of all three NOS isoforms (93,94) by binding at the dimeric interface between oxygenase domains, one pterin binding site per subunit. Structurally, the pterin-free monomeric form of iNOS is partially unfolded in the pterin binding pocket and the dimeric interaction surface is nearly completely unformed, resulting in an overall rms difference[9] of 3.41 Å between monomeric pterin-free and dimeric pterin-bound iNOS (32,40,41,114), Figure 1-9. The H_4B-bound and -free dimers of eNOS show that the H_4B binding site is preformed in the H_4B-free dimer (32,42), and the structures differ by only 0.22 Å rmsd. Thus either pterin binding could induce dimer formation, or sampling of the dimeric conformation under normal equilibrium conditions eventually would present the correct pterin-binding conformation; both modes would effectively drive dimerization.

This important role for pterin in dimerization is coupled to catalytic function through cooperative binding with the substrate Arg (89,90) and through stimulation of conversion of the iron from low to high spin (91) and of iron reduction to the ferrous form (92). H_4B redox activity is strictly required for catalysis, since structural analogs of H_4B, such as dihydrobiopterin and 4-aminotetrahydrobiopterin, can still produce the same structural and allosteric effects but do not catalyze NO· production (90,92,98-100).

[9] Calculation of rmsd between two NOS oxygenase domain structures was performed for murine iNOS structures (PDB codes 1DWX, 1NOS) and human eNOS structures (4NSE, 8NSE) and can be viewed at http://molmovdb.mbb.yale.edu/, ID=524054-12087, and 518259-9002 respectively.

Furthermore, a cationic radical intermediate has been detected for the pterin during catalysis (95,96,220).

H_4B has an important stimulatory effect on electron transfer involved in an alternate NOS activity, the production of oxygen radical species. In the absence of ligands, CaM-binding to nNOS and eNOS stimulates superoxide production and NADPH consumption termed as "uncoupling" (221-223), but H_4B binding has been shown to decrease this superoxide activity. In the case of nNOS, pterin binding increases hydrogen peroxide at the expense of superoxide (224), leading to the proposal that pterin increases the reduction rate of the oxyferrous intermediate, Figure 1-6. *L*-Arg reduces the superoxide and NADPH consumption activity of nNOS (225), but not in the case of eNOS (221). Even iNOS has been demonstrated to produce superoxide, an activity that is reduced in the presence of high levels of *L*-Arg, but unlike eNOS and nNOS, this activity is associated with the reductase domain (226).

The relative stability of NOS dimers has been studied under kinetic conditions as resistance to denaturation by SDS (93,109,115) or urea (98,111,112,227), and in equilibrium conditions by gel filtration chromatography (94,112). Both *L*-Arg and H_4B have significant stabilization effects in these assays. iNOS is apparently more sensitive to the absence of ligands, because it loses its heme prosthetic group in the total absence of H_4B and *L*-Arg (94,112), whereas eNOS and nNOS retain significant dimeric content in the absence of these ligands as observed by gel filtration chromatography. In a low temperature SDS-PAGE assay, H_4B has been shown to greatly stabilize nNOS against dimer loss (93), and partially stabilize eNOS (115). However, iNOS dimers bound to *L*-

Arg and H_4B are still SDS-labile (109,115). Similar trends have been observed by urea denaturation assays of isolated NOS oxygenase domains that showed that eNOS dimers are more urea resistant, followed by nNOS and then iNOS (227). In the forward direction, monomers produced by urea treatment can be induced to re-dimerize by supplementing with heme, *L*-Arg, and H_4B for full length iNOS (98,111,112) and for the NOS oxygenase domains from all three isoforms (227). In the oxygenase domain re-dimerization studies, the order of ability to recover from urea treatment is iNOS > nNOS > eNOS, and the best recovery was observed when the proteins were supplemented with both *L*-Arg and H_4B (227).

From this collection of observations, eNOS is considered to be the tightest dimer, and iNOS the weakest, of the three isoforms in denaturation studies (227) and in yeast-two-hybrid analysis (109). Interestingly, within the cellular context of the yeast two-hybrid system, eNOS and nNOS reductase domains were shown to interact with both oxygenase and reductase domains but iNOS reductase domains did not (109), leading to the possibility that the weak iNOS dimerization could be due to the absence of reductase-mediated dimeric interactions. Truncated eNOS domains have previously been observed by co-immunoprecipitation in cell extracts to interact with full-length protein expressed in COS-7 cells. Such reductase domain interactions have not been observed in gel filtration chromatographic analyses of iNOS reductase domains (228), thus dimerization is thought to be mediated exclusively by the oxygenase domains in iNOS.

We report here the effects of ligands and calmodulin on the internal dimerization affinity of nNOS, iNOS, and eNOS wild-type proteins in solution under equilibrium

sedimentation conditions, as determined by analytical ultracentrifugation. Because eNOS is able to dimerize in the absence of CaM and H_4B and is apparently the most stable dimer, we have also analyzed the dissected eNOS oxygenase and reductase domains, as well as iNOS oxygenase domain constructs with and without the CaM recognition element. Additionally, we have analyzed conserved mutants of the aromatic residues at various positions near the dimeric interface: W74F, Y467F, and W445L. W74 is found within the N-terminal element that is found to swap between oxygenase domains of iNOS; Y467 is near the C-terminus of the oxygenase domain, and W445 is found within the pterin-binging pocket. Our analytical ultracentrifugation method is non-perturbing and uses native protein conditions favored for *in vitro* activity measurements. Furthermore, the method of sedimentation equilibrium analytical ultracentrifugation detects the protein distribution under equilibrium conditions, thus allowing measurement of ligand binding effects on NOS dimer stability.

III. Experimental

Materials – TRIS and agarose were from Fisher. DNA manipulations were done using enzymes, buffers, and reagents from New England Biolabs (Beverly, MA) and purification kits from QIAGEN (Chatsworth, CA), which also supplied the Ni-NTA resin. Oligonucleotide primers were synthesized and the DNA sequenced by the Biomolecular Resource Center (University of California, San Francisco). Agar was from GibcoBRL (Rockville, Maryland), H_4B from Alexis (San Diego, CA), IPTG from Promega (Madison, WI), and LB, yeast extract, and tryptone from DifCo (Detroit, MI).

All other materials were purchased from Sigma. Novex tris-glycine 4-12% acrylamide gels were from Invitrogen (Carlsbad, CA).

PCR production of the mutant eNOS clones – A Progene thermocycler from Techne (Cambridge, UK) was employed. Mutagenesis of the human eNOS gene was accomplished by overlap extension PCR, utilizing as the template previously constructed human eNOS expression vector pCWori that contains a 6-histidine tag at the N-terminus (229). Two complimentary primers were designed to encode the aromatic amino acid mutation and a silent endonuclease restriction site. Two sets of reactions were prepared for PCR, combining the reverse mutagenic primer with a primer that annealed in the polyhisitidine tag of pCWori to generate the N-terminal (A) fragment, and then the forward mutagenic primer was combined with a primer that binds at the *KpnI* site for generating the C-terminal (B) fragment. These partial reactions were separated by agarose gel electrophoresis and extracted, then recombined in a 1:1 stoichiometry for a final PCR step, combining the partial fragments with only the end primers binding at the polyhistidine and post-*KpnI* sites. The resultant full-sized (AB) fragment and the wild-type eNOS poly-His-pCWori vector were digested with *NdeI* and *KpnI*, and the fragments were purified by gel separation and extraction. The full-sized mutated fragment was then ligated with the wild-type vector from which the corresponding fragment was removed. The ligation mixture was used to directly transform DH5α subcloning competent cells, and the colonies were screened for the new restriction sites created by the mutation. Positive clones were then sequenced at the University of California San Francisco sequencing facility to confirm the desired mutations. The forward mutagenic primers are as follows, with the mutated bases designated by bold-

type. *W445L*: 5' GGCTGCCCCG CGGACTTGGC CTGGATCGTG CCC incorporating a new *SacII* site; *W74F:* 5' CGTGTGAATA ACTTCGAAGT GGGGAGC with a new *BstBI* site; *Y467F*: 5' GGAGATGGTT AACTTTTTCC TGTCCCCGGC C with a new *HpaI* site. The primer used to anneal in the polyhistidine site is 5' GATGCTTAGG AGGTCGAATG CATCATCACC ATCAC, and the primer annealing at the *KpnI* site is 5'-GGCGCTCAGC CGGTACCTCT GGGCG.

PCR production of the eNOS oxygenase and reductase domains -- The bovine eNOS oxygenase and reductase domain constructs were a gift from Dr. Ignacio Rodríguez-Crespo. These clones were not reported, and therefore their PCR production is included here. Primers for creating the eNOS oxygenase domain were forward: 5' GCCCCAGCCA TATGGCAAAC TTGAAAAGCG TGGGTCAGGA, incorporating an *NdeI* site, and reverse: 5'-GGTCTAGAGT CACTACTATC ATTTCACTCG CTTGGCCAT, incorporating an *XbaI* site and three stop codons. This PCR product and the wt-bovine-eNOS-pCWori expression vector were then treated with *NdeI* and *XbaI,* and the fragments were purified by gel separation and extraction using Quiagen DNA purification kits. The fragment encoding the oxygenase domain was then ligated with the wild-type vector from which the full-length gene was removed. The ligation mixture was used to directly transform DH5α subcloning competent cells, and DNA purified from isolated colonies was screened for the appropriate band sizes by restriction digests with *NdeI* and *XbaI* before sequencing. The final oxygenase construct then contained residues 1-521 with a 6-His N-terminal tag and the CaM-recognition element at the C-terminus. The reductase domain primers were forward: 5'-AAGGGAGCGC GCATATGGGC GCAGGCA, incorporating a new *NdeI* site, and reverse primer that anneals at the *KpnI*

site: 5'- CAGCCGGTAC CTCTGG. The short 769 nucleotide insert as well as the wild type bovine eNOS-pCWori vector were treated with *NdeI-KpnI*, and the short fragment was ligated into the NdeI-KpnI sites, resulting in the reductase construct in pCWori. The resulting reductase domain construct contained residues 489-1206 of eNOS, including the CaM-recognition motif at the N-terminus but with no 6-His tag.

PCR production of the iNOS oxygenase domains -- Primers for creating the iNOS oxygenase domain with ($iNOS_{1-531}$) and without ($iNOS_{1-495}$) the CaM-recognition element were forward: 5' CGAATGCATC ATCACCATCA CC which anneals in the poly-His tag region and includes the *NdeI* site at the N-terminus of the wild-type murine macrophage iNOS pCWori vector, and reverse: for $iNOS_{1-531}$: 5'-AAATCTAGAC TACTATCAGA CCCGTGAAGC CATGACCTTT CG, and for $iNOS_{1-495}$: 5'-GCTCTAGACT ATCACTACCA GATGTGGGTC TTCC, incorporating an *XbaI* site and three stop codons after residues 495 or 531, respectively. This PCR product and the wt-iNOS-pCWori expression vector were then treated with *NdeI* and *XbaI*, gel purified, ligated, screened and sequenced according to the procedure described above. The final oxygenase construct then contained iNOS residues 1-531 or 1-495 with a 6-His N-terminal tag.

Expression and Purification of NOS -- Wild-type human and bovine eNOS, mouse macrophage iNOS, and rat brain nNOS were expressed and purified according to published methods with some modifications (22,115,166,175,230). Each protein was coexpressed with human CaM using a pACYC-derived expression vector under the control of both a T7 and *trc* promoter (230). For the purposes of coexpression, the BL-21

(DE-3) cells were first transformed with the pACYC-CaM vector then plated on LB-agar Petri dishes supplemented with chloramphenicol (25 μg/ml). Isolated colonies were then sub-cultured in 5 ml chlroamphenicol-LB medium and pelleted while still in the logarithmic growth phase by centrifugation. These cells were made competent (231), then retransformed with the desired pCWori-NOS vector, and selected with ampicillin (200 μg/ml) and chloramphenicol. The clones were selected and expressed as previously reported (22,115,166,175,230).

In the cases where CaM-free protein was desired, CaM was omitted from the expression, resulting in significantly reduced protein yields in the case of iNOS, but reasonable yields in eNOS expressions. Proteins were purified via affinity chromatography on nickel-nitrilotriacetic acid (Ni-NTA) agarose and 2',5'-ADP sepharose to >90% purity as judged by SDS-polyacrylamide gel electrophoresis stained by silver stain (232). For the analysis of CaM-bound subdomains, the eNOS and iNOS oxygenase or eNOS reductase domain construct was coexpressed with CaM. Coexpression of CaM with $iNOS_{1-495}$ did not alter the yield. The oxygenase domain constructs $eNOS_{oxy}$ and $iNOS_{1-531}$ were purified by Ni-NTA agarose, and CaM-sepharose. The reductase domain construct $eNOS_{red}$ was purified by 2',5'-ADP sepharose alone. 2 mM *L*-Arg and or 25 μM H_4B were included in the lysis and purification buffers when desired. These concentrations should be sufficient for saturation; the Ks for *L*-Arg is ~2 μM (22,115,166), and the K_d for H_4B is 0.23 μM for nNOS (90). Additionally, FMN was supplemented to the reductase preparations, and the protein was concentrated to 10-30 μM before freezing at -70° C for storage.

Gel filtration -- For AUC analysis, a gel filtration step was added to collect the dimeric fraction of the proteins, using a Superdex 200 column attached to a Pharmacia FPLC system, with detection at 280 nm. If desalting of a sample was required (to simulate inactivated Ca^{2+} levels) the protein was loaded on a PD10 column from Amersham Pharmacia and exchanged into the desired Ca^{2+}-depleted buffers. Standard running buffer conditions were: 50 mM TRIS pH 7.6 at 4 °C, 200 mM NaCl, 0-10% glycerol, with the addition of 2 mM $CaCl_2$, 2 mM Arg, and or 20 μM H_4B where indicated. Purification after gel filtration was estimated at >95% based on SDS-PAGE analysis with silver staining.

For analytical purposes, Stokes radii (R_S) were calculated based on a calibration curve using the Laurent and Killander method (233) with the following standards purchased from Sigma: cytochrome c (17.7 Å), myoglobin (21.2 Å), carbonic anhydrase (23.5 Å), bovine serum albumin (35.6 Å), alcohol dehydrogenase (45.0 Å) and apoferritin (61.0 Å). A linear plot of $[-\log(K_{av})]^{1/2}$ versus R_S gave an empirical formula for calculation of the apparent R_S for observed peaks of monomer and dimer, listed in Table 1. (K_{av} was defined as $(v_e - v_o)/(v_t - v_o)$; where v_e is the elution volume of sample, v_o is the void volume and v_t is the bed volume of the column.) Sedimentation parameters were calculated using the public domain program Sednterp v. 1.03 by D.B. Hayes, T. Laue, and J. Philo (http://www.rasmb.bbri.org/).

Hydrodynamic calculations -- The program HydroPro, v. 3.C (234) was used to calculate expected R_S value for active eNOS complex models, based on models of the eNOS reductase domain in either monomeric or dimeric form (37), discussed in Chapter

4. The docked models were manually assembled using the program Swiss PDB viewer v. 3.7b2 (88), from subdomain complexes predicted by the molecular recognition algorithm GRAMM (235). The best model from GRAMM was selected visually for surface property complementarity of electrostatic patches, calculated using GRASP (236) and phylogenetic conservation of surface residues, visualized using the program ConSurf (237). Models calculated for the large active NOS complex of CaM-bound full-length dimer were found to significantly underestimate the R_S in control calculations. This is likely due to the absence of approximately 10% of the total structure, for example in eNOS 135 residues are missing from the N-terminus, the AI element, and a large portion of the CaM-recognition region and contains per subunit, residues 69-482, 496-594, 693-1201 and CaM residues 9-144.

Spectral Characterizations -- Protein concentration was calculated based on an extinction coefficient of 100 mM^{-1} for the heme Soret band near 400 nm. Extinction coefficients for each protein construct at 280 nm were calculated according to the Edelhoch method (238) based on amino acid composition using the program Sednterp. The following values of ε_{280} were calculated (mM^{-1} cm^{-1}): rat nNOS 176.8, bovine eNOS 149.2, murine iNOS 165.4, bovine eNOS oxygenase domain 79.8, bovine eNOS reductase domain 70.8, murine $iNOS_{1-531}$ or $iNOS_{1-495}$ 103.8, and human CaM 1.49. The Soret band was used preferentially for calculation of heme-containing protein concentration when within the 0.1-1.0 AU linear absorbance range of the detector. For the reductase domain, the 280 nm bands were used preferentially to avoid underestimation of concentration by flavin bands due to loss of FMN. Activity measurements were taken for the full-length proteins using the oxyhemoglobin assay

(239). Spectral measurements of all samples were taken to confirm proper-ligand binding, detected on a Cary 1E UV-Vis spectrophotometer.

Analytical Ultracentrifugation -- Sedimentation analyses were performed with a Beckman Optima XL-A/I analytical ultracentrifuge (Beckman-Coulter Inc., Palo Alto, CA), equipped with absorbance and interference optical detectors. Two rotors were used interchangeably, the AnT-50 and AnT-60 rotors. Sample cells were assembled from sapphire or quartz lenses and six-sector charcoal-filled epon centerpieces for equilibrium analyses, and two-sector charcoal-filled epon or aluminum centerpieces for velocity analyses. Scans were acquired at multiple wavelengths, at 235 nm, 277 nm, and at the Soret near 400 nm as appropriate, allowing sample detection between the high nanomolar and low micromolar concentration range. Sample concentrations were tested from 0.3 - 10 μM for each protein condition, calculated based on the Soret absorbance measured in initial wavelength scans.

Sedimentation equilibrium -- To stabilize the protein, the experiments were performed at 4 °C. Buffer used was 50 mM TRIS, 200 mM sodium chloride and 0-10% glycerol, and 2 mM calcium chloride when calmodulin was present. Multiple data scans of absorbance versus radial position were collected at three rotor speeds, 7, 10, and 14k rpm, for proteins at 0.3 - 10 μM concentrations. Each data set was collected at high resolution: 0.001 cm radial step size and with 7-10 replicates, then trimmed using the program WinReedit v. 0.999.027 (ftp://alpha.bbri.org/rasmb/spin/ms_dos/uconn_uaf/). Multiple data sets (9-15) were then fit in a global analysis using a non-linear least squares regression calculated with WinNONL3 v. 1.03 (240). Concentration distribution plots

were fit to the following equation describing a monomer-dimer, self-association model (241).

$$(1) \qquad [C_{total}] = [C_{1,0}]e^{\sigma(r^2-r_0^2)/2} + K_2[C_{1,0}]^2 e^{2\sigma(r^2-r_0^2)/2} + \delta C$$

C_{total} is the total concentration of individual NOS subunits observed as a function of radius, r; $C_{1,0}$ is defined as the monomer concentration at the innermost radial position, at the meniscus, r_0; σ is the reduced molecular weight as defined by equation 2 below; and K_2 is the equilibrium association constant for the monomer-dimer equilibrium. In the simplified single species model, K_2 is set to zero. A full derivation of this formula is given by Laue and Stafford (241).

$$(2) \qquad \sigma = \frac{M_1(1-\bar{\nu}\rho)\omega^2}{RT}$$

M_1 is the monomeric molecular weight; $\bar{\nu}$ is the partial specific volume; ρ is the buffer density; ω is the angular velocity; R is the gas constant and T is the temperature. The program Sednterp was used to calculate M_1, $\bar{\nu}$, and ρ at the given temperature, rotation speed, and buffer and protein compositions.

For reporting results of the sedimentation equilibrium analyses, the data fits from WinNONL3 were reformatted using a Python script (written by S.D. Mooney, available upon request) for import into Microcal Origin v. 3.78 for graphic manipulation. A template was generated for display of all 9-15 curves, in the upper window plotting Abs *vs.* the normalized values of the square of the radial position, and in the lower window

plotting the residuals of the data curve fits, ΔAbs. *vs* normalized values of the square of the radial position. The normalized radial position value was created *only* for graphical purposes in order to display all the data sets along the same axes in a single panel. Using a 6-sector equilibrium centerpiece, the center of each "window" is positioned at 6.0, 6.5, or 7.0 cm from the center of rotation. Therefore, to normalize, the values of $r^2/2$ were corrected by 0, 3.125, and 6.5 cm^2 for each window to place the center of each window at zero.

The association constant K_2 was solved in the natural-logarithmic form, $Ln(K_2)$, with standard deviations at the 95% confidence level. To report a dissociation constant, K_d, it is necessary to calculate the negative exponential of $Ln(K_2)$, and the upper and lower limits of $Ln(K_2)$ are drawn as error bars in graphs used to compare K_d values measured under various conditions. Calculation of the Gibbs free energy of dimerization used the upper and lower limits of K_d to calculate the limits of ΔG, and is reported in units of kcal/mol using equation 4.

(4) $$\Delta G = -RT\ln(K_d) = \Delta H - T\Delta S$$

ΔG is the free energy of a given transformation, R is the gas constant, T is the temperature, set at 37 °C, ΔH is the enthalpic contribution to free energy measured under equilibrium conditions, and TΔS is the entropic component of free energy.

Sedimentation velocity -- Samples were prepared in an identical manner to the equilibrium experiments; however, concentration was increased to give signal of 0.7-1.0

absorbance units at desired protein wavelengths at 230 or 280 nm or at the Soret band of the heme near 400 nm, as appropriate for a given concentration. The scans were recorded at 50k rpm, at 20 °C (because stability was not a problem for the short duration of the experiment), and data was collected for a single sample, one wavelength at a time. Scan settings were chosen to give good resolution but also fast scan rates of approximately 2-3 min per scan, using the smallest radial step size of 0.001 cm, selecting no delay time between scans, and recording a single replicate. Sedimentation was essentially complete within three hours of the experiment, and typically only the first 70 scans were analyzed.

Data analysis was performed by modeling of the Lamm equation using the program SedFit (http://www.analyticalultracentrifugation.com) by P. Schuck (242). To avoid bias of forcing a model onto the data by defining discrete species, instead a continuous distribution model C(S) was fitted to 50-70 scans by an iterative modeling process as described (242). Sedimentation parameters were calculated using the program Sednterp, and solved sedimentation coefficients found in the C(S) distribution were then corrected to the standardized value in water $S^0_{w,20}$. R_S was then calculated according to equation 5.

(5) $$R_S = \frac{M_1(1-\bar{\nu}\rho)}{\eta S N_o}$$

M_1 is the monomeric molecular weight; $\bar{\nu}$ is the partial specific volume; ρ is the buffer density; η is the buffer viscosity; S is the observed sedimentation coefficient, and N_0 is Avogadro's number.

IV. RESULTS

A. The active NOS complex

To assay the holo form of each NOS isoform, the proteins were coexpressed with CaM, and purified in the presence of sufficient *L*-Arg and H_4B to assure that most of the protein was in the fully ligand-bound form. In the case of the constitutive isoforms, additional units of CaM were incubated with the protein before gel filtration, and calcium chloride was supplemented to preparations of CaM-coexpressed protein to assure a shift to the calmodulin-bound forms (45,243). When these proteins were analyzed by gel filtration using fast phase liquid chromatography, the running buffer contained the *L*-Arg and H_4B ligands, as well as calcium chloride. Under these conditions, the NOS isoforms show a significant monomer-dimer distribution at concentrations near 1 μM, Figure 4-1. Estimation of the dimeric fraction is inherently difficult from these traces due to poor resolution of peaks; however, the Stokes radius (R_S) could be calculated (233) in Table 4-1 based on the R_S of standard proteins using the equation shown in Figure 4-1.

Table 4-1. Stokes radii observed for full-length and oxygenase domains. The standard error estimate for R_S based on the error in v_e from n = 4 chromatograms is ± 0.7 Å.

Protein	R_S monomer (Å)	R_S dimer (Å)
iNOS + CaM	46.8	57.9
eNOS + CaM	51.2	61.4
nNOS + CaM	57.6	68.6
iNOS -CaM	45.6	54.6
eNOS -CaM	50.3	58.4
$iNOS_{1-495}$ -CaM	39.7	-
$iNOS_{1-531}$ +CaM	41.4	51.6
$eNOS_{1-521}$ -CaM	38.5	50.2
$eNOS_{red}$ +CaM	43.5	54.2

Figure 4-1 The gel filtration profiles for nNOS, eNOS and iNOS copurified with calmodulin and in the presence of Arg and pterin are shown. These traces are representative of four replicates. Stokes radii were calculated based on a calibration curve (inset) calculated by the Laurent and Killander method (233) using the following standards purchased from Sigma: cytochrome c (CytC), R_S = 17.7 Å; myoglobin (Mb), R_S = 21.2 Å; carbonic anhydrase (CA), R_S = 23.5 Å; bovine serum albumin (BSA), R_S = 35.6 Å; alcohol dehydrogenase (ADH), R_S = 45.0 Å; and apoferritin (AF), R_S = 61.0 Å. K_{av} was defined as $(v_e - v_o)/(v_t - v_o)$; where v_e is the elution volume of sample, v_o is the void volume and v_t is the bed volume of the column.

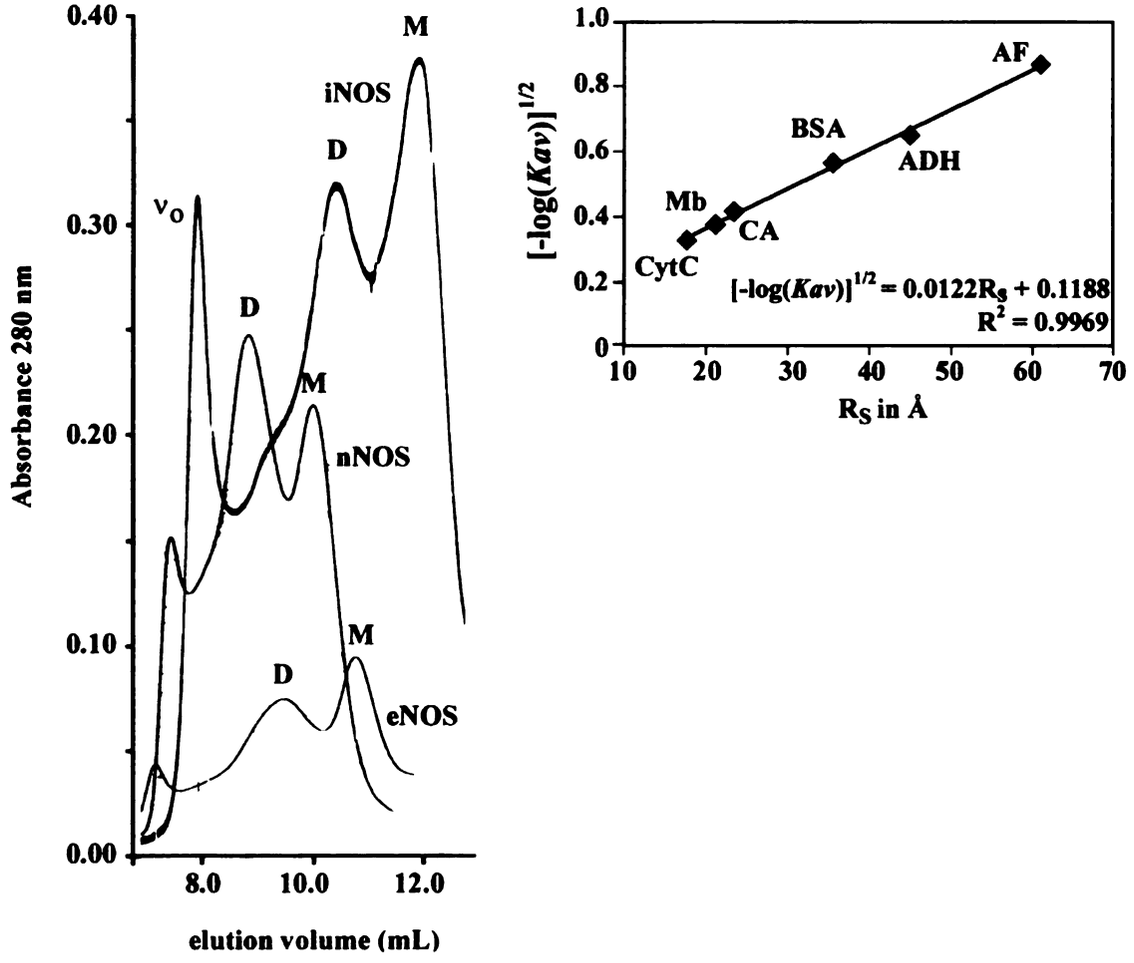

Figure 4-2 A single radial scan of nNOS (A), iNOS (B), and eNOS (C) in the presence of CaM is shown (black dots), compared with three curves representing the distribution expected for monomer, dimer, and trimer. The radial scan was recorded at 290 or 280 nm, during a 10,000 rpm sedimentation equilibrium experiment at 4 °C. The buffer used was 50 mM TRIS pH 7.6, 200 mM NaCl, plus 2 mM $CaCl_2$ for nNOS and eNOS preparations, and included 10% glycerol to stabilize eNOS. The appropriate sedimentation parameters were calculated using Sednterp. The calculated distributions were derived from a single species version of equation 1, inserting sigma values for monomer, dimer and trimer. The K_2 term is zero for a non-associating model, and the values of δC and $[C_{1,0}]$ were solved empirically for the individual radial scan by WinNONL3. Graphic manipulations were done in Origin 3.78. Monomer, dimer and trimer values of σ were for nNOS: 2.282, 4.564, and 6.846; iNOS: 1.8891, 3.7782, and 5.6673; and finally eNOS: 1.7743, 3.5486, and 5.3229.

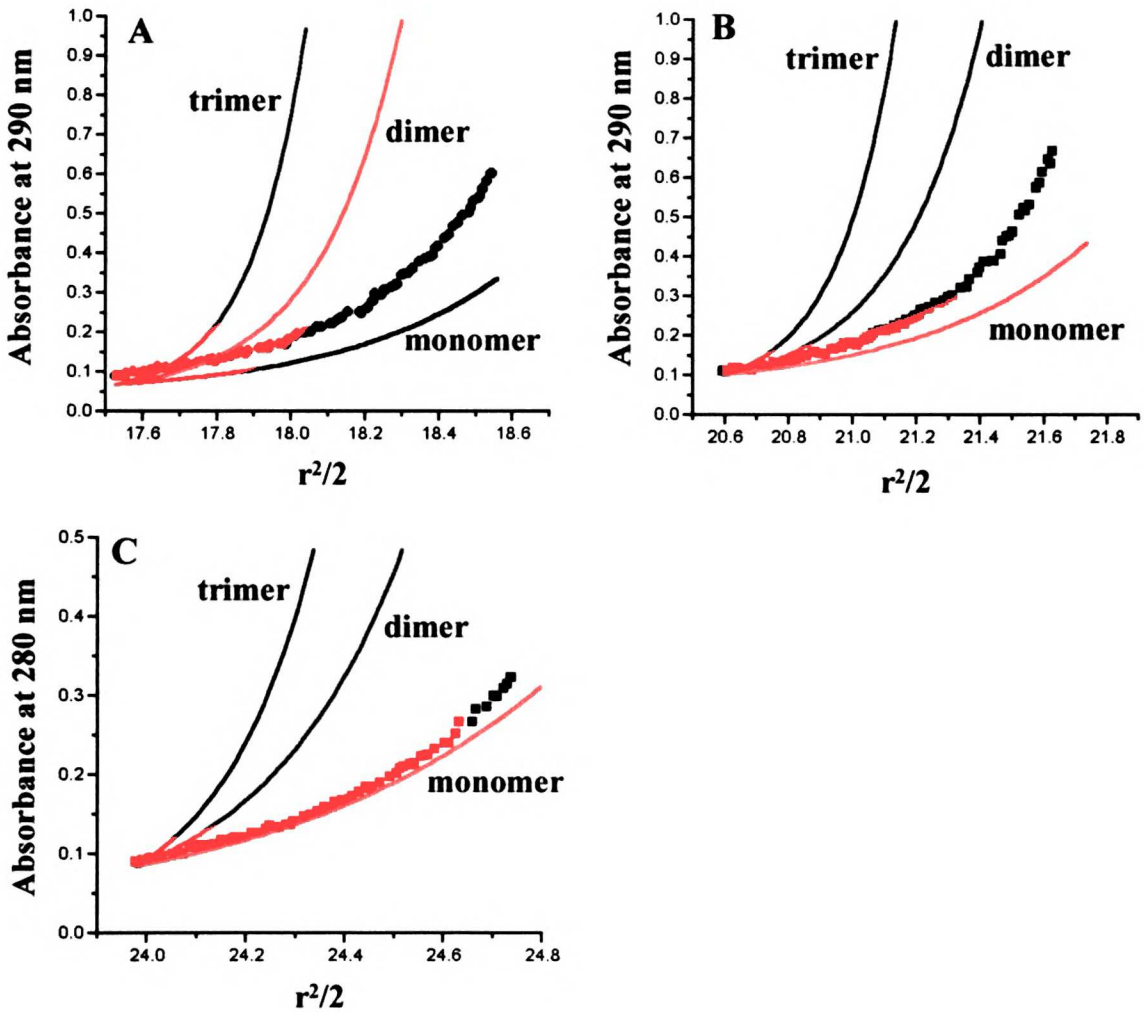

Figure 4-3 Sedimentation equilibrium fits of CaM-bound nNOS in the presence of *L*-Arg and H_4B. Fifteen data sets, measured at three velocities and five concentrations and observed at 290 or 385 nm (off-peak) wavelengths, were fitted to a single model at a time. Shown here is the monomer-dimer fit, resulting in a K_d of 61 μM. For the purpose of graphical display, the x axis values of $r^2/2$ were normalized to the center of each window of the 6-sector centerpiece, thus zero corresponds to 18.0, 21.125, and 24.5 cm^2. Graphing was done in Origin v. 3.78. An even distribution of the residuals above and below the x axis indicates appropriate model fitting; also, the deviation about the x axis is within approximately 0.02 AU, which is within the measurement accuracy of the detector.

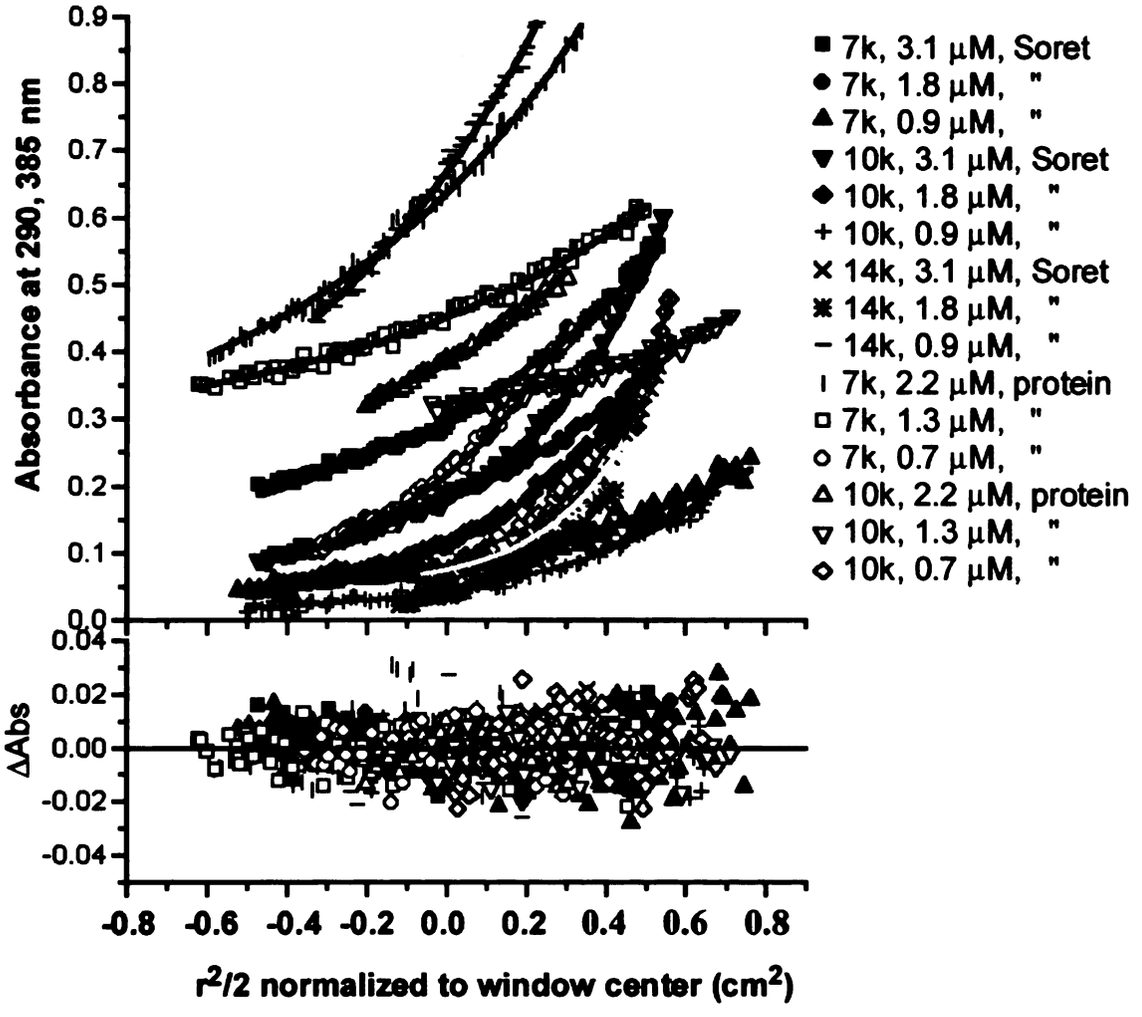

Figure 4-4 Sedimentation equilibrium fits of CaM-bound iNOS in the presence of *L*-Arg and H_4B. Fifteen data sets measured at three velocities and five concentrations and observed at 285 or 290 nm wavelength, were fitted to a single model at a time. Shown here is the monomer-dimer fit, resulting in a K_d of 185 nM. Graphing was done as described for Figure 4-3.

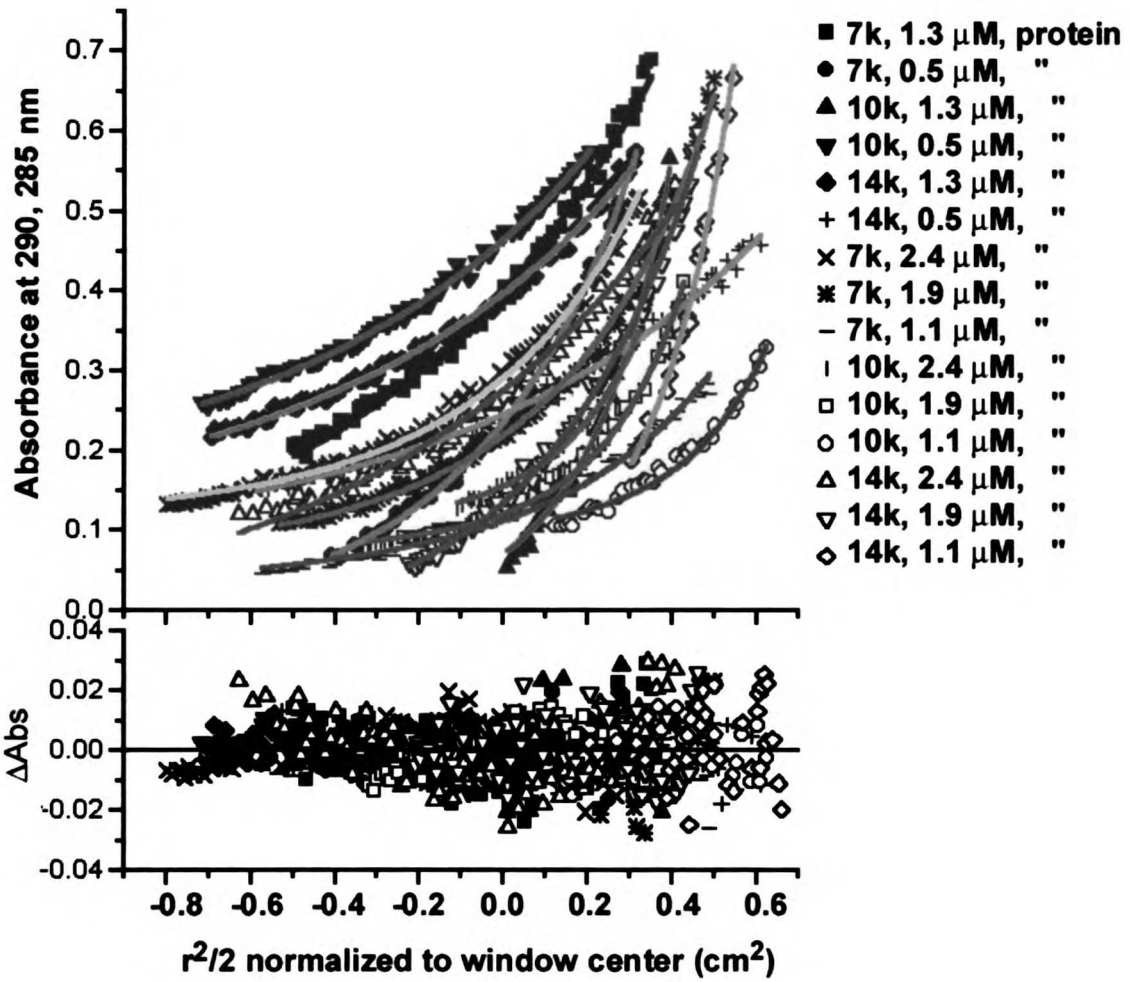

Figure 4-5 Sedimentation equilibrium fits of CaM-bound eNOS in the presence of *L*-Arg and H_4B. Fifteen data sets measured at three velocities and five concentrations, with detection at 280 nm wavelength, were fitted to a monomer-dimer model, resulting in a K_d of 4.4 μM. Graphing was done as described for Figure 4-3.

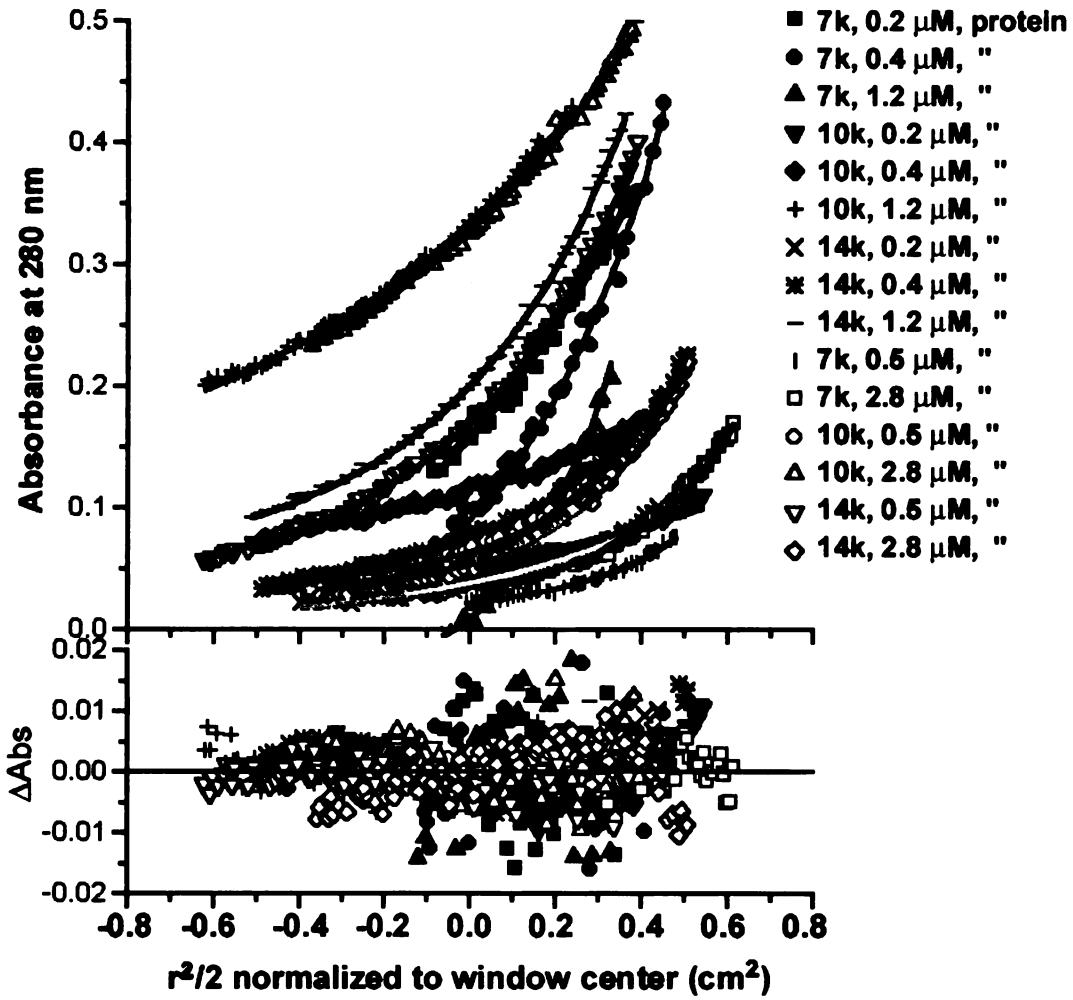

B. Ligand effects on CaM-bound full-length NOS

Next, ligand-binding effects on the dimer affinity of CaM-bound protein were examined. The wild-type NOS protein was coexpressed as before with CaM, but *L*-Arg and H_4B were omitted from the purification buffers during the affinity chromatography and the gel filtration purification steps. For nNOS and eNOS preparations, additional CaM was supplemented to the samples before gel filtration. Gel filtration was treated as a preparative step for collection of the dimeric fraction from each sample, Figure 4-1. Fractions of 1 mL volume containing the dimeric peak were collected and pooled from multiple injections, and concentrated by ultra-filtration. The K_d values discussed below are listed in Table 4-2.

In experiments with nNOS, the protein was concentrated to approximately 4 μM. To portions of this sample were added 2 mM *L*-Arg and/or 30 μM H_4B for sedimentation equilibrium analysis as described. Nine sedimentation conditions were evaluated, varying the rotation velocity as well as the protein concentration over a 0.5-4 μM range, with detection at the Soret and at protein bands of 277 or 235 nm as appropriate. Final K_d values are reported with upper and lower limits as error bars, as shown in Figure 4-6. nNOS in the presence of CaM but in the absence of ligands has a K_d of 23 μM (19-29 μM range). Arginine alone is significantly destabilizing, with a K_d of 65 μM (51-84 μM). As expected, H_4B alone had a stabilizing effect, resulting in a K_d of 17 μM (14-22 μM), a value that is statistically distinct from the ligand-free condition by the Student's T-test.

The K_d observed in the presence of *L*-Arg and H_4B together was reported earlier as 61 μM (48-79 μM).

Figure 4-6. Dissociation constants calculated for CaM-bound nNOS from sedimentation equilibrium analysis. Shown are the following conditions: ligand-free, 2 mM *L*-Arg, 30 μM H_4B, both *L*-Arg and H_4B, *L*-Arg with DTT alone, 2 mM *L*-Cit, and 30 μM HO-Arg. Error bars are calculated from the upper and lower limits for the logarithmic form of the association constant.

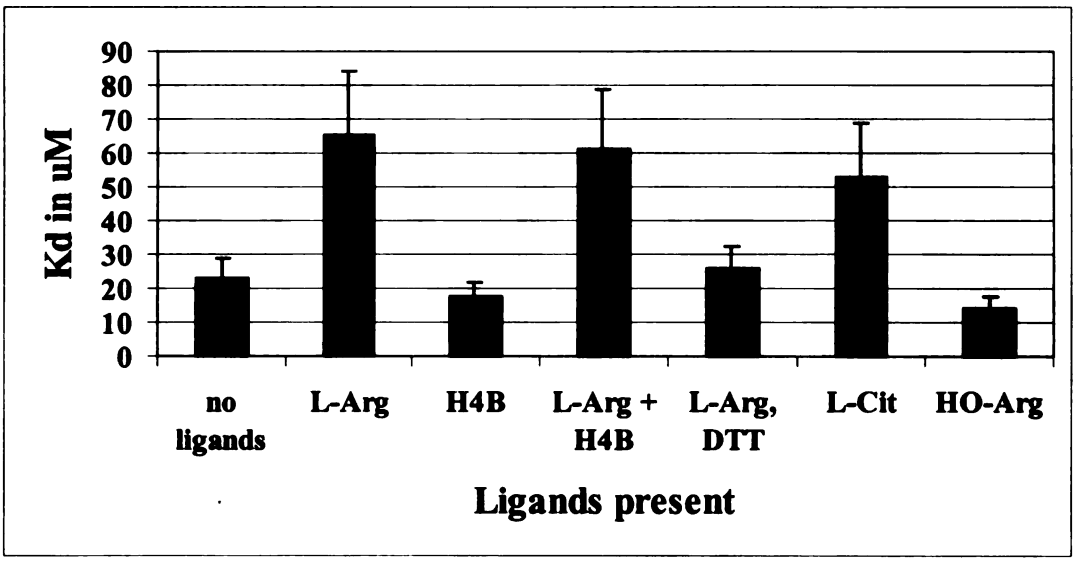

To further explore the destabilizing effect of the heme-pocket binding ligands, 300 μM DTT and 2 mM *L*-Arg were combined in the next condition, followed by 2 mM *L*-Cit or 30 μM HO-Arg alone. In all cases where H_4B is included, there is 10x DTT present to keep pterin in the reduced form; thus the 2 mM *L*-Arg, 30 μM H_4B condition also had 300 μM DTT present. *L*-Arg in the presence of DTT was stabilizing relative to the *L*-Arg plus H_4B (plus DTT) condition, thus it is the pterin that is destabilizing in the latter case. The K_d of *L*-Arg plus DTT was 26 μM (20-33 μM), similar to the ligand free value. *L*-Cit produced a high K_d of 53 μM (40-69 μM), similar to *L*-Arg; however HO-Arg had a unique stabilizing effect K_d = 14 μM (11-18 μM). Thus the second step of the

NOS catalytic reaction with intermediate HO-Arg bound could be protected from exchange into solvent by tight dimerization. It would follow that the product (*L*-Cit)-bound form should have a weaker dimerization affinity to allow product release. Thus it is quite interesting that the substrate-bound form with both *L*-Arg and pterin present is *de*stabilized by the pterin, which contradicts the predictions from SDS-resistance and thermal stability analyses (93). These experiments used 3-fold higher H_4B concentrations, but equivalent amounts of *L*-Arg (1 mM), and detected no change in secondary structure composition upon dimer stabilization by CD spectroscopic measurements (93); thus dimerization could involve shifting positions of preformed secondary elements. Our results may suggest that the first step of catalysis (with transient electron transfer to the pterin) has a different dimeric conformation than other tight dimers observed here and previously as SDS-resistant in the presence of *L*-Arg or H_4B (93).

iNOS was prepared in the CaM-bound, ligand-free state according to the procedure described for nNOS. Because the apparent K_d of ligand-bound iNOS was quite tight, the highest concentration employed was decreased to 1 μM, and detection was shifted to the protein band at 277 nm. Ligand free iNOS was surprisingly stable, with a K_d of 86 nM (71-106 nM range) Figure 4-7. *L*-Arg had a further mild stabilizing effect, resulting in a K_d of 61 nM (49-75 nM). H_4B alone had little effect, K_d = 72 nM (57-91 nM), but *L*-Arg and H_4B are again destabilizing to ligand-free iNOS (K_d was 185 nM). To explore the destabilizing effect of pterin and Arg together, further combinations of ligands were tested that bind to both sites at once. In the presence of H_4B, HO-Arg and *L*-Cit gave similar results to *L*-Arg, with K_d values of 153 nM (122-192 nM) and 260 (176-384 nM), respectively. *L*-Arg with H_2B instead of H_4B still gave a high K_d of 236 nM

(182-306 nM). Thus the identity of the ligand bound in either the pterin or heme-site pockets does not appear to alter dimerization; rather it is whether ligands are bound or not that determines the dimer affinity.

Figure 4-7. Dissociation constants calculated for CaM-bound iNOS from sedimentation equilibrium analysis with the following added ligands: ligand-free, 1 mM *L*-Arg, 25 μM H_4B, H4B with *L*-Arg, 20 μM HO-Arg, or 1 mM *L*-Cit, and 25 μM H_2B with *L*-Arg.

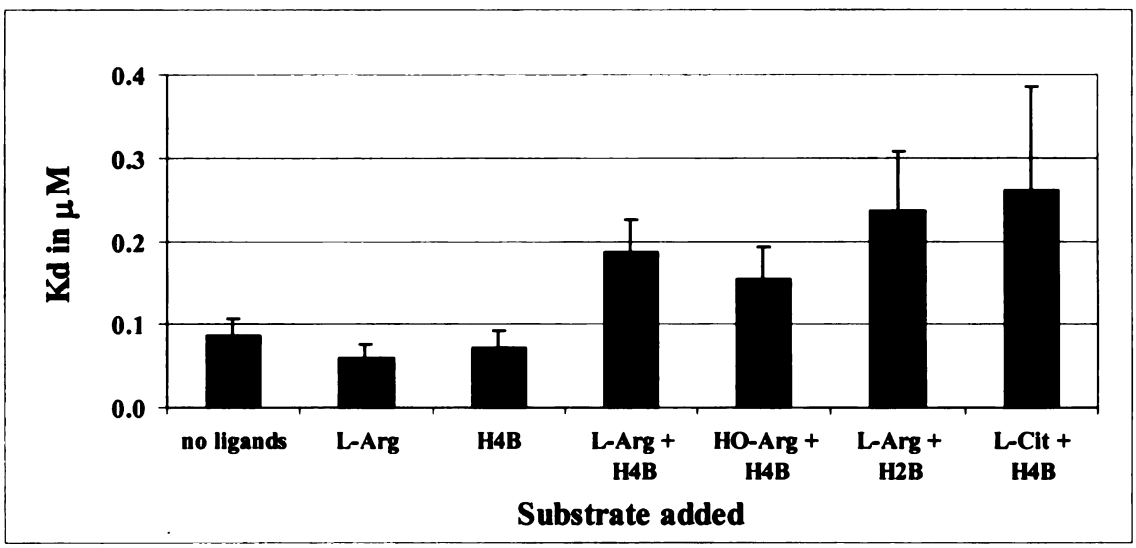

Next, CaM bound eNOS was studied. Before gel filtration, these samples were incubated with 1 μM additional CaM, and calcium chloride was kept in the solution throughout the sample preparation. In the ligand free case, a K_d of 5.7 μM (4.4-7.3 μM range) was observed. *L*-Arg was again destabilizing, as in CaM-bound nNOS, with a K_d of 9.1 μM (7.0-11.5 μM). However, *L*-Arg and H_4B in combination were stabilizing, giving a K_d of 4.4 μM (3.6-5.3 μM range). These values are shown in Figure 4-8. eNOS in the presence of H_4B, even with additional DTT present, gave anomalous results that were consistent with loss of signal due to degradation or chemical alteration of the sample. iNOS and nNOS samples prepared under identical conditions did not demonstrate such changes in signal. Therefore we believe that this pterin-dependent

behavior is specific to eNOS. The aromatic residue mutants of wild-type eNOS expressed with CaM were analyzed for alterations in dimer affinity, reported here in the *L*-Arg bound condition. These proteins all had a K_d approximately 10-fold weaker than that of wild-type human eNOS under similar conditions. W74F had a K_d of 25 μM (20-31 μM range), W445L was 26 μM (21-31 μM), and Y467F had a slightly lower K_d of 16 μM (13-20 μM).

Figure 4-8. Dissociation constants calculated for CaM-bound eNOS from sedimentation equilibrium analysis. Shown are the effects of 1 mM *L*-Arg plus or minus 10 μM H_4B. The ligand free case had a Soret maximum at 427 nm, indicating that residual imidazole remained bound.

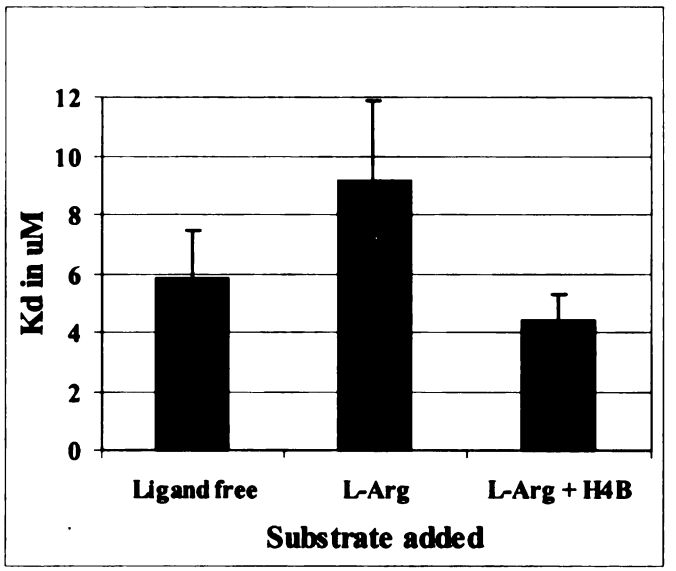

In summary, in the CaM-bound state, eNOS and nNOS are destabilized by the addition of *L*-Arg, but iNOS is stabilized, Table 4-2. Pterin may stabilize nNOS and iNOS but the K_d values found do not have a statistically significant difference from the ligand-free case in our measurements, and eNOS appears to lose signal in the presence of pterin alone. Interestingly, the addition of both *L*-Arg and H_4B are destabilizing to nNOS and iNOS, but eNOS is slightly stabilized from the ligand-free form.

Table 4-2. K_d values measured by sedimentation equilibrium analysis.

Protein	conditions	K_d (range)
nNOS + CaM	no ligands	23 μM (19-29)
	2 mM *L*-Arg	65 μM (51-84)
	30 μM H_4B	17 μM (14-22)
	L-Arg and H_4B	61 μM (48-79)
	2 mM *L*-Cit	53 μM (40-69)
	30 μM HO-Arg	14 μM (11-18)
iNOS + CaM	no ligands	86 nM (71-106)
	1 mM *L*-Arg	61 nM (49-75)
	25 μM H_4B	72 nM (57-91)
	L-Arg and H_4B	185 nM (152-225)
	1 mM *L*-Cit and H_4B	260 nM (176-384)
	20 μM HO-Arg and H_4B	236 nM (182-306)
eNOS + CaM	no ligands	5.7 μM (4.4-7.3)
	2 mM *L*-Arg	9.1 μM (7.0-11.5)
	L-Arg and 30 μM H_4B	4.4 μM (3.6-5.3)
W74F + CaM	2 mM *L*-Arg	25 μM (20-31)
W445l + CaM	2 mM *L*-Arg	26 μM (21-31)
Y467F + CaM	2 mM *L*-Arg	16 μM (13-20)

C. Ligand Effects on CaM-Free Full-Length NOS Dimers

To address non-Ca^{2+} activated nNOS dimers, half of the nNOS sample produced from coexpression with CaM (as described above) was handled under conditions that lead to loss of CaM binding. $CaCl_2$ was omitted from the purification, leaving basal buffer levels of Ca^{2+} at approximately 60 μM as previously determined by ICP atomic emission spectroscopic analysis[10]. In activity titrations at this concentration of Ca^{2+}, nNOS has been demonstrated to have less than 5% of the NO· synthesizing activity of the Ca^{2+}-saturated protein (45). In preparation for gel filtration chromatography, CaM was not supplemented and the protein was desalted after the affinity chromatography purification steps. Under these conditions CaM may remain present, but it is likely to be sub-stoichiometrically bound after the several steps of chromatographic preparation. CaM-deficient nNOS had a nearly identical gel filtration chromatograph from that shown in Figure 4-1. The resulting partially CaM-deficient, ligand-free nNOS had a K_d of 42 μM (31-56 μM), Figure 4-9, nearly two-fold weaker than the Ca^{2+}/CaM-saturated protein prepared from the identical expression, Figure 4-6. *L*-Arg supplementation did not alter the stability of CaM-deficient nNOS, and the K_d was 42 μM (34-51 μM). H_4B was however significantly stabilizing, with a K_d of 12 μM (8-16 μM). Interestingly, addition of both *L*-Arg and H_4B gave the most unstable dimeric form, with a K_d of 70 μM (53-92 μM).

[10] This ICP atomic emission spectroscopic analysis was performed by Dr. Ernest Appelhans of Garratt-Callahan Co. (Millbrae, CA).

Figure 4-9. Dissociation constants calculated for CaM-deficient nNOS prepared in the absence of Ca^{2+}/CaM supplementation. Shown are the effects of 2 mM *L*-Arg plus or minus 30 μM H_4B, in comparison to ligand free protein.

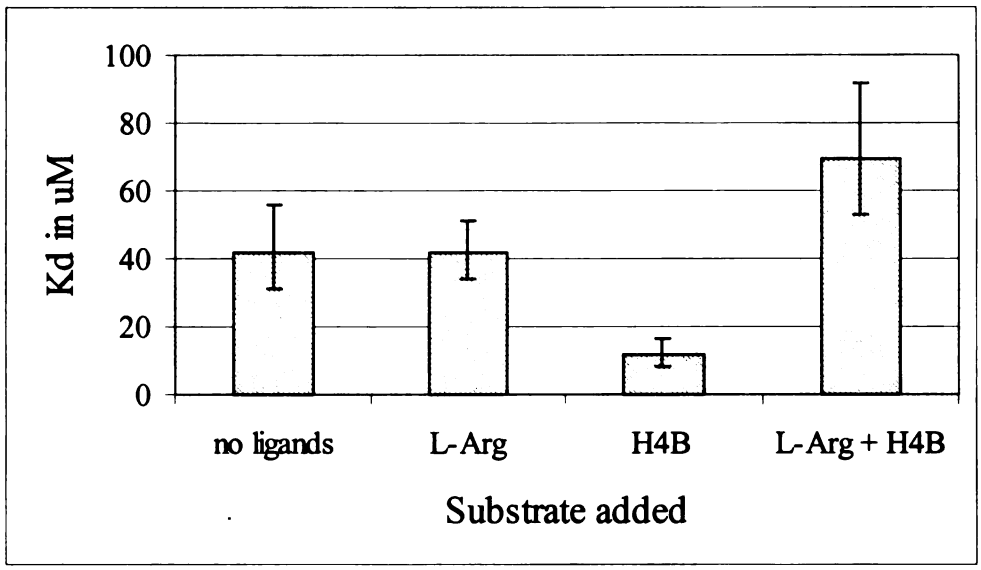

Because of the observed stability of iNOS and instability of eNOS detected under Ca^{2+}/CaM-saturating conditions, we desired protein that was completely naive of CaM for the next step of the analysis. CaM binds irreversibly to iNOS, therefore it was not coexpressed with this protein. For comparison, eNOS was also expressed in the absence of CaM, in spite of previous reports that coexpression with CaM greatly improves iNOS and eNOS yields (91,166). The current results reaffirm these observations, because even in the presence of protease inhibitors, these proteins were heavily degraded and required stringent Ni-NTA agarose, 2',5'-ADP sepharose and gel filtration chromatographic steps to produce a precious amount of CaM-free sample. CaM-free eNOS could be purified in the absence of ligands; however, *L*-Arg was required in the purification of CaM-free iNOS to prevent degradation. In Figure 4-10 are shown the gel filtration profiles for CaM-free eNOS and iNOS in the presence of 2 mM *L*-Arg. The Stokes radii calculated for these species are listed in Table 4-1.

Figure 4-10. Gel filtration profiles for bovine eNOS (A) and murine iNOS (B) expressed in the absence of CaM, and purified in the presence of *L*-Arg. Stokes radii are listed in Table 4-1.

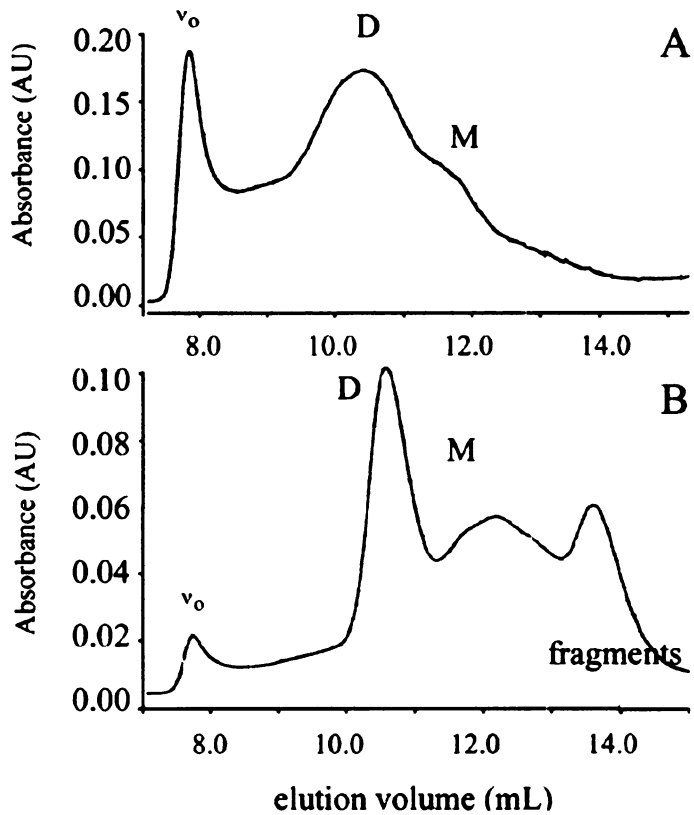

In the absence of CaM, iNOS dimers are considerably weakened relative to the CaM-bound form. In the presence of *L*-Arg alone, the K_d is 1.3 μM (1.0-1.7 μM range). In the presence of *L*-Arg and H_4B, this value does not change significantly, and the K_d is 1.5 μM (1.2-2.0 μM range), Figure 4-11. eNOS in the absence of CaM is surprisingly more stable than it was when CaM-bound, Figure 4-11. Ligand-free, CaM-free eNOS has a K_d of 0.88 μM (0.66-1.17 μM range). *L*-Arg-bound CaM-free eNOS has a K_d of 0.62 μM (0.47-0.81 μM), a value not statistically significant from the previous ligand free value. In the presence of both *L*-Arg and H_4B, the K_d is stabilized almost 10-fold to 0.09 μM (0.06-0.13 μM range). Again, in the presence of H_4B alone, spectral changes

indicated loss of signal, and appropriate data fits could not be made. An overall trend is apparent, especially in the *L*-Arg plus H_4B-bound state that eNOS is a tighter dimer than iNOS, and nNOS is the weakest dimer, Table 4-3.

Figure 4-11. Dissociation constants calculated for iNOS (dashed grey bars) and eNOS (white bars) completely naive of CaM. Shown are the effects of 1 mM *L*-Arg plus or minus 25 μM H_4B. Also shown is the K_d for eNOS bound to residual imidazole (Imd); ligand-free iNOS could not be purified.

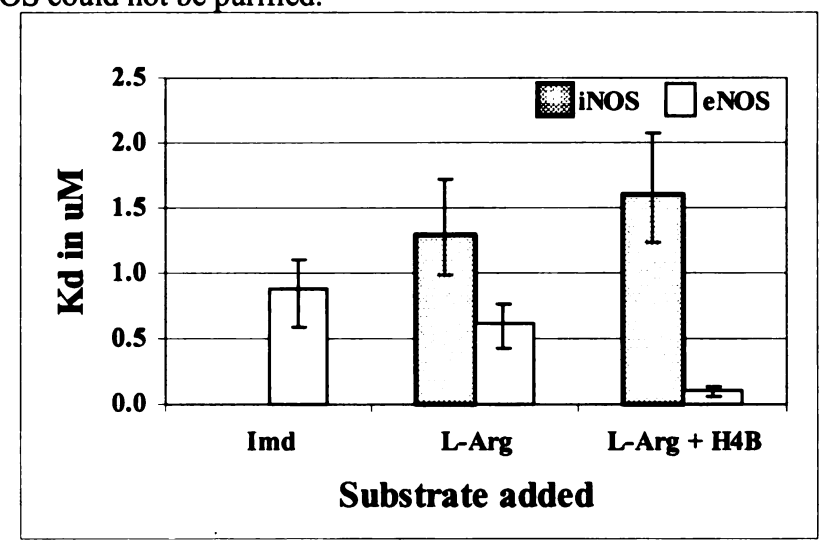

Table 4-3. K_d values of CaM-free NOS measured by sedimentation equilibrium analysis.

Protein	conditions	K_d (range)
nNOS - CaM	no ligands	42 μM (31-56)
	2 mM *L*-Arg	42 μM (34-51)
	30 μM H_4B	12 μM (8-16)
	L-Arg and H_4B	70 μM (53-92)
iNOS - CaM	1 mM *L*-Arg	1.3 μM (1.0-1.7)
	L-Arg and H_4B	1.5 μM (1.2-2.0)
eNOS - CaM	no ligands	0.88 μM (0.66-1.17)
	2 mM *L*-Arg	0.62 μM (0.47-0.81)
	L-Arg and 25 μM H_4B	0.09 μM (0.06-0.13)

D. CaM-Bound eNOS Subdomain Hydrodynamic Analysis

It has been reported by Venema *et al.* that significant interactions occur between eNOS reductase domains and reductase or oxygenase domains in yeast-two-hybrid analyses (109). This was the only evidence for potential interactions beyond those known at the oxygenase dimeric interface that may affect the behavior of eNOS in the full-length assays. We therefore undertook analysis of the eNOS oxygenase and reductase domains to analyze these components of dimerization individually for dimerization affinity dependence upon CaM-binding.

1. eNOS oxygenase domain

The eNOS oxygenase domain was coexpressed with CaM and prepared in the absence of ligands so as to be able to analyze their effects on dimerization. In Figure 4-12 is shown the gel filtration chromatogram of CaM-bound eNOS oxygenase domains in the absence of ligands. The experimental R_S for this peak is 50.2 Å, and that for the shoulder is 38.5 Å. The main peak as well as the early peaks in the 280 trace were collected and re-injected onto the column, but only the dominant peak re-equilibrated to the expected elution profile, Figure 4-12 inset. The main peak had a split Soret at 410 and 390 nm indicative of mixed-spin NOS bound partially to water, that shifted to 398 nm with *L*-Arg binding, consistent with spectra previously reported (244). *L*-Arg binding had a K_s in the absence of pterin of 2.3 μM similar to wild-type eNOS (115).

Figure 4-12. Gel filtration chromatogram for eNOS oxygenase domain recorded at 400 and 280 nm. The A280 trace indicates the presence of other proteins, but the dominant species is apparent from the heme signal, and further experiments used detection at the Soret.

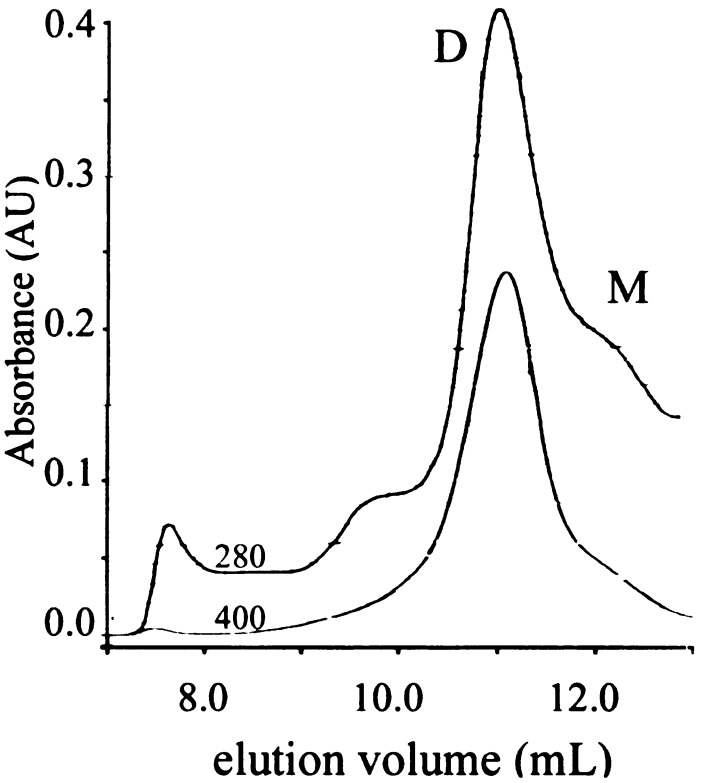

The main peak from gel filtration was collected for sedimentation analysis, with detection at 400 nm to avoid contaminants that are observed in the 280 nm trace of Figure 4-12. To test for the appropriate association model, the sedimentation velocity experiments were performed first. The program SedFit, used to model this data with a continuous distribution C(S) model, identified two distinct species, Figure 4-13. The standardized sedimentation coefficients for these species were calculated to have $S^0_{w,20}$ of .3.7 and 6.8 Svedbergs (S), respectively, using the program Sednterp. The 6.8 S species corresponded very nicely to the CaM-bound eNOS dimer when the given mass of the dimer was employed in the calculation, with a calculated R_S value of 51.9 Å (observed as

50.2 Å by gel filtration). Importantly, when the mass of the tetramer was input, the R_S value estimated became unreasonable given our gel filtration analysis, R_S ~190 Å. The 3.7 S species was minor, and was consistent with monomer, not dimer. Given the input mass of CaM-bound dimer, the Sednterp calculated R_S was again too high, 51.9 Å; CaM-free monomer gave, R_S = 37.3 Å; and for CaM-bound monomer, R_S = 48.2 Å. The former monomeric value fit better to that observed by gel filtration, 38.5 Å. Therefore, the dominant peaks were assigned as CaM-free monomer and CaM-bound dimer from sedimentation velocity analysis.

Figure 4-13. Continuous C(S) analysis of a sedimentation velocity experiment for eNOS oxygenase domain coexpressed with CaM but in the absence of ligands. The sample was prepared in 50 mM TRIS, 200 mM NaCl, 10% glycerol and 2 mM $CaCl_2$, without added ligands, at a temperature of 20 °C.

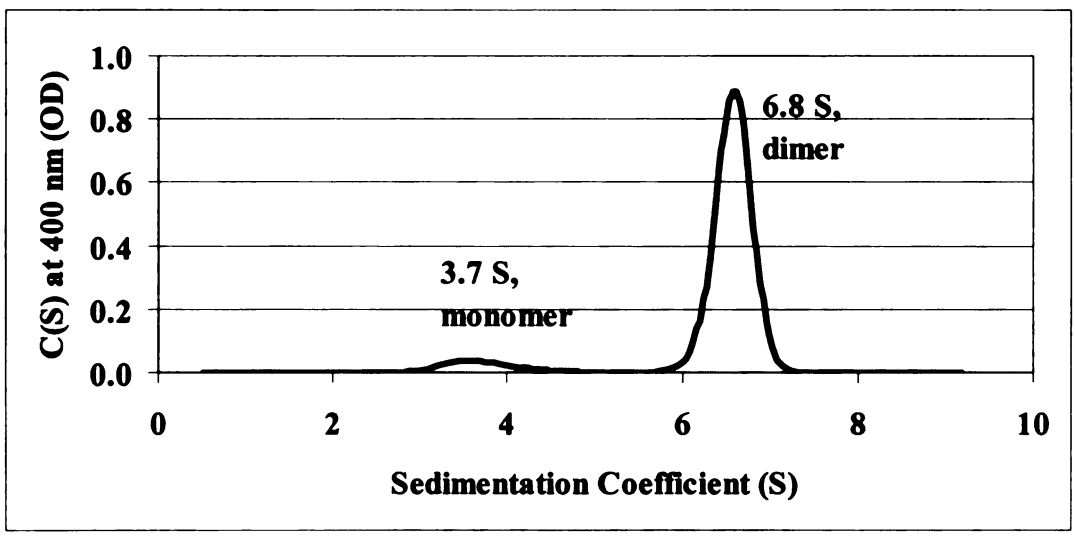

To determine the dissociation constant for this observed monomer-dimer distribution, sedimentation equilibrium analysis was performed on these samples under conditions identical to those described for full-length eNOS. The equilibrium sedimentation experiment was prepared at concentrations similar to those used for the velocity sedimentation analysis (5 μM), with detection at the Soret band and with no added ligands. The data fits well to a monomer-dimer model and gave a K_d of 0.10 μM (range 0.07-0.14 μM), Figure 4-14. Interestingly, the equivalent construct of the iNOS oxygenase domain, $iNOS_{1-531}$ in the presence of CaM, had much higher K_d values in the μM realm. With no added ligands, the K_d of CaM-bound $iNOS_{1-531}$ was 10.5 μM (9.1-12.2 μM), and with added *L*-Arg, the K_d was unchanged at 8.8 μM (7.6-10.1 μM). Thus, unlike the full-length CaM-bound constructs, eNOS oxygenase dimers are tighter than iNOS, in agreement with previous studies (227).

Figure 4-14. Sedimentation equilibrium fits of CaM-bound $eNOS_{oxy}$ in the absence of ligands. Nine conditions were measured at three velocities and three concentrations with detection at 415 nm. Shown here is the monomer-dimer fit, resulting in a K_d of 0.10 μM. Graphing was done as described for Figure 4-3.

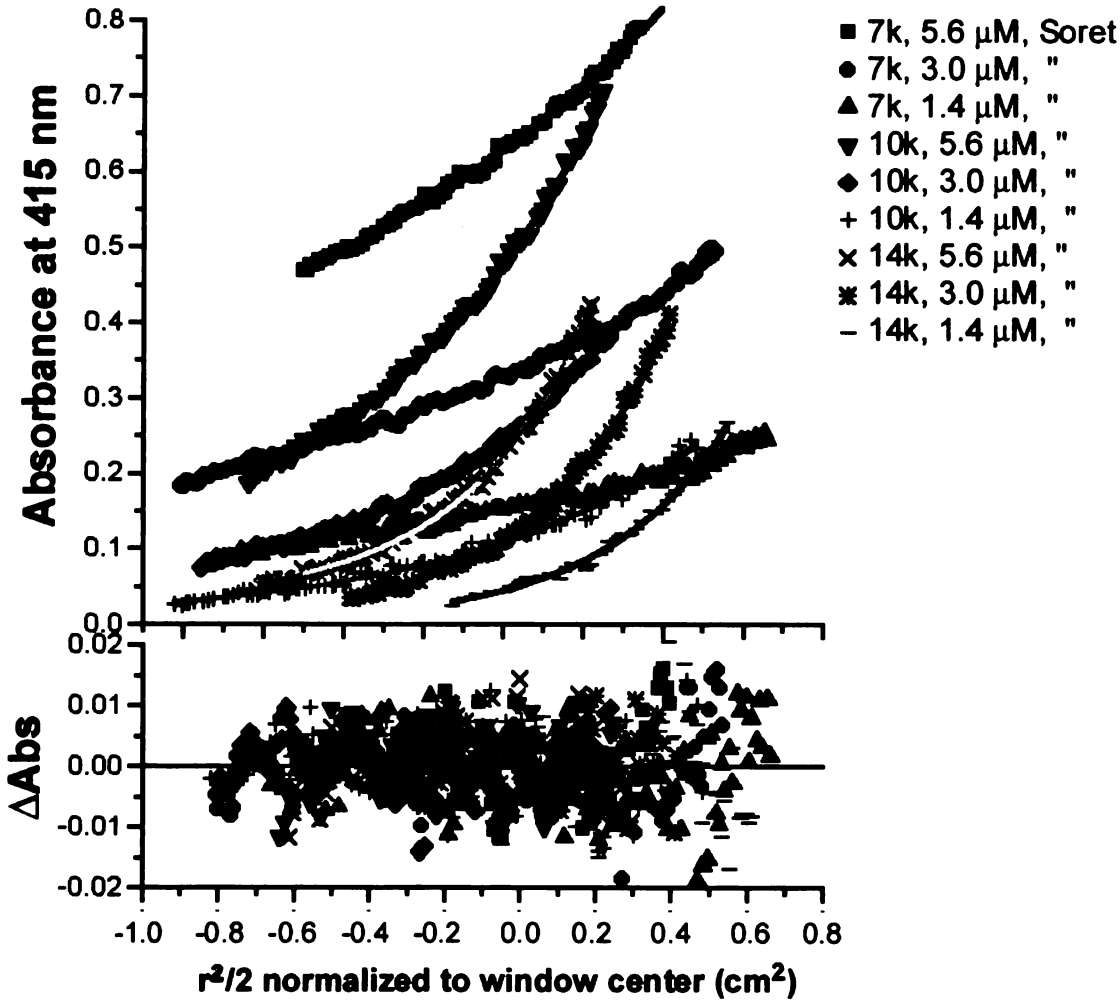

2. eNOS REDUCTASE DOMAIN

The eNOS reductase domain was coexpressed with CaM, and prepared in the presence of 2 mM *L*-Arg, 2 μM H_4B, and 20 μM DTT. This $eNOS_{red}$ was analyzed under aerobic conditions, and therefore in the oxidized form. UV-Vis spectra of the sample were identical to those reported for the nNOS reductase domain (186). The sample was analyzed by gel filtration chromatography and found to elute as two species, Figure 4-15, with an apparent R_S of 43.5 and 54.2 Å. Using the program HydroPro, models of the eNOS reductase domain dimer (as in the crystal structure of CPR, PDB: 1AMO) with the structure of CaM placed onto its predicted recognition site (as in Figure 3-5) had an R_S value of 46.5 Å, a value to be treated as a lower limit, due to missing residues in the AI element.

Figure 4-15. Gel filtration profile for CaM-bound $eNOS_{red}$.

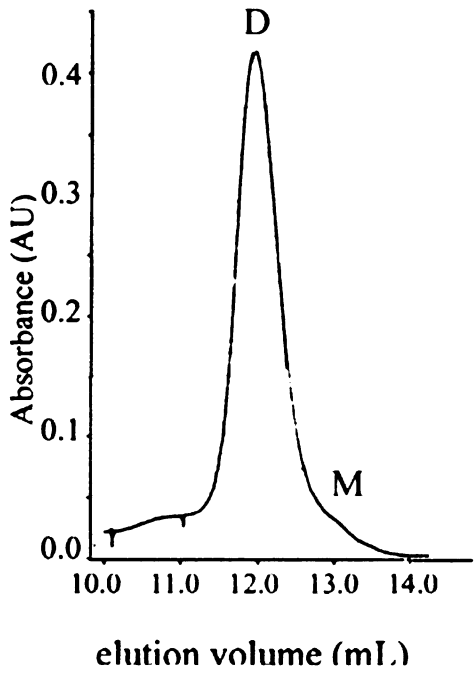

The dominant peak in the gel filtration chromatogram was collected for further analysis. Analysis by sedimentation velocity using a continuous distribution C(S) model revealed the presence of two distinct species in the sample, Figure 4-16. The standardized sedimentation coefficients for these two species, $S^0_{w,20}$ of 5.3 and 8.0 S, were calculated from the observed values using the program Sednterp. The first species at 5.3 S was assigned as CaM-bound $eNOS_{red}$ monomer, based on Sednterp calculations resulting in a calculated R_S of 43.5 Å, a perfect match to the 43.5 Å value observed by FPLC analysis. The second species at 8.0 S, corresponded to the gel filtration species at R_S of 54.2 Å and was assigned to a dimer. When the fully CaM-bound dimer molecular weight was input into this calculation, R_S was 57.9 Å, and when the molecular weight of CaM-free dimer was input, the R_S was 47.3 Å. Therefore, it is expected that this dimeric reductase species is partially CaM-deficient. Analysis of the same sample by sedimentation equilibrium fitted well to a monomer-dimer model, shown in Figure 4-17. Fifteen scans were fit to a monomer-dimer model, and resulted in a K_d of 24 μM (19-25 μM range), Figure 4-18. CaM-bound $eNOS_{red}$ was also separated by size exclusion chromatography in the absence of Ca^{2+} and with 3 mM EGTA treatment to remove CaM. Sedimentation equilibrium analysis of this CaM-deficient $eNOS_{red}$ resulted in a K_d of 40 μM (32-49 μM range).

Figure 4-16. Continuous distribution analysis of sedimentation velocity scans of $eNOS_{red}$, with standardized sedimentation coefficients $S^0_{w,20}$ of 5.3 and 8.0 S labeled at the monomeric (M) and dimeric (D) peaks.

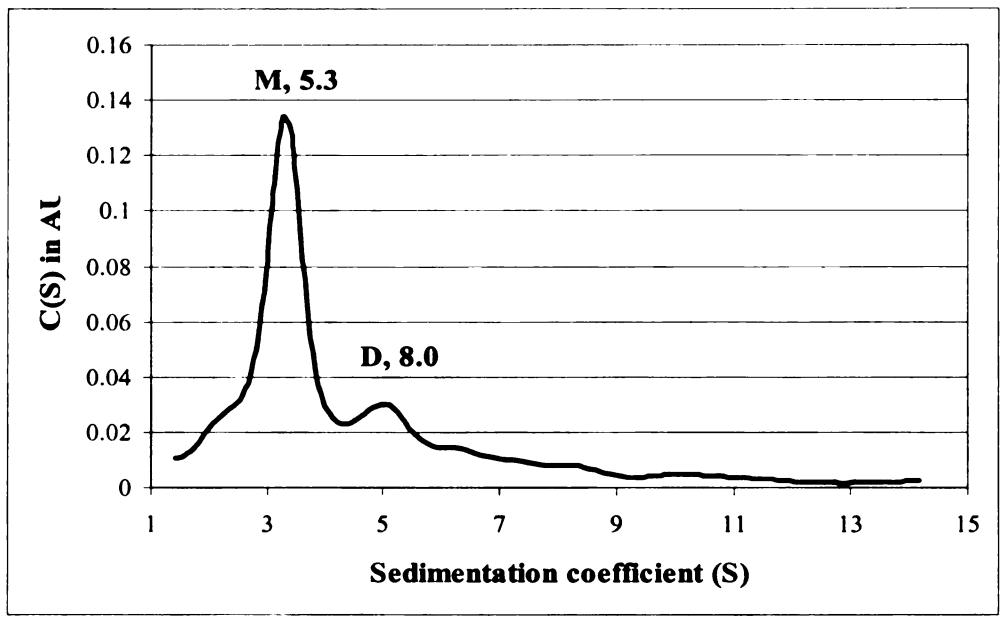

Figure 4-17. A sample radial scan of $eNOS_{red}$.in the presence of CaM is shown (black dots), compared with three curves representing the distribution expected for monomer, dimer, and trimer. This radial scan was recorded at 290 nm, during a 10,000 rpm sedimentation equilibrium experiment at 4 °C, in buffer containing 50 mM TRIS pH 7.6, 200 mM NaCl, 10 % glycerol, plus 2 mM $CaCl_2$ and 2 mM *L*-Arg. Calculations were performed as in Figure 4-3, using sigma values of 1.142 for monomer, 2.284 for dimer, and 3.426 for trimer.

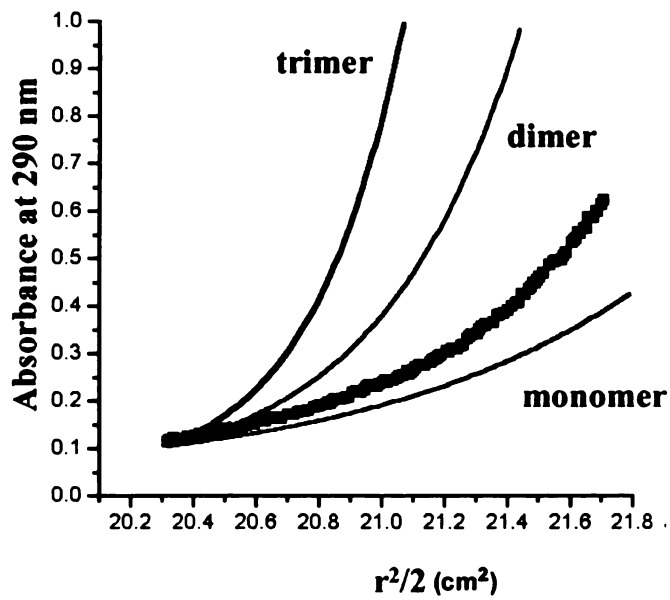

Figure 4-18. Sedimentation equilibrium fits of CaM-bound $eNOS_{red}$ in the absence of ligands. Fifteen conditions were measured at three velocities and five concentrations with detection at 290 nm. Shown here is the monomer-dimer fit, resulting in a K_d of 23 μM. Graphing was done as described for Figure 4-3.

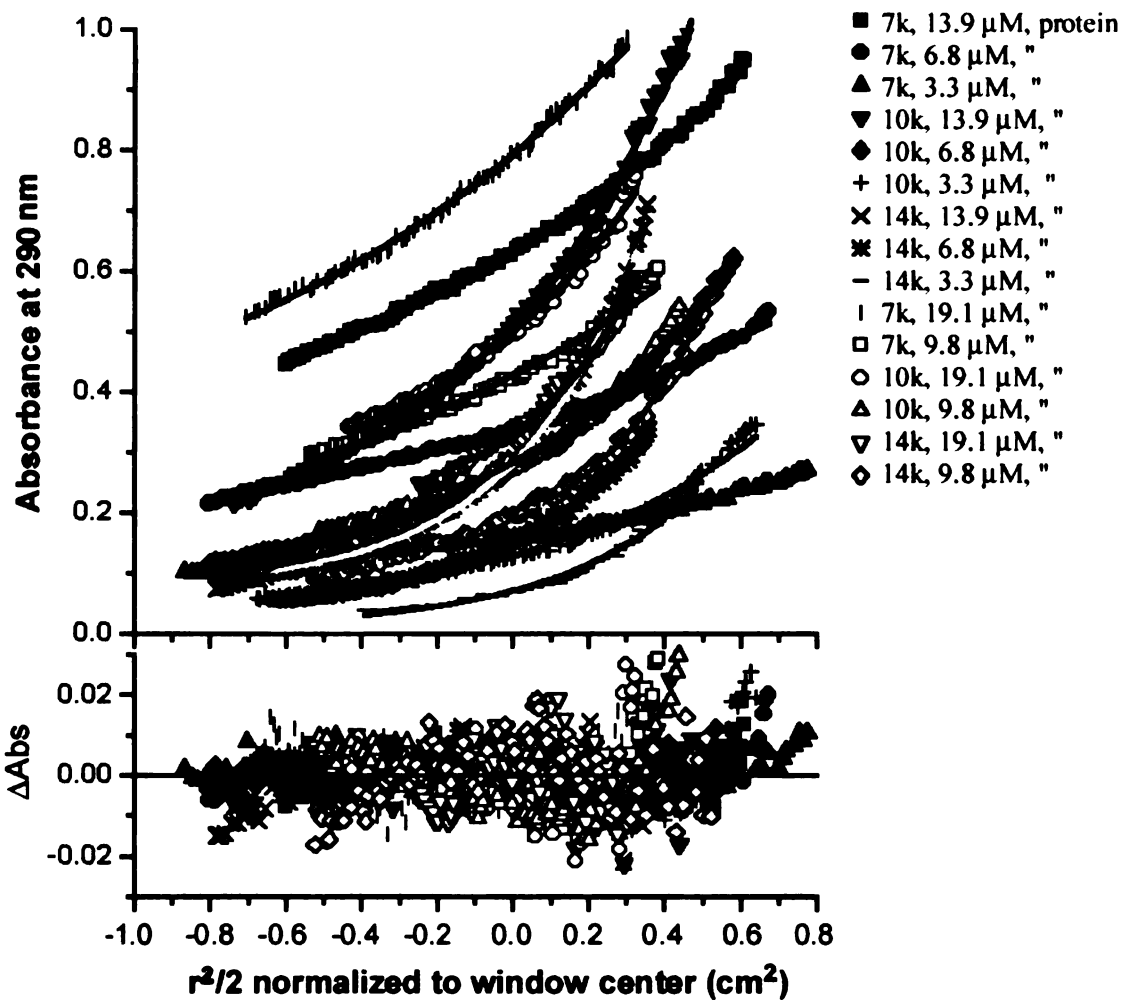

E. CaM-free eNOS and iNOS Oxygenase domain Dimerization

Using the same analysis procedure as described above, sedimentation equilibrium analysis was performed on the eNOS and iNOS oxygenase domain constructs in the absence of CaM. eNOS oxygenase domains expressed in the absence of CaM had approximately the same dimer stabilities as full-length CaM-free eNOS. The ligand free eNOS oxygenase domain had a K_d of 1.4 μM (1.2-1.7 μM range). The addition of *L*-Arg did not alter the dimer affinity significantly, with a K_d of 1.2 μM (1.0-1.4 μM). Nor did H_4B alone, K_d = 1.8 μM (1.6-2.1 μM), or in the presence of *L*-Arg, 1.7 μM (1.4-2.0 μM) alter the dimer affinity, Figure 4-19. This might have been expected, since eNOS is known to be able to dimerize in the absence of pterin (136). The interesting data to consider is the difference between the *L*-Arg/H_4B bound forms of the full-length versus the oxygenase domain construct of eNOS.

Figure 4-19. Dissociation constants calculated for CaM-free eNOS oxygenase domain from sedimentation equilibrium analysis. Shown are the K_d values for ligand-free, 1 mM *L*-Arg, 25 μM H_4B, or both *L*-Arg and H_4B-bound conditions.

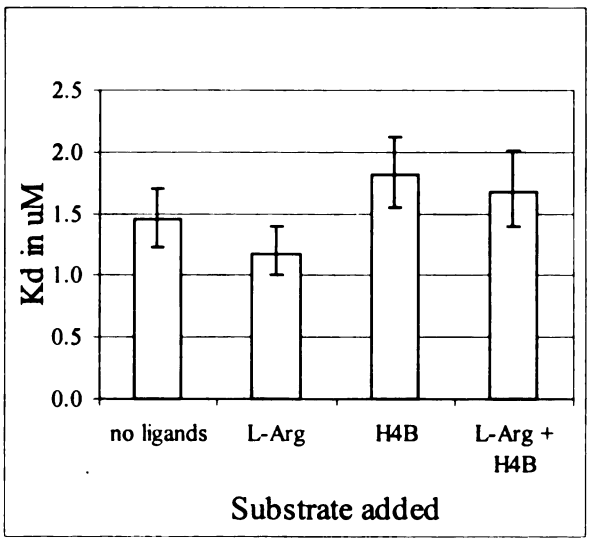

$iNOS_{1-495}$ that was expressed in the absence of CaM had K_d values in two realms, low-μM or mid-nM, depending on the ligands present. CaM-free iNOS oxygenase domains in the absence of ligands have a weak K_d of 4.6 μM (4.0-5.5 μM range). The addition of H_4B stabilizes this dimer by two-fold, K_d = 2.4 μM (2.1-2.9 μM). However, upon addition of *L*-Arg alone or in the presence of H_4B, the dimerization affinity is significantly improved, K_d = 0.16 μM (0.12-0.22 μM) or 0.14 μM (0.11-0.18 μM) respectively, Figure 4-13. Therefore, *L*-Arg binding shifts dimerization affinity to a tighter value, and pterin has only a mild effect that is observable in the *L*-Arg-free case. $iNOS_{1-531}$ in the absence of CaM was significantly destabilized and could not be analyzed.

Figure 4-20. Dissociation constants of CaM-free iNOS oxygenase domain without the CaM-recognition element, calculated from sedimentation equilibrium analysis. Shown are the K_d values for ligand-free conditions compared with 1 mM *L*-Arg and 25 μM H_4B, alone or together.

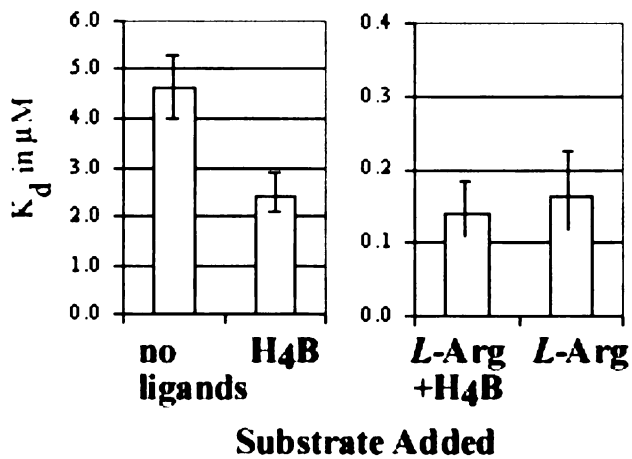

The K_d values measured for the eNOS and iNOS subdomain constructs are summarized in Table 4-4. In the ligand-free case, eNOS oxygenase dimers are tighter than the iNOS dimers, whether or not CaM is bound. eNOS oxygenase domains are

stabilized by CaM binding, but not by ligand binding. On the other hand, iNOS oxygenase domains are destabilized by CaM, but stabilized by *L*-Arg, with or without H_4B present. Finally with the completion of this table, a free energy relationship for dimerization in full-length eNOS can be derived, showing that CaM binding is stabilizing to both the oxygenase and reductase domains of eNOS, and that CaM is destabilizing to the full-length CaM bound eNOS complex.

Table 4-4. K_d values of eNOS and iNOS subdomains in the presence or absence of CaM.

Protein	conditions	K_d (range)
$eNOS_{oxy}$ + CaM	no ligands	0.10 μM (0.07-0.14)
$eNOS_{red}$ + CaM	no ligands	24 μM (19-25)
$eNOS_{red}$ - CaM	no ligands	40 μM (32-49)
$iNOS_{1-531}$ + CaM	no ligands	10.5 μM (9.1-12.2)
	1 mM *L*-Arg	8.8 μM (7.6-10.1)
$eNOS_{oxy}$ - CaM	no ligands	1.4 μM (1.2-1.7)
	2 mM *L*-Arg	1.2 μM (1.0-1.4)
	30 μM H_4B	1.8 μM (1.6-2.1)
	L-Arg and H_4B	1.7 μM (1.4-2.0)
$iNOS_{1-495}$ - CaM	no ligands	4.6 μM (4.0-5.5)
	2 mM *L*-Arg	0.16 μM (0.12-0.22)
	30 μM H_4B	2.4 μM (2.1-2.9)
	L-Arg and H_4B	0.14 μM (0.11-0.18)

V. DISCUSSION

This work is the first to report quantitative measurements of the K_d for NOS dimerization, and the significant effects of ligands and CaM upon dimer stability. The experiments described here begin with heme-bound dimeric protein, collected as the dimeric fraction in NOS preparations by gel filtration chromatography. Heme, in addition to *L*-Arg and H_4B, is required to reassemble and dimerize urea-treated iNOS (111) or nNOS monomers (245). Heme-free protein is expected to be significantly unfolded and destabilized, as observed in baculoviral expressions of nNOS in the presence of ferrochelatase inhibitors and in heme chemical extraction assays with holo NOS (G. Knudsen, *unpublished results*). Therefore we began our studies with heme-bound protein that can dimerize for certain, and we explored CaM, *L*-Arg and H_4B conditions for their effects on dimer stability. The equilibrium diagram in Figure 4-21 shows the connection of the K_d of dimerization with ligand and CaM binding.

In the CaM-free condition, eNOS is the tightest dimer consistent with previous kinetic stability analyses (109,246), and the K_{d1} (Figure 4-21) value was 0.88 μM. The unexpected result was that nNOS was the weakest dimer, with K_{d1} of 42 μM. If both eNOS and nNOS are expressed at similar low concentration levels, K_{d1} would be a significant factor for eNOS dimerization, but not for nNOS, since the cellular concentration of nNOS is on the order of 0.1 μM (*e.g.* human cerebellum (247)) and the cytosolic concentration of eNOS would be expected to be lower due to sequestration in

caveolae (58). K_{d1} for full-length iNOS could not be measured; however, the truncated $iNOS_{1-495}$ construct had an intermediate K_{d1} value of 4.6 μM.

Figure 4-21. Equilibrium diagram describing dimerization in the presence of CaM (blue spheres) and ligands such as *L*-Arg and H_4B (red triangles). The NOS subunit is drawn schematically with a brown sphere for the oxygenase domain and a green sphere for the reductase domain.

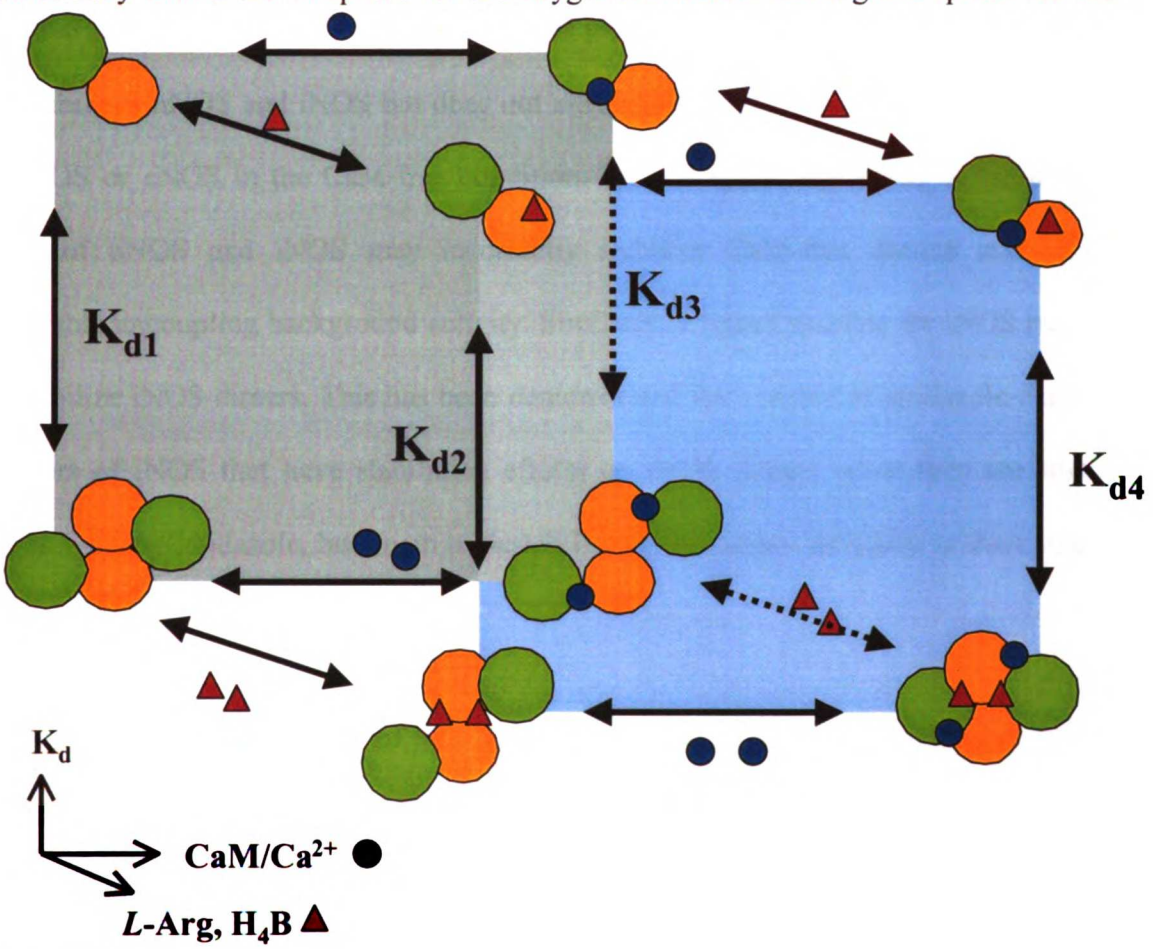

Next to be considered are ligand effects on K_{d2} in Figure 4-21. *L*-Arg did not stabilize K_{d2} for CaM-free nNOS, eNOS, or $eNOS_{oxy}$; however, it did stabilize $iNOS_{1-495}$ relative to the ligand-free case by greater than 30-fold to 0.16 μM K_{d2}. H_4B stabilizes the CaM-free dimer in full-length nNOS nearly four-fold over the ligand-free form, consistent with the extensive structural contacts formed between subunits of the dimer by

H_4B (41,42,248). Pterin also stabilizes the dimers of ligand-free $iNOS_{1-495}$ by approximately two-fold, to 2.4 μM, Figure 4-13. CaM-free $eNOS_{oxy}$ was analyzed in place of the full-length CaM-free eNOS (that displayed anomalous loss of signal) for comparison of K_{d2} and K_{d1}. CaM-free $eNOS_{oxy}$ had a K_{d1} of 1.4 μM in the ligand-free state, and was not stabilized by the addition of pterin, with a K_{d2} of 1.8 μM. Therefore, H_4B stabilizes nNOS and iNOS but does not alter eNOS, and *L*-Arg stabilizes iNOS but not nNOS or eNOS in the CaM-free condition. Thus a ligand that binds in the pterin-pocket of nNOS and iNOS may incorrectly stabilize CaM-free dimers and allow undesirable uncoupling background activity. Similarly, a ligand specific for iNOS may in fact stabilize iNOS dimers. This has been demonstrated for a series of imidazole-derived inhibitors of iNOS that have stabilizing effects on iNOS dimers when they are small, such as 1-phenylimidazole, but begin to destabilize iNOS dimers sterically as their size is increased (113).

Finally, in the presence of both *L*-Arg and H_4B, the dimers of CaM-free eNOS were significantly stabilized over the ligand-free form, with a K_{d2} of 0.09 μM. However, dimers of $eNOS_{oxy}$ were not stabilized from the ligand free form, satisfying the comparisons observed in previous studies (227). These results suggest that the presence of reductase in eNOS affects the ability of *L*-Arg and H_4B-binding to stabilize eNOS dimers, an important point that will be discussed later. Full-length nNOS with both *L*-Arg and H_4B present was destabilized relative to the ligand-free form. $iNOS_{495}$ was stabilized relative to the ligand-free condition, but unchanged relative to the *L*-Arg bound condition. Likewise, full-length CaM-free iNOS in the presence of *L*-Arg and H_4B had a K_d of 1.5 μM that was unchanged from the *L*-Arg-bound condition, with a K_d of 1.3 μM. Thus no

cooperative effect of *L*-Arg and H_4B stabilization of nNOS or iNOS dimers was observed under thermodynamic conditions as would have been expected from kinetic observations (227). Yet, CaM-free eNOS dimers were stabilized by the addition of H_4B to the *L*-Arg-bound protein.

CaM-binding effects on dimerization are the next comparisons to be made, between K_{d3} and K_{d1} in the ligand-free form, and K_{d4} and K_{d2} in the ligand-bound form, shown in Figure 4-21. CaM-bound eNOS is destabilized relative to CaM-free, yet nNOS is slightly more stable in the CaM-bound form. The K_d of eNOS is increased by six-fold, whereas the K_d for nNOS is decreased approximately two-fold, when compared to the CaM-free, ligand-free condition. Thus, the K_{d3} pathway in nNOS is slightly more stabilized relative to the K_{d1} pathway, but the converse is true for eNOS.

Surprisingly, iNOS is the tightest CaM-bound dimeric form of NOS. Full-length ligand-free iNOS dimers are greatly stabilized in the presence of CaM, with K_{d3} of 86 nM, compared to an un-measurable value for destabilized and degraded protein. Recent work has for the first time demonstrated the formation of "undisruptable" SDS- and boiling-resistant iNOS dimers (249) in eukaryotic systems that are distinct from the population of dissociable dimers extensively studied from *E. coli* sources such as ours. Formation of these iNOS dimers was dependent upon Zn^{2+}, but unaffected by deficiency in H_4B. Indeed, in our dimer stability measurements of CaM-bound pterin-free iNOS, the K_d was not significantly stabilized by pterin compared to the ligand-free form. By ICP atomic emission spectroscopic analysis, iNOS obtained by our preparation methods is replete in Zn^{2+}, and contains 2.5 equivalents[10] of Zn per monomer. Due to the stability of

the undisruptable iNOS dimers to boiling in Laemmli buffer (249), it is likely that these dimers are covalently linked via a non-reducible bond. Within a eukaryotic system (249), iNOS would be replete with cofactors and CaM, thus allowing tight dimerization (as observed here) as well as production of oxidative radicals. Thus it is concievable that oxidatively-formed covalent bonds could be generated between subunits, creating undisruptable dimers. The undisruptable iNOS dimers have demonstrably increased NO activity (249) over reversible dimers; therefore, this covalent crosslinking may be of true physiological relevance.

The effects of ligands on CaM-bound NOS differ from the patterns observed with CaM-free NOS, comparing K_{d2} and K_{d4} in Figure 4-21. Instead of having no effect as in the CaM-free condition, *L*-Arg now destabilizes nNOS and eNOS dimers by approximately two-fold from the ligand-free state. *L*-Cit destabilized CaM-bound nNOS to a similar extent as *L*-Arg; however, HO-Arg at low μM concentration was stabilizing. Whereas *L*-Arg significantly stabilized the CaM-free dimers of iNOS, this stabilization was no longer statistically significant for CaM-bound iNOS in either the full-length or $iNOS_{531}$ forms. Therefore, the ideal dimerization inhibitors may indeed bind at the heme pocket and effectively disrupt dimerization in all three NOS isoforms.

Similarly, the stabilization effect of H_4B on nNOS and iNOS in the CaM-free proteins was no longer statistically significant in the CaM-bound proteins. Pterin alone caused significant loss of signal for full-length eNOS in the CaM-bound form and could not be measured by the sedimentation equilibrium methods used here. The dimer stabilization effects of *L*-Arg or H_4B are apparently blocked in CaM-bound NOS. It is

known that CaM-induced changes in conformation stimulate electron transfer activity. Thus, the lost stabilization effects of *L*-Arg or H_4B physiologically could be a result of the conformational controls of dimerization designed to reduce the uncoupled production of superoxide and consumption of NADPH in the absence of one or the other ligands.

In the presence of both *L*-Arg and H_4B, the dimers of CaM-bound nNOS were destabilized relative to the ligand-free CaM-bound dimers, with a similar 2-fold increase in the K_d to that observed for the CaM-free form. The K_d for CaM-bound eNOS was not significantly reduced, compared to the K_d of the CaM-free form that was stabilized by nearly ten-fold. iNOS dimers in the CaM-bound form were destabilized in the presence of *L*-Arg and H_4B compared to ligand-free dimers, a reversed trend from CaM-free $iNOS_{1-495}$ that was stabilized by nearly ten-fold under these conditions. When *L*-Cit or HO-Arg were combined with H_4B in place of *L*-Arg, the CaM-bound iNOS dimers were similarly destabilized.

Dimerization is required for CaM-stimulated generation of superoxide by nNOS and eNOS, because electron transfer occurs in a *trans* mode between subunits, and superoxide production is heme-catalyzed in these proteins (221-223). From this work it has been shown that H_4B stabilizes nNOS dimers in the CaM-free and -bound forms. Thus, the tightening of the dimer could partially account for reduced production of superoxide and increased reduction of the oxyferrous form to produce hydrogen peroxide (224). *L*-Arg also has a diminishing effect on superoxide production; however, dimer stabilization by *L*-Arg is not statistically significant in CaM-bound nNOS. Therefore, the *L*-Arg effects on blocking superoxide production are likely heme-site electronic effects,

and it appears that the weaker dimer form displays improved superoxide production. Similarly, weaker eNOS dimers appear to favor superoxide production, since CaM-binding destabilizes dimers and stimulates superoxide production. We have also shown that *L*-Arg binding to eNOS has no statistically significant effect on dimerization, consistent with the non-effect of *L*-Arg upon superoxide production (221).

From the above experiments it was determined that CaM was destabilizing to dimers of full-length eNOS but not to dimers of $eNOS_{oxy}$; therefore, we dissected the dimerization interactions between oxygenase and reductase domains in the presence or absence of CaM, Figure 4-22. The free energy of dimerization is calculated using the formula $\Delta G = -RTln(K_d)$, calculated at 37 °C. From the values observed, the free energy contributions from the oxygenase domain, reductase domain, and CaM components can be derived. The free energy (ΔG) of dimerization for the eNOS oxygenase domain is -8.3 kcal/mol, and with CaM bound the free energy is -9.9 kcal/mol. The ΔG of dimerization for the eNOS reductase domain is -6.2 kcal/mol, and with CaM bound the free energy is -7.4 kcal/mol. Thus, the free energy difference, $\Delta\Delta G$, calculated for CaM stabilization of oxygenase domain dimerization is -1.6 kcal/mol, and of reductase domain dimerization is -0.4 kcal/mol. However, CaM is *de*stabilizing to full-length eNOS by 1.2 kcal/mol, a seemingly contradictory result.

From the free energies of dimerization compared between the subunits and the full-length proteins, it is apparent that another term is required to equate the total free energy with the sum of its components. This term is an entropy term, $-T\Delta S$, solved using the formula: $\Delta G_{tot} - \Delta G_{oxy} + \Delta G_{red} = -T\Delta S$. The entropic cost of dimerization for CaM-

bound full-length protein is 7.4 to 8.7 kcal/mol and for CaM-free NOS is 5.9 kcal/mol. Bringing four components together, two NOS subunits and two CaM molecules, is entropically more costly than bringing two NOS components together. Thus dimerization of NOS is a sum of both thermodynamic and kinetic components, and the results presented here from thermodyamic analyses are complementary to kinetic stability analyses.

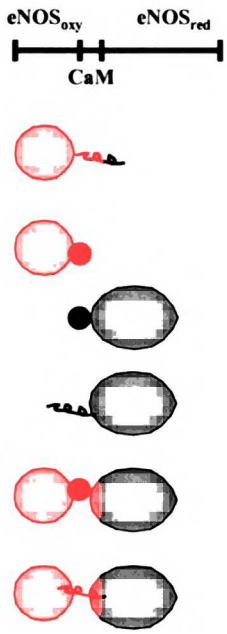

K_d (μM)	ΔG (kcal/mol)
1.4 (1.2 - 1.7)	-8.3 ± 0.1
0.10 (0.07 - 0.14)	-9.9 ± 0.2
24 (19 - 25)	-6.6 ± 0.1
40 (32 - 49)	-6.2 ± 0.1
5.7 (4.4 - 7.3)	-7.4 ± 0.2
0.88 (0.66 - 1.17)	-8.6 ± 0.2

Figure 4-22. Table of free energies calculated for eNOS$_{oxy}$ (brown), eNOS$_{red}$ (green) and full-length eNOS dimerization in the presence or absence of CaM (blue).

Using the same analysis, the free energy cost of mutating W445L or W74F is 0.6 kcal/mol, and Y467F is 0.3 kcal/mol. W445 is a pterin-binding residue previously characterized as an alanine mutant of iNOS, constructed as residues 1-498, and found to contain less than 10% dimer by gel filtration (250). W74 is part of the N-terminal beta-hairpin motif of NOS oxygenase domains that has been shown to swap between subunits (251). Finally, Y467 is connected to the pterin-binding helical lariat at its base (42), thus

it would be sensitive to dynamic changes in dimeric interactions but would not be expected to contribute significantly to the enthalpy of the dimeric interaction between oxygenase domains, Figure 4-23.

Figure 4-23. Location of the aromatic mutants of eNOS within the oxygenase domain dimeric structure, 4NSE (42).

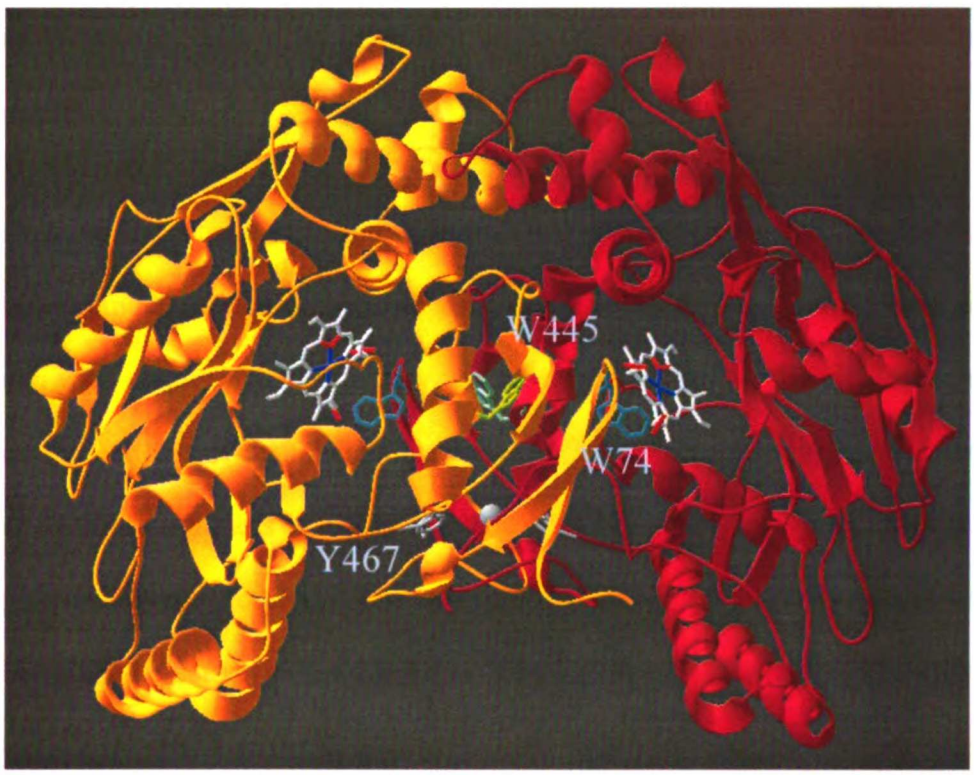

Each of these aromatic residues can serve as probes for the various elements involved in dimerization at the oxygenase interface, the helical-lariat, the N-terminal beta-hairpin, and H_4B dimerization stability, Figure 1-9. The conservative changes (rather than complete removal of the sidechain to alanine) made here to the buried surface area in these mutants are not expected to alter the thermodynamics of dimerization at the dimeric interface significantly; however, by their location within in the flexible elements involved in dimerization, any changes to the K_d would be expected to contribute to the entropic costs of dimerization. We find that these mutations are not severe effectors of

dimerization enthalpy or entropy, since the K_d values observed are altered by less than 1 kcal/mol in stability for these mutants. Thus, we expect that the entropy involved in dimerization of eNOS oxygenase domains in the absence of pterin is not the main contributor to the observed ~7.5-8.7 kcal/mol value for $T\Delta S$. Instead, it is likely that this entropy is a sum of the chain entropy of assembling the multi-domain NOS complex and an assembly entropic cost of bringing four separate subunits together in the fully active NOS complex.

This work contributes to the understanding of ligand-control of dimerization by direct measurement of thermodynamic dissociation constants in buffers that simulate catalytic *in vitro* conditions. In summary, we have demonstrated that CaM has significant effects on the patterns of ligand stabilization of NOS dimers. In the CaM-free condition, the order of dimer tightness is eNOS < iNOS < nNOS, from tightest to weakest. CaM-binding is destabilizing to eNOS, but is significantly stabilizing to iNOS, and nNOS is slightly stabilized relative to the CaM-free form. Thus the order of dimer tightness is iNOS < eNOS < nNOS in the CaM-bound form. In the absence of CaM, *L*-Arg has no effect on nNOS or eNOS dimer stabilities, but it does stabilize iNOS dimers by 30-fold. In the presence of CaM, *L*-Arg becomes destabilizing to nNOS and eNOS dimers, and only slightly stabilizes iNOS dimers. In the absence of CaM, H_4B stabilizes nNOS and iNOS but not eNOS. Pterin has no effect at all in the CaM-bound forms of nNOS and eNOS, and it destabilizes iNOS. Finally, *L*-Arg and H_4B are stabilizing to CaM-free eNOS and iNOS, but destabilizing to CaM-bound nNOS. However, in the CaM-bound condition, *L*-Arg and H_4B are destabilizing to nNOS and iNOS, and have no effect on eNOS. Therefore, ligand binding is generally stabilizing to CaM-free NOS dimers, but

not to the CaM-bound form. An analysis of eNOS oxygenase and reductase subdomains confirms that both can dimerize, and that CaM is stabilizing to the individual subdomains, but not full-length protein.

This work, has served to define the thermodynamics of NOS dimerization, and these results will provide useful direction for the design of NOS dimer dissociative inhibitors. Ligand-binding to CaM-free NOS is generally stabilizing for ligands of both the heme and pterin pocket, whereas ligand binding to the heme pocket of CaM-bound NOS is destabilizing to dimerization. Successful dimerization inhibitors might target the heme-binding pocket of CaM-bound protein selectively over the CaM-free conformation to dissociate NOS dimers.

SUMMARY OF STRUCTURAL REGULATION OF NITRIC OXIDE SYNTHASE ACTIVITY

CHAPTER 5

SIGNIFICANCE

As described in this work, nitric oxide synthase is an exquisitely controlled enzyme, as appropriate due to the noxious character of its oxidative products. This work has improved our understanding the differential regulation of the various NOS isoforms through the use of functional genomics analyses of sequence, structure, and function, answering several important questions: i) What is the unique chemical role of H_4B in an otherwise P450-like system? ii) Thermodynamically, how do H_4B, substrate *L*-Arg, and CaM affect dimerization within the oxygenase domain? iii) What are the structural elements within the NOS reductase domain that mechanically regulate electron transfer? These components together begin to paint a mosaic of isoform specific NOS regulation motifs, and a model for the active NOS complex is presented.

I. THE UNIQUE ROLE OF TETRAHYDROBIOPTERIN

H_4B is an important effector of NOS regulation through i) allosteric modulation of activity, ii) structural stabilization of dimerization, and iii) its function as a redox cofactor. It is now known that the formation of a pterin radical intermediate H_3B^+ is critical for the NOS mechanism, and this species is tightly linked to oxyferrous heme reduction and *L*-Arg hydroxylation (95,96,101,252). However, when the work in this thesis was initiated, the mechanistic role of pterin was unclear. Distant similarities found between the pterin binding sequence of NOS and aromatic amino acid hydroxylases as well as observed metal-dependant inhibition of NOS (102,29) implied a mechanistic similarity between these enzymes. The proposed mechanism involved the formation of a pterin-hydroperoxy intermediate and catalysis of hydroxyl transfer by a non-heme iron

center (26). Our contribution to the discussion, discussed in Chapter 2 (30), was a mutagenesis study aimed at removing all conserved potential metal-binding histidines in the oxygenase domain of eNOS. Indeed, several of these mutations were deleterious to function, but we found more reasonable structural arguments than the loss of metal binding, thus contradicting the AAH mechanism hypothesis. This project involved NOS preparation and spectral characterization, site-directed mutagenesis, and protein separation techniques and served as an excellent introduction to structure-function analysis of NOS.

An intriguing question from the mutagenesis study in Chapter 2 remained, however, in the allosteric function of pterin, as well as in the regulation of dimerization. In particular, the H461A mutant of eNOS was informative because it was a "corrigible" mutant, in that although it was defective in pterin binding it was able to slowly recover full activity given enough time (~90 minutes at room temperature). Our hypothesis for this slow recovery was that it involved a refolding of the dimeric interface coupled with pterin binding, as would be implied by comparison of monomer and dimer structures, Figure 1-9. Furthermore, other mutants displayed unpredictable changes in monomer-dimer distributions that depended on the preparation methods. It was clear that pterin binding was tightly linked to dimerization recovery, but thermodynamic and kinetic analyses were required to truly define these mechanical folding events. These observations served as a motivation for the careful biophysical analysis of dimerization discussed in Chapter 4.

II. Dimerization Regulation

The allosteric function of H_4B is attributed to its structural placement at the NOS dimeric interface, with two molecules of H_4B binding between oxygenase domains and providing H-bond interactions with the propionyl groups of the heme (32). Monomeric structures of iNOS oxygenase domains solved in the absence of pterin are missing structure at the dimerization interface, and some helices are unfolded (40). Comparison of dimeric structures of eNOS solved in the presence or absence of pterin revealed that the H_4B binding site was fully formed in the pterin-free structures (42). This evidence is strongly suggestive of stabilization of NOS dimerization by H_4B. However, until now, the only methods used to analyze dimerization were essentially qualitative, including gel filtration analyses and chaotropic resistance assays observed by urea denaturation or resistance to SDS in protein gel assays.

Gel filtration, although under relatively ideal equilibrium conditions, gave poor resolution of components, therefore statements such as "ligand-free eNOS is 98% dimeric compared to wild-type under similar conditions" (115) could be made for protein preparation quality control analysis, but were correct only with the caveat that temperature, concentration, and buffer conditions were held constant. Additionally, NOS is a non-globular protein, and therefore any predictions of mass from standard globular proteins were invalid. The other methods for studying NOS stability are kinetic in nature and involve measuring the resistance to denaturation by increased temperature, SDS or urea treatment of dimers. Through these methods, dimerization stabilization effects could

at least be qualitatively approximated (93,227,253), including the pterin stabilization effects on nNOS and iNOS dimers (93,94).

My contribution to the understanding of NOS structure involved the use of protein chromatography techniques required for absolutely pure protein preparation in combination with analytical ultracentrifugation methodology. Proper gel filtration chromatographic technique uses calibration by Stokes radius, not simply by mass. Stokes radius calculation methods were used to solve for an apparent Stokes radius for NOS full-length proteins, as well as oxygenase and reductase domains of eNOS, with some comparisons to the iNOS oxygenase domain. By sedimentation velocity analysis, the sedimentation coefficients for the subdomains were measured and the resulting Stokes radii for monomer or dimer species corresponded well to those observed by gel filtration. By comparison with structural models, we confirmed that these molecules are indeed elongated, rather than globular in nature.

The results obtained *in cellulo* for NOS dimerization have been largely overlooked by the protein-chemist community. Yeast-two-hybrid analysis showed that dimerization is mediated primarily by the oxygenase domains of NOS, but also indicated some interactions with reductase domains in the case of the constitutive isoforms (109). Alternately, expression in mammalian cells revealed that eNOS reductase domains can co-immunoprecipitate with full-length protein (254). The work included in Chapter 4 reports for the first time the formation of weak eNOS reductase domain dimers *in vitro.*

Under equilibrium conditions, our sedimentation analyses by analytical ultracentrifugation have resulted in extensive quantification of thermodynamic dimer

stability in the presence of various ligands and under the control of CaM. CaM has significant effects on the patterns of ligand stabilization of NOS dimers. In the CaM-free condition, the order of dimer tightness is eNOS < iNOS < nNOS, from tightest to weakest. CaM binding is destabilizing to eNOS, but is significantly stabilizing to iNOS, and nNOS is slightly stabilized relative to the CaM-free form. Thus, the order of dimer tightness shifts to iNOS < eNOS < nNOS in the CaM-bound form. In the absence of CaM, *L*-Arg has no effect on nNOS or eNOS dimer stabilities, but it does stabilize iNOS dimers by 30-fold. In the presence of CaM, *L*-Arg becomes destabilizing to nNOS and eNOS dimers, and only slightly stabilizes iNOS dimers. In the absence of CaM, H_4B stabilizes nNOS and iNOS but not eNOS, and it has no effect at all in the CaM-bound forms of nNOS and eNOS, and it destabilizes iNOS. Finally, *L*-Arg and H_4B are stabilizing to CaM-free eNOS and iNOS, but destabilizing to CaM-bound nNOS. However, in the CaM-bound condition, *L*-Arg and H_4B are destabilizing to nNOS and iNOS, and have no effect on eNOS. An analysis of eNOS oxygenase and reductase subdomains confirms that both can dimerize, and that CaM is stabilizing to the individual subdomains, but not full-length protein.

Our work represents an important contribution to the understanding of ligand-control of dimerization by direct measurement of thermodynamic dissociation constants in buffers that simulate catalytic *in vitro* conditions. This work has served to define the thermodynamics of NOS dimerization, and these results will provide useful direction for the design of NOS dimer inhibitors. Ligand binding to CaM-free NOS is generally stabilizing for ligands of both the heme and pterin pocket, whereas ligand binding to the heme pocket of CaM-bound NOS is destabilizing to dimerization. Successful

dimerization inhibitors might target the heme-binding pocket of the CaM-bound protein selectively over the CaM-free protein to dissociate NOS dimers.

III. Control of Electron Transfer by CaM

Similarity between NOS and the cytochrome P450 system was readily apparent from the cofactor requirements and oxidation reactions catalyzed by both enzymes. However, NOS is unique due to its dependence on pterin and also due to its regulation by Ca^{2+}-dependent CaM. CaM is known to function as an activation switch by binding to a conserved recognition motif found between the oxygenase and reductase domains, and is proposed to alter the quaternary conformation of the active NOS complex upon binding. Comparison of sequence and structure between NOS and CPR has resulted in the identification of a number of unique functional elements found in NOS. Those elements that differ between inducible and constitutive isoforms include the C-terminal tail, the autoinhibitory element, and a loop within the connecting domain that we identified, the CD2A, Chapter 3 (37). These loops, subdomains, and large domains have been extensively characterized through functional element complementation studies in this lab and by others (35-39).

My contribution to the analysis of electron transfer control was through structural modeling based on homology with related flavoproteins, including CPR, sulfite reductase, $P450_{BM-3}$, and ferredoxin reductase. Our final models included as a template the partial structure of nNOS reductase domain that became available after the modeling project was begun (43). Using our reductase domain models, we were able to present a functional model for CaM recognition in relation to the various known regulatory

elements, aided by the solution of the crystal structure of CaM bound to its eNOS recognition element (44). We showed that the location of the unique CD2A loop found by sequence analysis was placed within direct contact distance of the CaM-recognition site, which includes the linker region between oxygenase and reductase domains, and also the autoinhibitory element characterized with the FMN subdomain. We designed and characterized chimeras that swapped the CD2A loop in the wild-type protein and ΔAI chimeras, and we were able to demonstrate that this loop has its own modulatory effect on the Ca^{2+}-dependence of CaM stimulated activity (37) (Chapter 3). Both of these elements could participate in direct interactions with the CaM-binding region of the NOS reductase domain models, thus the modeling process yielded a very useful functional model for CaM-mediated regulation of activity.

IV. Models of the Active NOS Complex

With completion of the reductase models, the collection of structures that are now available are sufficient to build docked models of the complete active NOS complex. We used three criteria for predicting appropriate docking surfaces: surface complementarity, electrostatic complementarity, and surface residue conservation by isoform within the docking patch. The programs used for each step are independent, therefore, visual inspection was required to select the most reasonable model from a list of several candidates. Therefore these models are not to be taken as fact, rather they are intelligent fancy, in that we can use them to generate interesting hypotheses for the NOS active complex. In Figure 5-1 are shown the Poisson-Boltzmann electrostatic surface maps of eNOS generated using the program GRASP (236), and the conserved surface residue

patches using the program ConSurf (237,255). Phylogenetic methods were used build alignments of the NOS subdomains for input into ConSurf, using NOS family sequence conservation for the oxygenase domains, and CPR family sequence conservation for the reductase domains. From these predicted surfaces, we hypothesized that the positively charged conserved surface of the oxygenase domain (corresponding to the distal side of the heme) would dock with the negatively charged conserved core patch of cofactors in the reductase domain as shown in Figure 5-1. The next question was then to identify the correct orientation of these surfaces using molecular surface complementarity requirements in the program GRAMM (235). In Figure 5-2 is shown the docked model of the eNOS oxygenase dimeric structure 4NSE with our eNOS reductase domain model. The electron transfer route for this model can be visualized: the NADPH binding site is solvent accessible, as necessary for exchange of this substrate, and the FAD - FMN to heme - pterin electron transfer pathway is solvent protected, with several aromatic or Arg residues along a potential route for electrons to flow. Furthermore, the directionality of the CaM-recognition helix at the N-terminus of the reductase domain, leads toward the C-terminus of the oxygenase domain dimer in such a way that the protein subunit would transfer electrons in a *trans* mode from the reductase domain of one subunit to the heme of the other subunit.

Figure 5-1. Electrostatic (A) and conserved residue (B) patches on the surface of the eNOS oxygenase domain dimer and reductase domain. In panel A, the GRASP electrostatic potential range was from -8 (dark red) to+6 (dark blue) units of charge. In panel B highest conservation is colored in reds, and the cofactors are colored dark blue. The CONSURF alignments used were generated from i) an alignment of >25 NOS oxygenase domain sequences from multiple species and isoforms and ii) from the alignment of the reductase domain with the CPR family, therefore the conservation coloring is less conserved in the reductase. To assemble the complex in Figure 5.2, place the two structures in the palms of your hands and clap with the right hand over left.

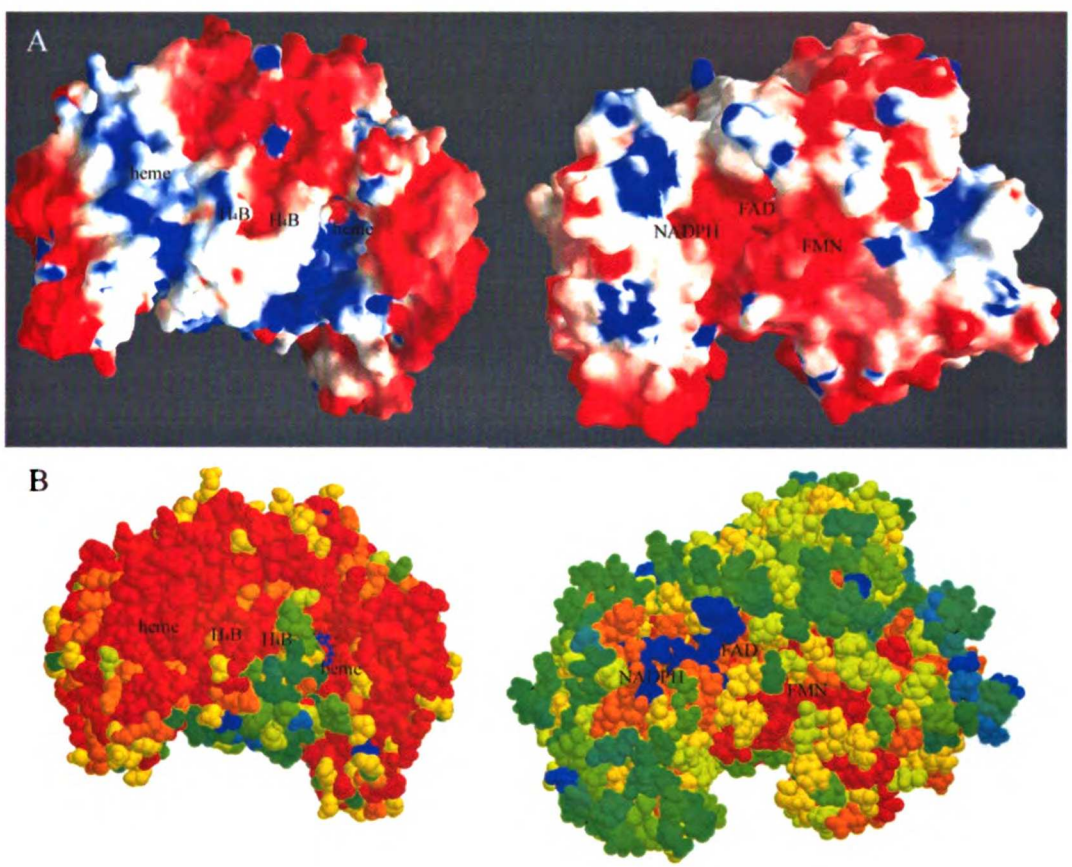

Figure 5-2. Oxygenase dimer (yellow and red) docking model with reductase domain (green), shown is eNOS. The CaM recognition site is along the back of the reductase module in this orientation. Relative to Figure 5-1, this structure would result from the palms of the hands held together.

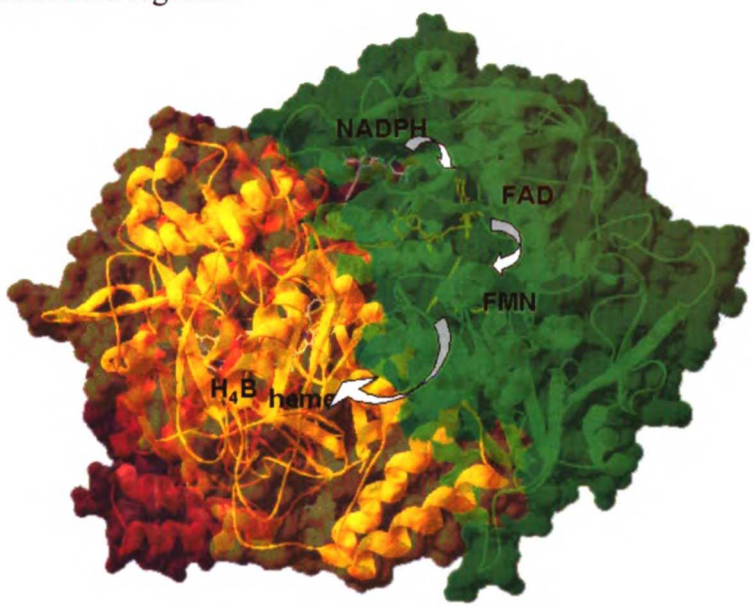

Figure 5-3. The iNOS large complex model, with the oxygenase dimer (red and yellow subunits), the reductase domains (green), and CaM (white) modules placed. The orientation of this model is looking up through the Zn binding site along the C2-rotational axis of the model, and electrons flow counter-clockwise, from the reductase of one subunit to the heme of the next. (The structure in Figure 5-2 would be rotated 90° upwards.) CaM has primary interactions with the reductase domain, but also interacts with the recognition element from the oxygenase domain.

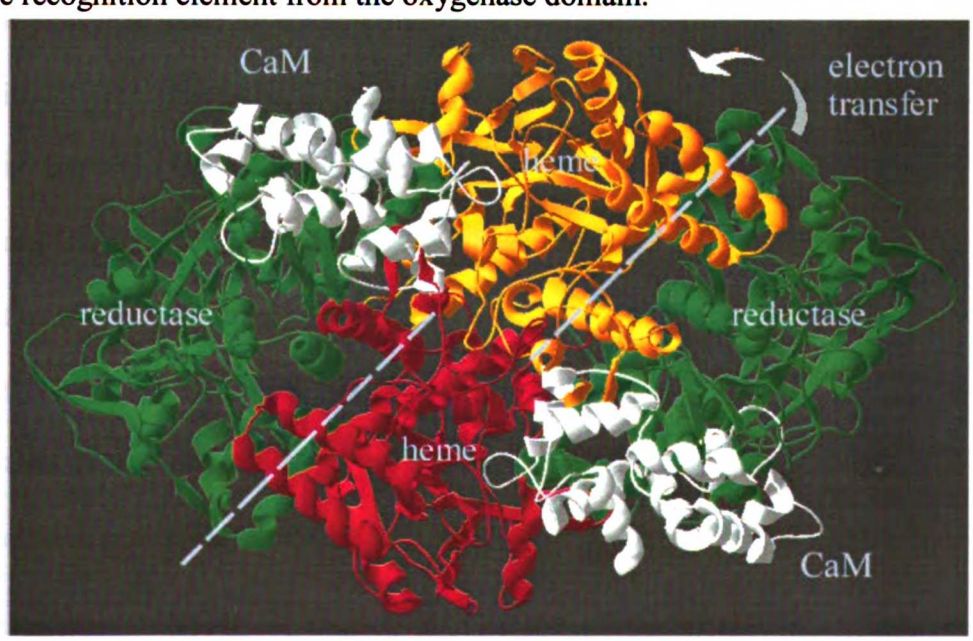

Finally, the docked model in Figure 5-2 of the reductase and oxygenase domains can be combined with CaM, to give a large complex model. Shown in Figure 5-3 is the iNOS model, built by replacing the eNOS subdomains with that of iNOS. Here, the orientation of CaM differs slightly from eNOS, Figure 3-5, but satisfies orientation requirements for the CaM-recognition element, placing this long helix along the back of the reductase domain and connecting it to the oxygenase domain.

V. NOS Regulation at the Level of Protein-Protein Interactions

The extensive networks of cellular protein-protein interactions that regulate NOS activity are growing. These interactions can be queried using biological screening techniques such as yeast two-hybrid analyses, and the use of genetic knockout organisms. Already, much is known about NOS motifs that are recognized by various proteins, and numerous sites have been mapped onto the NOS sequence. Phosphorylation is an important mode of NOS activity regulation in eNOS and nNOS. eNOS is phosphorylated by Akt, PKC (49-51), AMPK (52), and cyclic-nucleotide-dependent protein kinases (53); nNOS is phosphorylated by the CaM-kinases (54). Heat shock protein 90 has been shown to specifically recognize eNOS (55,56) and nNOS (57) through defined interactions that stimulate activity. Caveolin recognizes eNOS at a consensus binding motif in the oxygenase domain (55,58), and caveolin 3 also recognizes nNOS (59). Dystrophin recognizes the PDZ domain within the N-terminal portion of nNOS (60,61), serving to localize NOS to the sarcolemma membrane of skeletal muscle. Indeed, blockage or stimulation of any one signaling point within these complex pathways of interactions could serve as a reasonable method to address isoform-specific regulation of NOS.

In summary, NOS is regulated in multiple dimensions, i) on the order of transcription, ii) on the chemical level of enzymatic activity, and iii) on the mechanical level of protein-protein interactions. The research presented in this thesis contributes significantly to improving our understanding of the latter two points. On the level of enzymatic activity, the function of H_4B was explored through the use of site-directed mutation in the eNOS oxygenase domain (30), and the regulation of activity by the reductase domain was analyzed through structural modeling coupled with chimera mutagenesis that swapped regulatory elements between isoforms (37). On the mechanical level, dimerization regulation was carefully dissected using hydrodynamic analyses to characterize the structural properties of full-length NOS as well as oxygenase and reductase domain constructs of eNOS. These dimerization analyses found significant effects of ligands and CaM upon dimer stability, and we report for the first time quantitative measurements of dimer affinity in a standardized format that compares all three isoforms. Taken together, these studies approach a complete picture for the structural regulation of activity in Nitric Oxide Synthase.

References

1. Brightbill, H. D., Libraty, D. H., Krutzik, S. R., Yang, R. B., Belisle, J. T., Bleharski, J. R., Maitland, M., Norgard, M. V., Plevy, S. E., Smale, S. T., Brennan, P. J., Bloom, B. R., Godowski, P. J., and Modlin, R. L. (1999) *Science* **285**, 732-736.
2. Diefenbach, A., Schindler, H., Rollinghoff, M., Yokoyama, W. M., and Bogdan, C. (1999) *Science* **284**, 951-955.
3. Nathan, C., and Xie, Q. W. (1994) *Cell* **78**, 915-918.
4. Esplugues, J. V. (2002) *Br J Pharmacol* **135**, 1079-1095.
5. Raoul, C., Estevez, A. G., Nishimune, H., Cleveland, D. W., deLapeyriere, O., Henderson, C. E., Haase, G., and Pettmann, B. (2002) *Neuron* **35**, 1067-1083.
6. Abramson, S. B., Amin, A. R., Clancy, R. M., and Attur, M. (2001) *Best Pract Res Clin Rheumatol* **15**, 831-845.
7. Fischer, A., Folkerts, G., Geppetti, P., and Groneberg, D. A. (2002) *Pulm Pharmacol Ther* **15**, 73-81.
8. Boveris, A., Alvarez, S., and Navarro, A. (2002) *Free Radic Biol Med* **33**, 1186-1193.
9. Price, S., Mitchell, J. A., Anning, P. B., and Evans, T. W. (2003) *Eur J Pharmacol* **472**, 111-118.
10. Feron, O., Dessy, C., Moniotte, S., Desager, J. P., and Balligand, J. L. (1999) *J Clin Invest* **103**, 897-905.
11. Forte, P., Copland, M., Smith, L. M., Milne, E., Sutherland, J., and Benjamin, N. (1997) *Lancet* **349**, 837-842.
12. Persu, A., Stoenoiu, M. S., Messiaen, T., Davila, S., Robino, C., El-Khattabi, O., Mourad, M., Horie, S., Feron, O., Balligand, J. L., Wattiez, R., Pirson, Y., Chauveau, D., Lens, X. M., and Devuyst, O. (2002) *Hum Mol Genet* **11**, 229-241.
13. Johannesen, J., Pie, A., Pociot, F., Kristiansen, O. P., Karlsen, A. E., and Nerup, J. (2001) *J Clin Endocrinol Metab* **86**, 2792-2796.
14. Hobbs, A. J., Higgs, A., and Moncada, S. (1999) *Annu. Rev. Pharmacol. Toxicol.* **39**, 191-200.
15. Sato, S., Tominaga, T., Ohnishi, T., and Ohnishi, S. T. (1994) *Brain Res* **647**, 91-96.
16. Armengou, A., Hurtado, O., Leira, R., Obon, M., Pascual, C., Moro, M. A., Lizasoain, I., Castillo, J., and Davalos, A. (2003) *J Cereb Blood Flow Metab* **23**, 978-984.
17. Gu, Z., Kaul, M., Yan, B., Kridel, S. J., Cui, J., Strongin, A., Smith, J. W., Liddington, R. C., and Lipton, S. A. (2002) *Science* **297**, 1186-1190.
18. Southan, G. J., and Szabo, C. (1996) *Biochem Pharmacol* **51**, 383-394.
19. Huang, Z., Huang, P. L., Ma, J., Meng, W., Ayata, C., Fishman, M. C., and Moskowitz, M. A. (1996) *J Cereb Blood Flow Metab* **16**, 981-987.
20. Jiang, M. H., Kaku, T., Hada, J., and Hayashi, Y. (2002) *Brain Res* **946**, 139-147.
21. Geller, D. A., Lowenstein, C. J., Shapiro, R. A., Nussler, A. K., Di Silvio, M., Wang, S. C., Nakayama, D. K., Simmons, R. L., Snyder, S. H., and Billiar, T. R. (1993) *Proc Natl Acad Sci U S A* **90**, 3491-3495.

22. Gerber, N. C., and Ortiz de Montellano, P. R. (1995) *J Biol Chem* **270**, 17791-17796.
23. Gerber, N. C., Rodríguez-Crespo, I., Nishida, C. R., and Ortiz de Montellano, P. R. (1997) *J Biol Chem* **272**, 6285-6290.
24. Roman, L. J., Sheta, E. A., Martasek, P., Gross, S. S., Liu, Q., and Masters, B. S. (1995) *Proc Natl Acad Sci U S A* **92**, 8428-8432.
25. Rodríguez-Crespo, I., Gomez-Gutierrez, J., Encinar, J. A., Gonzalez-Ros, J. M., Albar, J. P., Peterson, D. L., and Gavilanes, F. (1996) *Eur J Biochem* **242**, 243-248.
26. Perry, J. M., and Marletta, M. A. (1998) *Proc Natl Acad Sci U S A* **95**, 11101-11106.
27. Goodwill, K. E., Sabatier, C., and Stevens, R. C. (1998) *Biochemistry* **37**, 13437-13445.
28. Teigen, K., Froystein, N. A., and Martinez, A. (1999) *J Mol Biol* **294**, 807-823.
29. Hegg, E. L., and Que, L., Jr. (1997) *Eur J Biochem* **250**, 625-629.
30. Rodríguez-Crespo, I., Nishida, C. R., Knudsen, G. M., and de Montellano, P. R. (1999) *J Biol Chem* **274**, 21617-21624.
31. Hemmens, B., Goessler, W., Schmidt, K., and Mayer, B. (2000) *J. Biol. Chem.* **275**, 35786-35791.
32. Li, H., Raman, C. S., Glaser, C. B., Blasko, E., Young, T. A., Parkinson, J. F., Whitlow, M., and Poulos, T. L. (1999) *J Biol Chem* **274**, 21276-21284.
33. Nishimura, J. S., Narayanasami, R., Miller, R. T., Roman, L. J., Panda, S., and Masters, B. S. S. (1999) *J. Biol. Chem.* **274**, 5399-5406.
34. Schrammel, A., Gorren, A. C., Stuehr, D. J., Schmidt, K., and Mayer, B. (1998) *Biochim Biophys Acta* **1387**, 257-263.
35. Nishida, C. R., and Ortiz de Montellano, P. R. (1998) *J Biol Chem* **273**, 5566-5571.
36. Nishida, C. R., and Ortiz de Montellano, P. R. (2001) *J Biol Chem* **276**, 20116-20124.
37. Knudsen, G. M., Nishida, C. R., Mooney, S. D., and Ortiz de Montellano, P. R. (2003) *J Biol Chem* **278**, 31814-31824.
38. Chen, P. F., and Wu, K. K. (2000) *J Biol Chem* **275**, 13155-13163.
39. Daff, S., Sagami, I., and Shimizu, T. (1999) *J. Biol. Chem.* **274**, 30589-30595.
40. Crane, B. R., Arvai, A. S., Gachhui, R., Wu, C., Ghosh, D. K., Getzoff, E. D., Stuehr, D. J., and Tainer, J. A. (1997) *Science* **278**, 425-431.
41. Crane, B. R., Arvai, A. S., Ghosh, D. K., Wu, C., Getzoff, E. D., Stuehr, D. J., and Tainer, J. A. (1998) *Science* **279**, 2121-2126.
42. Raman, C. S., Li, H., Martasek, P., Kral, V., Masters, B. S., and Poulos, T. L. (1998) *Cell* **95**, 939-950.
43. Zhang, J., Martasek, P., Paschke, R., Shea, T., Siler Masters, B. S., and Kim, J. J. (2001) *J Biol Chem* **276**, 37506-37513.
44. Aoyagi, M., Arvai, A. S., Tainer, J. A., and Getzoff, E. D. (2003) *Embo J* **22**, 766-775.
45. Nishida, C. R., and Ortiz de Montellano, P. R. (1999) *J Biol Chem* **274**, 14692-14698.

46. McMillan, K., Adler, M., Auld, D. S., Baldwin, J. J., Blasko, E., Browne, L. J., Chelsky, D., Davey, D., Dolle, R. E., Eagen, K. A., Erickson, S., Feldman, R. I., Glaser, C. B., Mallari, C., Morrissey, M. M., Ohlmeyer, M. H., Pan, G., Parkinson, J. F., Phillips, G. B., Polokoff, M. A., Sigal, N. H., Vergona, R., Whitlow, M., Young, T. A., and Devlin, J. J. (2000) *Proc Natl Acad Sci U S A* **97**, 1506-1511.
47. Panda, K., Ghosh, S., and Stuehr, D. J. (2001) *J. Biol. Chem.* **276**, 23349-23356.
48. Siddhanta, U., Presta, A., Fan, B., Wolan, D., Rousseau, D. L., and Stuehr, D. J. (1998) *J Biol Chem* **273**, 18950-18958.
49. Dimmeler, S., Fleming, I., Fisslthaler, B., Hermann, C., Busse, R., and Zeiher, A. M. (1999) *Nature* **399**, 601-605.
50. Fulton, D., Gratton, J. P., McCabe, T. J., Fontana, J., Fujio, Y., Walsh, K., Franke, T. F., Papapetropoulos, A., and Sessa, W. C. (1999) *Nature* **399**, 597-601.
51. Michell, B. J., Griffiths, J. E., Mitchelhill, K. I., Rodríguez-Crespo, I., Tiganis, T., Bozinovski, S., de Montellano, P. R., Kemp, B. E., and Pearson, R. B. (1999) *Curr Biol* **9**, 845-848.
52. Chen, Z. P., Mitchelhill, K. I., Michell, B. J., Stapleton, D., Rodríguez-Crespo, I., Witters, L. A., Power, D. A., Ortiz de Montellano, P. R., and Kemp, B. E. (1999) *FEBS Lett* **443**, 285-289.
53. Butt, E., Bernhardt, M., Smolenski, A., Kotsonis, P., Frohlich, L. G., Sickmann, A., Meyer, H. E., Lohmann, S. M., and Schmidt, H. H. (2000) *J Biol Chem* **275**, 5179-5187.
54. Hayashi, Y., Nishio, M., Naito, Y., Yokokura, H., Nimura, Y., Hidaka, H., and Watanabe, Y. (1999) *J Biol Chem* **274**, 20597-20602.
55. Fontana, J., Fulton, D., Chen, Y., Fairchild, T. A., McCabe, T. J., Fujita, N., Tsuruo, T., and Sessa, W. C. (2002) *Circ Res* **90**, 866-873.
56. Garcia-Cardena, G., Fan, R., Shah, V., Sorrentino, R., Cirino, G., Papapetropoulos, A., and Sessa, W. C. (1998) *Nature* **392**, 821-824.
57. Bender, A. T., Silverstein, A. M., Demady, D. R., Kanelakis, K. C., Noguchi, S., Pratt, W. B., and Osawa, Y. (1999) *J. Biol. Chem.* **274**, 1472-1478.
58. Garcia-Cardena, G., Martasek, P., Masters, B. S., Skidd, P. M., Couet, J., Li, S., Lisanti, M. P., and Sessa, W. C. (1997) *J Biol Chem* **272**, 25437-25440.
59. Venema, V. J., Ju, H., Zou, R., and Venema, R. C. (1997) *J Biol Chem* **272**, 28187-28190.
60. Wells, K. E., Torelli, S., Lu, Q., Brown, S. C., Partridge, T., Muntoni, F., and Wells, D. J. (2003) *Neuromuscul Disord* **13**, 21-31.
61. Brenman, J. E., Chao, D. S., Xia, H., Aldape, K., and Bredt, D. S. (1995) *Cell* **82**, 743-752.
62. Forstermann, U., Gath, I., Schwarz, P., Closs, E. I., and Kleinert, H. (1995) *Biochem Pharmacol* **50**, 1321-1332.
63. Schmidt, H. H., Pollock, J. S., Nakane, M., Gorsky, L. D., Forstermann, U., and Murad, F. (1991) *Proc Natl Acad Sci U S A* **88**, 365-369.
64. Abu-Soud, H. M., and Stuehr, D. J. (1993) *Proc Natl Acad Sci U S A* **90**, 10769-10772.
65. Cho, H. J., Xie, Q. W., Calaycay, J., Mumford, R. A., Swiderek, K. M., Lee, T. D., and Nathan, C. (1992) *J Exp Med* **176**, 599-604.

66. Marsden, P. A., Heng, H. H., Scherer, S. W., Stewart, R. J., Hall, A. V., Shi, X. M., Tsui, L. C., and Schappert, K. T. (1993) *J Biol Chem* **268**, 17478-17488.
67. Kishimoto, J., Spurr, N., Liao, M., Lizhi, L., Emson, P., and Xu, W. (1992) *Genomics* **14**, 802-804.
68. Ogura, T., Yokoyama, T., Fujisawa, H., Kurashima, Y., and Esumi, H. (1993) *Biochem Biophys Res Commun* **193**, 1014-1022.
69. Brenman, J. E., Xia, H., Chao, D. S., Black, S. M., and Bredt, D. S. (1997) *Dev Neurosci* **19**, 224-231.
70. Silvagno, F., Xia, H., and Bredt, D. S. (1996) *J Biol Chem* **271**, 11204-11208.
71. Laine, R., and de Montellano, P. R. (1998) *Mol Pharmacol* **54**, 305-312.
72. Chartrain, N. A., Geller, D. A., Koty, P. P., Sitrin, N. F., Nussler, A. K., Hoffman, E. P., Billiar, T. R., Hutchinson, N. I., and Mudgett, J. S. (1994) *J Biol Chem* **269**, 6765-6772.
73. Marsden, P. A., Heng, H. H., Duff, C. L., Shi, X. M., Tsui, L. C., and Hall, A. V. (1994) *Genomics* **19**, 183-185.
74. Bloch, K. D., Wolfram, J. R., Brown, D. M., Roberts, J. D., Jr., Zapol, D. G., Lepore, J. J., Filippov, G., Thomas, J. E., Jacob, H. J., and Bloch, D. B. (1995) *Genomics* **27**, 526-530.
75. Kent, W. J., Sugnet, C. W., Furey, T. S., Roskin, K. M., Pringle, T. H., Zahler, A. M., and Haussler, D. (2002) *Genome Res* **12**, 996-1006.
76. Wood, E. R., Berger, H., Jr., Sherman, P. A., and Lapetina, E. G. (1993) *Biochem Biophys Res Commun* **191**, 767-774.
77. Adams, V., Krabbes, S., Jiang, H., Yu, J., Rahmel, A., Gielen, S., Schuler, G., and Hambrecht, R. (1998) *Nitric Oxide* **2**, 242-249.
78. Bredt, D. S., Hwang, P. M., Glatt, C. E., Lowenstein, C., Reed, R. R., and Snyder, S. H. (1991) *Nature* **351**, 714-718.
79. Porter, T. D., and Kasper, C. B. (1985) *Proc Natl Acad Sci U S A* **82**, 973-977.
80. Sagami, I., Daff, S., and Shimizu, T. (2001) *J. Biol. Chem.* **276**, 30036-30042.
81. Knowles, R. G., and Moncada, S. (1994) *Biochem J* **298**, 249-258.
82. Marletta, M. A. (1993) *J Biol Chem* **268**, 12231-12234.
83. Moali, C., Boucher, J. L., Sari, M. A., Stuehr, D. J., and Mansuy, D. (1998) *Biochemistry* **37**, 10453-10460.
84. Renaud, J. P., Boucher, J. L., Vadon, S., Delaforge, M., and Mansuy, D. (1993) *Biochem Biophys Res Commun* **192**, 53-60.
85. Li, H., Shimizu, H., Flinspach, M., Jamal, J., Yang, W., Xian, M., Cai, T., Wen, E. Z., Jia, Q., Wang, P. G., and Poulos, T. L. (2002) *Biochemistry* **41**, 13868-13875.
86. Ravichandran, K. G., Boddupalli, S. S., Hasermann, C. A., Peterson, J. A., and Deisenhofer, J. (1993) *Science* **261**, 731-736.
87. Poulos, T. L., Finzel, B. C., and Howard, A. J. (1987) *J Mol Biol* **195**, 687-700.
88. Guex, N., and Peitsch, M. C. (1997) *Electrophoresis* **18**, 2714-2723.
89. Rafferty, S. P., Boyington, J. C., Kulansky, R., Sun, P. D., and Malech, H. L. (1999) *Biochem Biophys Res Commun* **257**, 344-347.
90. Klatt, P., Schmid, M., Leopold, E., Schmidt, K., Werner, E. R., and Mayer, B. (1994) *J Biol Chem* **269**, 13861-13866.

91. Rodríguez-Crespo, I., and Ortiz de Montellano, P. R. (1996) *Arch Biochem Biophys* **336**, 151-156.
92. Presta, A., Siddhanta, U., Wu, C., Sennequier, N., Huang, L., Abu-Soud, H. M., Erzurum, S., and Stuehr, D. J. (1998) *Biochemistry* **37**, 298-310.
93. Klatt, P., Schmidt, K., Lehner, D., Glatter, O., Bachinger, H. P., and Mayer, B. (1995) *Embo J* **14**, 3687-3695.
94. Baek, K. J., Thiel, B. A., Lucas, S., and Stuehr, D. J. (1993) *J Biol Chem* **268**, 21120-21129.
95. Bec, N., Gorren, A. C., Voelker, C., Mayer, B., and Lange, R. (1998) *J Biol Chem* **273**, 13502-13508.
96. Hurshman, A. R., Krebs, C., Edmondson, D. E., Huynh, B. H., and Marletta, M. A. (1999) *Biochemistry* **38**, 15689-15696.
97. Gorren, A. C., Bec, N., Schrammel, A., Werner, E. R., Lange, R., and Mayer, B. (2000) *Biochemistry* **39**, 11763-11770.
98. Mayer, B., Wu, C., Gorren, A. C., Pfeiffer, S., Schmidt, K., Clark, P., Stuehr, D. J., and Werner, E. R. (1997) *Biochemistry* **36**, 8422-8427.
99. Pfeiffer, S., Gorren, A. C., Pitters, E., Schmidt, K., Werner, E. R., and Mayer, B. (1997) *Biochem J* **328**, 349-352.
100. Crane, B. R., Arvai, A. S., Ghosh, S., Getzoff, E. D., Stuehr, D. J., and Tainer, J. A. (2000) *Biochemistry* **39**, 4608-4621.
101. Wei, C.-C., Wang, Z.-Q., Wang, Q., Meade, A. L., Hemann, C., Hille, R., and Stuehr, D. J. (2001) *J. Biol. Chem.* **276**, 315-319.
102. Chen, D., and Frey, P. A. (1998) *J Biol Chem* **273**, 25594-25601.
103. Almas, B., Haavik, J., and Flatmark, T. (1996) *Biochem J* **319 (Pt 3)**, 947-951.
104. Riethmuller, C., Gorren, A. C. F., Pitters, E., Hemmens, B., Habisch, H.-J., Heales, S. J. R., Schmidt, K., Werner, E. R., and Mayer, B. (1999) *J. Biol. Chem.* **274**, 16047-16051.
105. Witteveen, C. F., Giovanelli, J., and Kaufman, S. (1996) *J Biol Chem* **271**, 4143-4147.
106. Nishida, C. R., Knudsen, G., Straub, W., and Ortiz de Montellano, P. R. (2002) *Drug Metab Rev* **34**, 479-501.
107. Ortiz de Montellano, P. R. (1989) *Trends Pharmacol Sci* **10**, 354-359.
108. Tantillo, D. J., Fukuto, J. M., Hoffman, B. M., Silverman, R. B., and Houk, K. N. (2000) *J. Am. Chem. Soc.* **122**, 536-537.
109. Venema, R. C., Ju, H., Zou, R., Ryan, J. W., and Venema, V. J. (1997) *J Biol Chem* **272**, 1276-1282.
110. Klatt, P., Pfeiffer, S., List, B. M., Lehner, D., Glatter, O., Bachinger, H. P., Werner, E. R., Schmidt, K., and Mayer, B. (1996) *J Biol Chem* **271**, 7336-7342.
111. Ghosh, D. K., Abu-Soud, H. M., and Stuehr, D. J. (1996) *Biochemistry* **35**, 1444-1449.
112. Albakri, Q. A., and Stuehr, D. J. (1996) *J Biol Chem* **271**, 5414-5421.
113. Sennequier, N., Wolan, D., and Stuehr, D. J. (1999) *J. Biol. Chem.* **274**, 930-938.
114. Crane, B. R., Rosenfeld, R. J., Arvai, A. S., Ghosh, D. K., Ghosh, S., Tainer, J. A., Stuehr, D. J., and Getzoff, E. D. (1999) *Embo J* **18**, 6271-6281.
115. Rodríguez-Crespo, I., Gerber, N. C., and Ortiz de Montellano, P. R. (1996) *J Biol Chem* **271**, 11462-11467.

116. Sennequier, N., and Stuehr, D. J. (1996) *Biochemistry* **35**, 5883-5892.
117. Moulton, P., Martin, H., Ainger, A., Cross, A., Hoare, C., Doel, J., Harrison, R., Eisenthal, R., and Hancock, J. (2000) *Eur J Pharmacol* **401**, 115-120.
118. Olken, N. M., and Marletta, M. A. (1993) *Biochemistry* **32**, 9677-9685.
119. Olken, N. M., and Marletta, M. A. (1992) *J Med Chem* **35**, 1137-1144.
120. Moore, W. M., Webber, R. K., Jerome, G. M., Tjoeng, F. S., Misko, T. P., and Currie, M. G. (1994) *J Med Chem* **37**, 3886-3888.
121. Frey, C., Narayanan, K., McMillan, K., Spack, L., Gross, S. S., Masters, B. S., and Griffith, O. W. (1994) *J Biol Chem* **269**, 26083-26091.
122. Raman, C. S., Li, H., Martasek, P., Babu, B. R., Griffith, O. W., Masters, B. S., and Poulos, T. L. (2001) *J Biol Chem* **276**, 26486-26491.
123. Babu, B. R., Griffith, O.W. (1998) *Curr. Opin. Chem. Biol.* **2**, 491-500.
124. Fischmann, T. O., Hruza, A., Niu, X. D., Fossetta, J. D., Lunn, C. A., Dolphin, E., Prongay, A. J., Reichert, P., Lundell, D. J., Narula, S. K., and Weber, P. C. (1999) *Nat Struct Biol* **6**, 233-242.
125. Hallinan, E. A., Tsymbalov, S., Finnegan, P. M., Moore, W. M., Jerome, G. M., Currie, M. G., and Pitzele, B. S. (1998) *J Med Chem* **41**, 775-777.
126. Huang, H., Martasek, P., Roman, L. J., Masters, B. S., and Silverman, R. B. (1999) *J Med Chem* **42**, 3147-3153.
127. Green, B. G., Chabin, R., and Grant, S. K. (1996) *Biochem Biophys Res Commun* **225**, 621-626.
128. Lee, Y., Martasek, P., Roman, L. J., Masters, B. S., and Silverman, R. B. (1999) *Bioorg Med Chem* **7**, 1941-1951.
129. Blasko, E., Glaser, C. B., Devlin, J. J., Xia, W., Feldman, R. I., Polokoff, M. A., Phillips, G. B., Whitlow, M., Auld, D. S., McMillan, K., Ghosh, S., Stuehr, D. J., and Parkinson, J. F. (2002) *J. Biol. Chem.* **277**, 295-302.
130. Rozzelle, J. E., Dauber, D. S., Todd, S., Kelley, R., and Craik, C. S. (2000) *J Biol Chem* **275**, 7080-7086.
131. Gaudreau, P., Michaud, J., Cohen, E. A., Langelier, Y., and Brazeau, P. (1987) *J Biol Chem* **262**, 12413-12416.
132. Divita, G., Baillon, J. G., Rittinger, K., Chermann, J. C., and Goody, R. S. (1995) *J Biol Chem* **270**, 28642-28646.
133. Zhang, Z. Y., Poorman, R. A., Maggiora, L. L., Heinrikson, R. L., and Kezdy, F. J. (1991) *J Biol Chem* **266**, 15591-15594.
134. Phung, Y. T., and Black, S. M. (1999) *IUBMB Life* **48**, 333-338.
135. Ohtsuka, M., Konno, F., Honda, H., Oikawa, T., Ishikawa, M., Iwase, N., Isomae, K., Ishii, F., Hemmi, H., and Sato, S. (2002) *J Pharmacol Exp Ther* **303**, 52-57.
136. Hellermann, G. R., and Solomonson, L. P. (1997) *J. Biol. Chem.* **272**, 12030-12034.
137. Gachhui, R., Presta, A., Bentley, D. F., Abu-Soud, H. M., McArthur, R., Brudvig, G., Ghosh, D. K., and Stuehr, D. J. (1996) *J Biol Chem* **271**, 20594-20602.
138. Matsuda, H., and Iyanagi, T. (1999) *Biochim Biophys Acta* **1473**, 345-355.
139. Abu-Soud, H. M., Feldman, P. L., Clark, P., and Stuehr, D. J. (1994) *J Biol Chem* **269**, 32318-32326.
140. Stevens-Truss, R., Beckingham, K., and Marletta, M. A. (1997) *Biochemistry* **36**, 12337-12345.

141. Kobayashi, K., Tagawa, S., Daff, S., Sagami, I., and Shimizu, T. (2001) *J Biol Chem* **276**, 39864-39871.
142. Rhoads, A. R., and Friedberg, F. (1997) *Faseb J* **11**, 331-340.
143. Brokx, R. D., Lopez, M. M., Vogel, H. J., and Makhatadze, G. I. (2001) *J Biol Chem* **276**, 14083-14091.
144. Zoche, M., Bienert, M., Beyermann, M., and Koch, K. W. (1996) *Biochemistry* **35**, 8742-8747.
145. Venema, R. C., Sayegh, H. S., Kent, J. D., and Harrison, D. G. (1996) *J Biol Chem* **271**, 6435-6440.
146. Lee, S. J., and Stull, J. T. (1998) *J Biol Chem* **273**, 27430-27437.
147. Chou, J. J., Li, S., Klee, C. B., and Bax, A. (2001) *Nat Struct Biol* **8**, 990-997.
148. Dasgupta, M., Honeycutt, T., and Blumenthal, D. K. (1989) *J Biol Chem* **264**, 17156-17163.
149. Yuan, T., Vogel, H. J., Sutherland, C., and Walsh, M. P. (1998) *FEBS Lett* **431**, 210-214.
150. Zhang, M., Tanaka, T., and Ikura, M. (1995) *Nat Struct Biol* **2**, 758-767.
151. Ruan, J., Xie, Q., Hutchinson, N., Cho, H., Wolfe, G. C., and Nathan, C. (1996) *J Biol Chem* **271**, 22679-22686.
152. Porter, T. D., and Kasper, C. B. (1986) *Biochemistry* **25**, 1682-1687.
153. Degtyarenko, K. N. (1995) *Protein Eng* **8**, 737-747.
154. Karplus, P. A., Daniels, M. J., and Herriott, J. R. (1991) *Science* **251**, 60-66.
155. Wang, M., Roberts, D. L., Paschke, R., Shea, T. M., Masters, B. S., and Kim, J. J. (1997) *Proc Natl Acad Sci U S A* **94**, 8411-8416.
156. Watt, W., Tulinsky, A., Swenson, R. P., and Watenpaugh, K. D. (1991) *J Mol Biol* **218**, 195-208.
157. Sevrioukova, I. F., Li, H., Zhang, H., Peterson, J. A., and Poulos, T. L. (1999) *Proc Natl Acad Sci U S A* **96**, 1863-1868.
158. Gruez, A., Pignol, D., Zeghouf, M., Coves, J., Fontecave, M., Ferrer, J. L., and Fontecilla-Camps, J. C. (2000) *J Mol Biol* **299**, 199-212.
159. Hoover, D. M., and Ludwig, M. L. (1997) *Protein Sci* **6**, 2525-2537.
160. Serre, L., Vellieux, F. M., Medina, M., Gomez-Moreno, C., Fontecilla-Camps, J. C., and Frey, M. (1996) *J Mol Biol* **263**, 20-39.
161. Bredt, D. S., and Snyder, S. H. (1990) *Proc Natl Acad Sci U S A* **87**, 682-685.
162. Roman, L. J., McLain, J., and Masters, B. S. (2003) *J Biol Chem* **278**, 25700-25707.
163. Fuziwara, S., Sagami, I., Rozhkova, E., Craig, D., Noble, M. A., Munro, A. W., Chapman, S. K., and Shimizu, T. (2002) *J Inorg Biochem* **91**, 515-526.
164. Roman, L. J., Martasek, P., Miller, R. T., Harris, D. E., de La Garza, M. A., Shea, T. M., Kim, J. J., and Masters, B. S. (2000) *J Biol Chem* **275**, 29225-29232.
165. Roman, L. J., Miller, R. T., de La Garza, M. A., Kim, J. J., and Siler Masters, B. S. (2000) *J Biol Chem* **275**, 21914-21919.
166. Gerber, N. C., Nishida, C. R., and Ortiz de Montellano, P. R. (1997) *Arch Biochem Biophys* **343**, 249-253.
167. Salerno, J. C., Harris, D. E., Irizarry, K., Patel, B., Morales, A. J., Smith, S. M., Martasek, P., Roman, L. J., Masters, B. S., Jones, C. L., Weissman, B. A., Lane, P., Liu, Q., and Gross, S. S. (1997) *J Biol Chem* **272**, 29769-29777.

168. Montgomery, H. J., Romanov, V., and Guillemette, J. G. (2000) *J. Biol. Chem.* **275**, 5052-5058.
169. Komeima, K., Hayashi, Y., Naito, Y., and Watanabe, Y. (2000) *J Biol Chem* **275**, 28139-28143.
170. Bassan, A., Blomberg, M. R., and Siegbahn, P. E. (2003) *Chemistry* **9**, 4055-4067.
171. Bassan, A., Blomberg, M. R., and Siegbahn, P. E. (2003) *Chemistry* **9**, 106-115.
172. Andersen, O. A., Stokka, A. J., Flatmark, T., and Hough, E. (2003) *J Mol Biol* **333**, 747-757.
173. Huang, C. C., Couch, G. S., Pettersen, E. F., Ferrin, T. E. (1996) *Pacific Symposium on Biocomputing* **1**, 724.
174. Pirskanen, A., Kaimio, A. M., Myllyla, R., and Kivirikko, K. I. (1996) *J Biol Chem* **271**, 9398-9402.
175. Huhmer, A. F., Nishida, C. R., Ortiz de Montellano, P. R., and Schoneich, C. (1997) *Chem Res Toxicol* **10**, 618-626.
176. Martasek, P., Liu, Q., Liu, J., Roman, L. J., Gross, S. S., Sessa, W. C., and Masters, B. S. (1996) *Biochem Biophys Res Commun* **219**, 359-365.
177. Demura, Y., Ameshima, S., Ishizaki, T., Okamura, S., Miyamori, I., and Matsukawa, S. (1998) *Free Radic Biol Med* **25**, 314-320.
178. Persechini, A., McMillan, K., and Masters, B. S. (1995) *Biochemistry* **34**, 15091-15095.
179. Martasek, P., Miller, R. T., Liu, Q., Roman, L. J., Salerno, J. C., Migita, C. T., Raman, C. S., Gross, S. S., Ikeda-Saito, M., and Masters, B. S. (1998) *J Biol Chem* **273**, 34799-34805.
180. Boucher, J. L., Genet, A., Vadon, S., Delaforge, M., Henry, Y., and Mansuy, D. (1992) *Biochem Biophys Res Commun* **187**, 880-886.
181. Boucher, J. L., Genet, A., Vadon, S., Delaforge, M., and Mansuy, D. (1992) *Biochem Biophys Res Commun* **184**, 1158-1164.
182. Nagase, S., Takemura, K., Ueda, A., Hirayama, A., Aoyagi, K., Kondoh, M., and Koyama, A. (1997) *Biochem Biophys Res Commun* **233**, 150-153.
183. Everett, S. A., Dennis, M. F., Patel, K. B., Maddix, S., Kundu, S. C., and Willson, R. L. (1996) *J Biol Chem* **271**, 3988-3994.
184. Poulos, T. L., Finzel, B. C., and Howard, A. J. (1986) *Biochemistry* **25**, 5314-5322.
185. Christopherson, K. S., and Bredt, D. S. (1997) *J Clin Invest* **100**, 2424-2429.
186. McMillan, K., and Masters, B. S. (1995) *Biochemistry* **34**, 3686-3693.
187. Noble, M. A., Munro, A. W., Rivers, S. L., Robledo, L., Daff, S. N., Yellowlees, L. J., Shimizu, T., Sagami, I., Guillemette, J. G., and Chapman, S. K. (1999) *Biochemistry* **38**, 16413-16418.
188. Perry, J. M., Moon, N., Zhao, Y., Dunham, W. R., and Marletta, M. A. (1998) *Chem Biol* **5**, 355-364.
189. Matsuda, H., Kimura, S., and Iyanagi, T. (2000) *Biochim Biophys Acta* **1459**, 106-116.
190. Lane, P., and Gross, S. S. (2002) *J Biol Chem* **277**, 19087-19094.
191. Adak, S., Sharma, M., Meade, A. L., and Stuehr, D. J. (2002) *Proc Natl Acad Sci U S A* **99**, 13516-13521.

192. (2001) in *Genetics Computer Group*, 10.1 Ed., Madison, WI, USA
193. Altschul, S. F., Madden, T. L., Schaffer, A. A., Zhang, J., Zhang, Z., Miller, W., and Lipman, D. J. (1997) *Nucleic Acids Res* **25**, 3389-3402.
194. Zhao, Q., Modi, S., Smith, G., Paine, M., McDonagh, P. D., Wolf, C. R., Tew, D., Lian, L. Y., Roberts, G. C., and Driessen, H. P. (1999) *Protein Sci* **8**, 298-306.
195. Sali, A., and Blundell, T. L. (1990) *J Mol Biol* **212**, 403-428.
196. Thompson, J. D., Higgins, D. G., and Gibson, T. J. (1994) *Nucleic Acids Res* **22**, 4673-4680.
197. Cuff, J. A., Clamp, M. E., Siddiqui, A. S., Finlay, M., and Barton, G. J. (1998) *Bioinformatics* **14**, 892-893.
198. Bateman, A., Birney, E., Cerruti, L., Durbin, R., Etwiller, L., Eddy, S. R., Griffiths-Jones, S., Howe, K. L., Marshall, M., and Sonnhammer, E. L. (2002) *Nucleic Acids Res* **30**, 276-280.
199. Hall, A. V., Antoniou, H., Wang, Y., Cheung, A. H., Arbus, A. M., Olson, S. L., Lu, W. C., Kau, C. L., and Marsden, P. A. (1994) *J Biol Chem* **269**, 33082-33090.
200. Sali, A., and Blundell, T. L. (1993) *J Mol Biol* **234**, 779-815.
201. Cornell, W., Cieplak, P., Gould, B. C. I., Merz, K., Ferguson, D., Spellmeyer, D., Fox, T., Caldwell, J., and Kollman, P. (1995) *J. Am. Chem. Soc.* **117**, 5179-5197.
202. Laskowski, R. A., MacArthur, M. W., Moss, D. S., and Thornton, J. M. (1993) *J. Appl. Cryst.* **26**, 283-291.
203. Sippl, M. J. (1993) *J Comput Aided Mol Des* **7**, 473-501.
204. Vriend, G., and Sander, C. (1993) *J. Appl. Cryst.* **26**, 47-60.
205. Hooft, R. W., Vriend, G., Sander, C., and Abola, E. E. (1996) *Nature* **381**, 272.
206. Sanchez, R., and Sali, A. (1997) *Proteins* **Suppl**, 50-58.
207. Ferrin, T. E., Huang, C. C., Jarvis, L. E., and Langridge, R. (1988) *J. Mol. Graph.* **6**, 13-27.
208. Ke, S. H., and Madison, E. L. (1997) *Nucleic Acids Res* **25**, 3371-3372.
209. Vol. 2001, National Center for Biotechnology Information, National Library of Medicine
210. Leclerc, D., Wilson, A., Dumas, R., Gafuik, C., Song, D., Watkins, D., Heng, H. H., Rommens, J. M., Scherer, S. W., Rosenblatt, D. S., and Gravel, R. A. (1998) *Proc Natl Acad Sci U S A* **95**, 3059-3064.
211. Rao, S. T., Shaffie, F., Yu, C., Satyshur, K. A., Stockman, B. J., Markley, J. L., and Sundarlingam, M. (1992) *Protein Sci* **1**, 1413-1427.
212. Walsh, M. A., McCarthy, A., O'Farrell, P. A., McArdle, P., Cunningham, P. D., Mayhew, S. G., and Higgins, T. M. (1991) *Eur. J. Biochem.* **258**, 362-371.
213. Sauder, J. M., Arthur, J. W., and Dunbrack, R. L., Jr. (2000) *Proteins* **40**, 6-22.
214. Chang, Y. T., and Loew, G. (2000) *Biochemistry* **39**, 2484-2498.
215. Hubbard, P. A., Shen, A. L., Paschke, R., Kasper, C. B., and Kim, J. J. (2001) *J Biol Chem* **276**, 29163-29170.
216. Champier, L., Sibille, N., Bersch, B., Brutscher, B., Blackledge, M., and Coves, J. (2002) *Biochemistry* **41**, 3770-3780.
217. Gutierrez, A., Paine, M., Wolf, C. R., Scrutton, N. S., and Roberts, G. C. (2002) *Biochemistry* **41**, 4626-4637.
218. George, S. E., Su, Z., Fan, D., Wang, S., and Johnson, J. D. (1996) *Biochemistry* **35**, 8307-8313.

219. Sagami, I., Daff, S., and Shimizu, T. (2001) *J Biol Chem* **276**, 30036-30042.
220. Hurshman, A. R., and Marletta, M. A. (2002) *Biochemistry* **41**, 3439-3456.
221. Xia, Y., Tsai, A.-L., Berka, V., and Zweier, J. L. (1998) *J. Biol. Chem.* **273**, 25804-25808.
222. Pou, S., Pou, W. S., Bredt, D. S., Snyder, S. H., and Rosen, G. M. (1992) *J Biol Chem* **267**, 24173-24176.
223. Vasquez-Vivar, J., Kalyanaraman, B., Martasek, P., Hogg, N., Masters, B. S., Karoui, H., Tordo, P., and Pritchard, K. A., Jr. (1998) *Proc Natl Acad Sci U S A* **95**, 9220-9225.
224. Rosen, G. M., Tsai, P., Weaver, J., Porasuphatana, S., Roman, L. J., Starkov, A. A., Fiskum, G., and Pou, S. (2002) *J. Biol. Chem.* **277**, 40275-40280.
225. Vasquez-Vivar, J., Hogg, N., Martasek, P., Karoui, H., Pritchard, K. A., Jr., and Kalyanaraman, B. (1999) *J. Biol. Chem.* **274**, 26736-26742.
226. Xia, Y., Roman, L. J., Masters, B. S., and Zweier, J. L. (1998) *J Biol Chem* **273**, 22635-22639.
227. Panda, K., Rosenfeld, R. J., Ghosh, S., Meade, A. L., Getzoff, E. D., and Stuehr, D. J. (2002) *J. Biol. Chem.* **277**, 31020-31030.
228. Ghosh, D. K., and Stuehr, D. J. (1995) *Biochemistry* **34**, 801-807.
229. Rodriguez-Crespo, I., Gerber, N. C., and Ortiz de Montellano, P. R. (1996) *J Biol Chem* **271**, 11462-11467.
230. Rodriguez-Crespo, I., and Ortiz de Montellano, P. R. (1996) *Arch Biochem Biophys* **336**, 151-156.
231. Inoue, H., Nojima, H., and Okayama, H. (1990) *Gene* **96**, 23-28.
232. Shevchenko. (1996) *Anal. Chem.* **68**, 850-858.
233. Siegel, and Monty. (1966) *Biochim Biophys Acta* **112**, 346-362.
234. Garcia De La Torre, J., Huertas, M. L., and Carrasco, B. (2000) *Biophys J* **78**, 719-730.
235. Katchalski-Katzir, E., Shariv, I., Eisenstein, M., Friesem, A. A., Aflalo, C., and Vakser, I. A. (1992) *Proc Natl Acad Sci U S A* **89**, 2195-2199.
236. Nicholls, A., Sharp, K. A., and Honig, B. (1991) *Proteins* **11**, 281-296.
237. Armon, A., Graur, D., and Ben-Tal, N. (2001) *J Mol Biol* **307**, 447-463.
238. Pace, C. N., Vajdos, F., Fee, L., Grimsley, G., and Gray, T. (1995) *Protein Sci* **4**, 2411-2423.
239. Hevel, J. M., and Marletta, M. A. (1994) *Methods Enzymol* **233**, 250-258.
240. Johnson, M. L., Correia, J. J., Yphantis, D. A., and Halvorson, H. R. (1981) *Biophys J* **36**, 575-588.
241. Laue, T. M., and Stafford, W. F., 3rd. (1999) *Annu Rev Biophys Biomol Struct* **28**, 75-100.
242. Schuck, P. (2000) *Biophys J* **78**, 1606-1619.
243. Tsien, R., and Pozzan, T. (1989) *Methods Enzymol* **172**, 230-262.
244. Chen, P. F., Tsai, A. L., Berka, V., and Wu, K. K. (1996) *J Biol Chem* **271**, 14631-14635.
245. Bender, A. T., Nakatsuka, M., and Osawa, Y. (2000) *J. Biol. Chem.* **275**, 26018-26023.
246. Panda, K., Suresh, J. R., Ila, H., and Junjappa, H. (2003) *J Org Chem* **68**, 3498-3506.

247. Klatt, P., Heinzel, B., Mayer, B., Ambach, E., Werner-Felmayer, G., Wachter, H., and Werner, E. R. (1992) *FEBS Lett* **305**, 160-162.
248. Li, H., Martasek, P., Shimizu, H., Masters, B.S.S., Poulos, T.L., Raman, C.S. (deposition 24-Feb-03) *The Protein Databank*
249. Kolodziejski, P. J., Rashid, M. B., and Eissa, N. T. (2003) *Proc Natl Acad Sci U S A* **100**, 14263-14268.
250. Ghosh, S., Wolan, D., Adak, S., Crane, B. R., Kwon, N. S., Tainer, J. A., Getzoff, E. D., and Stuehr, D. J. (1999) *J. Biol. Chem.* **274**, 24100-24112.
251. Ghosh, D. K., Crane, B. R., Ghosh, S., Wolan, D., Gachhui, R., Crooks, C., Presta, A., Tainer, J. A., Getzoff, E. D., and Stuehr, D. J. (1999) *Embo J* **18**, 6260-6270.
252. Wei, C. C., Wang, Z. Q., Arvai, A. S., Hemann, C., Hille, R., Getzoff, E. D., and Stuehr, D. J. (2003) *Biochemistry* **42**, 1969-1977.
253. Abu-Soud, H. M., Loftus, M., and Stuehr, D. J. (1995) *Biochemistry* **34**, 11167-11175.
254. Lee, C. M., Robinson, L. J., and Michel, T. (1995) *J Biol Chem* **270**, 27403-27406.
255. Glaser, F., Pupko, T., Paz, I., Bell, R. E., Bechor-Shental, D., Martz, E., and Ben-Tal, N. (2003) *Bioinformatics* **19**, 163-164.

APPENDIX A.

Figure A-1. The major splice forms of nNOS, eNOS and iNOS were aligned using ClustalW v. 1.82 (196), and manually adjusted within the N-terminus that does not share significant sequence identity until the beginning of the oxygenase domain. (Periods, colons, and asterisks designate increasing degrees of sequence conservation.) Swissprot accession numbers: Q9Z0J4, P29474; P35228. The PDZ domain of nNOS is highlighted in turquoise, the oxygenase domain is highlighted in yellow, and the reductase domain is highlighted in green. The Zn, heme, H_4B, L-Arg, CaM, FMN, FAD, and NADPH binding sites are labeled above the sequences. Alterations found in the different splice forms are designated with boxed text: The nNOS-1β start site at residue 236 has the alternate sequence MRGLGS. nNOS-1γ begins at residue 337. The nNOS-1μ inserted sequence at residue 834 replaces K with KYPEPLRFFPRKGPSASHVD-SEAHSLVAARDSQHR. The deleted sequence from nNOS-2 is from 509-613. NS2A-2 has residues 2640288 and 298-311 deleted.

```
nNOS-1a         MEDHMFGVQQIQPNVISVRLFKRKVGGLGFLVKERVSKPPVIISDLIRGGAAEQSGLIQA 60
nNOS-1a         GDIILAVNGRPLVDLSYDSALEVLRGIASETHVVLILRGPEGFTTHLETTFTGDGTPKTI 120
nNOS-1a         RVTQPLGPPTKAVDLSHQPPAGKEQPLAVDGASGPGNGPQHAYDDGQEAGSLPHANGLAP 180

nNOS-1a         RPPGQDPAKKATRVSLQGRGENNELLKEIEPVLSLLTSGSRGVKGGAPAKAEMKDMGIQV 240
eNOS            -------------------------------------------------------MGN 3
iNOS2A          ----------------------------------------MACPWKFLFKTKFHQYAMN 19

nNOS-1a         DRDLDGKSHKPLPLGVENDRVFNDLWGKGNVPVVLNNPYSEKEQPPTSGKQSPTKNGSPS 300
eNOS            LKSVAQEPGPPCGLGLGLGLGLCGKQGPATPAPEPSRAPASLLPPAPEHSPPSSPLTQPP 63
iNOS2A          GEKDINNNVEKAPCATSSPVTQDDLQYHNLSKQQNESPQPLVETGKKSPESLVKLDATPL 79

                                              |-Zn-|
nNOS-1a         KCPRFLKVKNWETEVVLTDTLHLKSTLETGCTEYICMGSIMHPSQHARRPE-DVRTKGQL 359
eNOS            EGPKFPRVKNWEVGSITYDTLSAQAQQDGPCTPRRCLGSLVFPRKLQGRPSPGPPAPEQL 123
iNOS2A          SSPRHVRIKNWGSGMTFQDTLHHKAKGILTCRSKSCLGSIMTPKSLTRGPRDKPTPPDEL 139
                . *:. ::***       ***  ::     *    *:**:: * .    *     .  :*

                                                                      |-----
nNOS-1a         FPLAKEFIDQYYSSIKRFGSKAHMERLEEVNKEIDTTSTYQLKDTELIYGAKHAWRNASR 419
eNOS            LSQARDFINQYYSSIKRSGSQAHEQRLQEVEAEVAATGTYQLRESELVFGAKQAWRNAPR 183
iNOS2A          LPQAIEFVNQYYGSFKEAKIEEHLARVEAVTKEIETTGTYQLTGDELIFATKQAWRNAPR 199
                :. * :*::***.*:*.   : *  *:: *  *: :*.****   **:::.:*:*****.*

                -heme--|
nNOS-1a         CVGRIQWSKLQVFDARDCTTAHGMFNYICNHVKYATNKGNLRSAITIFPQRTDGKHDFRV 479
eNOS            CVGRIQWGKLQVFDARDCRSAQEMFTYICNHIKYATNRGNLRSAITVFPQRCPGRGDFRI 243
iNOS2A          CIGRIQWSNLQVFDARSCSTAREMFEHICRHVRYSTNNGNIRSAITVFPQRSDGKHDFRV 259
                *:*****.:*******.* :*: ** :**.*::*:**.**:*****:****  *: ***:

nNOS-1a         WNSQLIRYAGYKQPDGSTLGDPANVQFTEICIQQGWKPPRGRFDVLPLLLQANGNDPELF 539
eNOS            WNSQLVRYAGYRQQDGSVRGDPANVEITELCIQHGWTPGNGRFDVLPLLLQAPDEPPELF 303
iNOS2A          WNAQLIRYAGYQMPDGSIRGDPANVEFTQLCIDLGWKPKYGRFDVVPLVLQANGRDPELF 319
                **:**:*****:  ***  ******::*::**: **.*  *****:**:*** .. ****

nNOS-1a         QIPPELVLEVPIRHPKFEWFKDLGLKWYGLPAVSNMLLEIGGLEFSACPFSGWYMGTEIG 599
eNOS            LLPPELVLEVPLEHPTLEWFAALGLRWYALPAVSNMLLEIGGLEFPAAPFSGWYMSTEIG 363
iNOS2A          EIPPDLVLEVAMEHPKYEWFRELELKWYALPAVANMLLEVGGLEFPGCPFNGWYMGTEIG 379
                 :**:*****.:.**. ***  * *:**.****:*****:*****...**.****.****
```

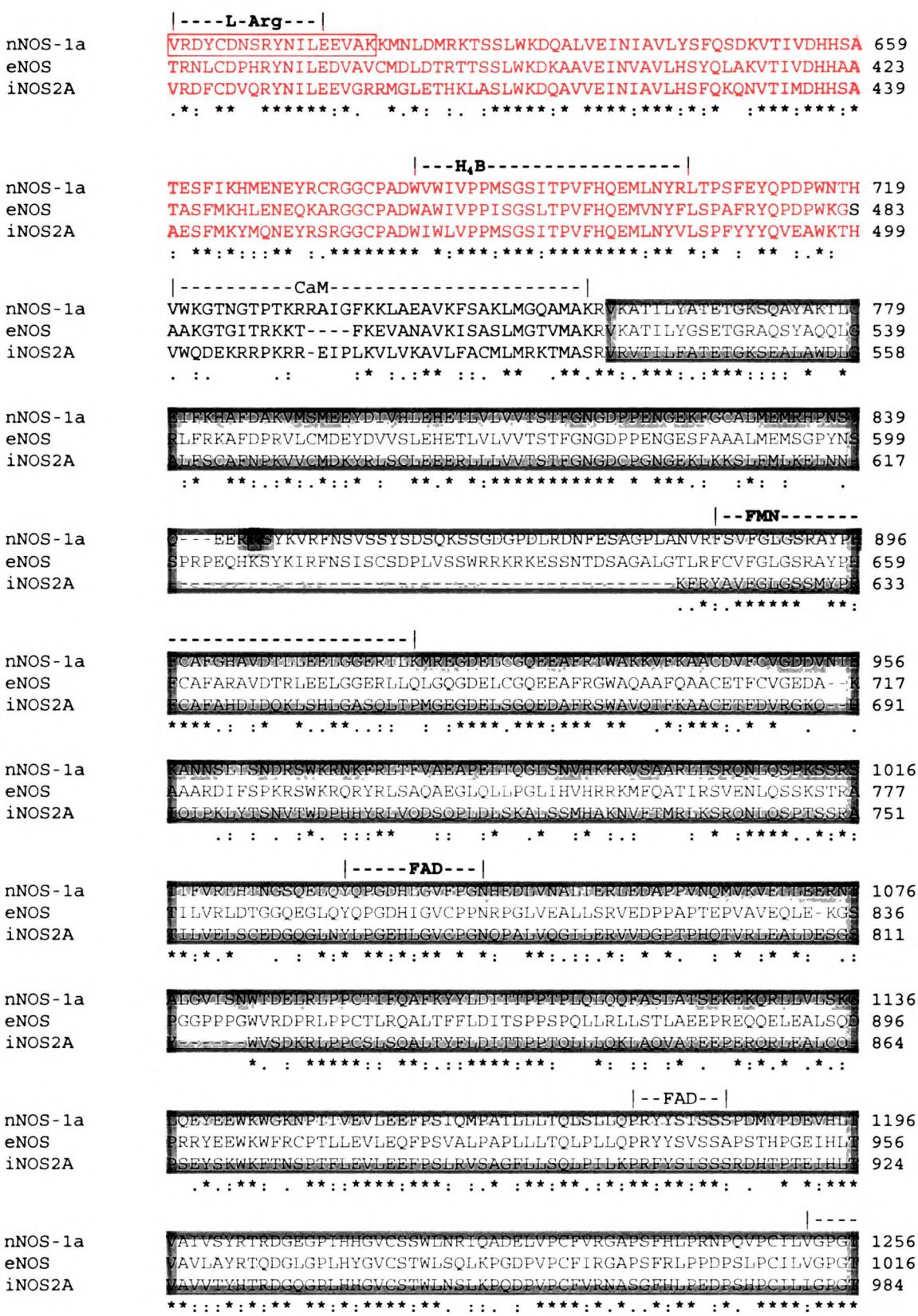
|----L-Arg---|
nNOS-1a VRDYCDNSRYNILEEVAKKMNLDMRKTSSLWKDQALVEINIAVLYSFQSDKVTIVDHHSA 659
eNOS TRNLCDPHRYNILEDVAVCMDLDTRTTSSLWKDKAAVEINVAVLHSYQLAKVTIVDHHAA 423
iNOS2A VRDFCDVQRYNILEEVGRRMGLETHKLASLWKDQAVVEINIAVLHSFQKQNVTIMDHHSA 439
|---H4B----------|
nNOS-1a TESFIKHMENEYRCRGGCPADWVWIVPPMSGSITPVFHQEMLNYRLTPSFEYQPDPWNTH 719
eNOS TASFMKHLENEQKARGGCPADWAWIVPPISGSLTPVFHQEMVNYFLSPAFRYQPDPWKGS 483
iNOS2A AESFMKYMQNEYRSRGGCPADWIWLVPPMSGSITPVFHQEMLNYVLSPFYYYQVEAWKTH 499
|----------CaM----------|
nNOS-1a VWKGTNGTPTKRRAIGFKKLAEAVKFSAKLMGQAMAKRVKATILYATETGKSQAYAKTLC 779
eNOS AAKGTGITRKKT----FKEVANAVKISASLMGTVMAKRVKATILYGSETGRAQSYAQQLG 539
iNOS2A VWQDEKRRPKRR-EIPLKVLVKAVLFACMLMRKTMASRVRVTILFATETGKSEALAWDLG 558
|--FMN-------
nNOS-1a QFRKHAFDAKVMSMEEYDIVHLEHETLVLVVTSTFGNGDPPENGEKFGCALMEMRHPNSV 839
eNOS RLFRKAFDPRVLCMDEYDVVSLEHETLVLVVTSTFGNGDPPENGESFAAALMEMSGPYNS 599
iNOS2A ALFSCAFNPKVVCMDKYRLSCLEEERLLLVVTSTFGNGDCPGNGEKLKKSLFMLKELNNP 617
|--FAD--|
nNOS-1a QEYEEWKWGKNPTIVEVLEEFPSIQMPATLLLTQLSLLQPRYYSISSSPDMYPDEVHLT 1196
eNOS PRRYEEWKWFRCPTLLEVLEQFPSVALPAPLLLTQLPLLQPRYYSVSSAPSTHPGEIHLT 956
iNOS2A PSEYSKWKFTNSPTFLEVLEEFPSLRVSAGFLLSQLPILKPRFYSISSSRDHTPTEIHLT 924
|----
nNOS-1a VAIVSYRTRDGEGPIHHGVCSSWLNRIQADELVPCFVRGAPSFHLPRNPQVPCILVGPGT 1256
eNOS VAVLAYRTQDGLGPLHYGVCSTWLSQLKPGDPVPCFIRGAPSFRLPPDPSLPCILVGPGT 1016
iNOS2A VAVVTYHTRDGQGPLHHGVCSTWLNSLKPQDPVPCFVRNASGFHLPEDPSHPCILIGPGT 984

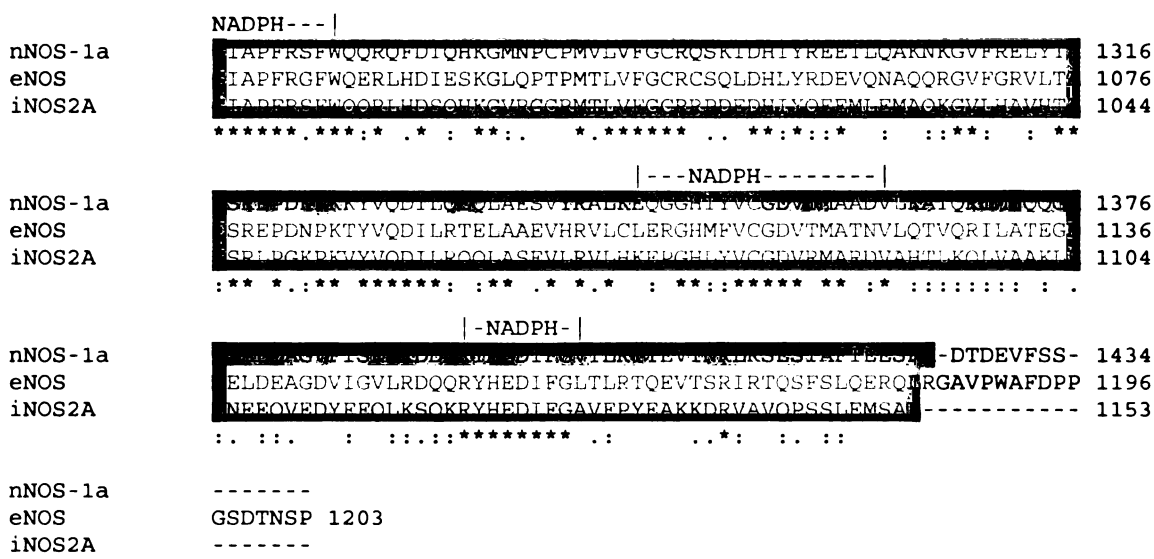

EXON/INTRON SPLICE SITES AND REDUCTASE MODELING

Exon/intron splice sites are not typically used for sequence alignment; however, an interesting argument can be made for the inclusion of splice sites in the alignment of NOS with related reductases. In the case of NOS, the reductase is modular in nature, and several functional elements are distinctly located within a single exon or set of exons. This modular correlation of function with exons is interesting enough that it merits inclusion within this appendix, although it was not included in the publication of our reductase models (37).

Because of the uniqueness of the NOS oxygenase domain fold, it seems logical that the three isoforms resulted from divergent evolution from an ancestral NOS (rather than convergent evolution to independently discover the fold). The ancestral NOS must have been a fusion protein of oxygenase and reductase domains very similar in fold and

function to our current NOS version, hence the first observation that the individual exons in the NOS isoforms have similar length and sequence.

Using several alignment tools, including PSI-BLAST, ClustalW and PFam, the alignments within the more conserved regions between sequences of NOS and CPR agreed, often defining conserved domains and subdomains. Interestingly, the exon splice sites within the domains and subdomains aligned nearly perfectly (within 1-2 amino acids). In regions where sequence conservation was low, the splice sites were often also un-aligned, such as at the interfaces of exons: 14-15, 16-17, 19-20, & 21-22 (nNOS numbering). These un-aligned splice sites were found in regions expected to be divergent between NOS isoforms, and include the transitions between: i) the CaM recognition element and the FMN domain, ii) the AI insertion position within the FMN domain, iii) the insertion position of the disjointed β-sheet portion of the FAD domain inserted within the CD-1, and finally iv) the insertion position of the CD2A loop. By marking and adjusting the exon splice sites to realign these regions, I was able to close most of the gaps within the alignments within unconserved regions to generate my final alignment for the NOS reductase domain models, shown in Figure 3-3.

An important list of exon numbering, included elements and residues is cross-referenced between nNOS, eNOS and iNOS in Table A-1 below.

Table A-1. Exon splice sites within the NOS reductase domain cross-referenced between the three NOS isoforms.

nNOS exon#	*residue numbers*	*function*	*structures included*	*eNOS exon#*	*iNOS exon#*
13	712-740	CaM			
14	741-788	CaM	helix + S + H	12	13
15	789-823		S + S	13	14
16	824-843		H	14	15
17	844-882	A.I.	S	15	-
18	883-940	FMN pyridine	H + S + S	16	16
19	941-986	CD-1	coil	17	17
20	987-1012	FAD-PPi	H	18	18
21	1013-1077	CD-2 (B-sheet)	S + S + H + S	19	19
22	1078-1135	CD-2 (helical)	H + H + H	20	20
23	1136-1205	CD-2/FAD isoallox.	H + H + H + S + S	21	21
24	1206-1231		S + S	22	22
25	1232-1272	NADPH ribose	S + H	23	23
26	1273-1322		S + H + S	24	24
27	1323-1387	NADPH adenosyl	S + H + S + H + H	25	25
28	1388-1427		S + tail	26	26
29	1428-1431	3'-UTR		27	27

APPENDIX B.

PRACTICAL TIPS FOR AUC EXPERIMENTS

Day of experiment:

Wash and prepare all the cell assemblies to the point of sample loading. Put the rotor and monochromator arm into the instrument, set the temperature and pull a vacuum for 2 hours to equilibrate the instrument while preparing samples. I recommend spending time preparing the equipment because cleanliness and equilibration gives good data. For sample loading I prefer gel-loading tips for my P200 pipette. Useful materials for experimental setup include lens paper for cleaning and handling the lenses, standard paper wipes (such as Kimwipes from Fisher) for the other parts, methanol for cleaning, gloves, a tiny flat-head screwdriver, fine-tipped forceps, and a small air canister for removing dust.

Equilibrium Sedimentation Experiment

Protocol:

1. Prepare one sample of ~250 µl at a concentration that gives ~0.7 O.D. at a wavelength that is appropriate for this sample (280 nm is the most common selection). Also reserve the blank buffer from this sample. The best blank is dialysate, using a buffer with low background absorbance at the desired wavelength. It is possible to run up to seven samples using the An50-Ti rotor.

A. *Association stoichiometry analysis*. Prepare a series of samples that vary the stoichiometry, and ask whether the fraction in the associated form increases as a function of component A or component B. Thus, for the system A + B → AB, one would prepare a 1:1, 1:2, 1:4 or 1:10 type of series. These experiments are nicely done when in parallel to activity assays for AB that demonstrate activity dependence upon component stoichiometry.

B. *Association constant analysis*. If instead the stoichiometry is known, for example B + B → B_2, then one would fix the stoichiometry at the optimum 1:1, but vary the concentration range. The concentration range is limited by detection limits for the spectrophotometer. I recommend using as many signals as possible; thus, in my hemoprotein case I observed 230, 280, and 400 nm wavelengths. The extinction coefficient should be estimated as best as possible--either from experimental determination or by calculation from composition using the Edelhoch method (238). The lowest reasonable signal is at 0.1 AU, and the highest is 0.8, because after equilibrium is reached, the concentration distribution will cover a range of signals, for example from 0.03-0.3 and 0.5-1.2 AU for the previous values. One must then trim data that is outside of the linear range of the detector; in practice this is the data outside of the 0.05 to 0.95 O.D. range. Therefore selection of a wavelength to detect depends on the concentration and extinction coefficient of each sample.

2. Prepare the dilutions for each sample during loading. For a standard 6 sector, 1.2 cm centerpiece, load 110 µl of sample into the innermost window position, then 55 µl into the second, and 28 µl into the third. With a fresh tip, load 125 µl of blank into each of the

blank window positions, and then enough blank to complete the 110 µl needed in the last two sample wells (55 µl and 82 µl). The result is a two- and four-fold dilution of the sample. The highest concentration sample should go in the well closest to the center of rotation (*i.e.* at 6.0 cm) because this position is under the least centrifugal force, and the concentration distribution will sediment with less extreme curvature at a smaller radius, giving more data points within the 0.05-0.95 AU window. Also, a good pipetting technique is to point the gel-loading tip into the corner of the sample well and slowly fill the well, allowing the solution to catch the wall and slide to the bottom so that no air-bubbles form. This assures accurate volume measurement. Complete the cell assembly for this sample before loading the next one. In theory this prevents evaporation of a small volume sample, but for more practical reasons this prevents tipping the sample.

3. Release the vacuum on the instrument and check the cell and counterbalance masses to be sure the rotor is balanced. Place the rotor and the monochromator arm into the instrument and pull the vacuum. When the vacuum has reached 50 microns, begin spinning at 3,000 rpm. The first scan to take at this setting is a wavelength scan that covers the wavelengths of interest as well as the 280 nm band. Record at least 3 replicates using a 2 nm step-size. Later this initial scan will be used to calculate the working extinction coefficient for a given sample. Typically I would calculate the 280 nm extinction coefficient based on protein sequence using the Edelhoch method, and then use the ratio of the absorbances at 280 nm and the wavelength observed to determine an experimental extinction coefficient. Set the radial position at 6.0, then 6.5 and 7.0 cm to record wavelength scans for each of the three sample wells.

4. While the wavelength scans are running, the data acquisition settings can be decided. The general plan is to acquire enough data to i) ascertain whether equilibrium has been reached and ii) fit accurately to an equilibrium model.

i) The first time an equilibrium experiment is performed, I recommend recording low resolution scans every one or two hours at a given wavelength to prove to oneself that equilibrium has been reached. Using graphing software such as Microcal Origin, two raw scans can be opened and subtracted, and at equilibrium the difference spectrum should be flat with only noise variation due to the error of detection (~0.01 AU, depending on the wavelength and lamp output). A simple low-resolution setting would record a radial scan using 0.002 cm step-size, taking 3 replicates at each radial step. Equilibrium is usually reached within 19 hours. One should use equation 2 in Chapter 4 to select an angular velocity that will give a sigma value of ~2. In fact three speeds (or more!) should be used for this experiment (each taking >18 hours), which combined with three concentration settings will give a minimum of 9 scans for each sample. Sigma should be varied by two-fold with each speed selected. So, for example my typical rotation speeds were 7, 10, and 14k rpm. The ratio of the sigma values for $7^2/10^2$ is 0.49, and for $14^2/10^2$ is 1.96.

ii) Good data for non-linear least squares regression analysis is acquired at high resolution, using a step size of 0.001 cm, with 7-10 replicates per step. This setting should only be used for the last scan at 18 or 19 hours into the experiment, since these scans can take 30 minutes each. Up to three wavelengths can be chosen for each sample, and if one has 7 samples, the 21 scans can take 10.5 hours, thus slightly lower resolution scans may be desirable for large scale experiments.

5. *Data analysis.* I recommend downloading the WinReedit, and WinNonlin software of D. Yphantis, M. Johnson *et al.* (240). This software is freely available at ftp://alpha.bbri.org/rasmb/spin/spin.html. Reedit is used to trim manually the radial scans into truncated files. Again, data outside of the 0.05-0.95 AU range should be trimmed. 9-15 truncated scans are then loaded and fitted globally in WinNonlin. The program allows one to fit scans from different conditions at once by using concentration and speed factors. The ratio of ω^2 for each speed is used to calculate the speed factor by which sigma is multiplied to give the sigma value appropriate for a given scan. A concentration factor is required when multiple wavelengths are included, but the reader is suggested to derive this factor long-hand given the fitting formula equivalent to formula 1 of Chapter 4. The goal of the calculation is to realize that an association constant fitted by WinNonlin is in OD units at the exact wavelength chosen. Thus, a correction factor is needed to calculate the association constant in concentration units. For the simple homo-dimerization model $B + B \rightarrow B_2$ the derivation is as follows:

1) $\mathrm{Abs(OD)} = \varepsilon\, C\, l$ Beer's law, note l = 1.2 cm. Also, ε of dimer will be twice that of monomer.

2) $K_a(OD^{-1}) = \dfrac{Abs_{dimer}}{(Abs_{monomer})^2}$ The association constant fitted by WinNonlin.

3) $K_a(OD^{-1}) = \dfrac{2\varepsilon_{moner} C_{dimer} l}{(\varepsilon_{monomer} C_{monomer} l)^2}$ Substituting in Beer's law.

$$4)\ K_a(\mu M^{-1}) = \frac{C_{dimer}}{(C_{monome})^2} = K_a(OD^{-1}) * \frac{\varepsilon_{moner} l}{2}$$

One should derive the appropriate correction for each new model, because the association model will be different for each model. To keep things simple, one can begin by fitting scans all taken at the same wavelength.

Sedimentation Velocity Experiment

1. More sample is required for velocity experiments. Prepare ~450 μL of sample that has O.D. at a desired wavelength ~1.0 AU. Be sure to use the appropriate blank buffer that the sample was prepared in. Load 425 μL of blank, then 390 μl of sample into the two chambers of the sedimentation velocity cell. A good pipetting tip for this step is to touch the tip to the bottom of the well and allow the sample to fill from the bottom up, avoiding air bubbles that often cause loss of sample. Also, for the velocity cells, the most common leakage point is at the sample loading holes; I like to place the red seals over the sample loading holes and very gently press them with a pipette tip to create a seal before placing the tiny screws to complete the assembly. Prepare one sample per experiment for the best resolution data (to be discussed below).

2. Again, the sample cell and counterbalance must be balanced to within the tolerance of 0.5 g for the rotor. (One should be sure the counterbalance weighs less than the sample, so that if it leaks, the mass lost will bring the sample mass closer to rather than further from that of the counterbalance.) When the vacuum is below 50 microns, the spin can be started at 3,000 rpm, and the wavelength scan should be recorded at the 6.5 cm position,

in the center of the cell. After the wavelength scan is complete, stop the spin, release the vacuum, and remove the sample. Invert the cell several times to assure that the sample is homogeneously distributed. Repeat the setup and pull the vacuum.

3. For these experiments equilibration of temperature is critical; therefore, one must wait until there is less than 1 °C difference between set and actual chamber temperature. The hydrodynamic properties of proteins depend on the temperature of the experiment, but the analysis method does not allow for altered values of temperature during fitting. Meanwhile the experimental parameters can be set. Select only one wavelength per experimental run. The instrument does not accurately return to a given wavelength when it switches between two or three--the mechanical error in my experience can be 2-4 nm. Select the smallest radial step size of 0.001 cm, and only 1 replicate such that the scan speed is approximately 1 scan per 3 minutes. (Using interference spectroscopy all seven positions in the rotor can be filled, and scans can be recorded almost instantaneously.) Select "no delay" between scans. Set the rotation speed at 50,000 rpm to give the best resolution between species. Set the software to collect 100 scans; then stop the spinning after last scan is taken (~5 h experiment). Start the scan when all the settings are correct.

4. While the instrument is reaching full speed (the "ramp" portion of the experiment) it is smart to watch the position of the meniscus. If it moves, the sample is leaking, and one must unfortunately stop and start over. If there is a spill in the chamber clean it up with methanol and a tissue and allow it to air dry. Otherwise, the experiment is fine and one should return to check the sedimentation progress after 3 h. Usually it will be completely

sedimented and the instrument can be stopped before all the programmed scans are complete.

5. *Data Analysis:* Download the software SedFit by Peter Shuck, available at www.analyticalultracentrifugation.com. One should follow the SedFit tutorial to learn the general fitting method. For my analyses I prefer the continuous C(S) distribution to ask which species are present. Other models are available for known composition or self-association models. The other good distribution is the g*(S) method, useful for poly-disperse systems (say polymerization processes with many species). I suggest reading the support literature to choose the best method. An extremely useful program for calculation of sedimentation parameters is Sednterp by John Philo, available at http://www.jphilo.mailway.com/. The fitted value for the sedimentation coefficient of the species present can be converted to a standardized $S^0_{w,20}$ value using Sednterp. If a structure or model is available for the sample, a Stokes radius can be calculated using the program HydroPro, available at http://leonardo.fcu.um.es/macromol/programs/hydropro/.

APPENDIX C

Date: Mon, 24 Nov 2003 12:10:51 -0500
From: asbmb@asbmb.faseb.org
To: Giselle Knudsen <knudsen@cgl.ucsf.edu>
Subject: Re: reprint permission

Permission granted. Please acknowledge the source of the papers.

Charles C. Hancock, Executive Officer
American Society for Biochemistry and Molecular Biology
9650 Rockville Pike
Bethesda, MD 20814-3996
Phone: 301-634-7145
Fax: 301-634-7126

Date: 11/23/03 11:50
From: <knudsen@cgl.ucsf.edu>
To: asbmb@asbmb.faseb.org
Subject: reprint permission

Dear Sir or Madam,

I am a graduate student at UCSF, and I would like to request permission from the JBC to reprint within my Ph.D. dissertation two articles that I coauthored:

Knudsen, G. M., Nishida, C. R., Mooney, S. D., and P. R. Ortiz de Montellano (2003) "NOS Reductase Domain Models Suggest a New Control Element in eNOS that Attenuates CaM-dependent Activity" J. Biol. Chem. 278 (34), 3814-24.

Rodriguez-Crespo, I., Knudsen, G. M., Nishida, C. R., and P. R. Ortiz de Montellano (1999) "Mutation of the Five conserved Histidines in the Endothelial Nitric-oxide Synthase Hemoprotein Domain: No Evidence for a Non-heme Metal Requirement for Catalysis" J. Biol. Chem. 274 (31), 21617-21624.

Could you please direct me to the proper contact person from whom I should request reprint permission? I will of course be happy to agree to any citation requirements crediting the original publication source, and I have requested permission from my coauthors. If it is convenient, a response by fax or e-mail would be fine.

Thank you very much for your assistance.

Sincerely,

Giselle M. Knudsen
knudsen@cgl.ucsf.edu
Dept. of Pharmaceutical Chemistry
UCSF Genentech Hall, N574
San Francisco, CA 94143-2280
tel: (415) 476-4420
fax: (415) 502-4728

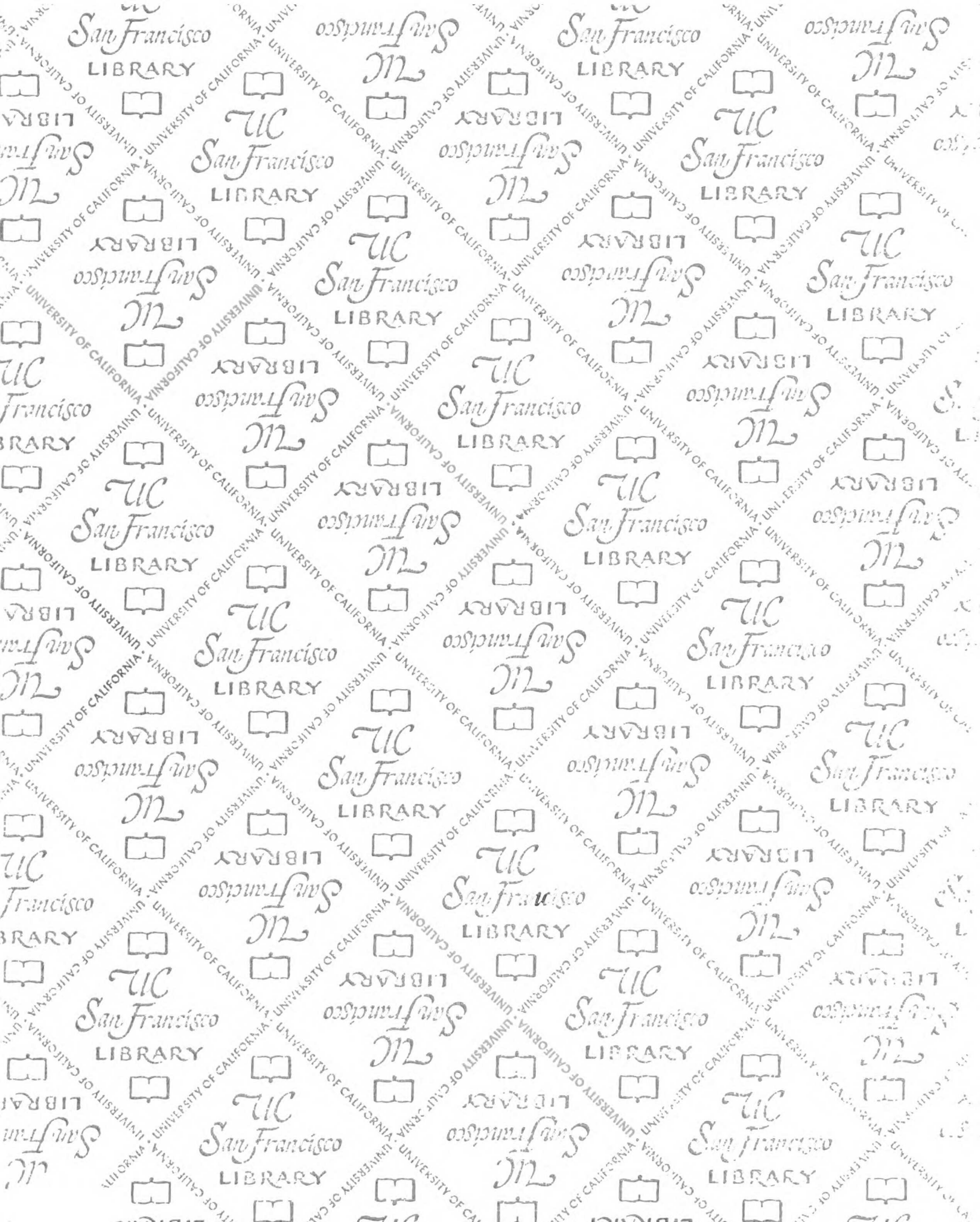
UC
San Francisco
LIBRARY
UNIVERSITY OF CALIFORNIA · UNIVERSITY OF CALIFORNIA